NUMERICAL MODELLING OF THE FLOW ABOUT ARTIFICIAL REEFS

By

YASSIR ALI ALBOURAEE

in partial fulfilment of
the requirements for
the Degree of
DOCTOR OF PHILOSPHY
March/ 2013

Submitted to the School of Marine Science
& technology in Faculty of Science,
Agriculture & Engineering
Newcastle University

Abstract

Artificial reefs have been serving the world in many fields, such as protecting beach erosion, enhancing recreational fishing, surfing and fostering biotic diversity, for many years. One major use for an artificial reef is to deploy it effectively to attract and aggregate fishes and marine life organisms for commercial and scientific purposes. The global hydrodynamic conditions in the vicinity of an artificial reef dictate its structural design (reef stability etc) and the nature of its large scale environmental impact (sediment transport and erosion etc), as well as its operational characteristics. On the West Coast of Scotland an artificial reef was deployed under the direction of Dunstaffnage Marine Laboratory in 2001. It was designed by the fishing industry to promote the economic potential of reef-based fisheries such as the European Lobster (*Homarus gammarus* (L.)). The size of the reef site equates to about 50 football pitches. There are forty two artificial reefs, comprising two different types of reef module, and 25,000 tons of concrete blocks have been used to create each one of them.

However, the investigation of global hydrodynamics requires solving the tidal flow in Loch Linnhe. A numerical model has been adopted to solve the 2D shallow water equations using a Finite Volume Godunov-type scheme. The scheme has the ability to deal with complicated topography such as Loch Linnhe. The initial and boundary conditions of the two-dimensional numerical model were imposed using tidal records obtained from the UK Hydrographical Office for the inlet and outlet of the Loch. A tidal field measurement was carried out using ADCP (Acoustic Doppler Current Profiler) instruments for the purposes of input to the model as well as its validation. These instruments were positioned on location near a group of artificial reefs to gather tidal wave elevations and currents profiles. The results of a two-dimensional numerical model were compared with the data given by the ADCP instruments and tides gauges station in the Loch. A good agreement was observed between the numerical model and data measurement taken from ADCP. The result of the two-dimensional numerical model indicates the ability of the model to represent the complex tidal conditions in the region convincingly. The local hydrodynamic conditions dictate flow separation and the production of turbulence generating eddies and vortices over a range of scales. This, in turn, determines the water quality characteristics, such as the oxygen content, and settlement patterns over the reef and regions favourable, or otherwise, to fish activity (predation, evasion, congregation etc). For these reasons, a reliable

procedure for determining the hydrodynamics of local and global of flows about artificial reefs is an essential prerequisite to their satisfactory design. The ADCP instruments were placed in three locations over a complete spring-neap tides cycle around a selected reef to investigate the three-dimensional hydrodynamics affecting it. The RNG k-ε turbulent model based on Fluent CFD (ANAYSIS 13) was matched to the global flows output from the shallow water flow model and used to simulate the hydrodynamic forces and flow fields with different flow velocity profiles of the tidal currents. The tidal current dynamics profile over a complete daily spring tidal cycle was investigated to identify the flow regimes on the reef. The results of the numerical model were compared with the data gained from the ADCP beside the chosen artificial reef.

"This Thesis is dedicated to my family, especially my mother for her endless love, support and encouragement"

Acknowledgements

My thesis is the end of my journey in obtaining my PhD and I am very thankful to numerous people who supported and encouraged me during this journey. Indeed, I would like to thank all those people who made this thesis possible and an unforgettable experience for me. I gratefully acknowledge King Abdulaziz University for her funding of this PhD research. I take this opportunity to sincerely acknowledge the Scottish Association for Marine Science Institute, Oban (SAMS) for carrying out the field measurements. Most of the results presented here would not have been obtained without the collaboration of SAMS. I am also extremely indebted to my two supervisors, Prof. Martin Downie and Dr. Qiuhua Liang who guided me in this research. This work would not have possible without their guidance, support and encouragement. Finally, I offer my heartfelt thanks to my family for their support over the past few years.

Table of contents

Abstract…… i

Acknowledgements…… iv

Table of content…… v

List of figures…… ix

List of tables…… xxvii

Nomenclature…… xxviii

Chapter 1: The importance of artificial reef numerical modelling **Page**

1. Introduction…… 1

1.1 Aims and objectives…… 3

1.2 Thesis structure…… 4

1.2.1 *Artificial reefs development and application with focus on Loch Linnhe reefs ecology and the physical characteristics affecting the artificial reef*…… 5

1.2.2 *The Finite Volume Method techniques applied to Loch Linnhe tidal flows*…… 6

1.2.3 *ADCP field measurement*…… 6

1.2.4 *The tidal simulation of the Loch Linnhe adopting the two-shallow water equations*…… 6

1.2.5 *The three-dimensional artificial reef turbulence modelling*…… 7

1.2.6 *Discussions and conclusions*…… 7

Chapter 2: Artificial reefs development and application with focus on Loch Linnhe reefs ecology and the physical characteristics affecting the artificial reef **Page**

2. Introduction…… 8

2.1 Artificial reef review…… 9

2.1.1 *Artificial reefs development*…… 9

2.1.2 *Artificial reefs application*…… 13

2.1.2.(A) *Fishing reefs and management*…… 13

2.1.2.(B) *Artificial reefs for marine restoration and habitat enhancement*……..…. 14

2.1.2.(C) *Artificial reefs for recreational purposes*…….…..…. 14

2.1.2.(D) *Other Artificial reef function and marine infrastructure*…….…….... 14

2.2 Introduction to Loch Linnhe artificial reef…….…… 15

2.2.1 *Loch Linnhe artificial reef and structure complexity*…….....…… 15

2.2.2 *Epiflora and Epifauna colonization and the Loch Linnhe artificial reef*……...……... 20

2.2.3 *The attraction-production debate and the Loch Linnhe artificial reef*……...……... 22

2.3 The physical oceanographic factors affecting the artificial reef……..……..…… 27

2.3.1 *The receiving environment and construction materials*…….…... 27

2.3.2 *Artificial reef surface and deployment time*……..… 28

2.3.3 *Artificial reef structure and hydrodynamics regime*……....…… 29

2.4 Cases for marine structure under hydrodynamics conditions……..…. 31

2.4.1 *Offshore wind-turbine as an artificial reef*……...…….…… 31

2.4.2 *Artificial reef in the Western Adriatic Sea, Italy*……..…… 35

2.5 Summary of artificial reef hydrodynamics and its environmental impacts…….…… 36

Chapter 3: Tidal phenomena and numerical modelling of the shallow water equations **Page**

3. Introduction.……...…….…….…. 37

3.1 The tides patterns and prediction……..…… 38

3.2 Summary of numerical method applied to model tides……...… 41

3.3 Review of Godunov-type Finite Volume solvers.……..... 44

3.4 Model governing equations……...…… 46

3.5 One-dimensional tidal wave flow tests…… 46

3.5.1 *Tidal wave test objective*……..……..…… 47

3.5.2 *Tidal wave flow in a channel over non-uniform bed topology*….. 47

3.5.3 *A tidal wave propagating inside a channel over an irregular bed*……..……..…. 51

3.6 The numerical modelling for the tidal dynamics of Cook Strait……..…. 54

3.7 The Finite Volume Method for Cook Strait tidal dynamics……..…. 57

3.7.1 *Model configuration*……..……...…. 60

3.7.2 *The initial and boundary conditions for the Cook Strait tidal simulation*…..……..……..…… 61

3.7.3 *The results of the Cook Strait tidal wave analysis*…… 64

3.8 The comparison between the numerical models…… 67

Chapter 4: Tides and tidal current profiling measurements **Page**

4. Introduction……...……..…… 71

4.1 ADCP geographical setting in the Loch Linnhe…… 74

4.2 The characteristics of ADCP data measurements……..…… 74

4.3 The spring and neap lunar period selection from the ADCP instruments……. 77

4.4 Tidal current profiles for spring and neap for a daily tidal wave period…. 87

Chapter 5: The numerical modelling of Loch Linnhe tides dynamics applying the 2D shallow water equations **Page**

5. Introduction……..……...…… 93

5.1 The Loch Linnhe tidal dynamics simulation……..…… 94

5.2 Model configuration……...……...…… 97

5.3 The Loch Linnhe harmonic analysis……...……...……..…… 101

5.4 The initial and boundary conditions for Loch Linnhe……....…. 103

5.5 The Loch Linnhe tidal analysis results……..…… 105

5.5.1 *The convergence curve of the Finite Volume Method numerical model*……...……...…… 106

5.5.2 *The daily tidal wave of the Loch Linnhe for spring and neap cycles*……...……...…… 110

5.5.3 *The tidal wave dynamics of the Loch Linnhe during a lunar cycle*……..…… 122

Chapter 6: The three-dimensional artificial reef turbulence modelling **Page**

6. Introduction.……...…..…….…… 129

6.1 The k-ε turbulence model.……...…...…… 130

6.2 Test case of a Backward Facing Step…….……...…..…… 131

6.3 The artificial reef with initial conditions of the tidal velocity flow profile……...……...…… 135

6.3.1 *The numerical method and model configuration*…….…… 135

6.3.2 *The results of the tidal current flow profile*……..... 138

6.4 A comparison between flows based on numerically and empirically derived starting conditions……..……..…….……... 140

6.5 The artificial reef under varying tidal current profiles…..……...…… 159

Chapter 7: Discussion and Conclusions **Page**

7.1 The tides hydrodynamics on the Loch Linnhe…..……..…….…...……..… 172

7.2 The detailed hydrodynamics about the reef…..……..……..…..……..…… 172

7.3 The ecological effect of hydrodynamics on the artificial reef habitats….. 173

7.4 Concluding comments…..……..……..……...……...……..……..… 174

7.5 Suggestions for future work……..……..……...……...……..……..…… 175

Appendix: (A)…..……...……..……..…..……...…..……..….. 176

Appendix: (B)……...……..…..…..…..… 181

Appendix: (C)……...……...…… 194

Appendix: (D)…….……...…….…… 201

References……...…….. 205

List of figures

Page

Figure 2.1	Artificial reef sites and fish species living near it in Japan (Thierry, 1988)……..……..	11
Figure 2.2	The artificial reef positions in Taiwan 1973-1979 (Chang and Shao, 1988)……..……	11
Figure 2.3	Early artificial reefs were made from scrap materials including old tyres which were cost millions of dollars to remove it (Diplock, 2008)….	12
Figure 2.4	The south of Loch Linnhe with the positions of the artificial reefs…….……	16
Figure 2.5	The artificial reef sits in the Loch Linnhe (Wilding, 2010)……..……	17
Figure 2.6	Block of the complex (right) and simple (left). The block dimensions 21 x 21x 42 cm (Wilding, 2010). ……	18
Figure 2.7	The crane on the surface barge deploying the blocks that construct the artificial reefs (Wilding, 2010)…….……	18
Figure 2.8	An example of the Multi-beam SONAR showing the seabed with section of six artificial reef modules (C1c,C2c, C3c) modules consist of complex blocks and (C1s,C2s and C3s) simple blocks reef (Beaumont, 2006)……..……..…	19
Figure 2.9	The four layers of marine biofouling (Davis, 1995)…….……..	20
Figure 2.10	Loch Linnhe complex module (a) shortly after deployment (b) more than 12 months of biofouling (Beaumont, 2006)…….……	22

Figure 2.11.a, b	The prediction of the attraction and production assumptions against artificial reef size (a) attraction hypothesis [fish production is constant] whereas (b) production hypothesis [fish production rises linearly as artificial reef create new habitat] (Wilson et al., 2001)……..……	24
Figure 2.12	Bohnsack (1989) predicted linear or saturation functions which indicate if the fish population is recruit limited it will not be matter to increase space of the artificial reef since it will not rises the fishery. However, if it is space limited, and artificial reefs increase the volume of space available, then they might serve to increase fish production……..……	25
Figure 2.13	The gradients predicted to be important for attraction versus production at artificial reef location which indicate a linear response as Bohnsack (1989) suggested……	26
Figure 2.14	Rock armour used around a monpile turbine foundation to protect it from scouring (Barton, 2006)……...…..……..……	32
Figure 2.15	A massive colonization of the common mussel on turbine foundation at Horns Rev (The Danish Forest and Nature Agency, 2006)……..……	33
Figure 2.16	The flow pattern variation as a steady current passes a vertical pile (Roulund et al., 2005)……..…	34
Figure 2.17	The flow pattern downstream schematic over a sill (Hoffmans and Verheij, 1997)……..…...……	35

Figure 2.18	The depth profile of a pyramid artificial reef indicting the sediment surrounding the reef due to Ocean conditions after 33 years of deployments (Manoukian et al., 2011)…….……..……	36
Figure 3.1	The tidal bulges centres may be set at any latitude from the equator with a declination angle 28.5^{o} on either side of the equator, depending on the season of the year (Trujillo, 2010)……..…..……..……	38
Figure 3.2	The monthly tidal range variations at various sites on the world with different daily tidal patterns (Trujillo, 2010)…….……...…….……	39
Figure 3.3	The relationship of phases seen in spring and neap tides explained by the harmonic constituents (Hicks, 2006)……..……..……	40
Figure 3.4	The water depth definition applied in the numerical scheme……...……...…	48
Figure 3.5	The tidal wave elevation compared with solution suggested by Bermúdez and Vázquez (1994) as a benchmark test for numerical scheme verification for unsteady flows……...…..……	49
Figure 3.6	The tidal current velocities of the each grid-size compared with the analytical solution……...……	49
Figure 3.7	The numerical model results of tidal wave velocity for each mesh size. It was subtracted from the analytical solution to investigate accuracy of the numerical model for each grid……..……..……	50
Figure 3.8	The appropriate time step estimation for each mesh-size in the *x*-direction as calculated by the CFL criterion……...……..…	50

Figure 3.9 The analytical tidal wave elevation compared with the selected group mesh-size over an irregular channel bed……...…… 53

Figure 3.10 The tidal wave velocities for each tested grid-size studied against the analytical solution……..……..… 53

Figure 3.11 The differences between the numerical results of every grid-size with the analytical solution…...…… 54

Figure 3.12 The CFL criterion calculation for the accepted time step during the numerical simulation of the four grid-size in the *x*-direction……...… 54

Figure 3.13 The two islands of New Zealand with the Cook Strait……..…….. 55

Figure 3.14 The computed M_2 high water tidal constituent around New Zealand made by the coastal hydrodynamics group in NIWA. Note that the figure shows the high water only for half cycle see Goring (2001).The grade between red (high) and blue (low) indicate the tidal range height……..… 56

Figure 3.15 The French pass in the Marlborough sound which is the narrowest gap between headlands of the New Zealand two islands (Begg and Johnston, 2000)……...…… 57

Figure 3.16 The Cook Strait numerical domain that was implemented in the tides numerical simulation is represented with the red quadrilateral……...… 58

Figure 3.17 The numerical domain of the Cook Strait with the seabed (m) as recognize in the GIS format……...… 58

Figure 3.18.a, b	The Cook Strait of New Zealand with seabed in Cartesian coordinate system in 3D as seen in (a) and 2D dimension shown in (b)……..…...…	59
Figure 3.19	The input tidal wave for lunar-tide generating force M_2 constituent……..	61
Figure 3.20	The still water elevation at time t=0 with the control input open boundary zone…….……	62
Figure 3.21	The Lunar tidal wave added to the water still elevation (η=$h_s + z_b$) which was applied in the present numerical tides simulation……..…..…	62
Figure 3.22.a, b	The initial conditions at time t=0 that indicate the free surafec elevation cells checkes represented in (a) with fixing the water elevation as seen in (b)….	63
Figure 3.23	The semi-diurnal tidal wave simulation results in the New Zealand Cook Strait region…….……	64
Figure 3.24.a, b	The tidal wave propagating the Cook Strait going through the French pass as demonstrated in (a). The location of the cells checker French pass as exhibited in (b)……..……	65
Figure 3.25.a, b	The velocity vectors in the Cook Strait especially in the Tory channel as shown in (a) and French pass as seen in (b)……..……	66
Figure 3.26.a, b, c	The tidal amplitude of the Cook Strait for the two driving and Gerris numerical models compared with the present Finite Volume Method numerical model…….....	68
Figure 3.27	The positions of the measured tidal amplitude stations around New Zealand……..……...…	69

Figure 3.28	The amplitude of tides for observation with the numerical models results of Gerris Flow solver and the results of the present Finite Volume Method numerical model.……	70
Figure 4.1	The ADCP velocity data series as it recorded by the instrument (Wall et al., 2006)……..…	72
Figure 4.2	The Loch Linnhe artificial reef modules with the chosen group-E at the measurement site……...……	72
Figure 4.3.a, b, c	The position of the ADCP instruments on the chosen artificial reef site from group-E of the artificial reef modules in the Loch Linnhe is spotted in (a) along with the selected reef surrounded by the ADCP instruments is shown in (b) and the installation of the ADCP photography at the reef site is seen in (c) (picture taken from Wilding 2010)……..……...……	73
Figure 4.4	The wave tides as registered by the ADCP instruments after the deployment at the artificial reef in the Loch Linnhe……...……	74
Figure 4.5.a, b	The bins averaged tidal current components of *U* are presented in (a) and *V* is viewed in (b) which was recorded by ADCP instrument presented in the whole time period ……..……	75
Figure 4.6	The *U* (m/sec) component of the velocity profile within a daily spring tidal cycle……..…	76
Figure 4.7	The *V* (m/sec) component of the velocity profile with the same period of the *U* component for a daily spring tidal cycle……	76

Figure 4.8	The daily spring and neap periods adopted in the present work and taken from the data records length……..……	77
Figure 4.9.a, b, c	The analysis of the ADCP No.6358 sited in the Loch Linnhe seen in (a) with the tidal wave and current seeing in (b) with the *U* and *V* component profile contours represented in (c) during the neap period……..……	79
Figure 4.10.a, b, c	The spring tidal wave and currents component for *U* and *V* exhibited in (b) with the ADCP location in (a) and the velocities of *U* and *V* contour profiles in (c) analysis for the ADCP No.6358 data collection……...…	80
Figure 4.11.a, b, c	The ADCP No.3821 data records in (a) for the neap cycle tidal wave with tidal current average are beneath it as seen in (b). The velocity components of *U* and *V* profiles are presented in contours as exposed in (c).....……	82
Figure 4.12.a, b, c	The spring cycle of the ADCP No.3821 measurements is shown in (a) with the tidal wave and current as demonstrated in (b) that includes the velocity profile contours seen in (c)……	83
Figure 4.13.a, b, c	The average tidal current under tidal waves and associated velocities *U* and *V* components is displayed in (b) with profile contours shown in (c) as recorded by the third ADCP No.2260 sited in the Loch Linnhe as seen in (a)……	85

Figure 4.14.a, b, c	The spring period of the ADCP No.2260 measurements positioned in Loch Linnhe as spotted in (a) that shows the tidal current with tidal waves in (b) and the contour of the tidal current *U* and *V* components profiles in (c)…..……	86
Figure 4.15.a , b	The point's position of tidal current profiles selected on the tides wave of spring cycle viewed in (a) and neap cycle seen in (b) which was taken from ADCPNo.6358 measurements. Note that the spring cycle tidal wave indicates unsymmetrical pattern as recorded by the ADCP instrument…...…	88
Figure 4.16.a, b	The process of smoothing the tidal current profiles by implementing the three point moving average technique to the tidal current profiles of the spring and neap tidal wave periods. As the figure indicates the pair-wise velocity profiles in spring cycle are dissimilar due to the unsymmetrical tidal wave pattern existed in the Loch Linnhe as demonstrated in Figure 4.15.a, b…….....…	89
Figure 4.17	The spring tidal current profiles for the first point as represented in the previous Figure 4.15.a, b……	91
Figure 4.18	The neap tidal current profiles for the first point as shown in the previous Figure 4.15.a, b……..…	92
Figure 5.1.a, b	The selected areas of Loch Linnhe with the artificial reef zone as seen from the Admiralty chart with the reefs are near Lismore Island……	95
Figure 5.2.a, b	The focused zone displayed in GIS foramt as seen in (a) and Cartesian coordinate system as presented in (b)……..……	96

Figure 5.3	The tidal strength at the interaction between the Loch Linnhe and Loch Creran from the seafarer's navigation information……	98
Figure 5.4	The sample of a matrix of grid cells (94 × 89) of Longitude and Latitude in the Cartesian system with the blocked dry cells and the location of the weather station as displayed……...……	99
Figure 5.5.a, b	The wind roses during the full deployment period demonstrating the frequency and the amplitude (m/sec) distrubtion of hourly mean winds presnted in (a) and the maximum gust winds within each one houre sample interval in (b). It has been notice that dominant winds were approximatley aligned with the axis of the Loch Linnhe……...……	100
Figure 5.6	The location of the stations required to control the inflow and outflow boundaries……...……	100
Figure 5.7	The harmonic analysis for Port of Oban compared with the measured tides data……...……	102
Figure 5.8	The harmonic analysis for Port of Appin compared with the measured tides data……	102
Figure 5.9	The tidal wave constituent's solution given by UK Hydrographic Office for Pier of Barcaldine……..…	103
Figure 5.10	The still water level at t=0 in the Loch Linnhe with the inflow and outflow boundaries as presented by the numerical model……..…	104
Figure 5.11	The long-section was implemented for checking the water elevation of Loch Linnhe tidal dynamics simulation…….……..	105

Figure 5.12	The montoring cells in the Loch Linnhe during the tidal wave simulation……...……	106
Figure 5.13.a, b	The U and V velocities components of the different mesh grid sizes correlated with the ADCP field measurement for one day cycle……	108
Figure 5.14	The Finite Volume Method convergence curve was performed to judge an adequate fine mesh grid size that provides an accurate numerical solution for mean tidal wave elevation…….……	109
Figure 5.15	The sufficiently refined mesh was converged in the grid cell size of 43.3 m which give a good numerical accuracy for the mean tidal current…….……	109
Figure 5.16	The CFL criterion calculation provides the numerical model with a suitable time step for mesh refinement during the convergence study…….....……	110
Figure 5.17.a, b	The tidal wave elevation for both numerical modelling results and the tides data measurment in a dialy spring(a)-neap(b) tide cycle……...…	111
Figure 5.18.a, b	The numerical monitoring cell at the Port of Appin shown in Figure 5.12 compared with the tides observation taken from Hydrographic Office during a selected daily spring-neap tidal wave cycle……...…	113
Figure 5.19	The long-section cells checker in the Loch Linnhe seen above during the simulation time which indicates the tidal wave traveling in the Loch Linnhe region……	114

Figure 5.20	The tides and tidal current time relationship conditons (NOAA, 2012)……	115
Figure 5.21	The relationship between tides and tidal currents in Loch Linnhe……..……	116
Figure 5.22.a, b	The numerical tidal current *U* and *V* components against the ADCP measured *U* and *V* components at the reef location for spring daily period……	117
Figure 5.23.a, b	The *U* and *V* components for the daily neap tidal current cycle of both the numerical model and the ADCP record in the reef position……...……	119
Figure 5.24	The *U* and *V* components of the tidal current record at station 226 near the artificial reef with the mean wind speed data during the filed measurement……..……	120
Figure 5.25	The Loch Creran inlet inspection cell and the comparison of the numerical results against the seafarer's navigation information…….	120
Figure 5.26.a, b	The *U* and *V* components of the numerical model at the entrance of Loch Creran for the daily spring-neap tidal current cycles as registered by the monitored cell……..…	121
Figure 5.27.a, b	The tidal waves for numerical results with ADCP measurements comparison during a period of 13 day's time duration in (a). The tidal wave data was taken from the tides gauge station at port of Appin site against the numerical conclusion in (b)……	123
Figure 5.28.a, b	The comparison of *U* and *V* tidal current components between the numerical calculation results and ADCP measured data quantification….	125

Figure 5.29	The velocity vector of a positive tidal wave propagating in the Loch Linnhe. The position of the artificial reef is represented by the diamond marker……	126
Figure 5.30	The Loch Linnhe complex topology with the indication of the narrow outlet that has shallower seabed compared with other region in the Loch……...…	127
Figure 5.31	The velocity vectors of a tidal wave in the negative cycle with a marker for the reef site……	127
Figure 6.1.a, b	The numerical domain of the test case for Re=5100 is exhibited in (a) and the stream-wise velocity contour is spotted in (b)……...……	133
Figure 6.2.a, b, c, d	The comparison of the stream-wise velocity at Re=5100 at (a) x/H=4, (b) x/H=6, (c) x/H=10 and (d) x/H=19……..…	134
Figure 6.3	The chosen velocity profile for reef hydrodynamics investigation. The point one refer to selected hour time as described in previous chapter four……...……	135
Figure 6.4.a, b	The numerical domain adopted in the numerical simulation with indication of the boundary condition applied during the simulation (a), whereas, (b) shows the wall roughness complexity in the randomly deployment of concrete blocks that creates the artificial reef as discussed in Rose (2005)……..……	137

Figure 6.5	The transformation of mean tidal current for the two-dimensional depth averaged uniform velocity profile gained from Finite Volume Method numerical model changed to a logarithmic profile that adopted as inlet in the present investigation….	141
Figure 6.6	The average tidal current gained from the two-dimensional tidal numerical model in the logarithmic profile……...……	142
Figure 6.7.a, b	The tidal current measured is spotted in (a) with it distinct feature due to the effect of surface and bottom boundary layers and numerical averaged tidal current with the logarithmic profile presented in (b)……	144
Figure 6.8.a, b, c, d	The tidal current at frame time 145 s in Y-Z plane section. The measured tidal current profile is shown in (a) and numerical average tdial current is seen in (b).The turbulent kinetic energy in the same plane for the tidal current measured is spotted in (c) and numerical averaged tidal current is presented in (d)……....	145
Figure 6.9.a, b, c, d	The tidal current in the X-Z plane for the tidal current measured is exhibited in (a) and numerical averaged tidal current exposed in (b). The turbulent kinetic energy for the tidal current measured is displayed in (c) and numerical averaged tidal current is viewed in (d)……..……	146

Figure 6.10.a, b, c, d The X-Y plane of tidal current velocity of the measured is demonstrated in (a) and numerical averaged tidal current is exposed in (b).The turbulent kinetic energy of the measured is displayed in (c) and numerical averaged tidal current is seen in (d)…… 147

Figure 6.11.a, b, c, d The seafloor tidal current profile of both (a) the measured tidal current and numerical averaged tidal current is presented in (b). The seafloor turbulent kinetic energy for both (c) the measured tidal current and numerical averaged tidal current is spotted in (d)……..… 148

Figure 6.12.a, b, c, d The tidal current velocity of the measured profile is seen in (a) and for logarithmic profile is viewed in (b) as shown from the Y-Z plane (1345 s). The production of the turbulent kinetic energy for the measured current is displayed in (c) and for logarithmic profile is presented in (d)……...…… 149

Figure 6.13.a, b, c, d The tidal current profile in *x*-direction for measured profile from X-Z plane is exposed in (a) and logarithmic tidal current profile is exhibited in (b). The tidal current produce a turbulent kinetic energy for the inflow measured profile is spotted in (c) and logarithmic profile is viewed in (d)……...… 150

Figure 6.14.a, b, c, d The tidal current for measured current as pass the reef in *x*-direction is demonstrated in (a) and logarithmic current profile is presented in the X-Y plane on 50% of the reef height. The turbulent kinetic energy produced by the inflow measured current is exhibited in (c). The logarithmic inlet effect on the turbulent is seen in (d)……..…… 151

Figure 6.15.a, b, c, d The seafloor velocity contour in x-direction for measured current is displayed in (a) and for logarithmic current is viewed in (b). The seafloor turbulent kinetic energy with (c) the measured tidal current and logarithmic tidal current energy production as presented in (d) ……...…… 152

Figure 6.16.a, b, c, d The Y-Z plane on cross section position for measured profile in (a) and logarithmic profile in (b). The turbulent energy production of both measured profile (c) and logarithmic profile in (d) has a similarly pattern of the energy production (3600 s)……...…… 153

Figure 6.17.a, b, c, d The measured velocity profile is shown (a) for the X-Z plane and the logarithmic profile is presented in (b). Turbulent kinetic energy production for both tidal current profiles (c) measured profile and (d) logarithmic profile. Note that, the higher turbulent kinetic energy viewed in the measured one due to the high velocity at the peak of the artificial reef as demonstrated from the velocity profiles figures……...… 154

Figure 6.18.a, b, c, d — The velocity in the *x*-direction of (a) measured tidal current profile and logarithmic tidal current profile in (b). The turbulent kinetic energy production for the measured profile current is seen in (c) has higher value as the velocity is higher than the logarithmic tidal current shown in (d)…… 155

Figure 6.19.a, b, c, d — The velocity on the seafloor has similarity values and location as presented for measured tidal current profile in (a) and logarithmic profile one in (b). The positions of higher turbulent kinetic energy are the same in both figures of measured tidal current profile (c) and logarithmic profile current on (d)…… 156

Figure 6.20.a, b, c, d — The velocity vectors of both measured profile in (a) and logarithmic profile in (b) in the X-Y plane. The vectors velocity of both measured profile in (c) and logarithmic in (d) in the X-Y plane. It indicates the wake region in both profiles which demonstrates the different size of the created wake region…… 157

Figure 6.21.a, b — The shear stress of measured tidal current profile on the artifice reef is seen in (a) whereas, the shear stress of the logarithmic profile is shown in (b). Note that red dot for artificial reef wall and black dot for seafloor…… 158

Figure 6.22.a, b	The skin friction coefficient of the artificial reef as tidal current profile of measured data propagate the reef is presented in (a) along with the logarithmic profile tidal current cause a skin friction coefficient that is demonstrated in (b). Note that red dot for artificial reef wall and black dot for seafloor…….……..……	158
Figure 6.23.a, b	The drag coefficient caused by both tidal current on the artificial reef is presented in (a) for measured tidal current profile and (b) for the logarithmic tidal current profile……..……	159
Figure 6.24.a, b	The chosen two profiles selected from the tidal spring cycle as illustrated in Chapter four. These were interpolated to create unsteady condition similar to what the artificial reef affected under the normal ocean condition……..…	160
Figure 6.25.a, b, c	The velocity in the Y-Z plane of chosen time frames that inidcate the rises of the tidal current profile during unsteady flow conditions……...……	162
Figure 6.26.a, b, c	The turbulent kinetic energy production of the time dependent inlet conditions flow is seen in section Y-Z plane……..…	163
Figure 6.27.a, b, c	The X-Z plane velocity contour in the *x*-direction which indicates the increases in of the tidal current profiles as inlet interpolate between the two profiles spotted in Figure 6.24.a, b…..……	164
Figure 6.28.a, b, c	The vectors of the velocity profiles time frames displaying the development of vortex caused by the artificial reef during the simulation……..……	165

Figure 6.29.a, b, c	The turbulent kinetic energy as it generate during the unsteady flow modelling in a one hour time period…….……..	166
Figure 6.30.a, b, c	The X-Y plane of the tidal current velocity contour at the half about 50% of the artificial reef height presenting the turbulent occur on the reef due to the unsteady flow……..……	167
Figure 6.31.a, b, c	The production of turbulent kinetic energy due to the unsteady tidal current as presented in the X-Y plane viewed in time frames……...…	168
Figure 6.32.a, b, c	The effect of velocity contour on the seabed that indicate an increase of the outcome as the tidal current interpolated between the two adopted profile seen in Figure 6.24.a, b increases……..……	169
Figure 6.33.a, b, c	The X-Y plane the turbulent kinetic energy production on the reef increases as the speed of the tidal current rises due to the interpolation between the two adopted profiles for the unsteady condition……	170

List of tables

Page

Table 3.1 Semidiurnal and diurnal constituents related to the theoretical relative magnitude with periods of the constituents [360^o/speed] (Hicks, 2006)..... 40

Table 3.2 The bed topology for irregular bed in the *x*-direction..... 51

Table 3.3 The comparison of measured tidal amplitude around New Zealand islands with the Finite Volume Method numerical model..... 69

Nomenclature

A_0	The cosine lest square method term that gives the tidal amplitude.
α_k and α_ε	quantities represent the inverse effective Prandtl numbers for k and ε respectively.
β	A constant term given value of 0.012 used in the RNG k - ε model transport equations.
β_1	The slope limiter parameter.
B_0	The sine lest square method term that gives the tidal amplitude.
C	The tidal current which is the product of U and V tidal current. components in the x and y directions respectively.
C_D	The drag coefficient due to wind.
c_1	The shallow water wave celerity.
C_f	The bed roughness coefficient.
C_{SKf}	The skin friction coefficient.
$C_{1\varepsilon}, C_{2\varepsilon}$	These terms are constant given values of 1.42 and 1.68 respectively. applied in the RNG k - ε model transport equations.
C_μ	A constant given value of 0.09 applied in the estimation of the turbulent (or eddy) viscosity term.
D	The reef length scale taken as the diameter of the base of the reef
ε	Rate of dissipation of the turbulence kinetic energy.
$\bar{F}, F_b$	The force acting on the fluid due to the sloping bed.
$\mathbf{F}_E, \mathbf{F}_W, \mathbf{F}_N$ and $\mathbf{F}_S$	The flux function vectors that correspond to cell interface.

Fr	The Froude number.
f	The fit curve function that represent the tidal wave.
$\mathbf{g}_S, \mathbf{g}_N$	The fluxes through the south and north cell interfaces.
$f_{E,}, f_W$	The fluxes through the east and west cell interface of the current cell.
f_0	The lunar semi-diurnal frequency.
G_k	The generation of turbulent kinetic energy due to the gradient of the mean velocity.
g	The gravity acceleration.
η	The surface elevation above the datum.
η_t	The tidal wave represented in a cosine function form.
H	The height of the step used in the backward face step test.
h	The water depth.
h_s	The still water depth.
θ, θ_0	Terms applied in the RNG k - ε model transport equations.
ϕ	The tidal phase in degrees.
κ	The von Kármán's constant which is approximately equal to 0.41.
k	The turbulent kinetic energy.
k_r	The roughness height.
$\lambda_1, \lambda_2, \lambda_3$	The eigenvalues of the flux Jacobian.
$\Psi(r)$	The slope limiter to prevent numerical oscillations.

Ω	The control volume in the integral form of the shallow water equation.
μ	The dynamic viscosity.
μ_{eff}	The turbulent (or eddy) viscosity.
L	The channel length.
L_R	The characteristic length scale in the Reynolds number.
L_r	The reattachment length in the backward facing step test case.
v	The Kinematic viscosity.
M_1,M_2,N_2,K_1,S_2, O_1,P_1,K_2,$Q_1$$M_m$,$M_{S4}$	The harmonic constituents applied on the analysis of tides data.
μ	The dynamic viscosity.
n	The Manning coefficient.
n_x and n_y	The Cartesian components of the unit vector in x and y- directions for the eigenstructure of the flux Jacobian.
ρ	The water density.
ρ_a	The air density.
P_1,P_2	The pressure force.
Q	The discharge per unit width.
R	The global relative error.
R_0	The tidal amplitude.
Re	The Reynolds number.

R_ε	A term that improves the accuracy for high strain rate and large degree high turbulent flows.
$\mathbf{r}$	A vector from the cell centre on a point (x, y).
$S^2(t)$	The square of the differences between the observed and computed tidal level.
St	The mean rate of strain tensor in the RNG k - ε model transport equations.
t	Time.
τ_{bx}, τ_{by}	The bed friction stresses.
τ_w	The wall shear stress.
U and V	Velocity components in the x and y directions respectively.
U_0	The mean velocity.
U_{10}	The wind velocity measured at 10 m above the mean sea surface.
U_R	The fluid velocity in the Reynolds number.
U^*	The friction velocity.
U_∞	The free stream velocity applied in the skin friction coefficient.
$U(z)$	The velocity as a function of Z.
u, f, g, and S	Vectors representing the conserved variables in the non-linear shallow water equations.
u and v	The depth-averaged velocity components in the x and y directions respectively.
∇u_i	The gradient vector.

Δx	The grid size in the x-direction.
W_s	The wind stress effect on sea surface.
x and y	Cartesian coordinates in space.
ω_0	The angular frequency in radians per hour.
Z	The still water depth.
Z_0	Frequently termed a roughness length
Z_f	The lest square term in the fit curve function to represent tidal wave.
z_b	The bed elevation above the reference.

Chapter 1. The importance of artificial reef numerical modelling

1. Introduction

The term *artificial reef* has been defined by many marine scientists, including the Oslo-Paris Commission (OSPARCOM) who defined an artificial reef as "a submerged structure placed on the substratum deliberately, to mimic some characteristics of a natural reef" (Anon, 1998). This definition has subsequently been adopted by the European Artificial Reef Research Network (EARRN). A more specific description was provided by Seaman and Jensen (2000) who defined an artificial reef as "one or more objects of natural or human origin deployed purposefully on the seafloor to influence physical, biological, or socioeconomic processes relating to living marine resources". There are in addition many general definitions of an artificial reef, such as "a deliberately or accidentally deployed structure that lies on the seabed and which functions as habitat for marine life" (Wilding, 2003). In fact, piers (Glasby and Connell, 1999), seawalls (Chapman, 2006) and gas platforms (Wolfson et al., 1979) have all been used as marine organism's habitats. An artificial reef placed on the seabed works as a Fish Aggregating Device (FAD) that attracts fish to it (Chou, 1997). Marine organisms benefit from artificial reef sites as sources of food and places for fish reproduction as well as shelter for small size fish (Bohnsack and Sutherland, 1985).

Artificial reefs have a long history. The construction of artificial reefs has been used in Japan since 17th century to attract fish (Weisburd, 1986). Fisherman discovered a method of increasing productivity by making "Jakagos" which are bamboo baskets filled with rocks (Thierry, 1988). Developments of this type of artificial reef are well known to fishermen today for their ability to attract fish, leading to increased fishing opportunities in their near vicinity (Santos et al., 1997). Such artificial reefs are now referred to as Fish Aggregating Devices and the Catch Per Unit Effort (CPUE), a measure of increased fishing opportunity, can be seen to be very high in their localities. Artificial reefs also have other applications and they can be divided into two main categories (Baine, 2001): those specifically designed for purposes such as artificial reefs used for scientific research; and those occurring incidentally from causes such as dumping waste or from shipwrecks. They can, for example, be used to restore marine life to areas damaged by construction projects, or to enhance the ecology of existing habitats. For example, even though coral reefs are one of the most productive of sea regions, artificial reefs can be used to enhance them as a marine habitat for a particular

target species (Clark and Edwards, 1999). Another use for artificial reefs is to provide an environment for leisure activities. Reefs used for this purpose are often designed for discrete locations which gather large numbers of sizeable or otherwise exotic fish. Usually they are constructed from vessels, rubble or tyres and concrete (McGurrin et al., 1989). The development of, and wide variety of applications for, artificial reefs will be described in more details in the following chapter.

This study focuses on modelling flow field effects in and around artificial reefs partly because of their ecological impact on marine fisheries (Lin and Zhang, 2006) but also for their importance in artificial reef design in general. With regard to the former, failure or success of the artificial reef colonization depends on the recruitment of the marine organisms, such as larvae, that settled on the reef. A major factor controlling the recruitment of marine life organisms is artificial reef hydrodynamics, which potentially leads to a high level of success or failure the artificial reefs (Sheng, 2000). The artificial reef deployment on the seabed creates a wide range of flow patterns which can be characterized by intense velocity gradients, vortices and developing flow turbulence that depend on the reef physical characteristics. The artificial reef performance can be affected by factors such as the size and the geometrical design of the reef blocks, and the kind of materials applied to construct the artificial reef, and their interaction with the ambient flow. Therefore several researchers have been investigating aspects of the flow field on artificial reefs, such as Wang and Sato (1986) who studied the hydrodynamics characteristics of a series of representative models (i.e. cylinders, prisms, and other regular structure) that have been used in constricting artificial reef structures. Zhang and Sun (2001), for example, have shown that local upwelling current fields and eddy current fields at the front and back of an artificial reef structure led to an enhancement of the marine life productivity on the reef site.

This study will be set in the context of the hydrodynamic modelling of a sub-element (known as the E-group) of an artificial reef complex constructed in Loch Linnhe off the west coast of Scotland. The selected reefs lie in a water depth range between 19 – 28 m and so an important factor is that the tidal current plays a major role in the artificial reefs hydrodynamics. The global tidal hydrodynamic characteristics in the wider Loch Linnhe environs have been simulated with a 2D model based on the shallow water equations (Liang et al., 2004 and Liang, 2008). Output from this model in the locality of the reef has been used as input to a 3D Navier Stokes solver used to

determine the details of the flow on and around the reef. Some experimental measurements have been made at the reef site partly for their own intrinsic value, but also for validating and refining the numerical models.

1.1 Aims and Objectives

The overall aim of the study is to develop a methodology, and provide the tools for its implementation, for the determination of the detailed hydrodynamic characteristics of an artificial reef with a specified topology at a given location defined only by its bathymetry and tidal information from Admiralty charts, or their equivalent. The impetus for the study was to provide design tools for marine scientists and engineers developing artificial reef systems with regard to the hydrodynamics influencing the structural integrity, the habitat character and the marine environmental impact, of a reef of a specified design at a given locality.

The idea is that the reef designer can compare the respective merits of different designs at the preliminary design stage with the aid of the methodology and the numerical models developed in the project. To this end, the following objectives were identified:

- To choose an actual location and a realistic artificial reef design to use as the basis of the study, and define all their characteristics needed for the study.
- To obtain experimental measurements on site to determine environmental conditions.
- To implement a 2D hydrodynamic model capable of determining the global hydrodynamics in the general area of the reef.
- To demonstrate the model's capabilities and suitability for the project by using it to solve problems with known validated outcomes.
- To implement a 3D model capable of determining the detailed reef hydrodynamics.
- To integrate the two models in a case study based on the Loch Linnhe artificial reef by using output from the 2D model as input for the 3D model.
- To compare where possible the output from the numerical models with experimental data.

- To correlate flow parameters in the vicinity of the reef with design parameters of interest with respect to the reef's ecology and its structural integrity.

It was planned to achieve the aims and objectives through following the programme of work outlined in the next section and described in the following chapters.

1.2 Thesis Structure

The study is constructed of three major parts:

- Part one: The tides and associated hydrodynamics are essential to the study especially after the deployment of a structure such as an artificial reef. In fact, it is important to understand the existing hydrodynamic characteristics of the artificial reef in order to assess its impact on the marine life inhabiting the reef. The detailed features of the Loch Linnhe tides have not been studied before. Therefore, the simulation of the Loch Linnhe tidal cycles is required to understand of the hydrodynamics associated with tide's variation. The tide-induced waves and current velocities in Loch Linnhe have been modelled by solving the two-dimensional shallow water equations that adopt a finite volume Godunov-type scheme. The study allows the determination of the interaction between the tidal current and the Loch Linnhe artificial reef and the comparison with the measured field data obtained at the reef site.
- Part two: The tidal flow propagates at the speed of the shallow water wave as determined from the shallow water equations solver. An instrument like the ADCP (Acoustic Doppler Current Profiler) has the ability to physically measure the tidal current in the water column. It has been used in the vicinity of the artificial reef as this will be described in chapter four which also presents the results. The data record was taken for 57 days to examine the hydrodynamic characteristics during the spring and neap tidal periods. In addition, the measurement was compared with the two-dimensional numerical solver to explore its ability and accuracy. A set of the tidal current profiles was implemented as an initial condition for three-dimensional numerical modelling for comparison with initial conditions taken from the 2D model.

- Part three: The artificial reef was modelled using a three-dimensional model named FLUENT applying a RNG turbulence model. A comparison between computations with initial conditions based on an average velocity profile determined from the two-dimensional tidal model and the measured current profile taken from the ADCP data was undertaken. The turbulence model computes the flow regime around the reef leading to an understanding of how the reef hydrodynamics affects the marine organism's habitat and its marine life productivity.

The thesis is divided to seven chapters with this chapter included that can be briefly described as follows:

1.2.1 *Artificial reef development and application focused on the Loch Linnhe reefs ecology and the physical characteristics affecting the artificial reef*

Chapter 2 discusses the development of artificial reefs their worldwide application. The Loch Linnhe artificial reefs objective, and their location and structural complexity have been described. It covers several aspects of the Loch Linnhe artificial reefs from an ecology point of view. The attraction-production debate for artificial reefs has been explained, focusing on the Loch Linnhe artificial reef habitat. The physical factors affecting the artificial reefs ecology has been reviewed. Beginning with the factors that affect the artificial reef marine environment, such as reef location and the materials that were used in their construction, the factors that must be considered in their deployment are also explained. Artificial reef profiles and hydrodynamic patterns were described with their relation to the marine life. The factors that affect fish colonization, such as fouling organisms, which usually settle on the reef after deployment, are considered, as well as the important physical parameters that dictate biological reef colonization. The offshore wind-turbine was investigated from an ecological and hydrodynamic prospective as an example of the effect of the flow hydrodynamics on the marine organisms that live on it. Finally, an acoustic investigation of artificial reef structural stability, which depends on the balance of sediment scouring and settlement, and carried out by Manoukian et al. (2011) for an artificial reef's in Italy has been discussed.

1.2.2 *The Finite Volume Method techniques applied to Loch Linnhe tidal flows*

After covering the artificial reef ecology, the numerical methods begin with Chapter three that describes the shallow water equation (SWE) and the associated numerical algorithms, starting with literature reviews of the numerical methods implemented for modelling the tides. The Finite Volume Method using a Godunov-type scheme for the nonlinear shallow water equations was reviewed. The Godunov method and approximate Riemann problem solvers have been defined, followed by a description of a HLLC approximate Riemann Solver. The numerical tidal wave tests in one-dimension were implemented to validate the tidal numerical model. Further, two-dimensional benchmark tests were applied to clarify the capability and numerical accuracy of the model for which examples of model validation can also be found in the literature (Liang, 2008). In addition, the numerical model was examined by simulating the tidal dynamics of Cook Strait in New Zealand that demonstrate the accuracy of the adopted numerical model.

1.2.3 *ADCP field measurement*

Chapter four presents the field measurements that were taken near the artificial reef in Loch Linnhe. It shows the ADCP station positions near the group which have been selected from the artificial reefs. Several scripts of MATLAB code were created for the data analysis study. In the data analysis of the tidal wave cycle the velocity of the tidal current within the water column is investigated. The length of the record gives the spring-neap period during the lunar month. Therefore, a daily cycle from the spring and neap duration was selected and current profiles were generated to exhibit the velocities of these daily spring and neap cycles. The numerical modifications adopted to smooth the velocity profile so it can be applied as an initial condition for three-dimensional numerical modelling have been described.

1.2.4 *The tidal simulation of the Loch Linnhe adopting the two-shallow water equations*

In Chapter five the tidal numerical modelling was presented with the description of the initial and boundary conditions of the numerical model. The tidal simulation was executed for 13 days' time duration to analyse the tidal current during the spring-neap periods. The results of the numerical model were compared with the ADCP

measurements taken for the artificial reefs sites. Moreover, navigation information from seafarer's model about the kind of the tidal current expected in zones of Loch Linnhe was used in the comparison of results.

1.2.5 *The three-dimensional artificial reef turbulence modelling*

The three-dimensional numerical method implemented to study the localized flow in the vicinity of the Loch Linnhe reef has been introduced. The turbulence model theoretical background is described and the backward step flow test in two-dimensions has been applied to validate the turbulence model. The three-dimensional RNG turbulence model was adopted in the simulation, and setting its initial and boundary conditions is described. A maximum of a chosen spring tide velocity profile taken from the field measurement records was examined on the assumption of slowly varying flow over the tidal cycle to investigate the flow pattern surrounding the reef and identify the regions of turbulence occurring during the simulation. Initial conditions based on an average tidal profile predicted by the two-dimensional shallow water equations model was compared with those of a velocity profile measured by ADCP instruments. In addition, an hour from the velocity profiles of the spring tide data measurement was examined in unsteady conditions to demonstrate the tidal current turbulence pattern can be assumed to be slowly varying during an hour in the spring period. This will give an indication of eco-efficiency of the artificial reef based on the previous information mentioned in chapter two.

1.2.6 *Discussions and conclusions*

Chapter seven presents a concluding discussion elucidating how the artificial reef is affected by the fluid dynamics and its implications for fish and crustacean colonization near the Loch Linnhe Reefs. The conclusions drawn from the present study are then presented. Finally, suggestions for further research in the subject are made.

Chapter 2. Artificial reefs development and application with a focus on Loch Linnhe reefs ecology and the physical oceanographic characteristics affecting the artificial reef

2. Introduction

Man-made or natural reefs can have a potential impact on marine life. They attract fish and increase marine biomass (Bohnsack and Sutherland, 1985). The earliest record of artificial reefs can be found in Japan in the 17th century for attracting fish. The development of artificial reefs continued in Japan during the 18th century where they were used in seaweed farming with materials made from bamboo and wood (Dean, 1983). Improvements were made in building artificial reefs throughout the early 20th century, including the use of scrapped naval vessels for fish attraction (Simard, 1996). The Japanese engineers throughout the early 1960's continued tested a wide range of materials at early stage of artificial reef construction and found that the best choice is concrete because of its longevity and low cost. Thus, artificial reef from 1963 onwards are largely built of concrete (Duedall and Champ, 1991). Researchers around the world focused on artificial reef technology as a result of the Japanese success in this field. Artificial reef technology was considered to be a method of seafood production that could supplement commercial fishing in countries such as Japan (Grove et al., 1994), Korea (Kim, 2001) and Taiwan (Shyue and Yang, 2002).

However, there are many types of artificial reef and they can be divided more systematically according to their function and design. In fact, artificial reef application can be classified into four main categories as follows: for fishing and management, for marine restoration and habitat enhancement, for recreational objective and other function and marine infrastructure. In this work it will be seen that the Loch Linnhe artificial reefs have a major objective which is enhancing the marine-environment in the west coast of Scotland whilst providing a site purpose built for scientific study. The habitat complexity of Loch Linnhe artificial reefs has an influence on marine organism such as *Epifaunal* productivity. Therefore, fish that feed on *Epifaunal* can colonize these reefs (Gratwicke and Speight, 2005).

There are physical oceanographic factors that affect the colonization of an artificial reef such as hydrodynamics regimes, water depth, salinity and temperature. In fact, these physical characteristics have an impact on the recruitment and growth of

marine life such as sessile marine invertebrate which affect the artificial reef productivity (Dethier and Schoch, 2005). In addition, hydrodynamics force can affect the stability of artificial reef structure since the artificial reef may generate turbulence (Grove et al., 1991). An example to the effect of the hydrodynamics conditions is offshore wind-turbine scouring phenomenon. The current flow, as it passes a hydraulic structure, will create a flow pattern which may lead to changes in sediment transport and create scour which will affect the stability of the structure (Roulund et al., 2005). In fact, the structural stability of artificial reefs has been focused by Manoukian et al. (2011) in his study of sediment settlement on an artificial reef in Italy.

2.1 Artificial reef review

Artificial reefs deployed for a variety of purposes with a variety of designs have been purpose-built to enable the reefs to perform the intended function. For example, artificial reefs have been deployed to protect coasts by decreasing the wave energy and prevent beach erosion (Bruno, 1993). Further, artificial reefs can be used to enhance fisher's aquaculture and diving tourism and protect marine habitats. The common purpose of artificial reef development is related to common fishery and aquatic management practice that has been widely used in nearly all countries (Seaman and Jensen, 2000). In general, artificial reefs are built for production or protection purposes. Artificial reefs can be classified according to their application which indicates a wide range of artificial reefs applied in many regions of the world.

2.1.1 *Artificial reefs development*

In 1952, the Japanese government was involved with coastal fisheries improvement and promoted the scaling up of artificial reefs from small to large scale. Throughout the early 1960's Japanese companies began installing large scale artificial reefs (Yamane, 1989). In Japan during this period the total volume of assembled artificial reefs reached 1213390 m^3 making up 721065 units of size of 1 m^3 and 328217 units of size of 1.5 m^3 (Ino, 1974). Today the Japanese government spends approximately $10 million annually (Polovina and Sakai, 1989). In fact, 9.3% of Japanese coastline sea beds at less 200 m depth contain artificial reefs as seen in Figure 2.1 (Thierry, 1988). The Japanese public and government alike continue to place great importance on artificial reefs for the fishing industry.

The success of the artificial reef technology encourages the Taiwan government to deploy 358 concrete blocks in the water of Linbien in 1957 (Chen and Chen, 1957). Later, from 1973 Taiwan adopted a variety of sea farming methods using many types of materials like scrapped vessels, fly-ash, old tyres and concrete blocks. The Fishery Bureau of Taiwan Provincial Government invested about $2 million in this program and 19 artificial reef sites were constructed around the coast of Taiwan as presented in Figure 2.2 (Chang and Shao, 1988). Korean researchers adopted the same approach regarding artificial reef construction materials and as a result, 90% of the 1200 artificial reefs that exist are made from concrete (Kim, 2001). In USA in the early days of artificial reefs there was no dumping of any scrap materials until the mid19th century and reefs were made from trees and bushes (Stone, 1985). Subsequently some reefs were constructed of waste materials, including scrapped cars. In 1968, an artificial reef of about 400 tonnes built from used car tyres was deployed in Humboldt Bay as an experiment (Dewees and Gotshall, 1974). However, due to a lack of experience in USA compared with Japan, early experiments brought many failures (Sheehy, 1982). It was found that dumping tyres created an environmental problem resulting in poor fishing grounds, and it was costly to remove them from the marine environment as shown by Figure 2.3.

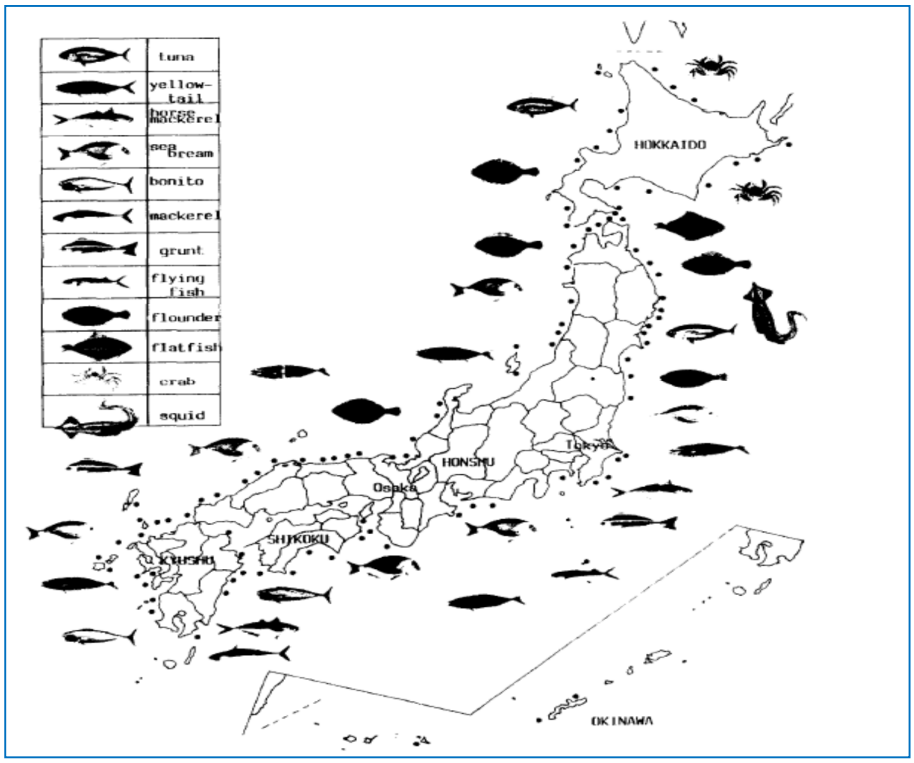

Figure 2.1 Artificial reef sites and fish species living near it in Japan (Thierry, 1988).

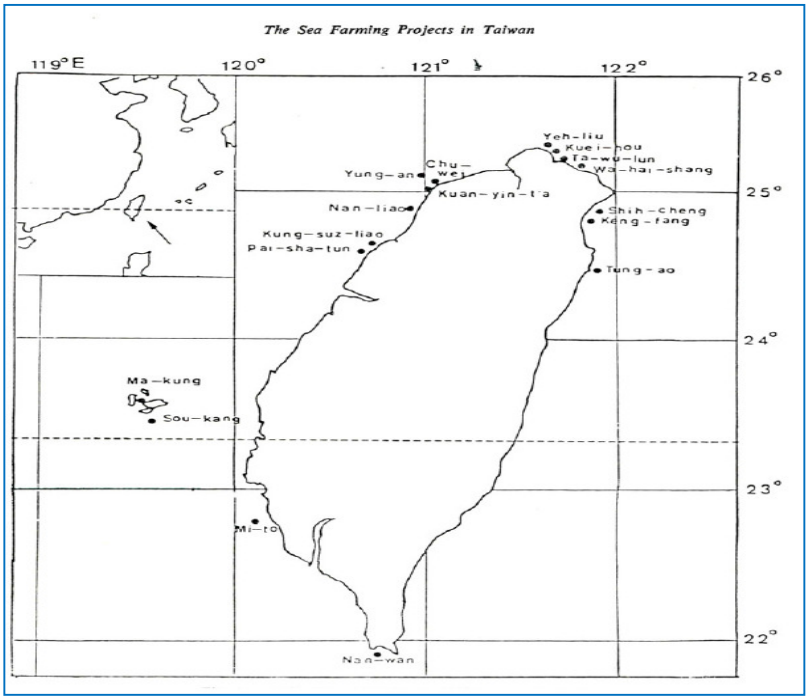

Figure 2.2 The artificial reef positions in Taiwan 1973-1979 (Chang and Shao, 1988).

Figure 2.3 Early artificial reefs were made from scrap materials including old tyres which were cost millions of dollars to remove it (Diplock, 2008).

Amongst them were such examples as the 'Beer Case Reef' in Fire Island Inlet built from 14,000 concrete filled beer cases. On the other hand, an artificial reef constructed from 250 cars off the coast of Alabama that did gave some indication of success in terms of the resulting fisheries grounds (Dean, 1983).

In Australia artificial reefs were made from a variety of materials including waste concrete pipes deployed in the sea. Tyres and decommissioned vessels were also used in early artificial reef experiments with approximately 40,000 un-ballasted tyres deployed as artificial reefs (Branden et al., 1994). Whereas, in Europe the sinking of any materials that effect the marine environment was restricted by regulation. This legislation can be seen in the European Artificial Reef Research Network [EARRN] (Wilding, 2003). The European leader in artificial reef technology is Italy. The majority of artificial reefs constructed in Europe have been deployed for research reasons (Jensen et al., 2000). The materials used to build these reefs were prefabricated materials like concrete blocks (Kress et al., 2001) or made from steel that can used for marine environment (Antsulevich et al., 2000). The objectives of these reefs are for biological improvement which will form a foundation for research or lead to commercial applications. UK is the strongest from Europe in the artificial reef research, with a high publication rate. In UK artificial reefs have been used for coastal protection from flooding and coastal erosion such as Happisburgh-to-Winterton on the north-east facing Norfolk coast in the UK (Gardner et al., 1996). Whatever differences exist between

countries like USA, Japan, Korea, Australia and Taiwan in cultural application they all have in common a continual development and construction of artificial reefs. In UK the first experimental artificial reef licensed under the revised draft OSPARCOM guidelines was located at Loch Linnhe on the west coast of Scotland. The Loch Linnhe artificial reef was funded by the Dunstaffnage Marine Laboratory to be a tool in scientific research for aquaculture. An important criterion in selecting the artificial reef location at Loch Linnhe was its acceptability to fisherman (Sayer and Wilding 2002).

2.1.2 *Artificial reefs application*

Artificial reefs occur in two main forms: those deliberately placed on location for an explicit purpose, such as for scientific research; and those occurring incidentally from causes like shipwrecks. In fact, artificial reefs application can be separated due to their functions as follows:

2.1.2.(A) *Fishing reefs and management*

Artificial reefs have a long history of being used for attracting fish. In fact, artificial reefs can stimulate food chains such as, for example, herbivorous fish feeding on the algae growth on the reef and larger fish feeding on the sheltering juveniles (Chou, 1997). Most new artificial reef structures sunk in the sea and fish colonization will occur within hours or days (Bohnsack, 1991). Even if the food resource is still in the developing stage on the reef shelter is an important issue to certain species (Sale, 1980). In addition, fish living near artificial reefs may be better developed than fish living near natural reefs, which if the reef is well managed reduces the fishermen's running costs and increases their profit (Whitmarsh et al., 2008). Fishermen deploy artificial reefs and FADs to attract fish near to the shore using lightweight natural materials that dissipate over a short time period. Such reefs are usually small in size (Collins et al., 2000). In contrast, overfishing is one of the major threats to the successful commercialization of artificial reefs and they must be managed carefully to avoid this condition and produce good profits (Chou, 1997). Management strategies involve procedures such dividing the reef into zones by using particular gear such as trawls to decrease the conflict between different species of fish. This will create zones in the managed area that have different size of fishes in each zone (Revenga et al., 2000).

2.1.2.(B) *Artificial reefs for marine restoration and habitat enhancement*

The decline of coral reefs is a widespread threat to ocean ecosystems (Hinrichsen, 1997). The provision of artificial reef as alternative sites for the restoration of marine life could make a significant contribution to solving this marine environmental problem (Seaman and Sprague, 1991). In addition, the introduction of artificial reefs can protect the coral reef by providing an alternative habitat for marine organisms that otherwise seek refuge in the coral reefs. The marine organisms will reproduce in the artificial reef and reduce the human activity on natural reefs (Abelson and Shlesinger, 2002). In fact, when artificial reefs sited in Marine Protected Areas (MPA) they will accelerate the development of threatened fish populations and increase the chances of their recovery by creating nursery grounds for the target species in these regions (Pitcher et al., 2002). The process is often reinforced in these areas by preventing the catch of certain kind of fish or by controlling the size of fishing gear allowed (Bombace et al., 2000).

2.1.2.(C) *Artificial reefs for recreational purposes*

Recreational reefs increase fish population and attract more interesting fish which give the sites an economical interest because they attract divers due to their fish variety (Ditton et al., 2002). These artificial reef locations are diving preferred which release pressure from natural reef dive sites. These kinds of artificial reefs may include surfing reef which is used to create waves suitable for surfacing (Mead and Black, 1999). In USA recreational artificial reef has been enhancing surfing by creating regular ride waves (Borrero and Nelsen, 2003).

2.1.2.(D) *Other Artificial reef function and marine infrastructure*

Artificial reefs constructed for a specific job like algae and filter feeders that grow on these reefs to remove nutrient from water column (Angel and Spanier, 2002). Research artificial reefs can be included in this type of reefs. It is used to study the ecological processes on reefs as well as to investigate fisheries improvement on reefs (Jensen and Collins, 1997). In fact, research reefs can be used to test the materials suitability as the artificial reef substrate (Collins et al., 2002). Another, infrastructure such as coastline protection (Hamer et al., 1998), harbor walls (Stephens and Pondella, 2002), shipwrecks (Zintzen et al., 2008) and offshore platforms (Wolfson et al., 1979) can be classified as an artificial reef. In fact, most of the human made structure that lies

on seabed can be consider as an artificial reef. These structures can be colonized by marine organisms since it was built from material resist sea condition which will create marine life environment (Caselle et al., 2002). These reefs can create most significant regional biodiversity of marine life such as Sydney Harbor 50% of marine biodiversity found in these kind of artificial reef (Bulleri et al., 2005). Another example, in USA at state of Louisiana oil offshore platform create 90% marine life habitat (Polovina, 1991).

2.2 Introduction to Loch Linnhe artificial reef

The artificial reefs used as a case study in this work are located in Loch Linnhe, off the west coast of Scotland. Wilding (2003) provides in-depth analysis of Loch Linnhe licensing and design. The artificial reef was deployed at August 2001 which followed by pre-deployment other research reefs in several years (Wilding, 2003). It lies on the west coast of Scotland UK about 12 Km from city of Oban. The objective of these reefs is studying the control factors that affect the biological communities on fish and crustacean species such as the European Lobster (Homarus gammarus). In fact, the Loch Linnhe artificial reefs marine ecology has been studied by many researchers such as Wilding and Sayer (2002a), Rose (2005) and Beaumont (2006). The reefs consider being one of the largest artificial reefs known in Europe. The size of the reef site equates to about 50 football pitches (Grid reference 56^{o} 32` N $05^{o}$ 27` W) as exhibited in Figure 2.4 (Beaumont, 2007).

2.2.1 *Loch Linnhe artificial reef and structure complexity*

The artificial reef cited on silty sand overlain by cobbles and stones (Wilding and Sayer, 2002a). The site consist of 42 artificial reefs with two different kind of reef module and 25,000 tons of concrete blocks which cover an area about $0.4Km^2$ as explained in details in Beaumont (2006). The position of all groups of the artificial reefs is presented in Figure 2.5 showing the water depth that was deployed in it. It is clear from the figure the artificial reefs deployment was in water depth range starting from a minimum 3m to maximum 28m. For research purposes the Loch Linnhe artificial reefs has been deployed in the human diving range. The Loch Linnhe formed by dumping concretes blocks in selected sites. The block concrete size was 21 X 21 X 42 cm which made from granite dust with low levels of fly-ash that make physically and chemically stable (Wilding and Sayer, 2002b).

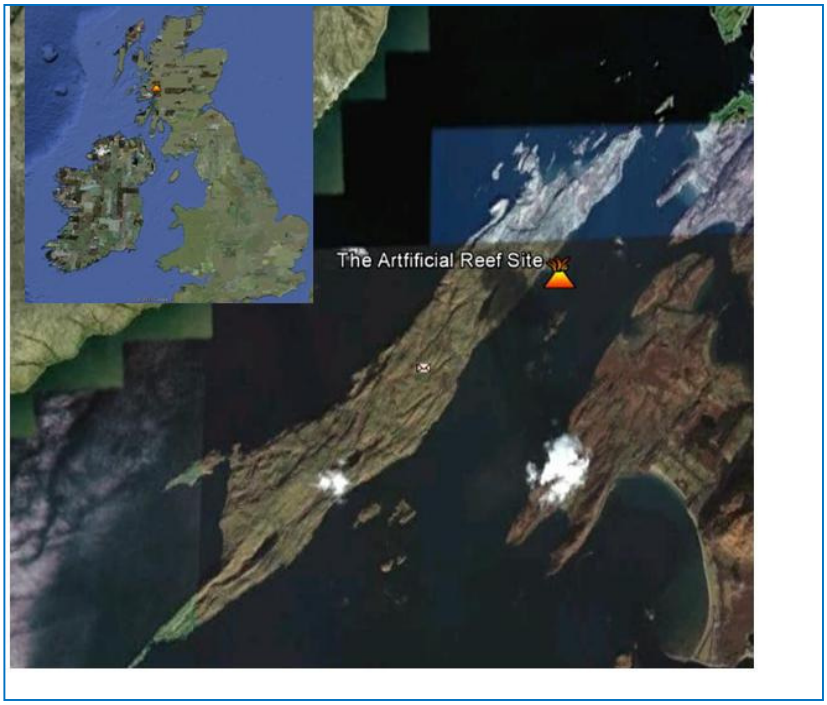

Figure 2.4 The south of Loch Linnhe with the positions of the artificial reefs.

In addition, there was two kind of concrete block a complex blocks with two voids in them to increase potential structure and simple one blocks as shown in Figure 2.6. The objective from the reef complex design is to give higher level complexity to marine habitat. Another reason for complex blocks is the boundary between sedimentary ground and rocky reefs that give a shelter to marine life like the lobster (Wickins, 1994). The artificial reef structure design must meet the aims of the overall programme with economical cost and logistics (Wilding, 2003). Thus, the best choice was deploying the block concrete using a crane from an anchored barge in the chosen sea regions as seen in Figure 2.7 (Wilding and Sayer, 2002b). A target buoy was used to drop the concrete blocks which was fell to the seabed. There were two kinds of artificial reef modules a solid forming conical shape and other complex forming a pentagon shape with approximately 3-4 m in height by 15-20 m across as exhibited in Figure 2.8 which shows a Multi-beam SONAR was applied to scan the artificial reef sites (Beaumont, 2006).

Nevertheless, the artificial reef concept is intended to create an ecosystem that encourages a rise in marine life productivity. In addition, the effectiveness of any artificial reef depends on the marine colonization as will be found in the following section.

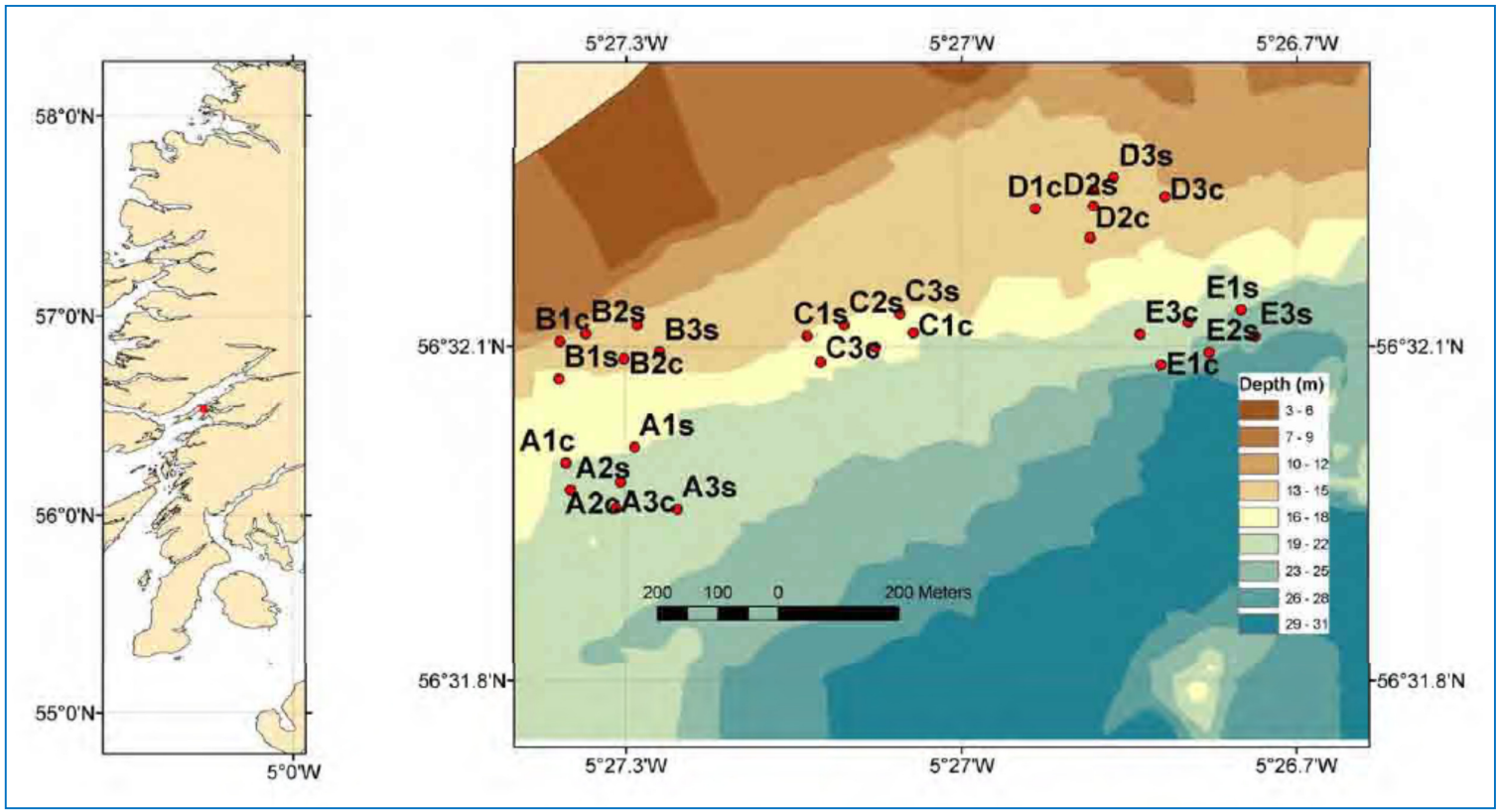

Figure 2.5 The artificial reef sits in the Loch Linnhe (Wilding, 2010).

Figure 2.6 Block of the complex (right) and simple (left). The block dimensions 21 x 21x 42 cm (Wilding, 2010).

Figure 2.7 The crane on the surface barge deploying the blocks that construct the artificial reefs (Wilding, 2010).

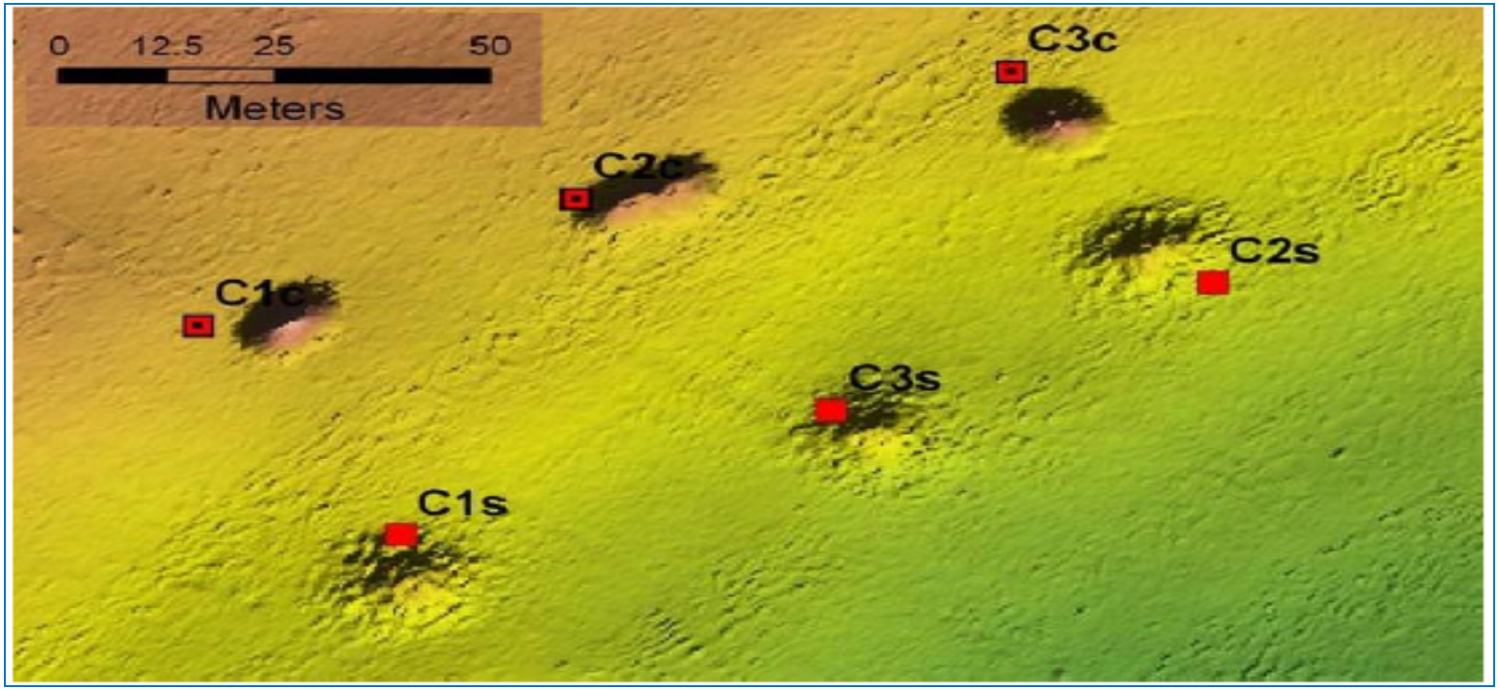

Figure 2.8 An example of the Multi-beam SONAR showing the seabed with section of six artificial reef modules (C1c,C2c, C3c) modules consist of complex blocks and (C1s,C2s and C3s) simple blocks reef (Beaumont, 2006).

2.2.2 *Epiflora and Epifauna colonization and the Loch Linnhe artificial reef*

Marine life colonizes artificial reefs by migration and the settlement of larvae and juveniles. In reality, marine organisms, such as algae, microorganisms and other marine animals that are attracting to new structures can colonize a reef in phenomenon known as biofouling. The biofouling consists of processes starting with organic and inorganic molecules settling on the new surface followed by microorganisms (Jonsson et al., 2004). The first layer is composed of organic molecules such as protein fragments and polysaccharides as presented in Figure 2.9. These microscopic suspended particles are governed by physical forces such as: the random motion of suspended particles (known as Brownian motion); van der Waals forces, which an electromagnetic forces acting between molecules; and electrostatic interaction (Davis, 1995).

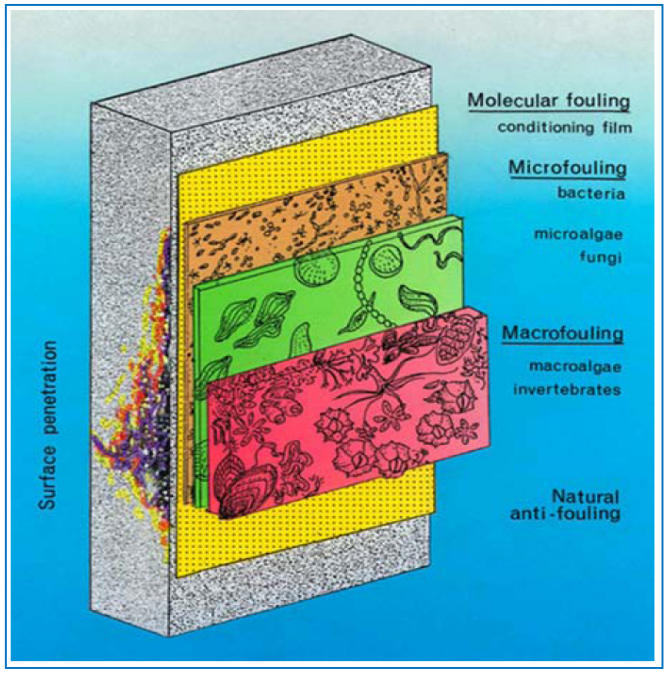

Figure 2.9 The four layers of marine biofouling (Davis, 1995).

A biofilm from microorganisms like bacteria, Diatoms, protozoa and yeasts colonizes the new reef structure (Woods Hole Oceanographic Institution marine fouling prevention [WHOI], 1952). The Diatoms adhere themselves to a specific type of antifouling coating which sticks to the surface by Extracellular Polymeric Substances (EPS). The adhesive cells multiply to form a biofilm colonizing the new surface and

may reach 500 μm in thickness (Callow and Callow 2002). The surface roughness and its irregularity will increase the microbial colonization. A complex marine community will follow the microbial colonization which includes multicellular primary marine life such as algal spores, marine fungi, protozoa and barnacle *cyprids* (WHOI, 1952). The last stage involves large marine invertebrates which settle as *macrofoulers*. Most macrofouling communities include hard calcium carbonate from tubeworms, barnacles, mussel and corals as well as soft organisms that will settle like sponges, ascidians and hydroids. Fouling organism's develop quickly with high density in warmer regions compared to cold ones. In addition, sun light and salinity will reinforce the rate of photosynthesis in marine life like marine plants and algae (WHOI, 1952). As a result, there is competition between marine microorganisms for the best area on the artificial reef with nutrients, light which can inhibit dissolved gases exchange (Steinberg et al., 1997). In fact, fouling species like *pelagic larvae* form 90% of the initial colonists that settle on the artificial reef (Osman, 1977). The fouling of *Epifaunal* specie creates marine habitat diversity and raises the heterogeneity of the artificial reef. Thus, there is a correlation between the rate of fouling on the artificial reef and its productivity as suggested by Relini (1997). An example of *Epifauna* is the *Epibiotic* community that colonizes the artificial reef and forms the basis of the chain food on the reef. The aggregate and resident reef fish feed on *Epibiota* as observed by Sanchez-Jerez et al. (2002) and Page et al. (2007). The productivity of *Epifaunal* biomass on the Loch Linnhe artificial reef modules has been investigated by Beaumont (2006). As matter of fact, she indicates that *Epifaunal* recruitment is heavy in summer compared to other seasons on the Loch Linnhe artificial reef. There are two types of module making up the artificial reef on Loch Linnhe: simple and complex as explained in previous section. Beaumont (2006) estimated that *Epifaunal* biomass on the complex reef modules for 12 months duration which indicates complex blocks is 1.6 times more productive than simple blocks. In addition, *Epifaunal* biomass on a complex Loch Linnhe artificial reef module is up to 30 times greater than the i*nfaunal* biomass losses due to sediment covering during 12 months of fouling time as exhibited by Figure 2.10. Therefore, there are high increases at the reef base of the food-web since preys exist for taxa in higher trophic levels. Literally, Steimle et al. (2002) studied *Epifauna* on his artificial reef and found its 44 times more productive than the *Infauna* beside it in sandy sediment. This agrees with results found by Beaumont (2006) on the Loch Linnhe artificial reef. Moreover, the habitat complexity has an influence on *Epifaunal* productivity as suggested by Guichard et al. (2001).

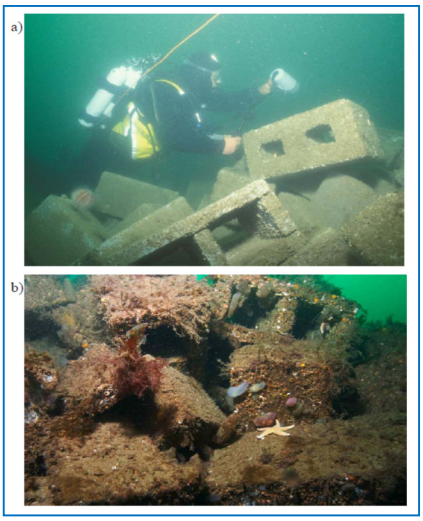

Figure 2.10 Loch Linnhe complex modules (a) shortly after deployment (b) more than 12 months of biofouling (Beaumont, 2006).

As a result, the higher complexity will give more opportunities for *Epifaunal* prey such as fish to feed and have shelter or nest on the artificial reef (Gratwicke and Speight, 2005). However, evaluation of artificial reef performance regarding productivity is important for artificial reef development as will be described in attraction-production debate.

2.2.3 *The attraction-production debate and the Loch Linnhe artificial reef*

The definition of the productivity of an artificial reef depends on the assumption that artificial reef creates a new critical habitat with an environment that can increase the abundance and biomass of reef biota (Bortone et al., 1994). The fouling biomass on an artificial reef structure will enhance local production for reasons such as an increase production of fish biomass. Fish and crustacean species are desirable due to their commercial importance (Steimle et al., 2002). However, there is an argument that an artificial reef may attract the fish with no increase in total biomass which shows local fish biomass is redistributed with no additional biomass exploitable (Bohnsack, 1991). In fact, the Attraction hypothesis predicates that biomass on an artificial reef redistributes fishes without an increase in production (Wilson et al., 2001). On the other hand, it could be said that an artificial reef not only creates new additional habitat, which increases fish production, but it redirects harmful human activity away from sensitive regions such as natural reefs (Sosa-Cordero et al., 1998). Thus, the effect of

artificial reefs regarding the 'Attraction versus Production' discussion is still controversial as each side represents his view (Bohnsack, 1989).

In the Attraction hypothesis the fish high density on artificial reefs may occur due to fish immigration from natural reefs that survive and grow with a comparable rate on artificial reefs as they do on a natural reef. Thus, fish biomass on the artificial reef will increase since fish are pulled from their natural reef habitat (Wilson et al., 2001). On the other hand, natural reefs will suffer from fish reduction which indicates a spatial distribution of fish production between natural habitat and artificial reef, but total production of the artificial reef and the natural still constant as seen from Figure 2.11.a. Moreover, In the Attraction hypothesis larval fishes skip from the pelagic environment and settle in the artificial reef environment (Keough and Downes, 1982). On the other hand, in the Production hypothesis, an artificial reef can increase fish production by providing a new marine environment so fish larvae can settle, otherwise they are never recruited into older age-classes to survive on the artificial reef. Since, the artificial reef is producing new fish biomass and not redistributing it fish production will increase as the artificial reef size rises whereas the natural reef production will remain constant (Wilson et al., 2001). Therefore the net fish biomass production will increase overall for the reef system as shown by Figure 2.11.b.

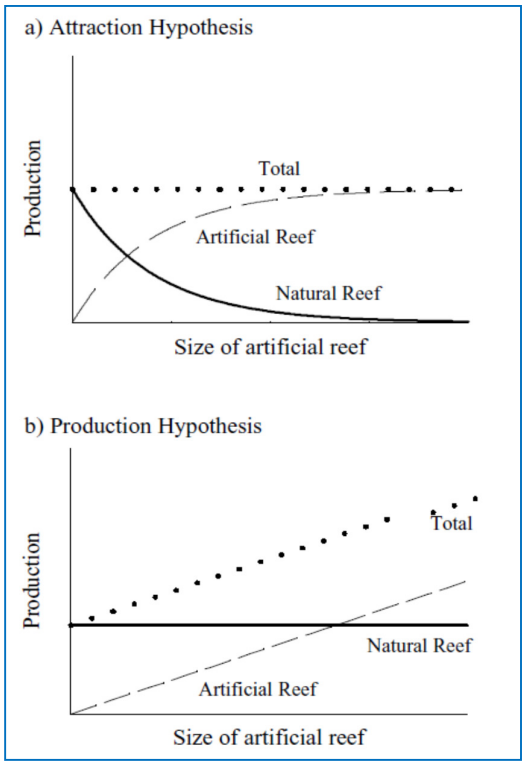

Figure 2.11.a, b The prediction of the attraction and production assumptions against artificial reef size (a) attraction hypothesis [fish production is constant] whereas (b) production hypothesis [fish production rises linearly as artificial reef create new habitat] (Wilson et al., 2001).

There are number of factors that lead to an increase in production such as increasing in feed efficiency, more shelter from predation or increase in tidal current and larval settlement that recruit larger fish populations (Bortone et al., 1994). The local fish that live on the artificial reef are attracted to it due to the surrounding environment, such as a shaded area that can protect it from approaching predators, or a sunlight area in which to feed. In fact, Bohnsack predicted the possibility of an artificial reef deployment effect with its attraction and production compared to non-reef regions as represented by Figure 2.12.

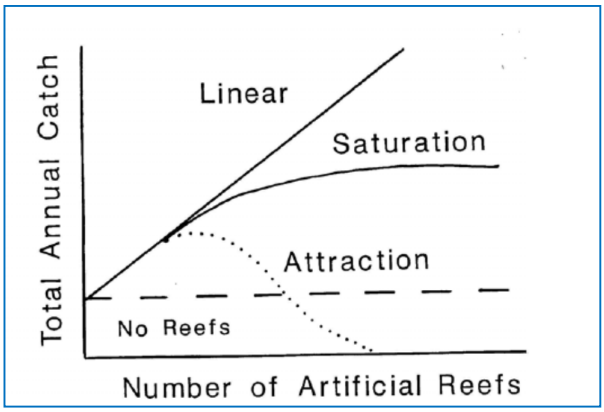

Figure 2.12 Bohnsack (1989) predicted linear or saturation functions which indicate if the fish population is recruit limited it will not be matter to increase space of the artificial reef since it will not raises the fishery. However, if it is space limited, and artificial reefs increase the volume of space available, then they might serve to increase fish production.

The natural reef is exposed to pressure from climate change which effects it's availability as well as its mechanisms of natural population limitation. Bohnsack (1989) predicted several important gradients for artificial reef that may attract fish or rise production as shown in Figure 2.13. He predicts an artificial reef can attract fish at locations with high natural reef availability which increases fishing intensity. Another factor predicted by Bohnsack (1989) is increasing production can be more important for habitat-limited such as damselfish than recruitment-limited species such as snapper fish. Reef dependency and site attachment altered according to species and with age for some species (Sale, 1969). In fact, enhancement in production can be connected with highly territorial, philopatric and obligatory reef species. Some of these predications gradients were partial tested by Polovina and Sakai (1989) in studying an obligatory demersal reef species such as *Octopus dofleini* which is territorial, philopatric and low mobility. The study concludes an increase in production of the Octopus which appears to be habitat-limited reef species.

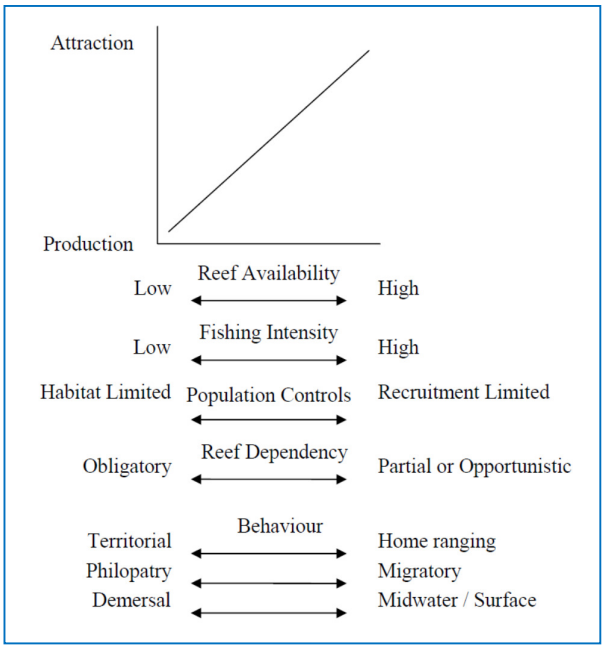

Figure 2.13 The gradients predicted to be important for attraction versus production at artificial reef location which indicates a linear response as Bohnsack (1989) suggested.

However, the attraction-production study was focussed on fish population (Svane and Peterson, 2001). Other marine species like crustacean fisheries have shown an enhancement of production on artificial reefs. It is practiced less commonly as economic benefits are modified due to the length of time needed for a majority of crustacean, such as lobsters, to reach market size (Jensen and Collins, 1997).

On the other hand, lobster ranching has benefits over other finfish species due to its high degree of habitat integrity as well as its juvenile's *Homarus sp.* commercial availability (Whitmarsh et al., 1995). In addition, many artificial reefs have been specifically deployed for lobster ranching in USA, Canada and UK and they have shown some success (Jensen and Collins, 1997). The crustacean fisheries can be discussed with the attraction-production debate, since artificial reefs with large size can attract and localize lobsters. Thus, a rise in lobster population will be found in natural and artificial reefs as Bohnsack (1989) using the same attraction assumption as for fish species. The Loch Linnhe artificial reef was designed as an experimental matrix in order to facilitate the study the impact of artificial reef on the marine environment (Wilding, 2003). The reef habitat complexity with its complex-blocks was considered to create a perfect habitat for crustacean fisheries. For one reason, the preferred environment for

some marine species such as lobsters found in the boundary layer between the concrete blocks and sedimentary substratum (Wickins, 1994). These areas provide protection with convenient access to sediment. As a result, Wilding (2003) speculated that the artificial reefs with longer edges might perform better due to their long boundary regions. The habitat complexity of the Loch Linnhe artificial reef was studied by Rose (2005) for the two types deployed in the site simple and complex modules. The results indicate that the lobster numbers on the complex modules are greater than on the simple one. In fact, Beaumont (2006) study results indicate that the Loch Linnhe reef modules may be more productive per unit area/volume for marine life compared to local natural rocky reefs in the same site.

2.3 The physical oceanographic factors affecting the artificial reef

There are physical factors can affect the species colonization on artificial reefs. These factors can be summarized in three main aspects as follows.

2.3.1 *The receiving environment and construction materials*

In general, artificial reefs are sited in water depths such that divers and fishermen can access them. The initial phase of any artificial reef project should be the investigation of the local hydrodynamic conditions that characterise the selected site and identification of the engineering and biological design constraints they impose (Grove et al., 1991). In addition, the relevant hydrodynamic parameters, such as current and wave data, should be recorded for at least one year so seasonal hydrodynamic variations can be observed. In addition the biotic parameters, such as temperature and salinity, should also be determined (Bohnsack et al., 1991). In reality, the location of the artificial reef will dictate the environmental conditions and the potential colonizing species (Zintzen et al., 2008). The marine environment of the artificial reef location like water quality can influence the eutrophic conditions that increase the alga growth as well as sessile fauna. The suspended particles found in water cause turbidity that effect assemblages on artificial reefs due to light limitation (Falace and Bressan, 2002). Moreover, the initial recruitment of *epifaunal* assemblages can be effected by light and sedimentation conditions as concluded by Maughan 2001. Indeed, pollution and turbidity cause low fish density on artificial reefs and it was found that fish catches can be reduced due to high water turbidity (Bohnsack et al., 1991). These higher concentrations of suspended particles are found with rise in nutrients and toxicants (Greilach et al., 1997). Also, the

accumulation of sediment on the reef will reduce the growth of sessile communities (Fabi and Fiorentini, 1997).

However, artificial reefs are made from a wide range of materials such as PVC, tyres, steel, old cars, offshore platforms and old vessels (Relini, 2000). In addition, in their early days some of the artificial reefs were found to be unstable due to material loss in strong currents and stormy weather (Turpin and Bortone, 2002). The artificial reef materials are generally the most inexpensive that can be used in their construction. Thus, waste materials have been used for creating artificial reefs and, in some cases, were found to be harmful to the marine environment. For this reason dumping regulations have been set in place by world countries such as those of Europe countries that specify the type of materials that can be deployed. Steel and concrete are most common materials used for artificial reef construction (Pickering and Whitmarsh, 1997). The best materials for construction have been found to be natural materials like rocks, which have been used very successfully as these kinds of materials, can integrate naturally with marine life habitats (Chapman and Clynick, 2006). In fact, construction materials with surface texture, such as rocks, can help in fouling assemblages whereas PVC is unsuitable for this purpose (Glasby, 2000).

2.3.2 *Artificial Reef surface and deployment time*

The surface texture of an artificial reef can affect its initial colonization since the roughness of its surface influences its settlement. Therefore, rougher surfaces can settle larvae that leach chemicals while colonizing the artificial reef more than smooth surfaces (Pawlik, 1992). It found that surfaces with vertical or sharp edges experience less sedimentation deposition, which encourages fouling settlement and colonization by sessile fauna. This kind of surface contains more fauna with biodiversity compared to horizontal surfaces (Chapman and clynick, 2006). In addition, the surface faces light will attract sessile invertebrates rather than shaded areas (Blockley and Chapman, 2006).

Nevertheless, time of deployment can affects the colonization of an artificial reef. As a matter of fact, the deployment of artificial reefs in the seasonal larval duration will support artificial reef colonization as concluded by Brown (2005) in his study of *epifaunal* colonization on the Loch Linnhe artificial reef. The larval supply and recruitment which can change according to seasonal variation may have an important

role in deciding the time of artificial reef deployment (Pondella and Stephens, 1994). The changes of temperature due to yearly fluctuation have an influence on artificial reef colonization (Karnofsky et al., 1989). Moreover, as the artificial reef increases its age the number of species, such as *polychaetes*, involved in colonization also increases (Nicoletti et al., 2007). The rise of soft-bottom species will increase the heterogeneity of the marine life settled on an artificial reef. As has been exhibited by Beaumont (2006) Loch Linnhe artificial reef marine complexity developed during two years of deployment time.

2.3.3 *Artificial reef structure and hydrodynamics regime*

The structural design and the form of the artificial reef can play a role in attracting fish by inducing hydrodynamic characteristics such as turbulence and variations in the strength of local vortices. A qualitative analysis carried out by Chang-Hai and Osamu (1986) to investigate the hydrodynamic characteristics on a group of regular shaped artificial reef models that could generate eddies. The scope was for understanding the hydrodynamic aspects of the artificial reefs and their implications for optimal artificial reef design. Truly, the artificial reefs with higher profiles expect to create higher levels of turbulence, which will increase *Epifaunal* growth and attract more fish (Brock and Kam, 1994). The stability of artificial reef structures can also be affected by water hydrodynamics (Sheng, 2000). The construction design of an artificial reef must be compatible with hydrodynamic forces existing on the reef site. Also, the construction materials used in building must be heavy and of high density, such as steel and concrete, to prevent the reef from moving (Mathews, 1985).

Yet, ocean hydrodynamics of tides and ocean waves can play an important role in macroalgae drifting. Marine life on the artificial reef will feed on this macroalgae including organisms of commercial importance such as abalone (Shepherd et al., 1992). The hydrodynamics concerning algae and macroalgae has been investigated by many researchers, such as kelp algae and its interaction with wave hydrodynamics for example (Massel, 1999; Lovas and Torum, 2001). Another example is the investigation of the hydrodynamics transport of drifting macroalge species like *Rhodophyta* during a tidal cut done by Biber (2007). In fact, invertebrates like plankton larvae or sessile species can disperse over great distances due to water hydrodynamics such as tidal and residual currents. The dispersed pelagic larvae will be transported to new marine habitats (Shepherd and Brown, 1993). The distance of dispersion may reach

several kilometres depending on the current direction, as has been observed by Tegner and Butler (1985) in his study of *Haliotis fulgens* larvae dispersal. In addition, a study by Shepherd et al. (1992) found *Haliotis laevigata* larvae may disperse to several kilometres. This long distance dispersion can be explained only with tidal current hydrodynamics, as suggested by Rodda et al. (1997). The productivity of the artificial reef may be enhanced by creating space between the reefs, which can distribute the drifting larvae and macro-algae, but still there is inadequate knowledge of this matter (Grove et al., 1991). In addition, strong currents can effect settlement, recruitment and growth of encrusting organisms that exhibit a planktonic stage (Baynes and Szmant, 1989). Wilding (2006) speculated that the entrapment of drifting macroalgae at the periphery of the Loch Linnhe reef resulted in the observed changes in the sediment infaunal community. Moreover, the current not only affects *Epifaunal* organisms' settlement and growth, it affects mobile animals which swim around the reef, and it has been found that fish are attracted to turbulent water (Lin and Su, 1994). A possible effect of currents on fish behaviour it is that they avoid swimming in laminar flow to save energy and to exploit prey swept-up and disorientated by the flow (Godoy et al., 2002).

However, reef movements related to sediment transport occur due to subsidence when it sinks into the seabed because of its weight and the water motion which redistributes the sediment erosion and accretion surrounding the artificial reef (Grove at al., 1991). As a result, the design of an artificial reef structure should minimize sediment erosion. For example, some reefs in regions with moderate or high current flow have been designed so that the structures have an opening at the reefs base to let water flow pass without raising the velocity at the base edge (Mottet, 1981). Scour prevention is important since the fine materials will be carried away by the current leaving coarse sediment remaining which affects the input of shell detritus originating from reef-encrusting organisms, as well as influencing sediment oxygenation, which has an impact on the benthic environment (Barros et al., 2001). An observation on the Loch Linnhe site showed a hydrodynamic energy gradient across it. It has higher energies in the northeast part that may cause sediment scouring with sediment suspension in this high energy region and subsequent sediment deposition in low energy region. This current regime with its effect on sediment causes distribution of benthic *Epifauna* and *Infauna* which was observed in Loch Linnhe artificial reef (Wilding and Sayer, 2002a).

The reason for this distribution is due to the role of water movement in delivering oxygen to the benthos marine organisms (Forster et al., 1996).

2.4 Cases for marine structure under hydrodynamics condition

The hydrodynamics condition affecting the marine structure is important to investigate due to effectiveness on many characteristics such as structure stability. In this section, two cases have been chosen for demonstrating the effect of the hydrodynamics regimes. The offshore wind-turbine and artificial reefs deployed in the Western Adriatic, Italy. These examples assist to understand the collinear relationships between the reef hydrodynamics and the marine life that settle and live in its surrounding.

2.4.1 *Offshore wind-turbine as an artificial reef*

Wind-turbines are one type of such platforms that have an impact on marine life. Since, the foundations of offshore wind turbines could be deliberately designed to function as artificial reefs intended to increase food availability and provide sheltered ecosystems for target fish species (Wilhelmsson et al., 2006). The foundations of wind turbines, which may be constructed by different techniques (Hammar et al., 2010), have an impact on the ecosystem according to their different sizes and the material used in their construction. In fact, the major difference between the commonly deployed artificial reefs and wind turbine foundations reviewed by Baine (2001) is that most of artificial reefs are sunken completely under water whereas wind-turbine artificial reefs penetrate the whole water column with dry parts of the turbines. Wind-turbine base can suffer from erosion or scour around due to strong currents which induce sediment transport and can cause damage to the wind turbine infrastructure. In fact, scour depends on the speed of the current, the sediment grain size and the nature of the structure (Linley et al., 2007) and it is crucial to be able to assess these factors reliably in order to produce a viable foundation/reef design. One method is increasing the depth of the pile into the sediment and placing a protective surface around the base of the turbine using rock armour as demonstrated by Figure 2.14. Rock armouring involves rock dumping around the turbine base and forming a circular reef of 10 – 15m in radius with the foundations at its centre (Linley et al. 2007). The materials used for scour protection may have an impact on the level of colonization that will be created.

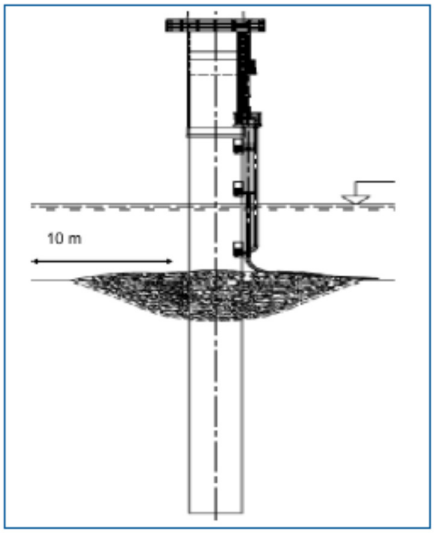

Figure 2.14 Rock armour used around a monpile turbine foundation to protect it from scouring (Barton, 2006).

Nevertheless, the current around the base of the wind-turbine will always be changed and it will affect the potential habitat surrounding the foundation. The varying strengths of current will create different types of bed forms, such as ripples to sand ribbons and hollows that may attract different benthic communities (Parkinson, 1999). The beginning of fouling colonization starts with same process described in section 2.2.2. In fact, most of larvae species have adopted strategies to maximize their competence and settling chances. For example, the common mussel, found with high numbers at Horns Rev wind farm in Denmark, is a superior competitor to any other sedentary species of invertebrates and macro algae and can cover much larger areas, leading to a massive colonization of the common mussel in this area (The Danish Forest and Nature Agency, 2006). The mussel densities observed ranged between 90,000 to 200,000 ind./m^2 in 2003, with most of the mussels found on the upper part of the monopoles and the shafts of the turbines as shown in Figure 2.15. Truly, species that settle on wind turbine foundations, or artificial reefs can be surprisingly diverse, and their presence depends partly on the water quality and conditions available.

Figure 2.15 A massive colonization of the common mussel on turbine foundation at Horns Rev (The Danish Forest and Nature Agency, 2006)

However, the flowing water offshore behaves as a boundary layer that is characterized by a velocity variation within the water column ranging from zero at the seabed to the full tidal flow at the free surface. The hydrodynamics of a surface piercing circular pier placed on a bed in steady current, for example, has been studied by many authors such as Roulund et al. (2005) also Sumer and Fredsoe (2001). The flow is accelerated around the pile and separates from its surface as it experiences an adverse pressure gradient on its downstream face. This process is commonly accompanied by vortex shedding and the formation of a disturbed wake downstream of the pile and a horseshoe vortex in the front of the pile as demonstrated in Figure 2.16. Depending on the flow conditions, turbulence may be generated due to the changes in the flow and, as a result, an increase of sediment transport near the structure will be observed. In generally, researchers found that the scour process depends on the flow velocity and the turbulence intensity at the transition between fixed body and erodible bed (Hoffmans and Verheij, 1997).

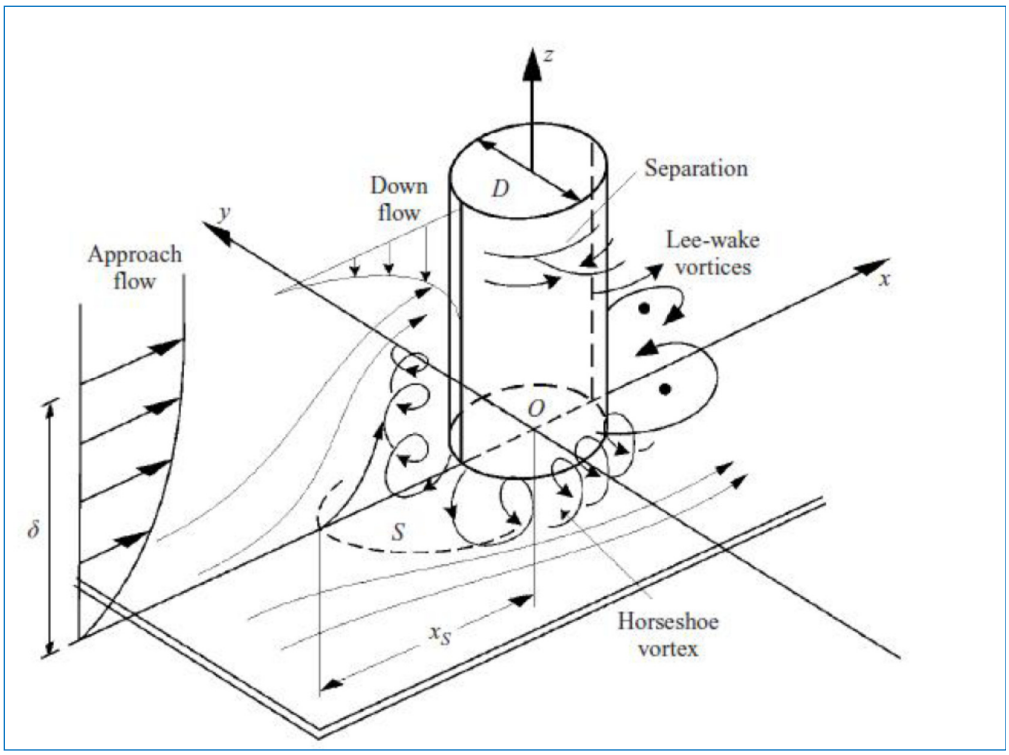

Figure 2.16 The flow pattern variation as a steady current passes a vertical pile (Roulund et al., 2005).

As a result, any fixed body can develop scour downstream as shown the schematic flow pattern in Figure 2.17 which shows a sill with bed protection. As Figure 2.17 indicates vortices with vertical axes may develop due to the influence of a flow pattern with a vertical wall or any fixed structure. The vortex intensity can be very large and scour hole development can potentially be seen to take the form as shown in Figure 2.17. There is danger of structural instability unless sufficient precautions are taken (Hoffmans and Pilarczyk, 1995). Very turbulent flow, as will be the case with artificial reefs, causes sediment erosion at the bed due to ascending currents and rotation in separating vortices which lead to sediment settling out sideways (Hoffmans and Verheij, 1997). The phenomena will effect on sediment causing distribution of benthic *Epifauna* and *Infauna* as observed in Loch Linnhe artificial reef in Wilding and Sayer, (2002a) study.

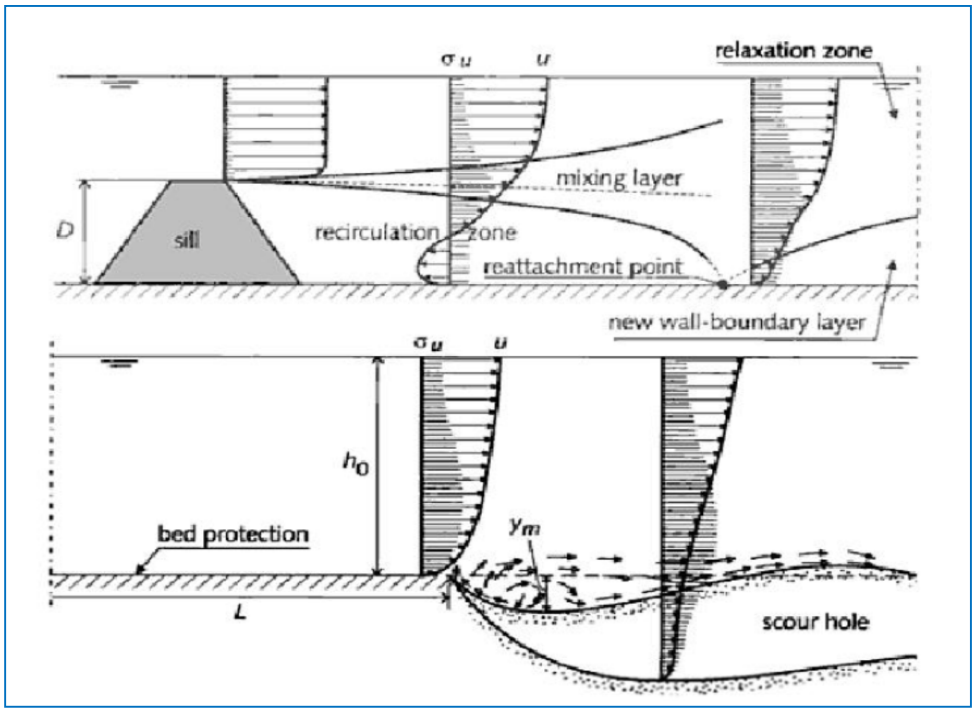

Figure 2.17 The flow pattern downstream schematic over a sill (Hoffmans and Verheij, 1997).

2.4.2 *Artificial reef in the Western Adriatic Sea, Italy*

An artificial reef's structural stability depends on the balance of sediment scouring and settlement, and an artificial reef can buried as a result of the ocean dynamic conditions over time. Manoukian et al. (2011) investigated acoustically an artificial reef that lies in the Western Adriatic Sea, Italy after thirty three years of deployment. The investigation was on sediment scouring, burial and any variation in the horizontal level. As shown from Figure 2.18 a pyramid artificial reef with 6 m height is suffering from currents parallel to the shoreline and an accumulation of sediment due to scouring can be clearly seen. The sediment surrounding the reef shows a sediment pile of about 1 m height as well as a scouring erosion site as multi-beam echo sounder indicates. The study concluded that artificial reef deployment can change the seabed topography due to local hydrodynamics raising the fluid velocity and the turbulence intensity. Manoukian et al. (2011) observed that several of their artificial reefs experienced geophysical processes such as scouring, sinking and deepening due to sediment instability. As a result, there is a decrease in the reef's finfish and living marine life which affects the role of these reefs as aggregation devices.

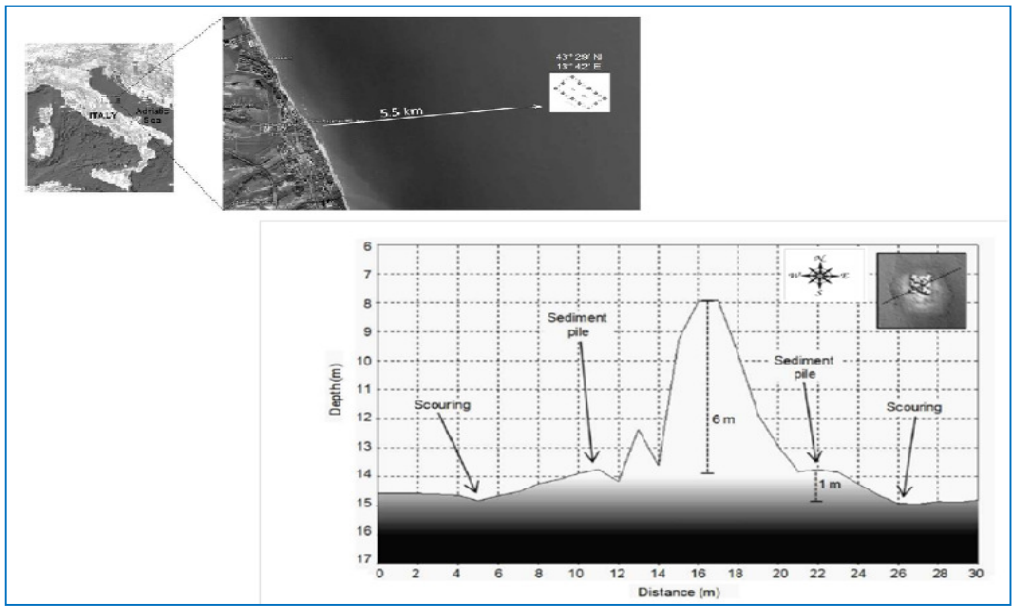

Figure 2.18 The depth profile of a pyramid artificial reef indicting the sediment surrounding the reef due to Ocean conditions after 33 years of deployments (Manoukian et al., 2011).

2.5 Summary of artificial reef hydrodynamics and its environmental impacts

In summary, the global hydrodynamic conditions in the vicinity of an artificial reef dictate its structural design (reef stability etc) and the nature of its large scale environmental impact (sediment transport and erosion etc). They also impose constraints on its functionality (it can only provide the ideal habitat for a target population if it can also maintain its structural integrity). The local hydrodynamic conditions dictate flow separation and the production of turbulence, generating eddies and vortices over a range of scale. This, in turn, determines the water quality (such as oxygen content), settlement patterns over the reef and regions favourable, or otherwise, to fish activity (predation, evasion, congregation etc). For these reasons, a reliable procedure for determining the hydrodynamics of local and global of flows about artificial reefs is an essential prerequisite to their satisfactory design.

Chapter 3. Tidal phenomena and numerical modelling of the shallow water equations

3. Introduction

The tides near coastlines can be very complex due to the presence of complicated bottom topographies, tidal flow hydrodynamics and irregular boundaries. In recent years, the effect of tidal flow hydrodynamics on artificial reef has been studied for its impacts on the artificial reef eco-efficiency. In fact, hydrodynamic process of ebb and flood tides can influence the seabed sediment that controls the activities of benthic marine organisms (Limpsaichol et al., 1994). In addition, intensive tidal current can cause stability problems in the form of local scour affecting the artificial reef structure as described in chapter two. Thus, the simulation of current hydrodynamics and water oscillation in artificial reef regions provides a powerful tool for understanding the different marine phenomena involved.

In previous decades there were many numerical methods proposed to simulate ocean problems. The shallow ocean area was focused on in these simulations due to its importance in marine environmental issues. The shallow water equations provide quite an efficient and effective method to be used in simulating shallow ocean area. Furthermore, shallow water equation models have been developed for many natural phenomena, such as predicting tidal ranges and storm surges, which is important in the development and planning of coastal areas. In addition, they can be used to study transport phenomena by coupling the shallow water equation models to transport models like that of pollution in bays and estuaries, which can affect commercial projects such as aquaculture operations in coastal water (Venayagamoorthy et al., 2011).

The shallow water equations have been used to model many flows such as rivers, estuaries, shallow lakes and coastal zones (Yu and Kyozuka, 2004). There are many models available to evaluate tidal flows based on different numerical methods to solve these equations. The numerical methods include: the Finite Element Method [FEM] found in Akanbi and Katopodes (1988), Bermudez et al. (1991), Kodama and Kawahara (1994), Li et al. (2003), Leupi et al. (2009); the Finite Difference Method [FDM] shown in Garcia and Kahawitha (1986); Fennema and Chaudhry (1989; 1990); the Discontinuous Galerkin Finite Element Method [DG FEM] described in Aizinger and Dawson (2002) as well as Yu and Kyozuka (2004); the Lattice Boltzmann Method

[LBM] seen in Chen and Doolen (1998); Banda et al. (2009); Zhou (2002); and the Finite Volume Method [FVM] reported by e.g. Zhao et al. (1994; 1996). The Finite Volume Method [FVM] is one of the most common methods that have been used to solve problems related to bioenvironmental flows and it has often been applied in marine and ocean environments (Zhao et al., 1994).

3.1 The tides patterns and prediction

The oscillation of the bodies of water has a natural period due to the tide-generating forces, some of which act as daily or diurnal forces, and others as semidiurnal forces. There are several features that can be observed from tides. These features may include the relationship between solar declination and lunar and high diurnal tides as demonstrated in Figure 3.1, and others such as the spring-neap cycle of semidiurnal amplitudes (Pugh, 1996). In fact, tidal range changes according to the intensity of tide-generating forces due to astronomical effects. The synodic month, which is referenced to the phase of the sun or the moon, causes spring and neap tides during periods of 29.530588 days in length (Hicks, 2006). When the tide's ranges are greater than the monthly averaged range they're called spring tides, which occur twice every synodic month. Further, the neap tides are tidal ranges that are less than the monthly average and happen twice in the synodic month as shown in Figure 3.2 (Trujillo, 2010).

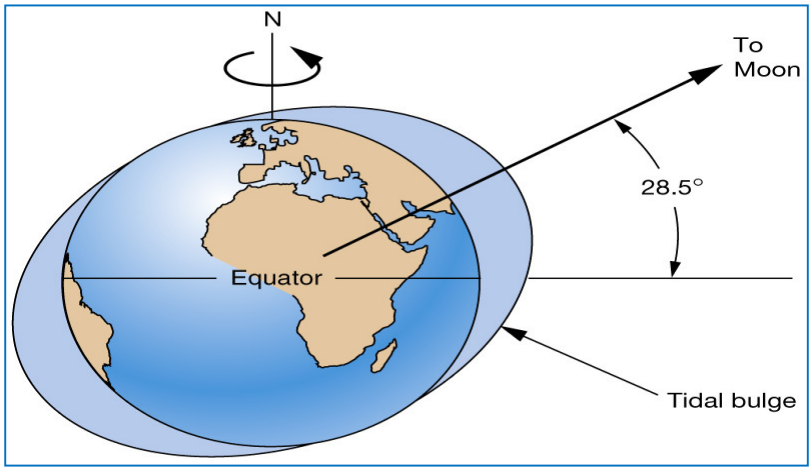

Figure 3.1 The tidal bulges centres may be set at any latitude from the equator with a declination angle 28.5° on either side of the equator, depending on the season of the year (Trujillo, 2010).

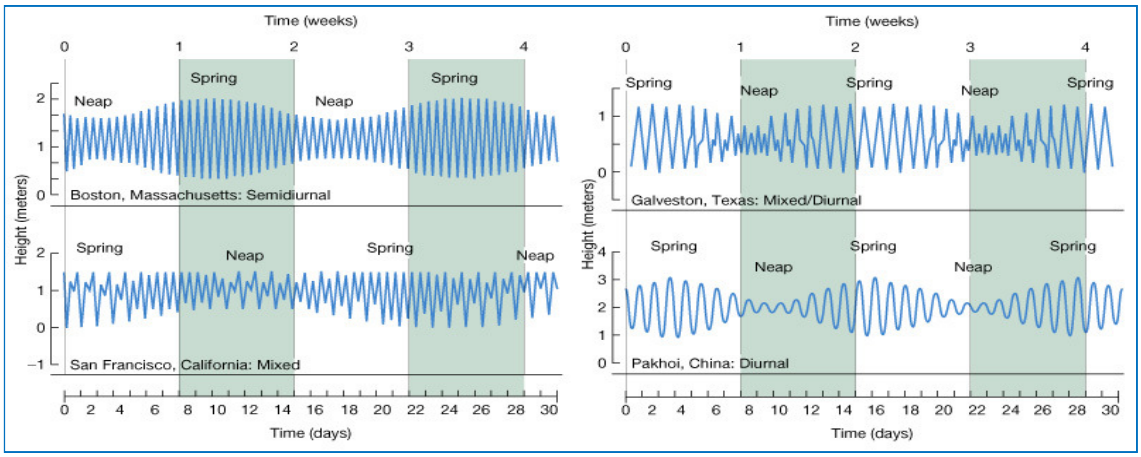

Figure 3.2 The monthly tidal range variations at various sites on the world with different daily tidal patterns (Trujillo, 2010).

On the other hand, the prediction of tides at a specific site can be estimated by an empirical determination that is based on harmonic analysis (Palmer et al., 1980). In addition, the rise and fall of water determined by the tide can be modelled in the form of a series of harmonic terms that represent the tide-generating forces related to astronomical conditions (Schurman, 1941). Every term in the series is represented by a hypothetical tide-generating force that is related to an orbiting earth, and a constituent tide with its own period (Marmer, 1954). In tidal analysis a constituent is usually described by its speed or frequency in degrees per hour forming one simple harmonic cosine curve see equation (3.1). In the equation (3.1), $\eta_t(t)$ represent water elevation of the tide at time (t), R_0 is the tide amplitude that is equal to one-half of the tidal range, ϕ is the phase degree and ω_0 is angular speed. For example, the principal solar semidiurnal S_2 the subscript $_2$ indicates two complete tidal cycles for each astronomic cycle which represents the earth spinning relative to the sun. Further, the period of the sun constituent is 12 mean solar hours which gives a speed of $S_2\ that \quad 360^o/12 = 30^o/hr$. Note the constituent (cosine curve) is consisting of 360^o from crest to crest (Hicks, 2006). Similarly the principle lunar semidiurnal constituent M_2 represents the earth spinning relative to the moon, which lasts 24.8412 mean solar hours known as lunar day. The period for a tidal cycle caused by the moon is 12.4206 mean solar hours that gives a speed of $M_2\ that \quad 360^o/12.4206 = 28.984^o/hr$. In fact, these tidal constituents can be shown as curves for every component which is described as oscillations about mean tide level. The S_2 and M_2 constituents combined in phase with its maxima gives the spring tide which will occur at new moon and full moon time (Hicks, 2006).

In addition, the neap tides happen when these constituents S_2 and M_2 don't match in phase at the time of the first and third quarter as represented in Figure 3.3. There are several of constituents (see table 3.1) which can be theoretically calculated such as the Luni-solar declinational diurnal constituent K_1 as well as the principal lunar declinational diurnal constituent O_1 (Parker, 1991). In fact, U.S. NOAA uses 37 constituents for standard analysis for most U. S. coasts to simulate the major motions and perturbations in the sun-moon-earth systems (Hicks, 2006).

$$\eta_i(t) = R_0 \cos(\omega_0 t - \phi) \qquad (3.1)$$

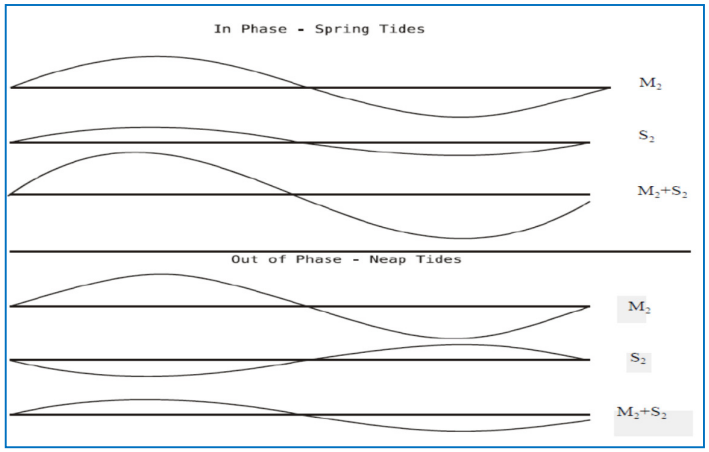

Figure 3.3 The relationship of phases seen in spring and neap tides explained by the harmonic constituents (Hicks, 2006).

M_2	**1.00**	**12.42hrs**
S_2	**0.46**	**12.00hrs**
O_1	**0.41**	**25.82hrs**
K_1	**0.40**	**23.93hrs**
N_2	**0.20**	**12.66hrs**
P_1	**0.19**	**24.07hrs**
L_2	**0.03**	**12.19hrs**

Table 3.1 Semidiurnal and diurnal constituents related to the theoretical relative magnitude with periods of the constituents [360°/speed] (Hicks, 2006).

Nevertheless, it must to be noticed that these constituents are computed theoretically depending on the equilibrium tides theory that calculate the tide-generating forces and it may not match the observed tide (Pugh, 1996). The harmonic constituents can be divided and solved for their amplitudes and phases from a tidal height record time series which can be analysis by a least squares fitting method that forms a series of sine and cosine curves. In fact, harmonic analysis uses the least-squares fitting method to fit and adjust so as to minimise the square of the differences $\sum S^2(t)$ between the observed and computed tidal level (Pugh, 1996). The schematic of least-squares fitting procedures which create a tidal function as follows:

$$\underset{\text{known}}{[\text{Observed level}]} = \underset{\text{known}}{[\text{Equilibrium Tide}]} \quad \underset{\text{unknown}}{[\text{empirical contants}]}$$

The function of tidal oscillation is formed by a finite number of N harmonic constituents and it depends on the length and quality of the tidal data records. Further, information can be found in many references such as Forrester (1983), parker (1991), Pugh (1996) and Hicks (2006).

3.2 Summery of numerical method applied to model tides

In tidal flow computer simulations the Finite Difference Method [FDM] solving the shallow water equations has been the most commonly used method so far. This method has a long history in tidal flow simulation having been used for calculations such as simulating the tidal flow in the English Channel and Southern North Sea (Praagman et al., 1989). The FDM method transforms the governing partial differential equations into difference equations using a scheme applied at grid points. It has been popular in applications in regional seas and basin-scale Ocean modelling (Chu and Fan, 1997). The solution of this method is strictly valid only at the grid points.

Usually, in FDM the coordinates are (*x, y*) in the horizontal direction and *z* in the vertical direction but many finite difference models apply variations on the vertical coordinate. For example, Bryan (1969) uses *z*-coordinates as well as Blumberg and Mellor (1987) use *sigma* as a vertical coordinate. However, the application of a terrain-following *sigma* coordinate as a vertical coordinate in the FDM causes truncation errors at sharp locations in the topography due to horizontal pressure gradient errors (Chu and Fan, 1997). An improvement in the accuracy of the *sigma*-coordinate in the FDM has

been worked by various researchers such as Gary (1973), McCalpin (1994) also Chu and Fan (1997).

There are many finite difference models, the Princeton Ocean Model uses primitive three-dimensional flow equations with an assumption of hydrostatic pressure distribution in the vertical direction, and the FDM is used to solve resulting equations (Casulli and Cheng, 1992). It was applied to simulate flooding and drying of tidal mud-flats by the marine environmental commission (MEC) in Japan. Another well-known Finite Difference Method for tidal flow has been presented by the Japanese Society of Naval Architects and Ocean Engineering who have been using the model to study the water level variations in the Caspian Sea (Yang et al., 2008).

For applications where the solution is smooth the Finite Difference Models may produce accurate results but they are not the preferred method for coping with more complex hydrodynamics which involve flow discontinuities (Yu and Kyozuka, 2004). The finite element method [FEM] is more suited to such flows and has been applied extensively in tidal flowing modelling. The most important characteristic of the FEM in this respect is its ability to handle complex geometries (and boundaries) with comfort. The FEM method has been illustrated in many oceanographic problems such as the numerical modelling carried out by Jones (2002) to study the coastal and shelf-sea in the European context, and Fortunato et al. (1997; 1999) who examined the influence of tidal hydrodynamics on the Tagus estuary. Walters Roy (1989) compared two Finite Element models: one model applied harmonic decomposition in time (Walters Roy, 1989) and the other used a time-stepping approach (Werner and Lynch, 1987) in his prediction for North Sea tides in the English Channel.

TELEMAC is a numerical modelling package that includes modules such as free surface modelling, sedimentology, water quality, sea waves and groundwater flow modelling. The TELEMAC system was developed by the Laboratorie National d'Hydraulique et Environment (L.N.H.E) which is a research department of the French Electricity Board [EDF-DRD] (Hervouet and Bates, 2000). The TELEMAC system has been developed applying the Finite Element Method which is available in two-dimensional with triangular or quadrilateral meshes, and in three-dimensional with tetrahedron or prism meshes (Hervouet et al., 2010). TELEMAC has been widely applied in coastal simulation to model tidal currents and shelf seas flow (Sauvaget et al., 2000; Jones and Davies, 2006; Hervouet, 2007). However, the finite element models

encounters similar obstacles when to the finite difference codes when it is applied to such flow problems. The FEM can experience difficulty when it encounters both sub-critical and super-critical flows (Akanbi and Katopodes, 1988; Zoppou and Roberts, 1999).

A numerical method that has recently gained popularity for solving the shallow water equations is the Discontinuous Galerkin Finite Element Method [DG FEM] (Aizinger and Dawson, 2002). The DG FEM method differs from the FEM which assembles a global system and solves very large set of linear equations (Zhixing and Kyozuka, 2004). In this method, mass conservation is locally enforced at each element in the DG FEM and it has ability to capture steep gradients and fronts. The DG FEM method doesn't have a limit on the selection of element basis pairs which improves the compatibility of velocity and pressure in it, and it is an important characteristic in this method, whereas it is difficult to achieve in the continuous FEM method (Zhixing and Kyozuka, 2004). It has produced promising results in applying the hyperbolic conservation laws (Krivodnova et al., 2004). In fact, it was implemented on a tidal flow in a narrow straight channel that connects two bodies of water and it gave good results due to its ability to capture high velocity flows in the narrow channel which Zhixing and Kyozuka (2004) studied. The disadvantage of DG FEM is that it is a computationally intensive technique requiring large computer resources.

Another numerical method that has been used by Zhou (2002) to solve the shallow water equations is the Lattice Boltzmann Method [LBM]. The LBM has the advantage of simple arithmetic calculations and its suitability for flow over complex geometries, such as porous media simulation, since it is easy to implement the boundary conditions and is well suited for implementation on parallel computer architecture (Banda et al., 2009). This method has also been applied to solve the shallow water equations that represent wind-driven circulation (Salmon, 1999; Zhong et al., 2005). In addition, it was implemented to study pollutant dispersion by tidal flow with a complicated geometry due to irregular bathymetry (Banda et al., 2009).

The Finite Volume Method [FVM] is a discretization method that transforms the partial differential equations into an integral equations form commonly used in ocean modelling (Chu and Fan, 2002). It is preferred in the numerical simulation of various types of hyperbolic systems that allow problems with discontinuities such as shocks (Valiani et al., 1999). FVM is conserved even on arbitrary grids due to the integral

equations that link the fluxes across the boundary with the temporal variability of the dependent variables for the volume (Kobayashi, 1999; Hermeline, 2000). The FVM has a similar flexibility in handling complex geometry and abrupt topography as the FEM, combined with similar advantages of the simplicity of the FDM (Mingham and Causon, 1998). In fact, FVM is closely related to the FDM since FVM can be interpreted directly as a finite difference approximation to the differential equations (LeVeque, 2002). Furthermore, FVM is computationally much more efficient than FEM. As a consequence FVM more commonly used than FEM for computing complex fluid flows. The Finite Volume Godunov-type scheme has been applied to simulate tidal flow modelling. In fact, Chippada et al. (1998) worked with it to simulate tidal waves in Galveston Bay in USA. The finite volume Godunov-type models compared with the aforementioned approaches have the ability to work with complex flow conditions like the discontinuities method and it's more efficient than the DG FEM models. It can be implemented efficiently on both structured and unstructured meshes (Aghajanloo et al., 2011). The FVM has been adopted by many CFD experts because of two main advantages (Lomax et al., 1999):

1. The discretization values such as momentum and, mass is conserved in a discrete sense due to the integral form of the conservation equations.

2. In order to be applied on irregular meshes finite volume methods do not necessitate a coordinate transformation. As a consequence, they can be applied on unstructured meshes consisting of arbitrary polygons in two dimensions as well as using arbitrary polyhedrals in three dimensions.

3.3 Review of Godunov-type Finite Volume solvers

The shallow water equation is a generalization of the dam break problem, which is similar to the Riemann problem. The Riemann problem consists of a conservation law together with piecewise constant data that have a single jump discontinuity. It appears in a natural way in the Finite Volume Methods in the solution of equation of conservation laws because of the discreteness of the grid. Godunov (1959) proposed in his paper a successful numerical approaches to solve a first-order hyperbolic system of equations that has been proven to be powerful in simulating discontinuous flows that can contained in the solution to the non-linear hyperbolic systems (LeVeque, 1992; Guinot, 2003). In the Godunov approach the variables are approximated as average

inside the element volumes whereas the advective fluxes at each cell interface is calculated by solving the Riemann problem (Guinot, 2003). Therefore, fluxes computed at each element edges are the results of the solution to the Riemann problem defined by two constant states to either side of the edge. In the context of a Godunov method, inter-cell fluxes may be obtained by solving local Riemann problem exactly, known as exact Riemann solver. The exact Riemann solver is complex in mathematical form and unreasonable in computational time (LeVeque, 2002). Therefore, it is common to apply an approximate Riemann solver. Several approximate Riemann solvers that have been derived to evaluate numerically convective fluxes such as conservative difference scheme van Leer (1977); Osher's scheme seen in Osher and Solomon (1982). Roe's scheme found in Roe (1981) has been one of the most commonly applied but its weakness is in ensuring the positivity of the discrete water height (Benkhaldoun et al., 1999).

Another is the Harten-Lax-van Leer (HLL) scheme shown in Harten et al. (1983) which was extended to a family of HLL schemes. This scheme was developed for the Euler equations of gas dynamics by Harten et al. (1983) to estimate the wave speed in a Riemann problem. Discontinue in the Riemann problem is constructed by a linear solution and the wave speed is evaluated for the wave propagating discontinuities (Toro, 1997). This approach generated a number of applied schemes after Davies (1988) and Einfeldt (1988) suggested several techniques to compute the speed of waves required to determine the inter cell flux. These produce forms of efficient Riemann solvers with powerful approximations to the Godunov method (Davies, 1988). Therefore, a family of HLL solvers was produced such as: HLLE (Harten-Lax-van Leer-Einfeldt) found in Einfeldt (1988); HLLC Harten-Lax-van Leer in which the "C" denotes contact, suggested in the Toro et al., (1994) paper; the HLLD (Harten-Lax-van Leer Discontinuities) which is an enhancement of the HLLC scheme for modelling magnetohydrodynamics (MHD) presented in Miyoshi and Kusano (2005). The HLL solver in the most efficient and robust of the Riemann solvers due to its simplicity, and it can easily be extended to its family. The major characteristic in this scheme is its ability to satisfy very natural properties like the conservation and non-negativity of water height, including the capability to compute dry areas that can be found in coastal flow (Audusse and Bristeau, 2007). Therefore, the HLLC approximate Riemann solver scheme (Toro et al., 1994) is adopted in the present numerical model. The tidal flow over very complicated bed topographic will create complex hydrodynamics conditions

such as subcritical flow, transitional flow, hydraulic drops and hydraulic jumps (Liang, 2008). The Godunov-type scheme is preferred for this kind of complex flow (Hu et al., 1999; Causon, 1999). This numerical scheme has the capability of capturing different type of flow with shock-type flow discontinuities, such as hydraulic jumps. Therefore, the Godunov-type finite volume solvers for the non-linear shallow water equations models are commonly applied in shallow flow modelling (Liang, 2008). As an example, Chippada et al. (1998) adopt the Godunov-type method to simulate the shallow flow on complicated physical domains arising from irregular coast-line and island. The results gave excellent agreement between the predication and analytical solutions, giving confidence in this type of method for application to coastal tidal flow. The Godunov-type Finite Volume Method has been adopted in the present work due to its accuracy in representing flow on complex seafloor geometry.

3.4 Model governing equations

The mathematics of shallow water equations can govern many physical phenomena, especially those with free surface flow under the influence of gravity, such as: flood waves, tides in oceans, wave breaking on beaches and dam-break wave modelling (Toro, 2001). It can be used to represent the hydrodynamics of a free surface in a vertically well mixed water mass where the horizontal length scale (wave length) is very large compared to the water depth. In this study, the shallow water equations were solved applying the finite volume Godunov-type scheme implemented with HLLC approximate Riemann solver. The original numerical model applied in the present work was developed by Dr.Qiuhua Laing and the numerical model scheme is explained in appendix A. The model has been intensively tested for fluvial flood modelling (Liang, 2010) but has not been applied in modelling tidal flow hydrodynamics. Therefore, the initial and boundary condition in the numerical model must be modified to simulate the tidal hydrodynamics flow.

3.5 One-dimensional tidal wave flow tests

The free surface tidal wave is considered to be a good test to validate the present numerical model. Two analytical tests were applied to study the computational accuracy of the used numerical scheme. The first test was a verification of a tidal flow in a channel with varying topography that has been solved analytical by Bermúdez and Vázquez (1994). Whereas, the second test was proposed by Goutal and Maurel (1997)

in a workshop on dam-break simulations to be applied for tidal wave flow over irregular bed topography. The effect of the mesh size and the numerical accuracy has also been investigated. These problem tests were studied by Zhou et al. (2001) to investigate the accuracy of his Godunov-type numerical scheme.

3.5.1 *Tidal wave test objective*

The finite-volume schemes of the Godunov type that solve the shallow water equations require treatment of the source terms to balance the equations. These terms are relevant to bed topology and bed shear stress and their effect on the solution of the equations. Therefore, it is essential to model it with realistic problems such as tidal wave flows in coastal water regions, and tidal flows in estuaries, both of which require an idealization of the bed topology. The numerical model was tested in a 1D-tidal wave flow condition to assess its numerical accuracy and usability.

3.5.2 *Tidal wave flow in a channel over non-uniform bed topology*

A channel has 14 km length (L) with 350 m wide with frictionless bed was proposed by Bermúdez and Vázquez (1994) to study tidal wave. The channel bed is defined with the following equation:

$$z_b(x) = 10 + \frac{40x}{L} + 10\sin\left[\pi\left(\frac{4x}{L} - \frac{1}{2}\right)\right] \tag{3.2}$$

Bermúdez and Vázquez (1994) asymptotic analytical solutions for the still water depth (h_s), water depth (h) as defined in Figure 3.4. The water depth and tidal flow velocity (u) equations are given follows:

$$h_S(x) = 50.5 - \frac{40x}{L} - 10\sin\left[\pi\left(\frac{4t}{86{,}400} - \frac{1}{2}\right)\right] \tag{3.3}$$

$$h(x,t) = h_S(x) + 4 - 4\sin\left[\pi\left(\frac{4t}{86{,}400} + \frac{1}{2}\right)\right] \tag{3.4}$$

$$u(x,t) = \frac{(x-L)\pi}{5400h(x,t)}\cos\left[\pi\left(\frac{4t}{86{,}400} + \frac{1}{2}\right)\right] \tag{3.5}$$

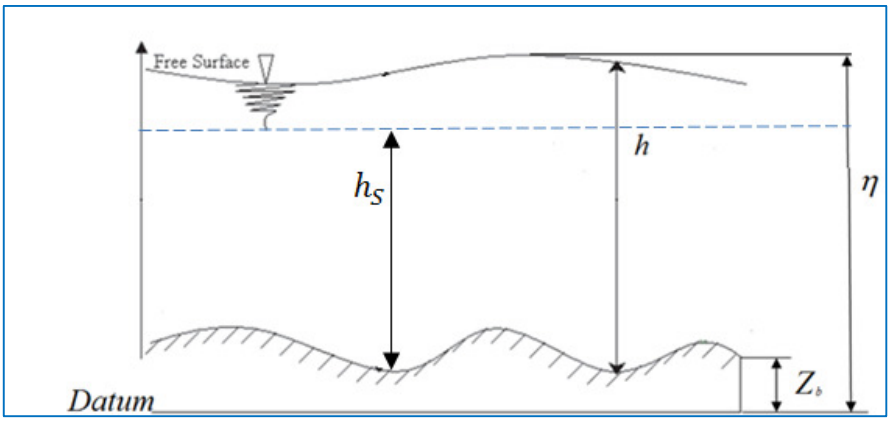

Figure 3.4 The water depth definition applied in the numerical scheme.

The initial and boundary conditions are given as:

$$h(x,0)=h_S(x) \quad ,\eta(x,0)=h(x,0)+z_b \text{ and } u(x,0)=0 \tag{3.6}$$

The inflow boundary condition at the western end of the numerical domain was set by $h(0,t)$ *and* $u(0,t)$. On the other side the outflow boundary at the eastern end of the channel was set to $u(L,t)$. The north and south boundary of the numerical domain was set to a slip boundary condition. The accuracy of the numerical model is demonstrated by comparing four uniform computational mesh sizes of 100, 200, 300 and 400 grid-sizes that were adopted to achieve a grid-independent solution. The numerical modelling results were compared with the analytical solution for time simulation equal to 7552.13 sec. The water elevation (η) of the four mesh sizes is presented in Figure 3.5 and tidal velocities with the four grid sizes is demonstrated in Figure 3.6. Avery good agreement has been found between the analytical solution and the numerical results. The tidal velocities of the four grid-sizes were subtracted from the analytical solution to indicate the differences between the numerical results and the analytical solution as seen in Figure 3.7. It shows that as the mesh size increases the differences between the two solutions decreases. The differences range of the tidal velocity component between the numerical model and the analytical solutions are of the order of 0.5×10^{-3} - 4.7×10^{-3}. Note that the time step of the numerical model is governed by the Courant-Friedrichs-Lewy (CFL) criterion to give stability to the numerical model by calculating the appropriate time step of each mesh size as shown in Figure 3.8. The smallest convenient time step is 0.35 sec adopted in the highest grid size. Whereas, the biggest relevant time step is 1.41 sec for the coarsest mesh. The good agreement of the numerical model

results with the analytical solution testifies to the capability of the present numerical model with regard to tidal flow simulation.

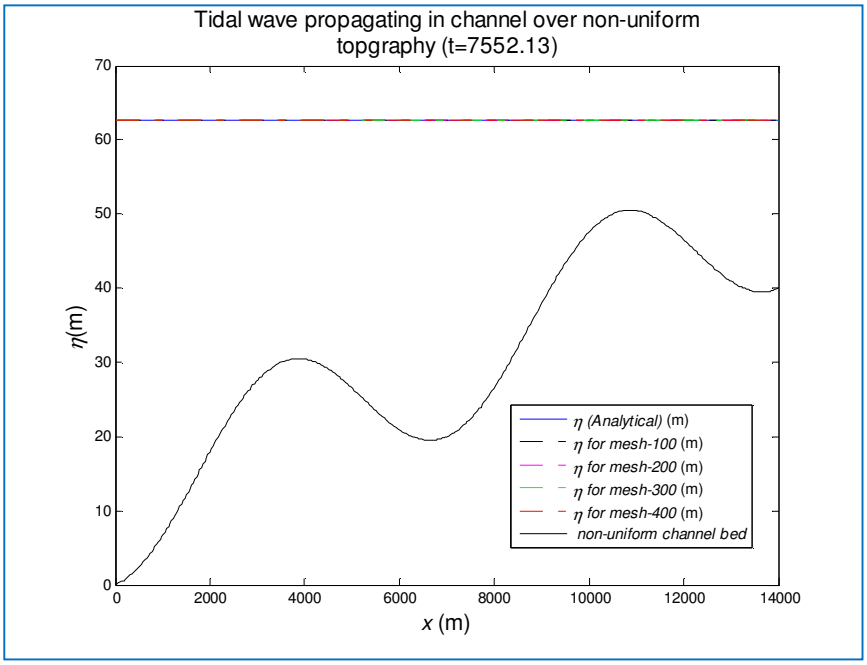

Figure 3.5 The tidal wave elevation compared with solution suggested by Bermúdez and Vázquez (1994) as a benchmark test for numerical scheme verification for unsteady flows.

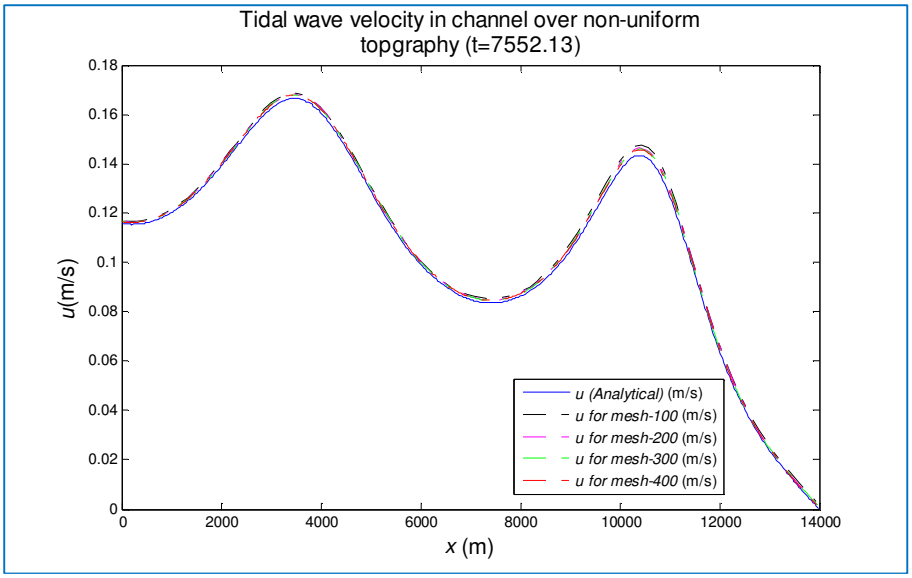

Figure 3.6 The tidal current velocities of the each grid-size compared with the analytical solution.

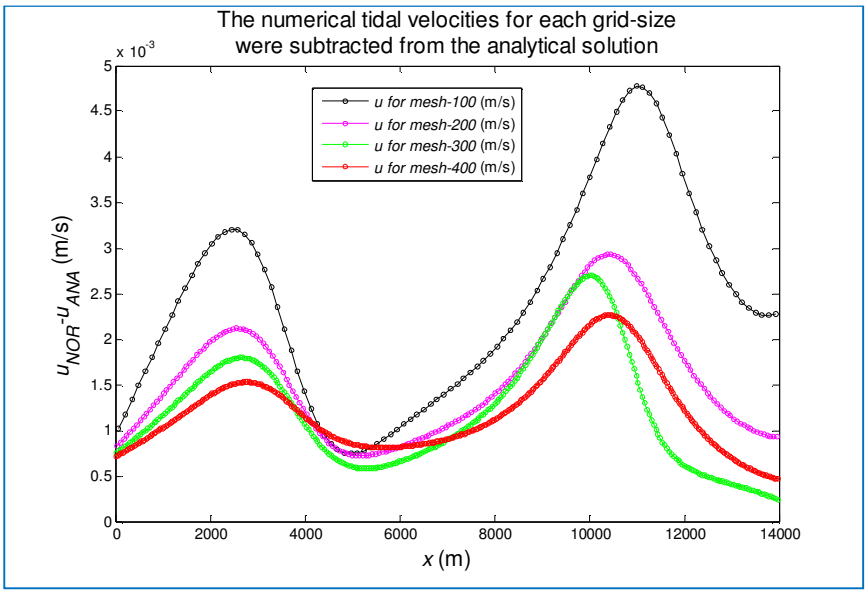

Figure 3.7 The numerical model results of tidal wave velocity for each mesh size. It was subtracted from the analytical solution to investigate accuracy of the numerical model for each grid.

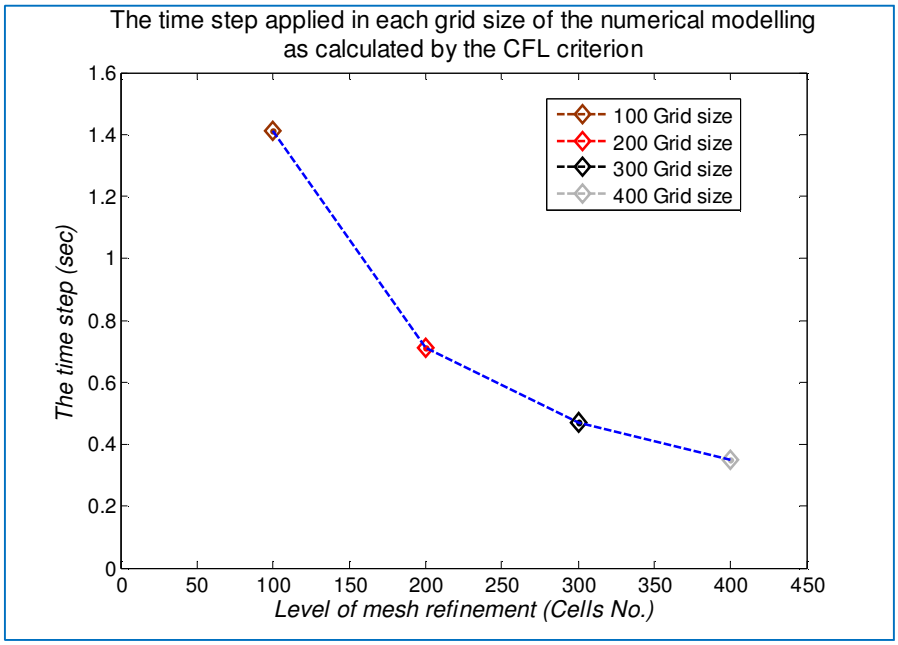

Figure 3.8 The appropriate time step estimation for each mesh-size in the *x*-direction as calculated by the CFL criterion.

3.5.3 *A tidal wave propagating in a channel over an irregular bed*

The numerical method has been validated by solving a tidal wave flow over an irregular bed, as proposed by Goutal and Mourel (1997) in the Dam-break Wave Simulation Workshop and as considered by Zhou et al. (2001). This test was applied to verify the effectiveness of the present numerical model on dealing with complex bed topography. In this case, the test considers a coastal tidal wave propagating toward and through an upstream inlet of a river mouth. It is a 1D-problem with a channel length L=1500 m in the x-direction and 150 m width in the y-direction with frictionless bed. The tidal wave is propagating in a channel with an irregular bed defined by table 3.2.

Table 3.2 The bed topology for irregular bed in the x-direction

x	0	50	100	150	250	300	350	400	425	435	450	475	500	505
z_b	0	0	2.5	5	5	3	5	5	7.5	8	9	9	9.1	9
x	530	550	565	575	600	650	700	750	800	820	900	950	1000	1500
z_b	9	6	5.5	5.5	5	4	3	3	2.3	2	1.2	0.4	0	0

The analytical solution of the water depth was solved by:

$$h(x,t) = 20 - z_b(x) - 4\sin\left[\pi\left(\frac{4t}{86{,}400} + \frac{1}{2}\right)\right] \tag{3.7}$$

The x-direction velocity component is defined by equation (3-5). The initial and boundary conditions applied to simulate the present numerical model are defined as:

$$h(x,0) = \eta(x,0) - z_b(x) \quad , \eta(x,0) = 16\ m \text{ and } u(x,0) = 0 \tag{3.8}$$

At the western inflow boundary was imposed with the following conditions:

$$h(0,t) = 20 - z_b(x) - 4\sin\left[\pi\left(\frac{4t}{86{,}400} + \frac{1}{2}\right)\right] \tag{3.9}$$

$$u(0,t) = \frac{(x-L)\pi}{5400h(x,t)}\cos\left[\pi\left(\frac{4t}{86{,}400} + \frac{1}{2}\right)\right] \tag{3.10}$$

Whereas, the eastern outflow boundary was given $u(L,t)=0$ that implies no flow boundary. Similar to the previous case, grid-independent solutions were investigated with four numerical domains with mesh sizes of 50, 100, 150 and 200 in the *x*-direction. The tidal wave was simulated for time record equal to 10,800 sec. The water elevation (η) of all chosen mesh sizes was correlated with the analytical solution. As Figure 3.9 implies there is a complete match between the two solutions the numerical results and the analytical one. The tidal wave velocities of the four grid-sizes has been analysed with the analytical solution and excellent agreement has been observed as presented by Figure 3.10. The numerical results of the four grid-sizes were subtracted from the analytical solution to inspect the accuracy of the numerical model. The numerical solution indicated a grid-independent solution since the range of the differences was between $0.5 \times 10^{-4} - 7 \times 10^{-4}$ as demonstrated in Figure 3.11. The time stepping convergence was estimated by CFL criterion for the numerical model stability. The time step of the four mesh sizes are presented in Figure 3.12. Similar to the previous case as the grid-size increase the time step convergence decreases. This good agreement of the theoretical solution with the numerical results for the two test cases confirms the capability of the present numerical model with its balanced governing equations. In addition, it shows the numerical scheme accuracy and its ability to simulate unsteady flow over a complex bed topology.

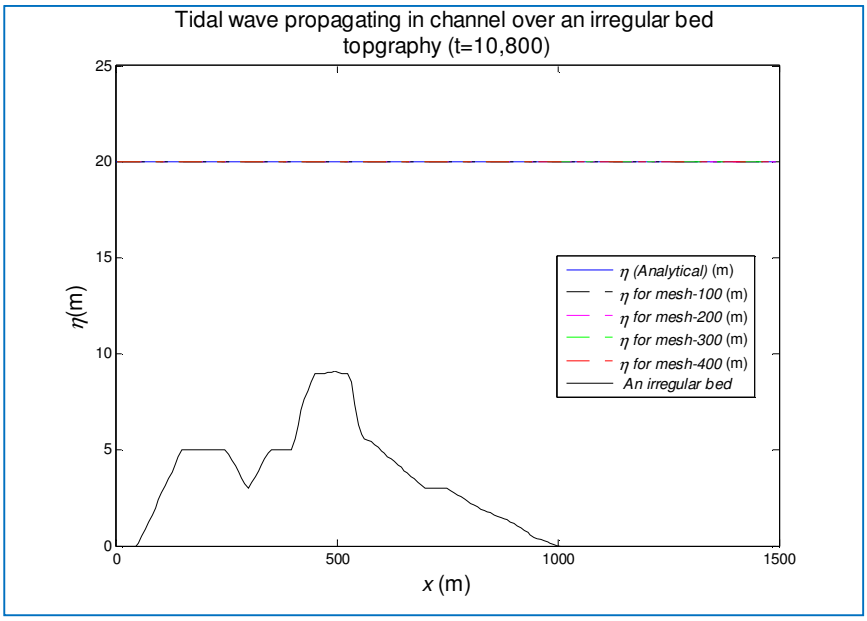

Figure 3.9 The analytical tidal wave elevation compared with the selected group mesh-size over an irregular channel bed.

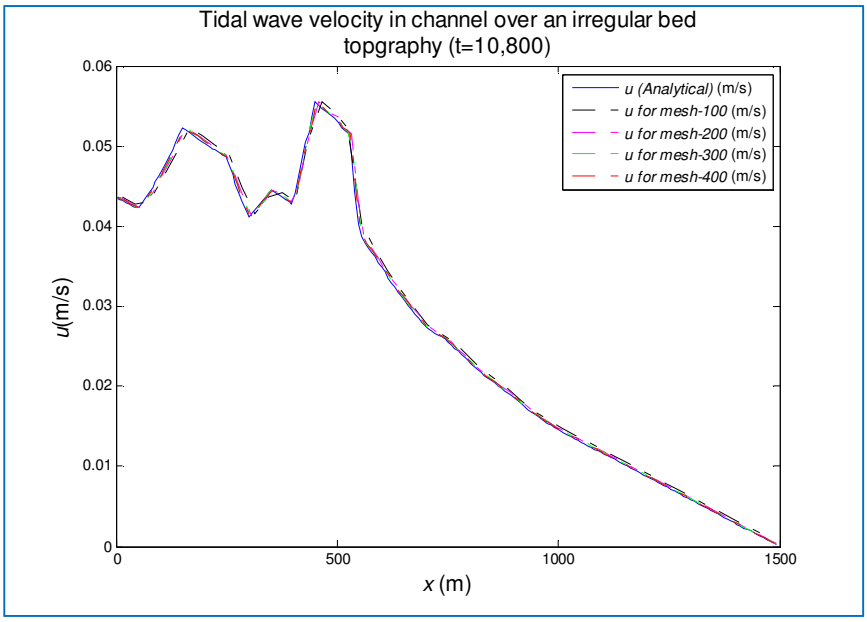

Figure 3.10 The tidal wave velocities for each tested grid-size studied against the analytical solution.

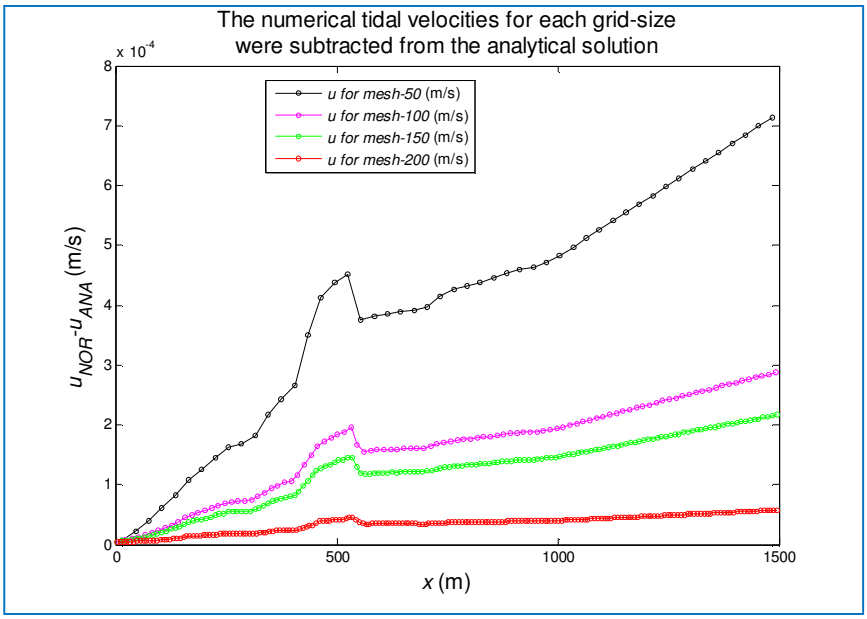

Figure 3.11 The differences between the numerical results of every grid-size with the analytical solution.

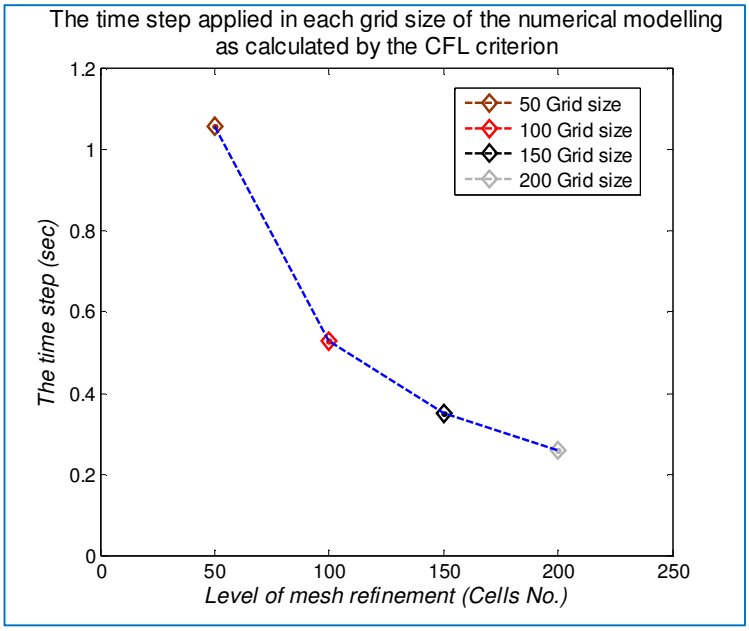

Figure 3.12 The CFL criterion calculations for the accepted time step during the numerical simulation of the four grid-sizes in the *x*-direction.

3.6 The numerical modelling for the tidal dynamics of Cook Strait

The islands of New Zealand lie on the South-West of the Pacific Ocean in the Southern Hemisphere. They consist of two big islands, as seen from Figure 3.13,

separated with a narrow channel known as the Cook Straits, which divide the Pacific Ocean into two voluminous water bodies. At their narrowest point the Straits are 24 Kilometres wide. Numerical models of the tidal flow can predicate the ocean tidal dynamics and provide critical information that can predict shoreline variation, and also pollutant transport in the coastal zones due to the tidal cycles. New Zealand tidal modelling has been practised by several researchers such as Bye and Heath (1975), Heath (1985) and Stanton et al. (2001).

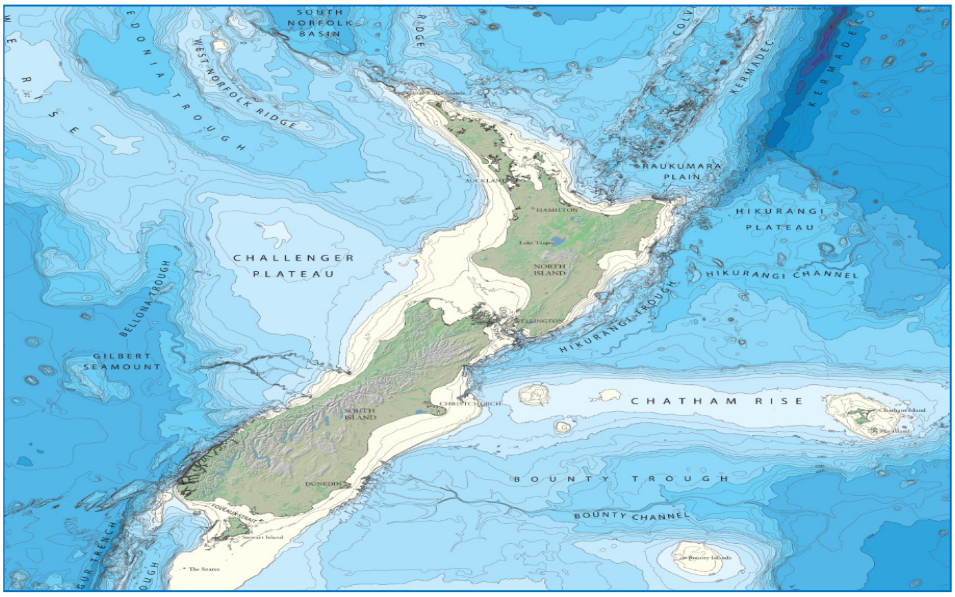

Figure 3.13 The two islands of New Zealand with the Cook Strait.

The tide can be determined by harmonic analysis as presented in section 3.1. In fact, tides can be represented with as many as 600 harmonic constituents of these tides components (Goring, 2001). There are eight major primary tides, four of them are diurnal tides (once daily) and the other four semi-diurnal tides (twice daily). Three of the semi-diurnal tides from the primary eight constituents contribute more than 90 % of the tidal energy in the world (Goring, 2001). Thus, the primary M_2 semi-diurnal tides in New Zealand have been investigated by many researchers including Le Provost et al (1994) who discovered a complete rotation of the lunar constituent M_2 around the New Zealand islands, as shown in Figure 3.14. The figure shows that the high water of the semi-diurnal M_2 tides generates a resonant trapped tidal wave moving in a counter-clockwise direction. It has a fairly uniform tidal current speed that completes the cycle every 12.4 hours. Further information of primary M_2 semi-diurnal tides numerical modelling results of Figure 3.14 can be found in Goring (2001).

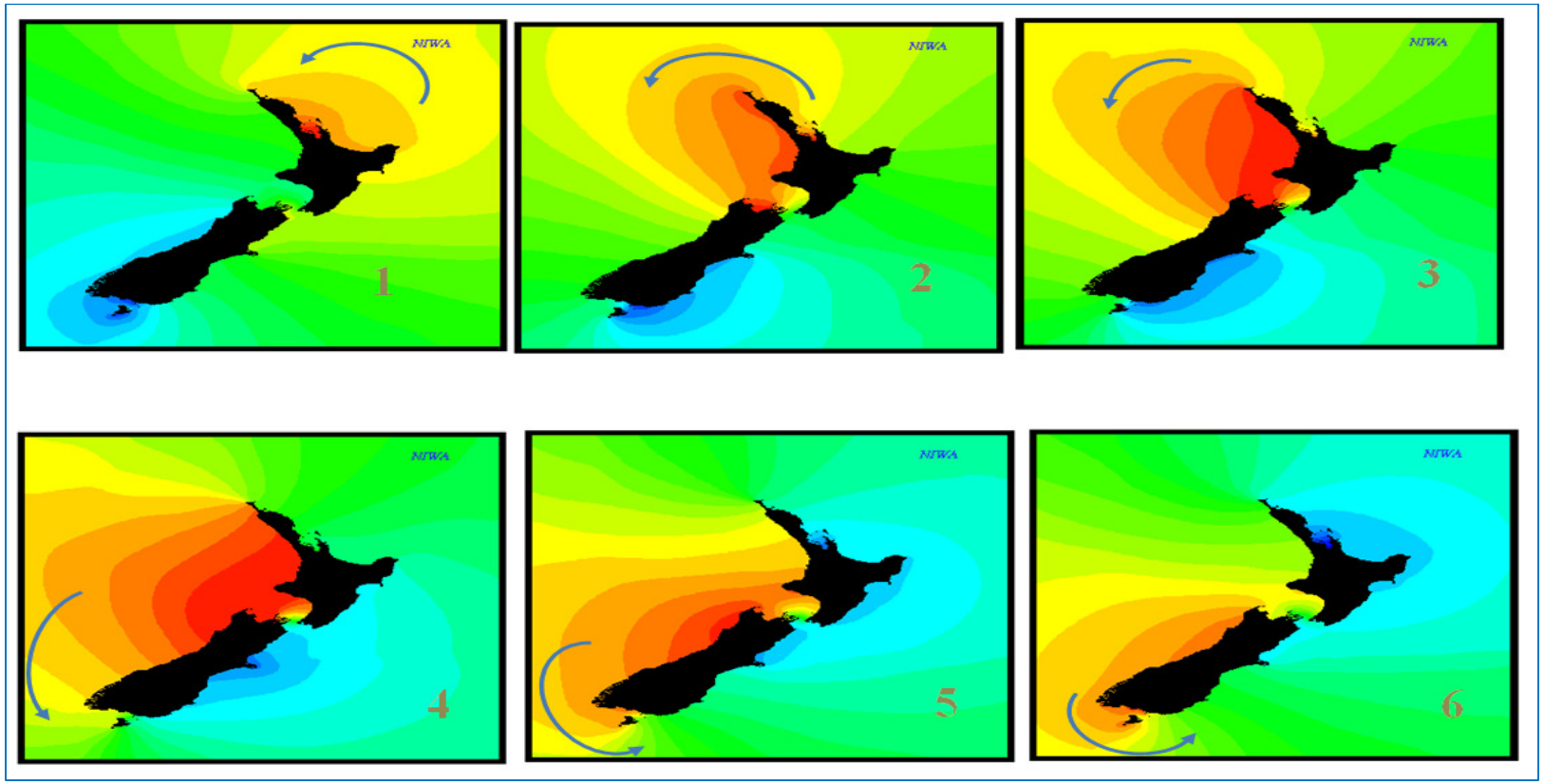

Figure 3.14 The computed M_2 high water tidal constituent around New Zealand made by the coastal hydrodynamics group in NIWA. Note that the figure shows the high water only for half cycle see Goring (2001).The grade between red (high) and blue (low) indicate the tidal range height.

This result was produced by a specific tidal finite-element hydrodynamic model run by the National Institute of Water and Atmospheric Research (NIWA) in Wellington New Zealand (Goring, 1995).

The tidal range is small in most places in New Zealand but in the area of Cook Strait, such as Te Aumiti (French pass), it can be as much as 4 m and the time differences of high tide on either side of the pass about 25 minutes (Heath, 1978). This difference in water level creates one of the strongest tidal currents in the world. It may reach up to 1.4 m/sec [3 knots] through the Cook Strait whereas in Tory channel and French pass it can achieve 2 m/sec [4 knots] as shown in Figure 3.15 (Stevens and Sutton, 2007). In fact, the Energy Pacifica Company claim that installing 10 marine turbines near the Cook Strait in the Tory channel could generate electrical power up to 1.2 MW (Clark, 2008).

Figure 3.15 The French pass in the Marlborough sound which is the narrowest gap between headlands of the New Zealand two islands (Begg and Johnston, 2000).

3.7 The Finite Volume Method for Cook Strait tidal dynamics

The Cook Strait was applied to simulate its M_2 semi-diurnal tide waves by the present numerical model due to the high tidal current passing through it. A numerical domain with a region of interest of 500 kilometres wide was defined as presented by Figure 3.16 and the bathymetry of the region was taken from the Gerris flow solver website (Popinet, 2011) and it was presented in seabed form as demonstrated by Figure 3.17. The figure demonstrates the numerical grid of the numerical modelled

region defined in terms of longitude and latitude in degrees with the seabed in meters. Whereas, the numerical domain is presented in a Cartesian coordinate system with Cook Strait seabed topography as Figure 3.18.a appears.

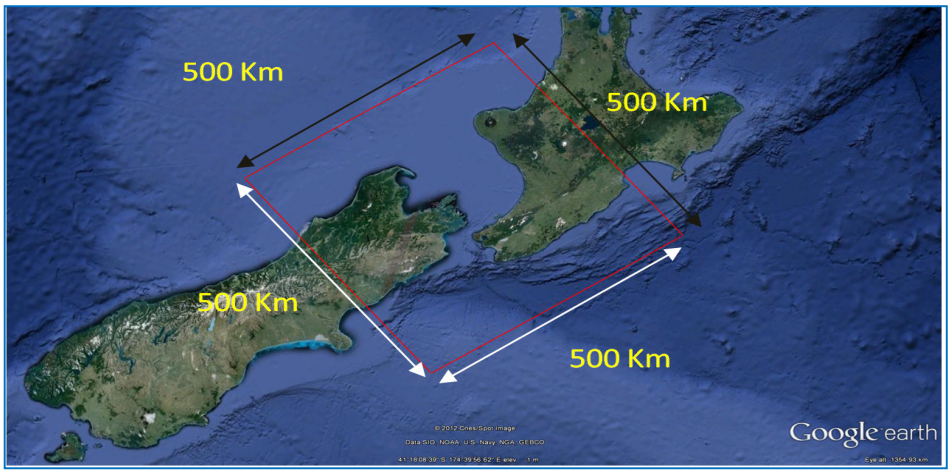

Figure 3.16 The Cook Strait numerical domain that was implemented in the tides numerical simulation is represented with the red quadrilateral.

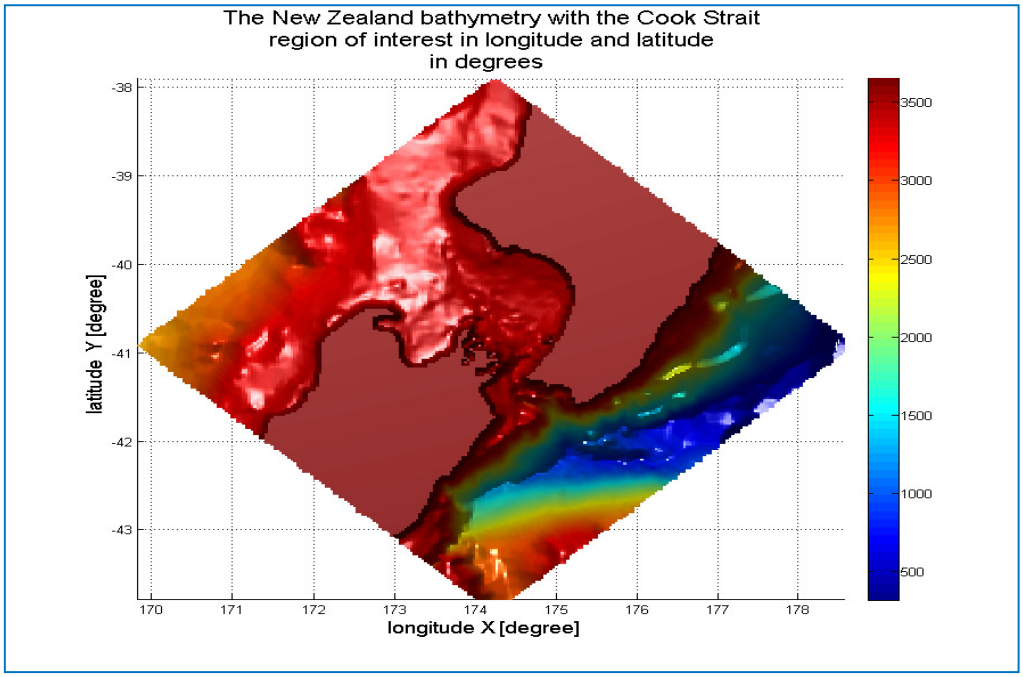

Figure 3.17 The numerical domain of the Cook Strait with the seabed (m) as recognize in the GIS format.

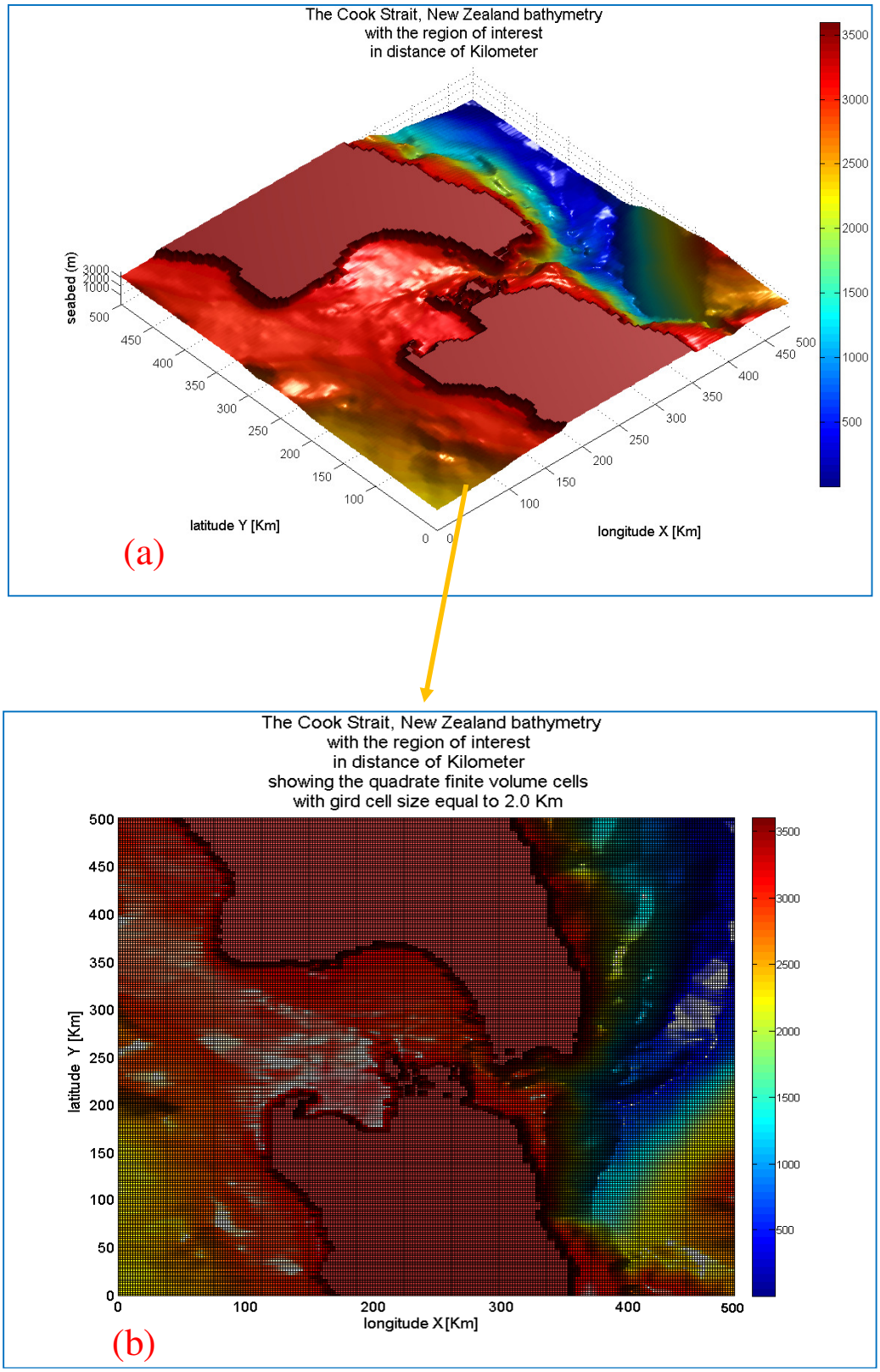

Figure 3.18.a, b The Cook Strait of New Zealand with seabed in Cartesian coordinate system in 3D as seen in (a) and 2D dimension shown in (b).

The numerical domain was discretized applying quadrilateral Finite Volume cells with an equal gird cell size of 2.0 Km as demonstrated from Figure 3.18.b.

3.7.1 *Model configuration*

The tides can be presented by harmonic constituents. The tidal constituents are estimated using cosine functions which analysis tide to determine the amplitude and phase of the cosine waves, as described in section 3.1 recalling equation (3.1).

$$\eta_t(t) = R_0 \cos(\omega_0 t - \phi) \qquad (3.11)$$

Here $\eta_t(t)$ is the water elevation of the tide at time (t), R_0 is the tide amplitude which is equal to one-half of the tidal range, ϕ is the phase in degrees and ω_0= 28.984 degrees per mean solar hour, representing the principal lunar semi-diurnal constituent M_2. Therefore, the lunar semi-diurnal frequency, known as $f_0 = \omega_0 / 2\pi$ was used to solve by the Least Squares method to find the corresponding tidal amplitude. The Least Squares method involved fitting measured data from the tide gauges with the best fit curve function which is represented by the following equation (3.12).

$$f(t) = Z_f + A_0 \cos(\omega_0 t) + B_0 \sin(\omega_0 t) \qquad (3.12)$$

The least square method solves the unknown parameters Z_f, A_0, B_0 which gives the amplitude and phase as follows:

$$R_0 = \sqrt{A_0^2 + B_0^2} \quad \phi = \arctan\left(\frac{B_0}{A_0}\right) \qquad (3.13)$$

The effect of tides on the coastal waters in the Cook Strait was investigated by National Institute of Water and Atmospheric Research (NIWA). The tides were simulated using Gerris Flow Solver which is based on two-dimensional and three-dimensional hydrostatic oceanic equations developed by Stephan popinet (Msadek, 2005). A tidal wave was generated at the inlet using the data provided by the Gerri's flow solver website (see references for website). In fact, the dominant component is the lunar-tide generating force M_2 constituent that was applied in the present work and the tidal wave range applied for the Finite Volume Method numerical modelling is displayed in Figure 3.19.

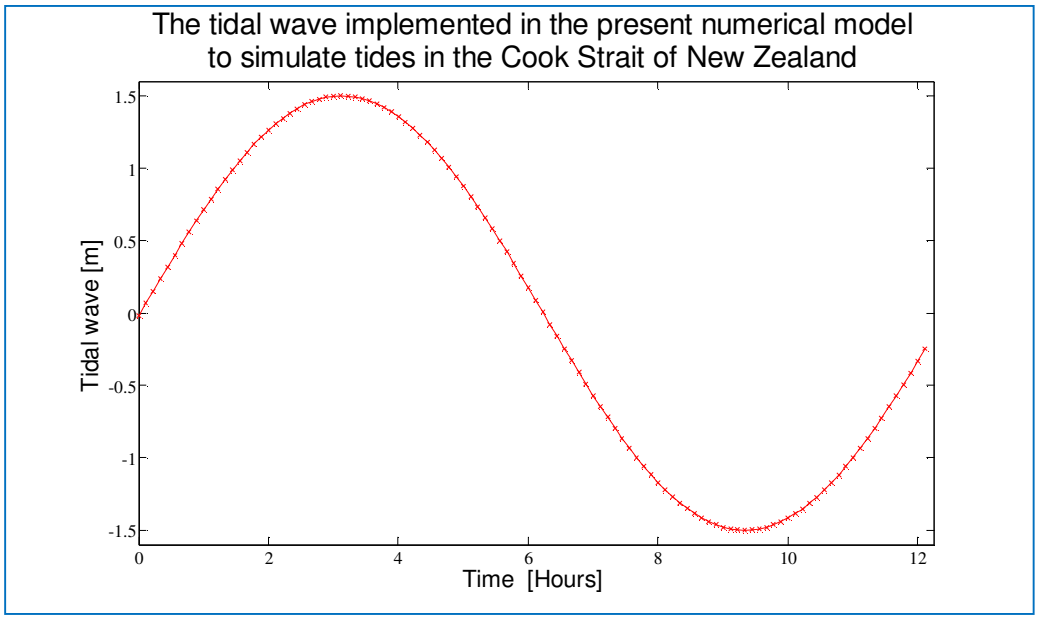

Figure 3.19 The input tidal wave for lunar-tide generating force M_2 constituent.

3.7.2 *The initial and boundary conditions for the Cook Strait tidal simulation*

The initial condition in the present numerical was set to still water elevation according to the water depth definition that was applied in the numerical scheme as presented in the above Figure 3.4.The two islands with the initial condition of still water elevation are shown in Figure 3.20. The inflow of the input zone was controlled by A FORTRAN program that fed the numerical domain with the tidal wave added to the still water elevation as presented in Figure 3.21. The initial condition of the water free surface was checked at time t=0 by creating a long-section of cells through the Cook Strait as shown in Figure 3.22.a. The water elevation was fixed with a still elevation at t=0 as Figure 3.22.b shows.

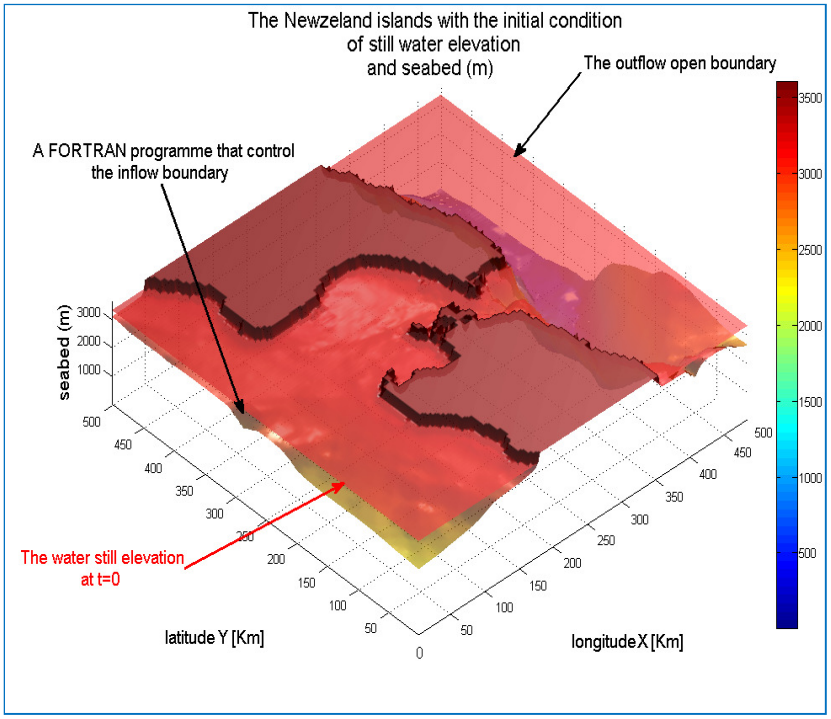

Figure 3.20 The still water elevation at time t=0 with the control input open boundary zone.

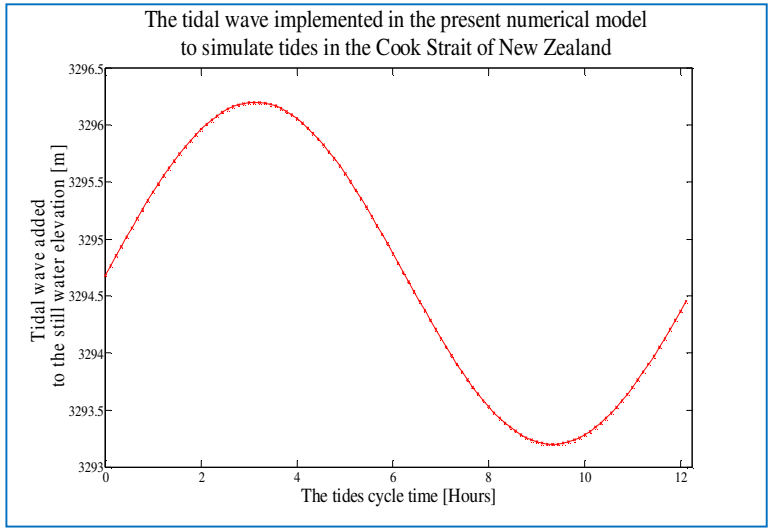

Figure 3.21 The Lunar tidal wave added to the water still elevation ($\eta = h_s + z_b$) which was applied in the present numerical tides simulation.

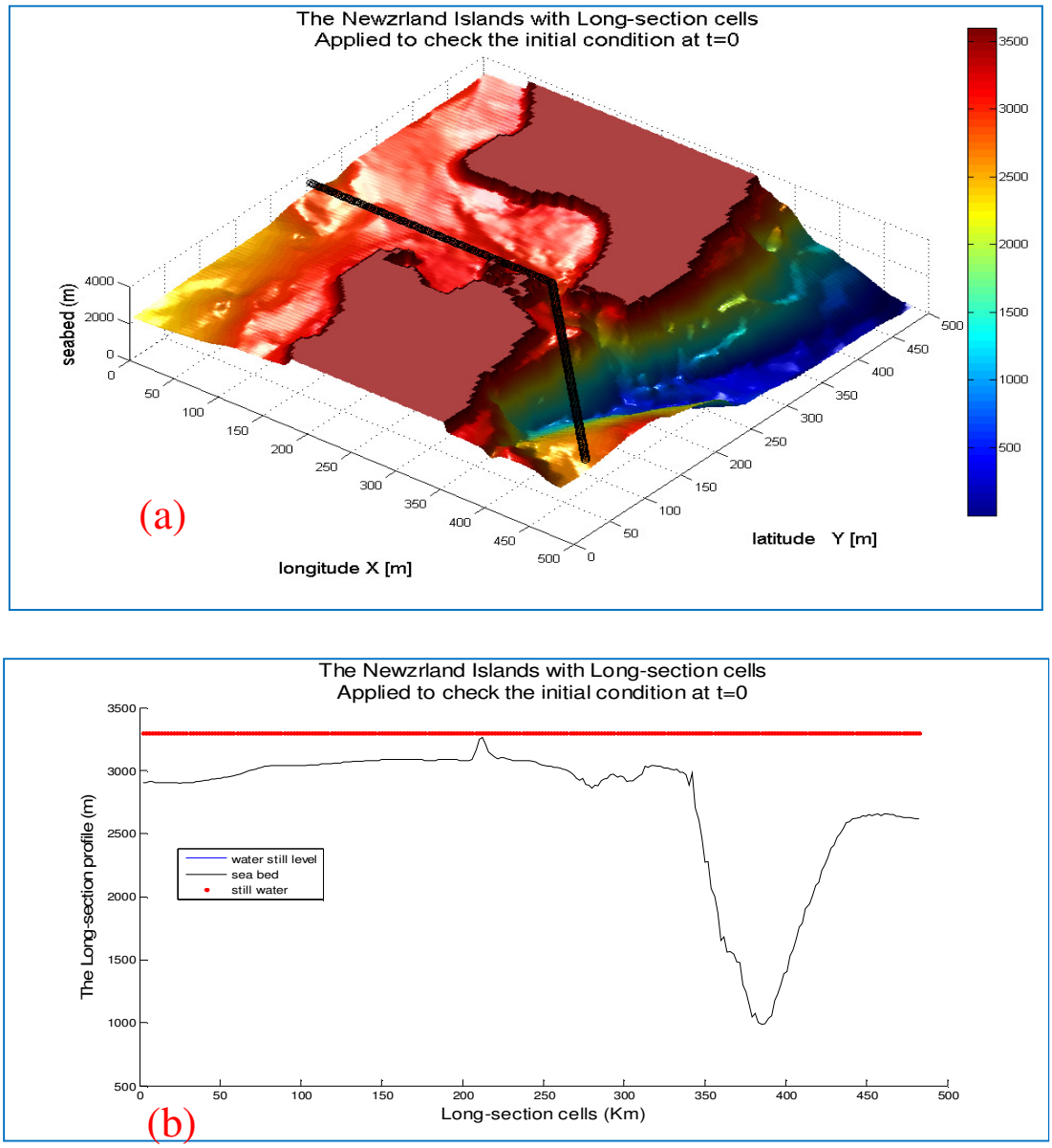

Figure 3.22.a, b The initial conditions at time t=0 that indicate the free surafec elevation cells checkes represented in (a) with fixing the water elevation as seen in (b).

The coastal land boundary was raised above the still water surface elevation since it's rigid and impermeable to water flow and the present model has the ability to work in wet-dry cell conditions suitable to coastal boundaries. In addition, the present Finite Volume model has the ability to capture the high speed tidal current which is appropriate for the observed strong tidal current in the Cook Strait. The output boundary was synchronized with the tidal

wave inflow so that the water free surface at this outer boundary oscillates similar to the manner suggested by Popinet (2005).

3.7.3 *The results of the Cook Strait tidal wave analysis*

The Figure 3.23 presents the lunar semi-diurnal M_2 tidal elevation and shows the differences in tidal elevation between the west side with a high water elevation and the east side with a low water elevation with a tidal range equal to 2.16 m. This tidal range is observed in the tidal elevation of Cook Strait.

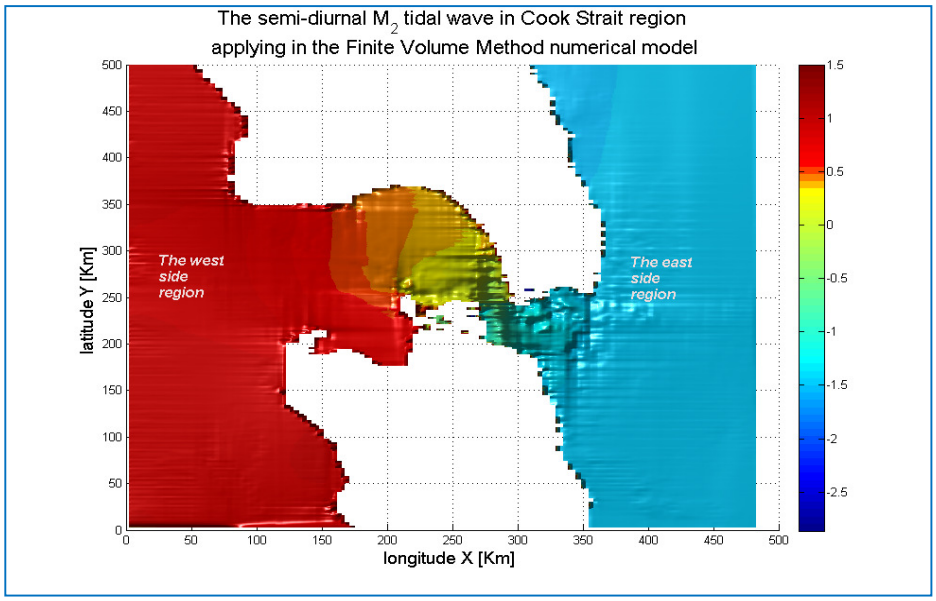

Figure 3.23 The semi-diurnal tidal wave simulation results in the New Zealand Cook Strait region.

An advantage of the present numerical model that its ability to capture the high tidal current with the water elevation. The long-section of the water elevation inside the Cook Strait was investigated to show the water elevation as the tidal wave enters from the west side to the east side in the narrowest gap that is called the French Pass, as shown in previous Figure 3.15. The Figure 3.24.a shows the tidal wave elevation as it propagates the Cook Strait traveling from the west to the east side's with about 2 m tidal range inside it and the cells checker for the French Pass is exposed in (b).

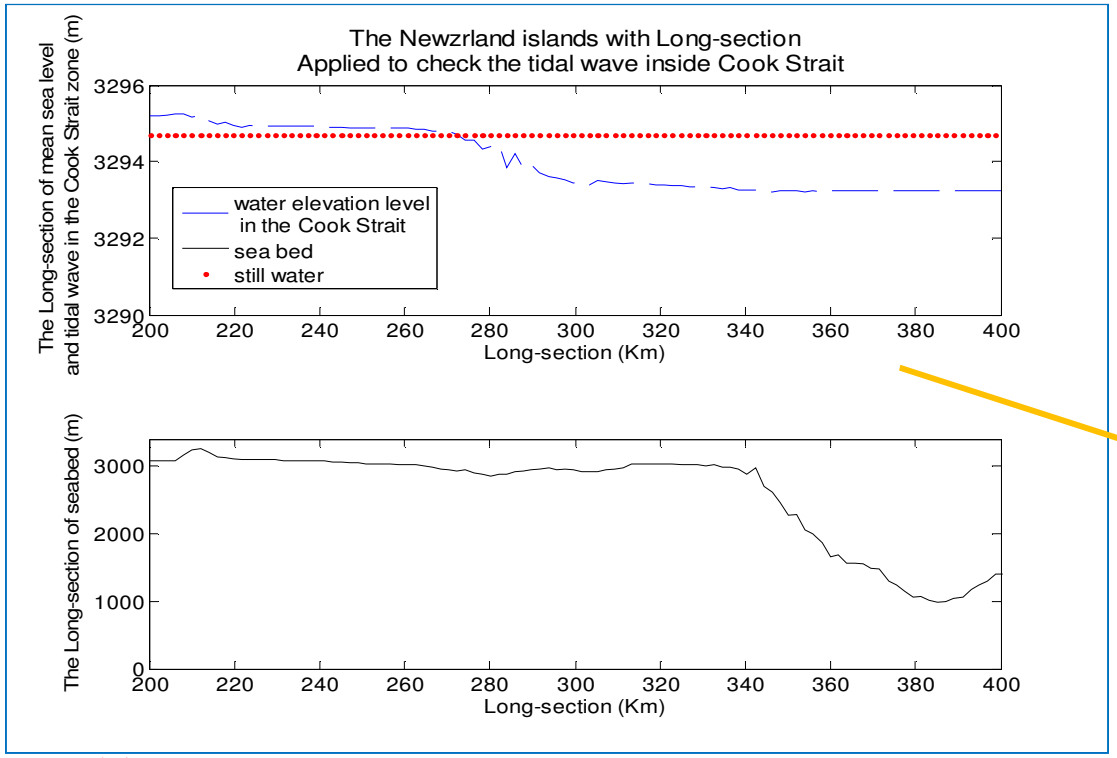

(a)

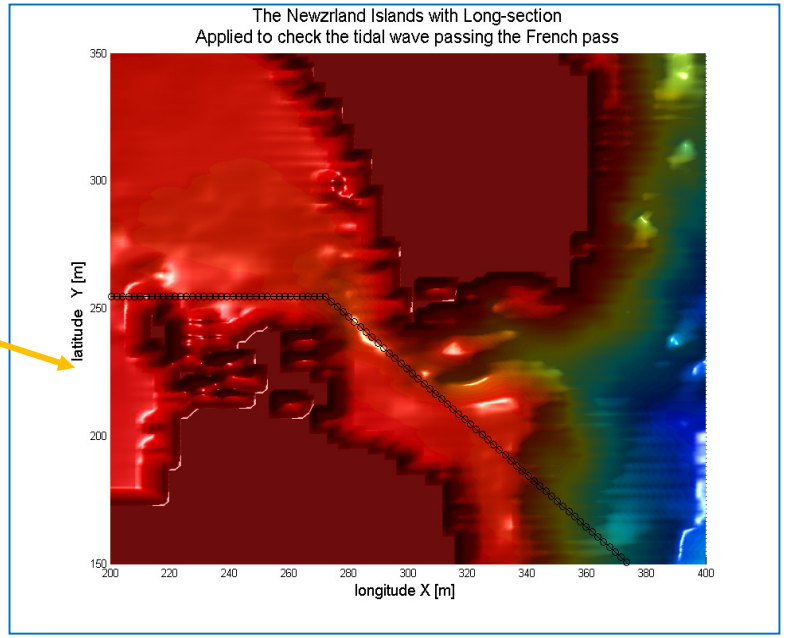

(b)

Figure 3.24.a, b The tidal wave propagating the Cook Strait going through the French pass as demonstrated in (a). The location of the cells checker French pass as exhibited in (b).

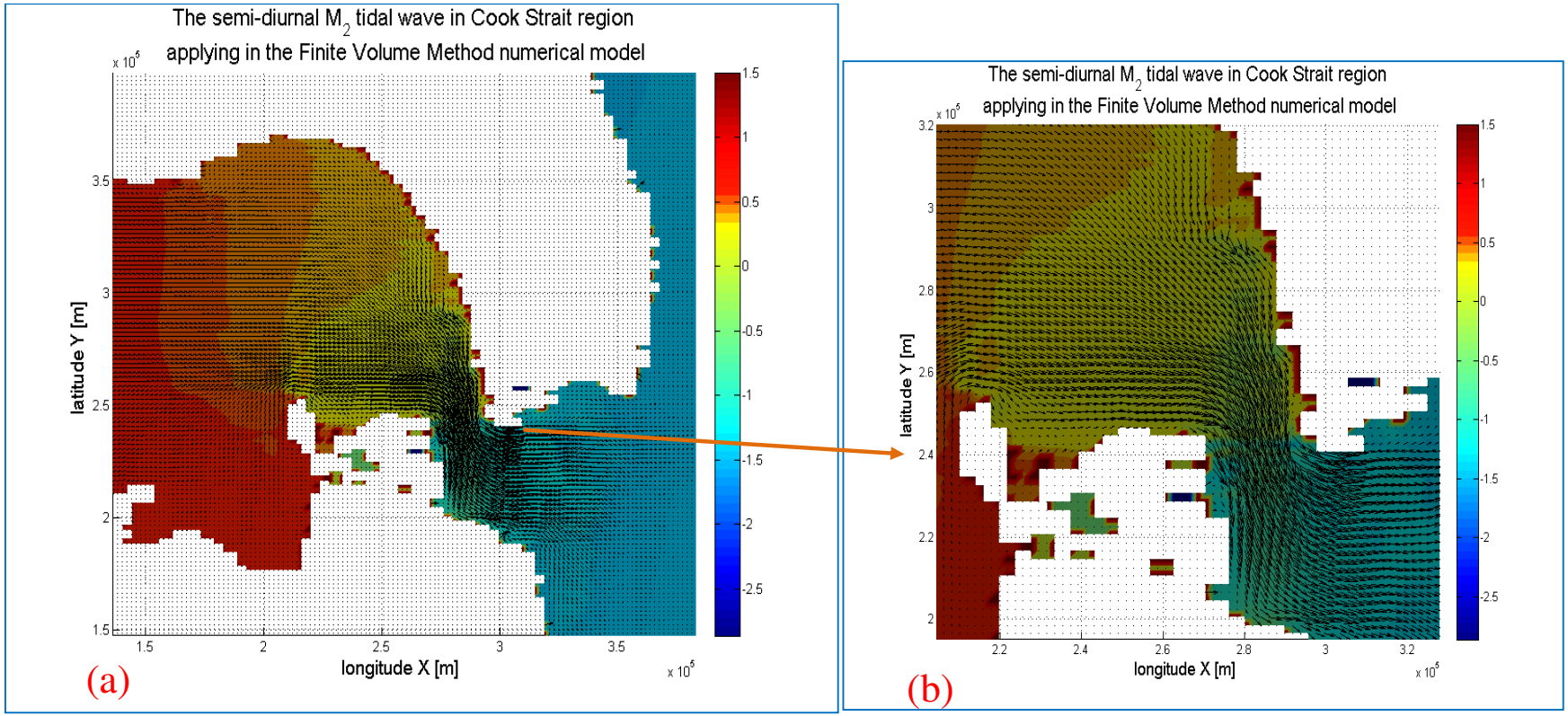

Figure 3.25.a, b The velocity vectors in the Cook Strait especially in the Tory channel as shown in (a) and French pass as seen in (b).

The figure shows the ability of the present numerical model in recording the disturbance of the water elevation as the tidal wave enters the Tory channel and French Pass which is can't be observed by other numerical models. The velocity vectors of the tidal current in Cook Strait have been computed, as defined in Figure 3.25.a, b above. The velocity inside the Cook Strait is strong due to the tidal range differences between the water surface elevations in the west and east regions. The maximum velocity may reach 1.98 m/sec which is approximately equal to the observed values 2 m/sec [4 Knots] in the Tory channel as spotted in Figure 3.25.a and French pass as viewed in Figure 3.25.b.

3.8 The comparison between the numerical models

The results from the Finite Volume Method were compared with the two numerical models results found in the Msadek (2005). The M_2 tidal elevation of the driving model and Gerris Flow Solver model is shown in Figure 3.26.a, and Figure 3.26.b respectively. Note, the tidal amplitude in both figures is colour shaded with a scale of decreasing colours correspond to reducing water level from a maximum value of 1.37 m for red zones to 0 m for the blue zones. The colour scale applied in the Msadek (2005) was adopted in presenting the results of studied numerical model. In Figure 3.26.c the Finite Volume Method model tidal amplitude is compared with the two numerical models. The figure indicates the west side region has high tidal amplitude with a maximum value of 1.33 m. whereas; the east side region has low tidal amplitude that has a minimum value of 0.17m. The comparison in Figure 3.26 indicates a good agreement of Finite Volume Method results with the two other numerical models results as shown in the report of Msadek (2005). However, there are some differences in the results of the driving numerical model and the Gerris Flow model in the Cook Strait compared to the Finite Volume numerical method due to the spatially mesh refined near the coastal boundaries adopted in other numerical models.

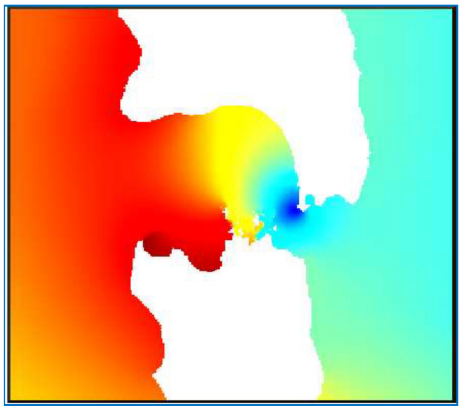

(a) The tides driving numerical model.

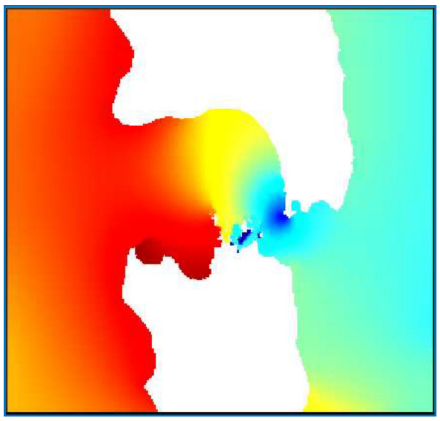

(b)The Gerris numerical model.

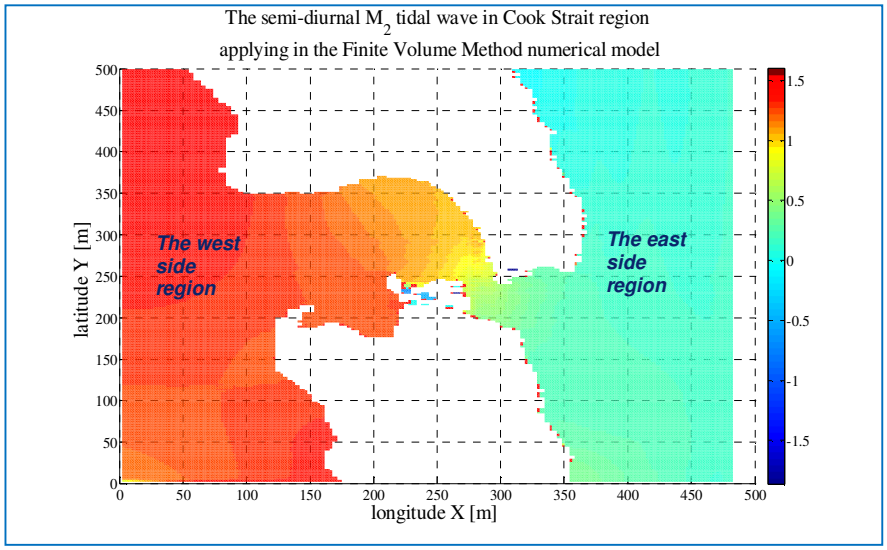

(c)

The Finite Volume Method numerical model results.

Figure 3.26.a, b, c The tidal amplitude of the Cook Strait for the two driving and Gerris numerical models compared with the present Finite Volume Method numerical model.

The tidal amplitude was compared with a group of measured tidal stations as well as results from the Gerris Flow model. The stations selected are presented in Figure 3.27. The results of Finite Volume Method numerical model and results from the Gerris Flow model with the observed measured data are demonstrated in table 3.3. It shows the differences between the measured and numerical models predication of the tidal amplitude. As presented in table 3.3 a small difference in the results values of the tidal amplitude. It demonstrates the capability of the Finite Volume Method in predicting tidal waves in straits such as the Cook Strait.

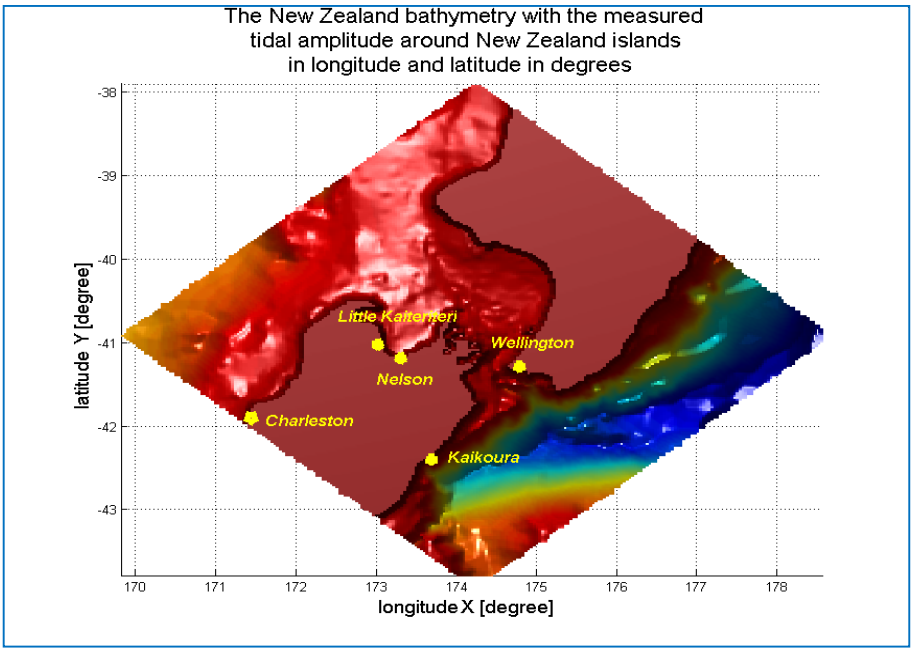

Figure 3.27 The positions of the measured tidal amplitude stations around New Zealand.

Table 3.3 The comparison of measured tidal amplitude around New Zealand islands with the Finite Volume Method numerical model and the Gerris numerical model.

The station location	The observed tidal amplitude (cm)	The predicted tidal amplitude from Gerris numerical model (cm)	The predicted tidal amplitude applying the Finite Volume Method numerical model (cm)
Little Kaiteriteri	130.9	133.2	127.1
Wellington	49.3	48.1	48.58
Nelson	129.8	134.3	126.9
Kaikoura	67.0	66.4	60.1
Charleston	105.7	119.0	120.3

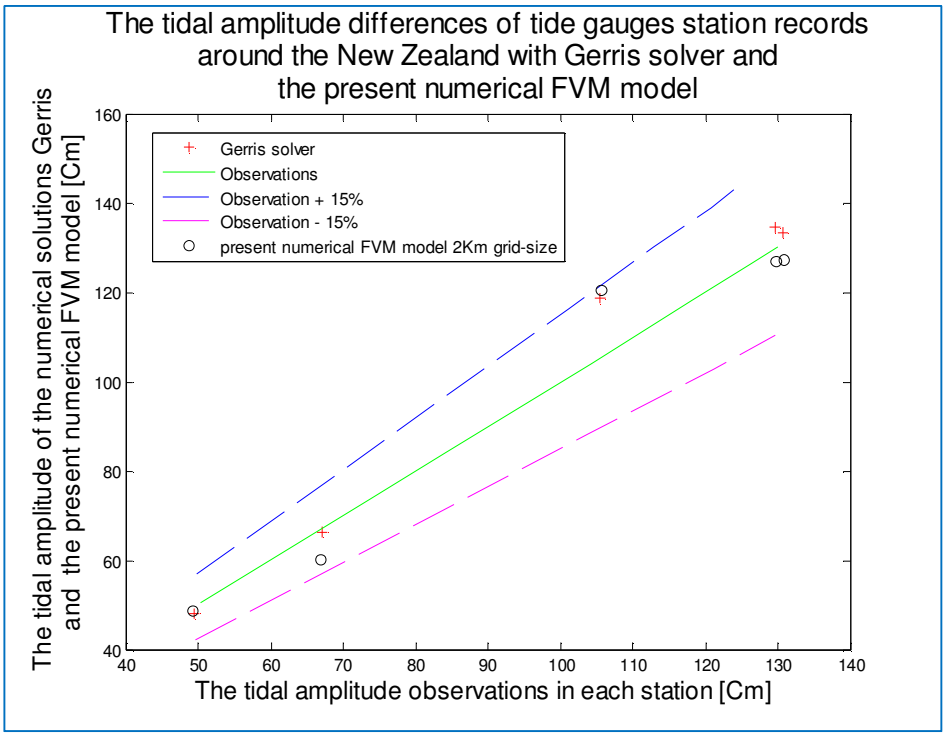

Figure 3.28 The amplitude of tides for observation with the numerical models results of Gerris Flow solver and the results of the present Finite Volume Method numerical model.

In Figure 3.28 the tidal amplitude observation against the Finite Volume Method numerical model with the Gerris Flow solver model was presented. The results from the present numerical model are in the range of ± 15% of the measured tides given from the tide gauge stations record. In fact, the results of tidal wave amplitude of the Finite Volume model are approximately equal to the values of the observation and nearly to the results solved by Popinet numerical model as presented in his report of NIWA written by Msadek (2005).

The targeted region Loch Linnhe which the tidal wave was simulated by Finite Volume Method numerical model required a field measurement to verify the numerical results. This measurement was conducted with the Acoustic Doppler Current Profiles (ADCP) during 57 day's time duration. In the next chapter, the data records is analysed during a chosen time periods of spring and neap cycles as presented in the following chapter.

Chapter 4.Tides and tidal current profiling measurements

4. Introduction

A major objective of the PhD research is carrying out field measurements in the interested artificial reefs area. This assessment was funded by King Abdulaziz University to investigate the artificial reef hydrodynamics and supporting the PhD research. The ADCP instruments and installation was done with the help of the Scottish Association for Marine Science Institute Oban (SAMS). On the Loch Linnhe artificial reef site, one reef was selected to carry out field measurements on it. The survey duration was chosen to last about two months to cover the tidal spring-neap cycle phenomenon. The recorded data was focused on the tidal wave cycles, and the *U* and *V* components of the velocity profile were measured over the duration of the field measurements. An ADCP (Acoustic Doppler Current Profiler) instrument system was deployed for the purpose on the Loch Linnhe artificial reef location in about 25 meters of mean sea level water depth.

An ADCP is an electronic instrument that transmits acoustic signals into the water column. In order to measure the water velocity the frequency of the transmitted signals is compared with the frequency of backscatter signals reflected off suspended particles, which are assumed to be moving at the same velocity as the water (WHOI, Ocean Instruments 2012). The ADCP can be anchored to the seabed which gives the current speed not only near the bottom, but it can also measure the velocities at equal vertical intervals in the water column, as seen from Figure 4.1. As the figure shows the bins, representing an upward vertical sequence of measurement cells, have a size that can be set for each instrument. For these experiments a three ADCP system was deployed surrounding the chosen Loch Linnhe artificial reef with two of the ADCP instruments having bins sizes of 0.5 meter, which resulted in 48 bins in a 24 meter water depth. Note that there is a one meter bottom unmeasured zone, as shown by Figure 4.1. The third ADCP was sufficiently far away from the selected reef for the water to be undisturbed by its presence, and it was given 24 bins with one meter for each bin size. The instruments were deployed in their selected locations to register the tidal elevation and currents so the data could be used for setting initial conditions and validating the numerical methods applied in the present work. The ADCP data records were studied and analysed over a tidal cycle to show the *U* and *V* velocity component as they relate to the tidal wave. The tidal current profiles of the *U* and *V* components were decomposed

during the lunar spring-neap cycle to be compared with the numerical results of the two-dimensional Finite Volume Method model. A daily cycle from the spring and neap lunar period of the tidal current profiles was taken to be used for defining the initial conditions for the three-dimensional k-ε turbulent model simulation. A group of scripts codes were created to analyse and display the ADCP data. It is crucial to inspect the accuracy of the raw data before applying it because instrument error can occur during the measurements. In this chapter the data records were interrogated, processed and presented after analysing it.

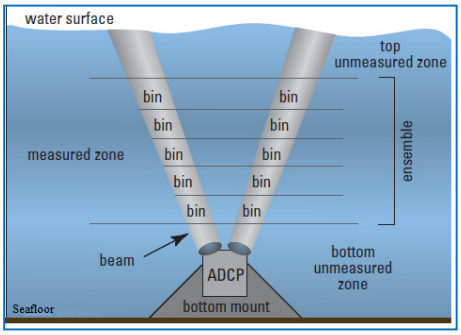

Figure 4.1 The ADCP velocity data series as it recorded by the instrument (Wall et al., 2006).

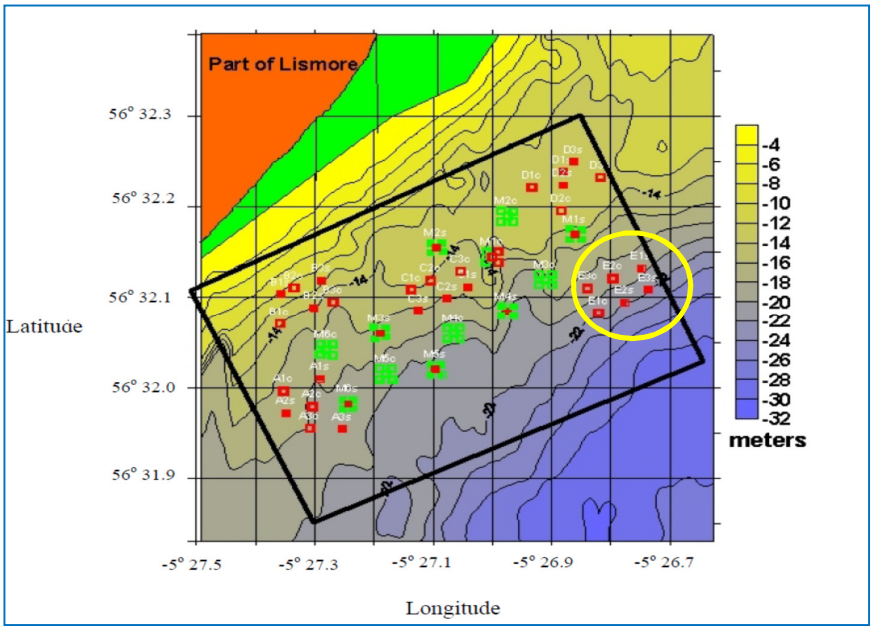

Figure 4.2 The Loch Linnhe artificial reef modules with the chosen group-E at the measurement site.

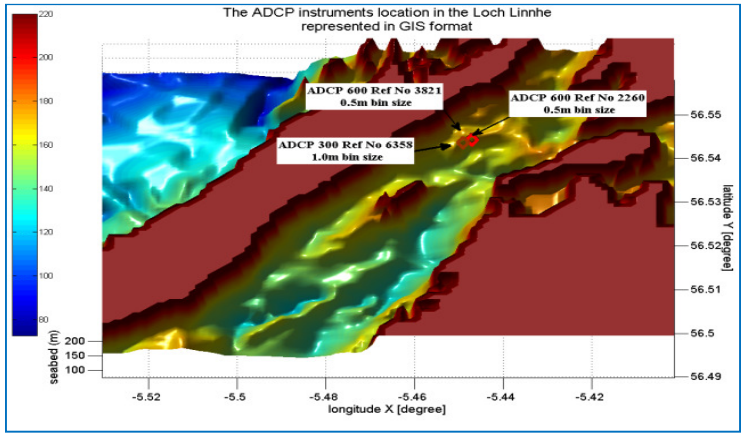

(a)

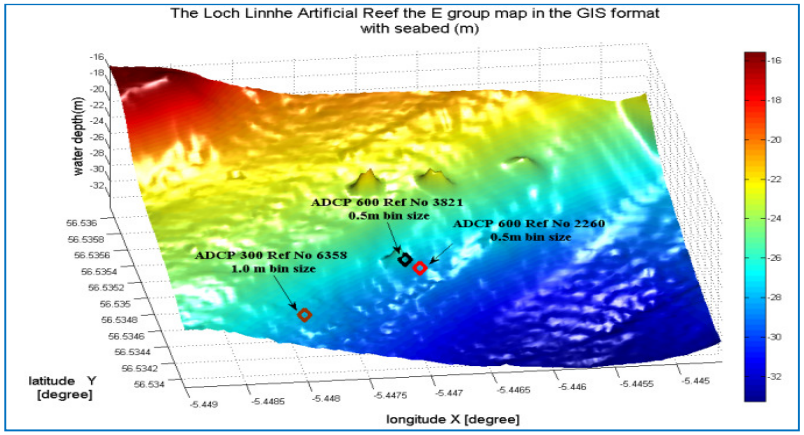

(b)

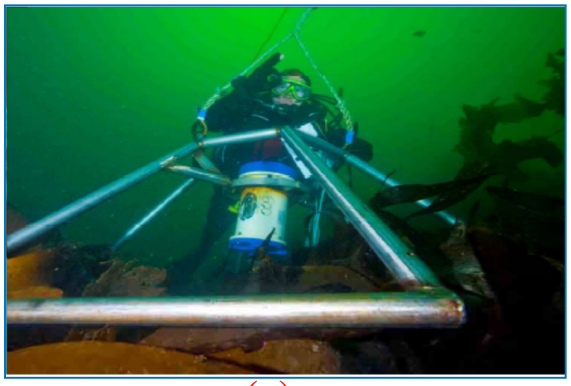

(c)

Figure 4.3.a, b, c The position of the ADCP instruments on the chosen artificial reef site from group-E of the artificial reef modules in the Loch Linnhe is spotted in (a) along with the selected reef surrounded by the ADCP instruments is shown in (b) and the installation of the ADCP photography at the reef site is seen in (c) (picture taken from Wilding 2010).

4.1 ADCP geographical setting in the Loch Linnhe

The artificial reefs on the Loch consist of several artificial reef modules as described in chapter two. One artificial reef module from group-E was selected for the measurement of the *U* and *V* velocity components of the tidal current profile using the ADCP instruments, see Figure 4.2 above. The ADCP instruments were set around the group-E reef module as illustrated overhead in Figure 4.3.a and the selected artificial reef surrounded by the ADCP instruments is seen up in Figure 4.3.b, which also shows a picture taken by Thomas Wilding of the ADCP installation in Figure 4.3.c above, (Scottish Association for Marine Science). Since, this artificial reef lay in the deeper zone with respect to other artificial reefs, the major influence of the water dynamics on the group-E artificial reef was caused by the tidal wave.

4.2 The characteristics of ADCP data measurements

The ADCP instruments recorded the tides and the *U* and *V* components of the tidal current velocity profiles every 6 minutes during the time series. The ADCP's are provided with pressure sensor that acts as wave gauge which record the tidal wave height. The tidal wave over the whole time duration of measurements, which was approximately 57 days, is shown in Figure 4.4.

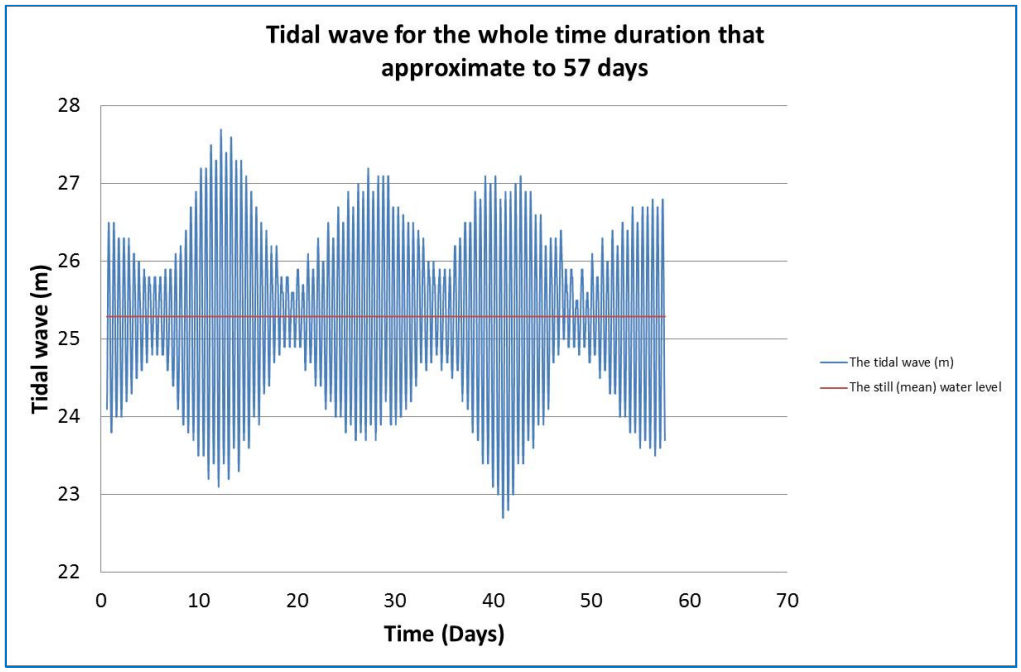

Figure 4.4 The wave tides as registered by the ADCP instruments after the deployment at the artificial reef in the Loch Linnhe.

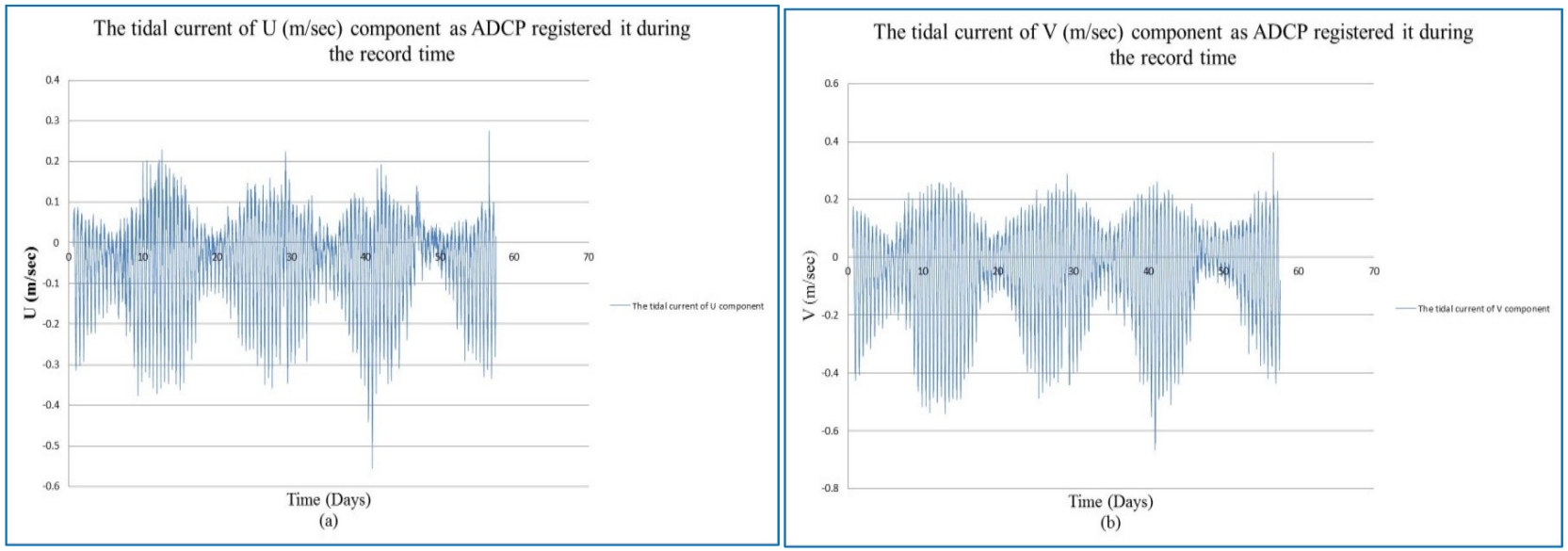

(a) (b)

Figure 4.5.a, b The bins averaged tidal current components of *U* are presented in (a) and *V* is viewed in (b) which was recorded by ADCP instrument presented in the whole time period.

The bins of *U* and *V* components recorded by the ADCP instrument No.2260 sited in the deeper region south of the artificial reef as demonstrated in Figure 4.3.b were averaged to represent the mean tidal current. The averaged *U* and *V* components data measurements are presented overhead in Figure 4.5.a, b showing the time duration of the records.

A sample of the vertical velocity of the *U* component measured by the ADCP instruments with 48 bins as defined in Figure 4.1 with 0.5 m for each bin which represents 25 m that include the one meter of the unmeasured zone is demonstrated in Figure 4.6.

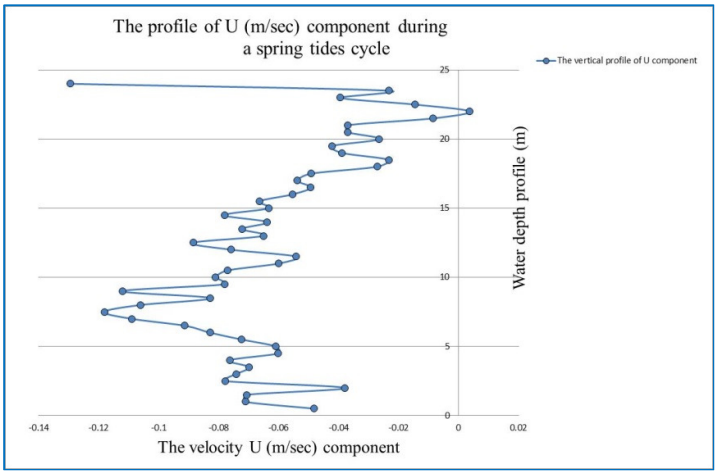

Figure 4.6 The *U* (m/sec) component of the velocity profile within a daily spring tidal cycle.

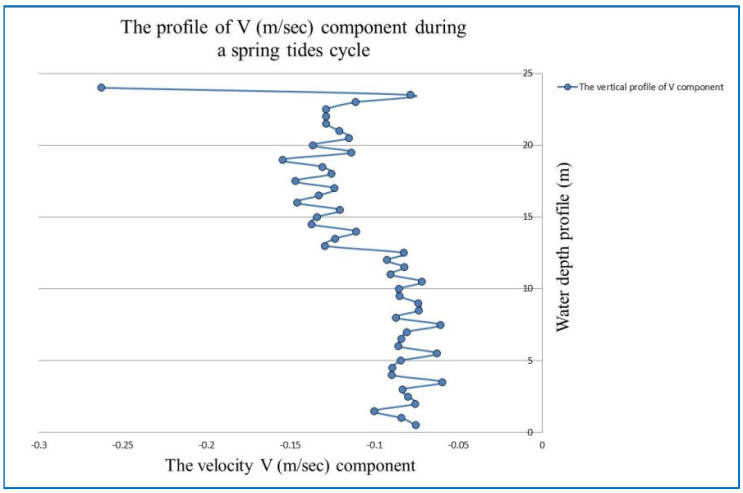

Figure 4.7 The *V* (m/sec) component of the velocity profile with the same period of the *U* component for a daily spring tidal cycle.

The Figure 4.6 above shows the *U* (m/sec) component tidal current velocity during a spring daily tidal cycle. Similarly, the *V* component of the profile was presented in Figure 4.7 overhead as recorded by the ADCP within the same time period of the spring tidal cycle. Note that, the near-surface boundary process is counted in the ADCP measurements, since the whole water column of the U and V components tidal current is covered. An indication of wind stress effect is clearly can be seen in both Figure 4.6 and Figure 4.7 at the near-surface boundary due to high wind speed in Loch Linnhe region as has been presented in previous study such as Matsuura and Cannon (1997).

4.3 The spring and neap lunar period selection from the ADCP instruments

Daily spring and neap period cycles were chosen from the ADCP data measurements for use as input into, and a source of validation for, the numerical models. Figure 4.8 shows the selected periods of the tidal wave shown in red for neap and green for spring tides.

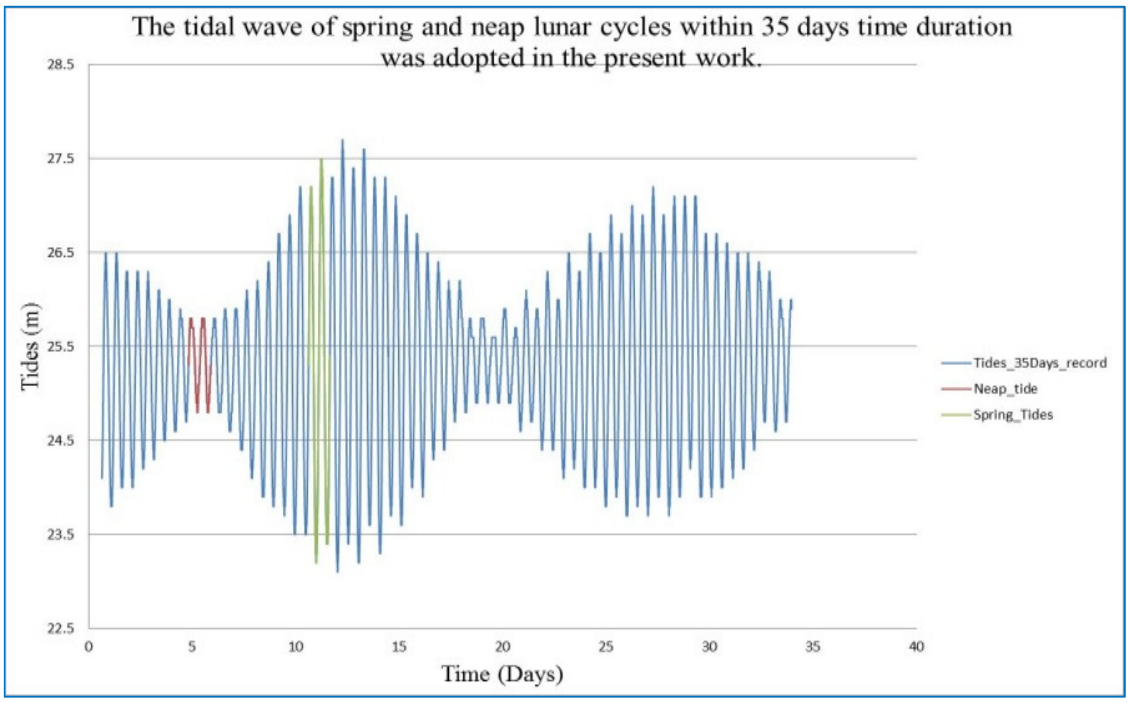

Figure 4.8 The daily spring and neap periods adopted in the present work and taken from the data records length.

The ADCP instruments data records were investigated and analysed during these spring-neap lunar cycles. The first ADCP investigated was the faraway ADCP No.6358. It was selected in this location to remove any velocity fluctuation my caused by the

water disturbance due to the presence of the artificial reef. The position of the instrument that collects the tidal current and wave tides is shown in Figure 4.9.a. The neap tidal wave and current taken over a time duration of two and half days is illustrated in Figure 4.9.b which shows the average of ADCP bins for tidal current pattern beneath the tidal wave. The *U* and *V* components averaged values shows a maximum of 4 cm/sec for *U* and *V* record a maximum of 8 cm/sec in flood whereas in ebb the *U* and *V* components are -12 cm/sec and -14 cm/sec respectively. The *U* and *V* components of the velocity profiles for the neap period are presented in the contour maps in Figure 4.9.c. The maximum neap tidal current registered by this instrument was around 9 cm/sec in the flood and -15 cm/sec in the ebb seen in the *V* component. Similarly, the spring tidal wave and current data from ADCP No.6358 was processed, as seen in Figure 4.10.a, b. Note that the tidal current reaches a peak of 25 cm/sec in the flood for the *V* component and 24 cm/sec for *U* component, whereas in ebb it my go to -45 cm /sec for the *V* component and -28 cm/sec for the *U* component during the spring tidal wave as seen from Figure 4.10.b. The tidal current profiles of the *U* and *V* component were plotted as contour velocities, as displayed by Figure 4.10.c. A comparison between the *U* and *V* component contour velocities for the spring period against the *U* and *V* velocity components contour velocities of the neap period show a rise in the spring cycle of about twice or more those of the neap cycle as Figure 4.9.c for neap cycle and Figure 4.10.c for spring cycle displays.

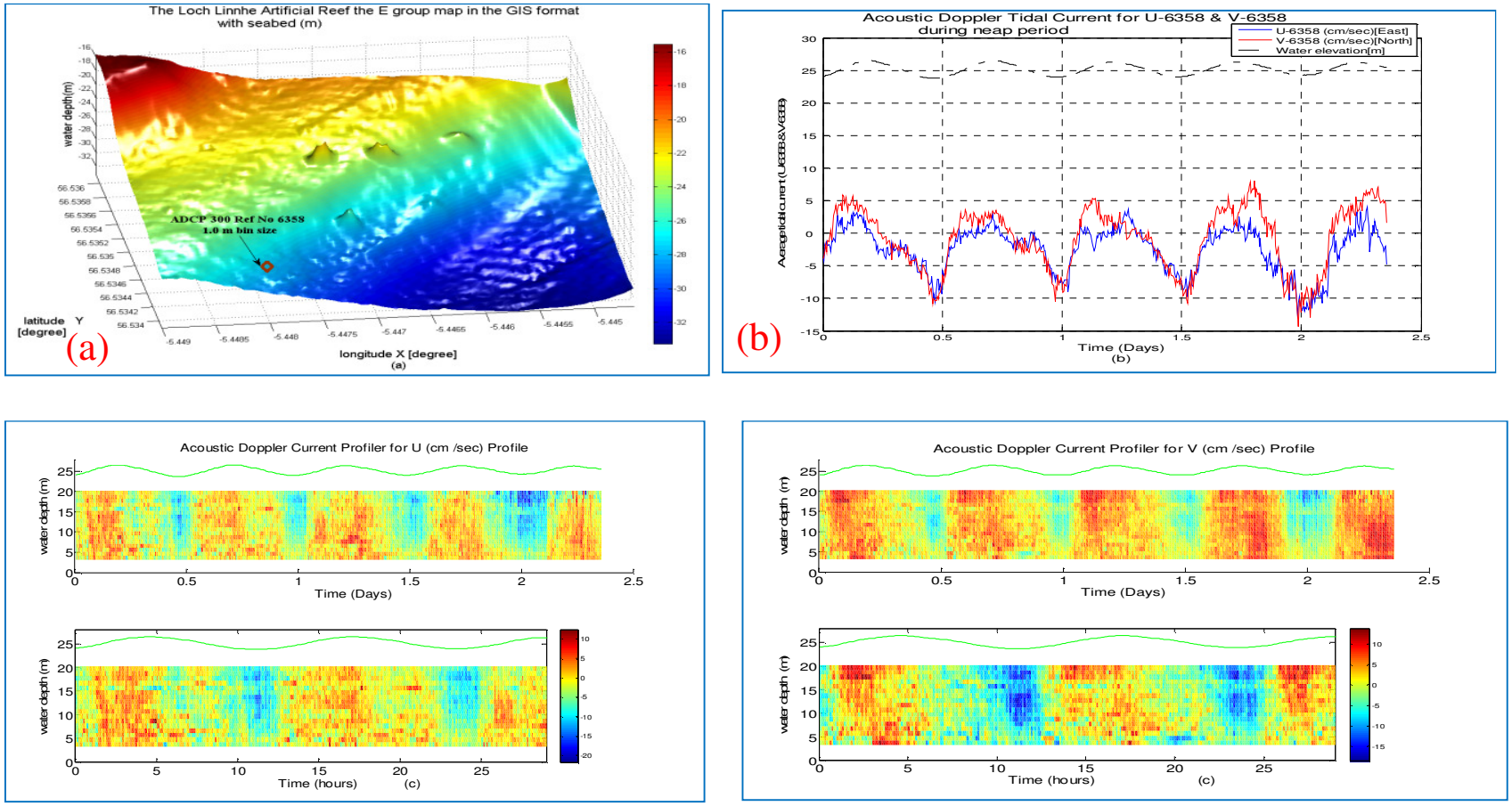

Figure 4.9.a, b, c The analysis of the ADCP No.6358 sited in the Loch Linnhe seen in (a) with the tidal wave and current seeing in (b) with the *U* and *V* component profile contours represented in (c) during the neap period.

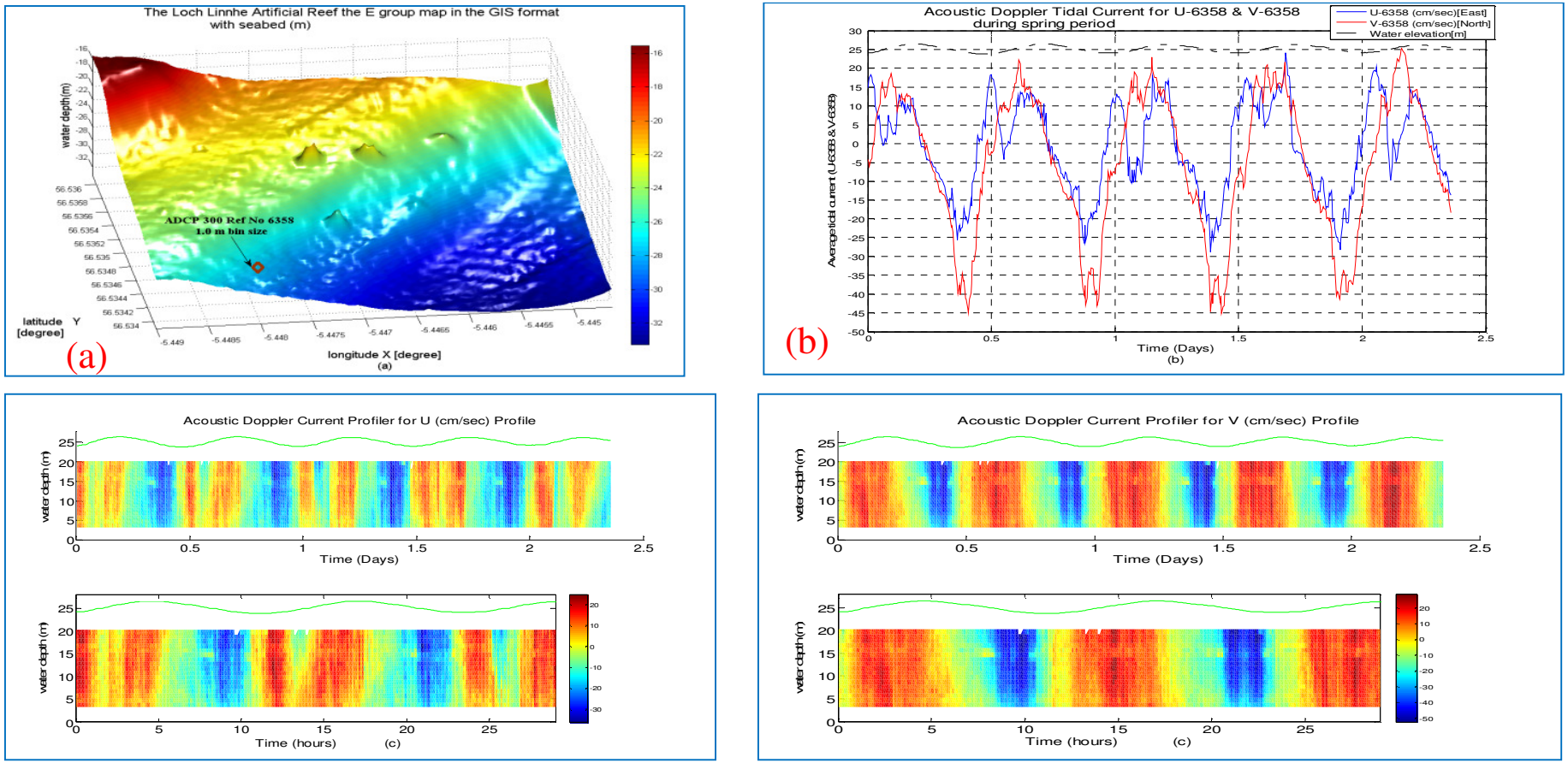

Figure 4.10.a, b, c The spring tidal wave and currents component for *U* and *V* exhibited in (b) with the ADCP location in (a) and the velocities of *U* and *V* contour profiles in (c) analysis for the ADCP No.6358 data collection.

The same tidal wave time periods displayed in the previous Figure 4.8, the data of tidal wave and current from the second ADCP No.3821 instrument location seen in Figure 4.11.a has been processed and the results of *U* and *V* components are displayed in Figure 4.11.b below. The averaged ADCP bins velocities of the *U* component reach a peak of 5 cm/sec and the *V* component equal to about 14 cm/sec in the flood tide. In the ebb flow, the *U* and *V* components scope to -14 cm/sec and -22 cm/sec respectively. The contour velocity profile for the *U* and *V* components is presented in Figure 4.11.c in which the *V* component velocity peaks can grasp 15 cm/sec in the flood tide. The *U* velocity components in the contour record are lower than the *V* components due to the disturbance of the flow occurring due to the position of the ADCP is near the artificial reef being investigated. The data recorded by the ADCP for the wave tides with the tidal current during the spring cycle is seen in Figure 4.12.b. The average ADCP bins velocity component of *U* can rise to 25 cm/sec as demonstrated by Figure 4.12.b whereas the *V* component can reach to 30 cm/sec in the flood and can orbit to around -63 cm/sec in the ebb tides and the *U* component give -33 cm/sec, which are larger magnitudes than achieved by the faraway ADCP results seen in the previous data. The velocity profile contours of the *U* component show reduce in the velocity profiles near the bottom that may imply to the influence of the artificial reef on the ADCP profile as exposed by Figure 4.12.c. The *V* component in the contour also exhibited increases in the velocity profile compared with the data recorded by the previous instrument.

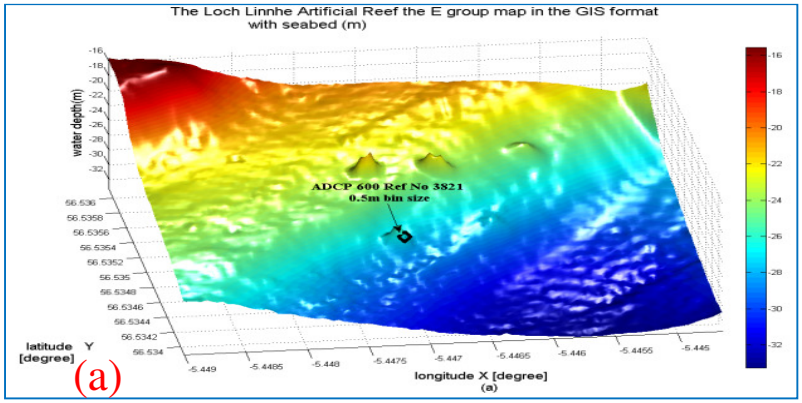

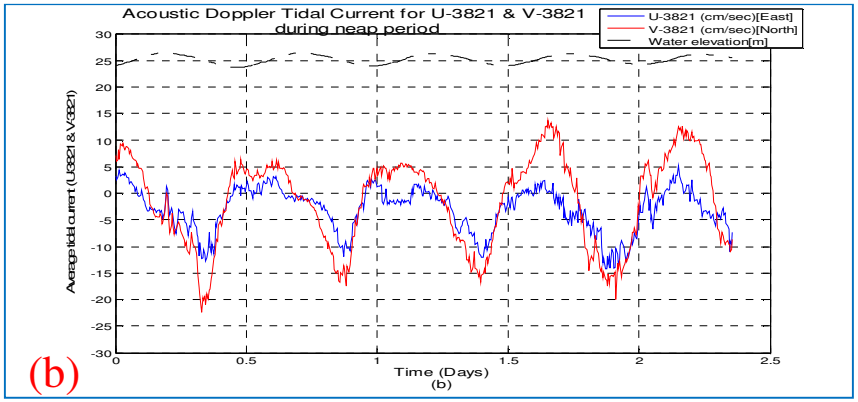

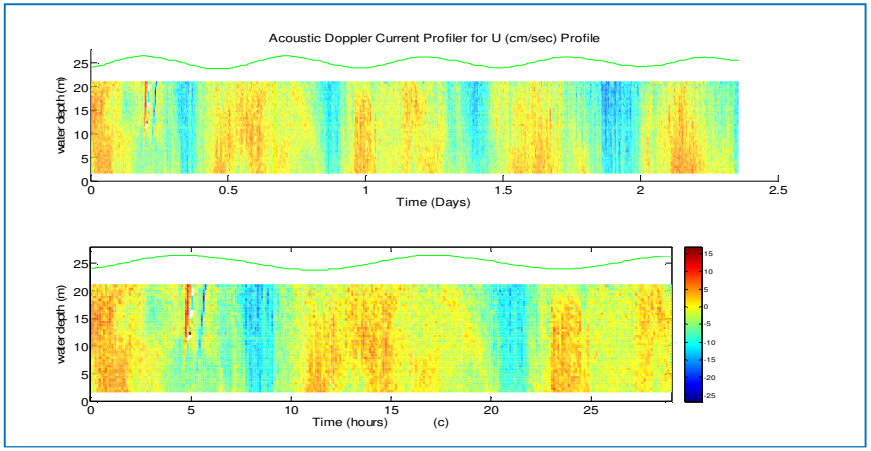

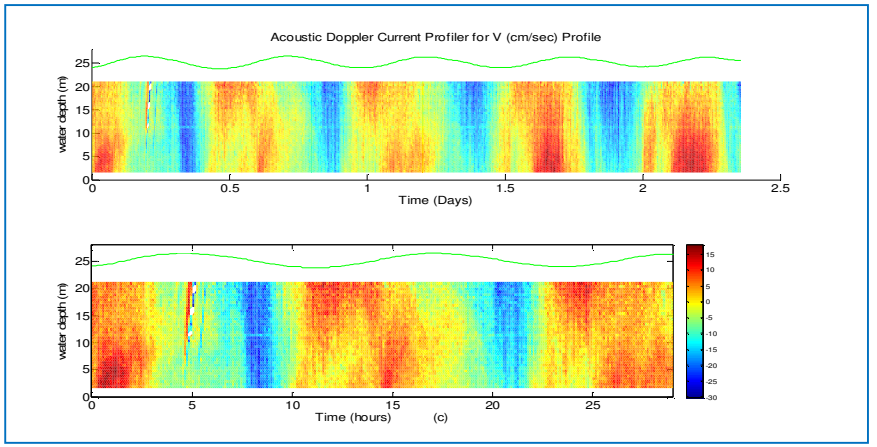

(c)

Figure 4.11.a, b, c The ADCP No.3821 data records in (a) for the neap cycle tidal wave with tidal current average are beneath it as seen in (b). The velocity components of *U* and *V* profiles are presented in contours as exposed in (c).

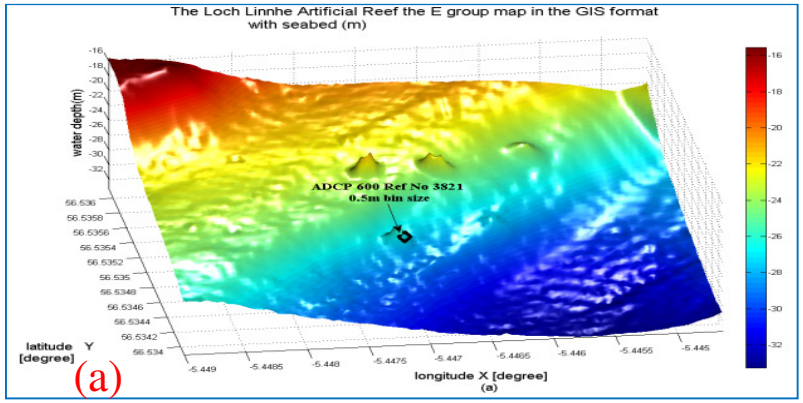

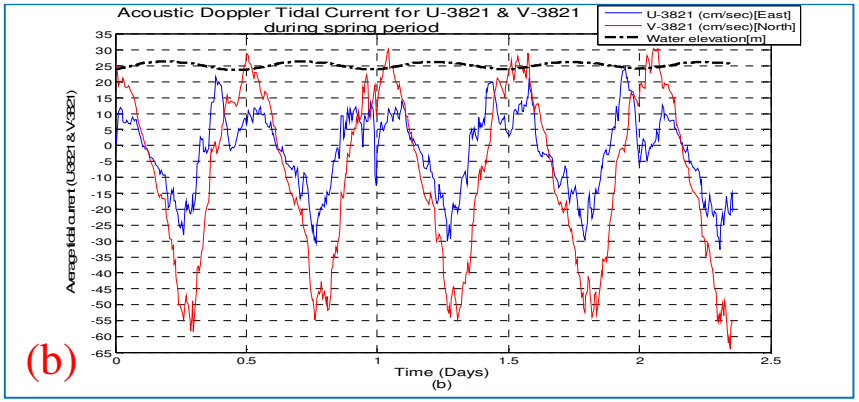

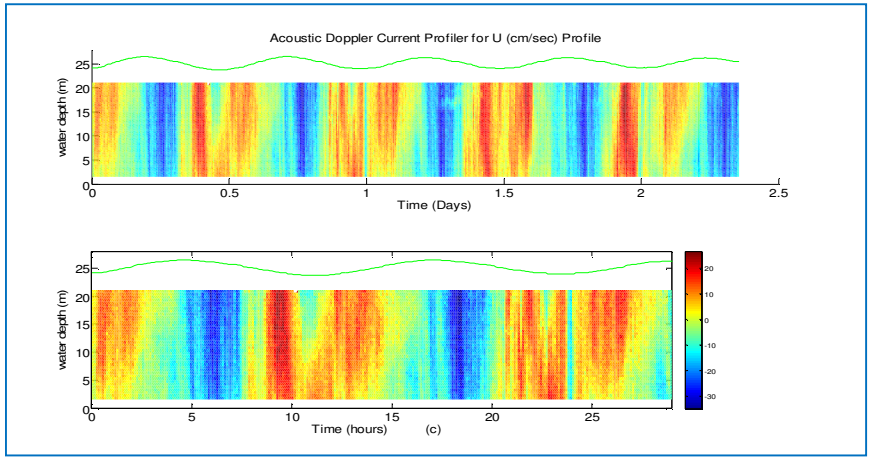

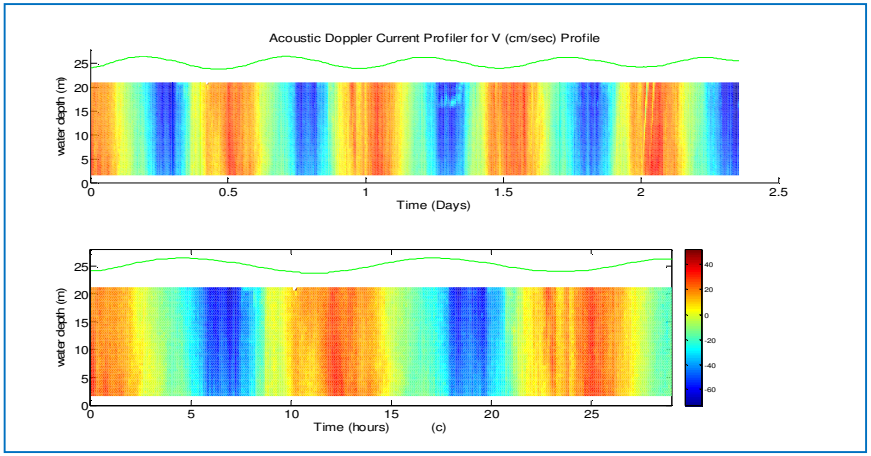

(c)

Figure 4.12.a, b, c The spring cycle of the ADCP No.3821 measurements is shown in (a) with the tidal wave and current as demonstrated in (b) that includes the velocity profile contours seen in (c).

The last ADCP No.2260 was located south of the artificial reef as shown in the Figure 4.13.a. The ADCP averaged bins tidal current and tidal waves during the neap cycle are spotted in Figure 4.13.b. The *U* and *V* velocity components maximum values vary between about 14 cm /sec for *V* component and 5 cm/sec for the *U* component during flood tide. In the ebb cycle they reach about -17 cm/sec for the *U* component and about -21 cm/sec for the *V* component of the neap cycle, as seen in Figure 4.13.b. Note the missing data gaps seen near the bottom of the Figure 4.13.c seen in the velocity contours, which may be due to the activity of fish living near the artificial reef. Since, the reflection of acoustic signal by the fish gives in velocity errors in the ADCP data (Freitag et al., 1992). On the other hand, for the spring tide and tidal current ADCP bins average achieved peaks of 22 cm/sec found in *U* component and 30 cm/sec for the *V* components in the flood period cycle. In the ebb cycle, the *U* and *V* components go to about -36 cm/sec and -54 cm/sec as exhibited respectively in Figure 4.14.b. The contours of *U* and *V* components of the profiles are exposing high values, as displayed in Figure 4.14.c. The *V* component profile through the water column is consistently large than *U* component. In summary, the ADCP data characteristic can be represented as having the following features: the ADCP No.6358 recorded the lowest values of *U* and *V* components of the tidal current profiles due to its installation in shallower region compared to other two ADCP instruments; the two ADCP instruments around the artificial reef registered data with higher values of the tidal current profiles for *U* and *V* components; the *V* components are consistently greater than the values of *U* components (indicating a tidal direction flowing toward North East); the ebb cycle was found to achieve higher tidal currents than the flood cycles in the preferred tidal periods; and finally, the maximum tidal current was recorded by ADCP No.3821 with -63 cm/sec shown in the *V* component during spring ebb cycle.

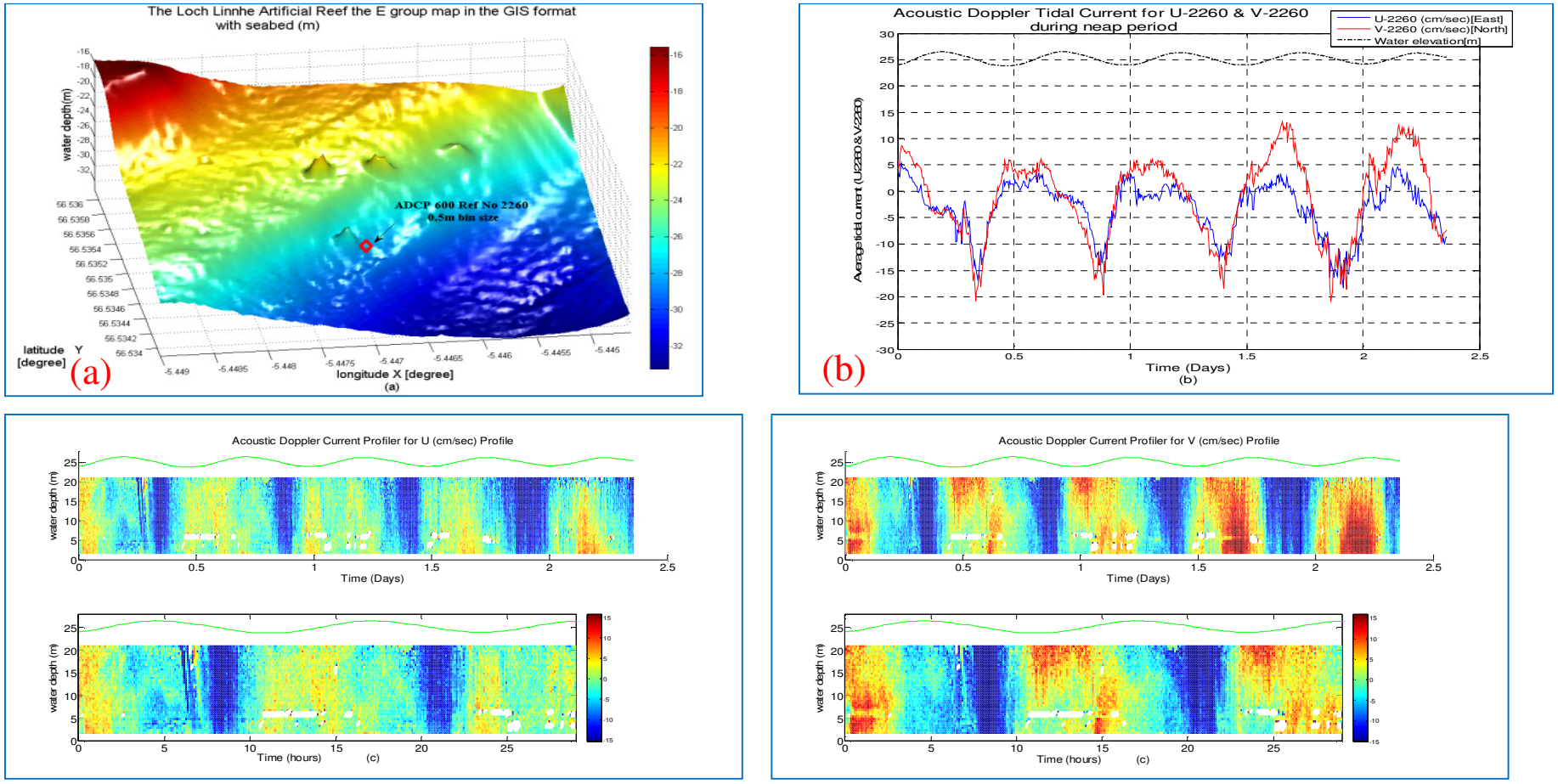

(c)

Figure 4.13.a, b, c The average tidal current under tidal waves and associated velocities *U* and *V* components is displayed in (b) with profile contours shown in (c) as recorded by the third ADCP No.2260 sited in the Loch Linnhe as seen in (a).

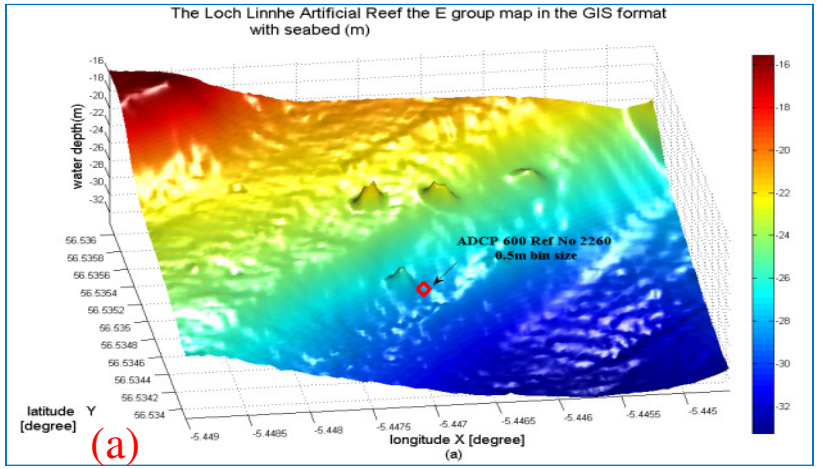

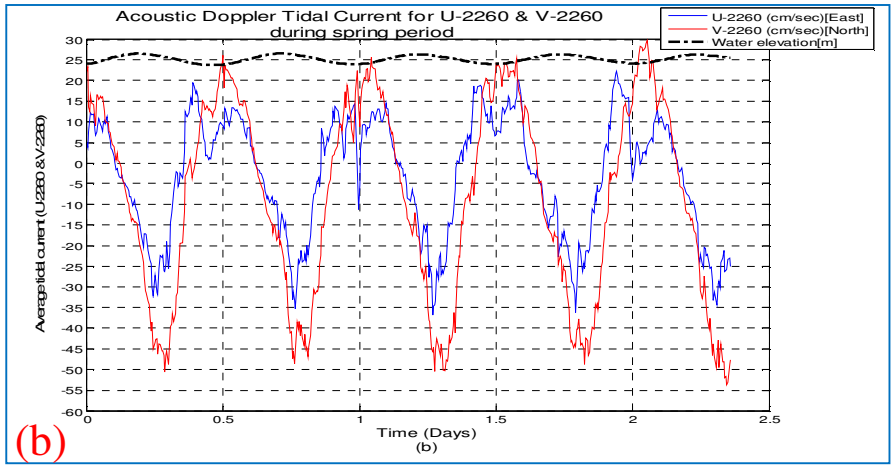

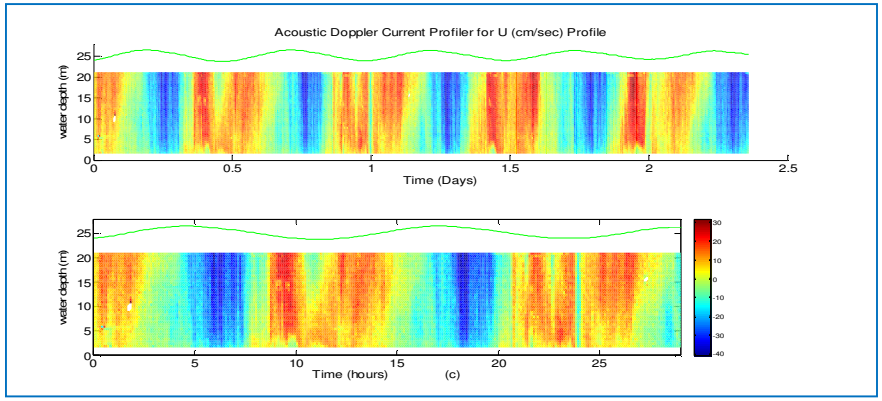

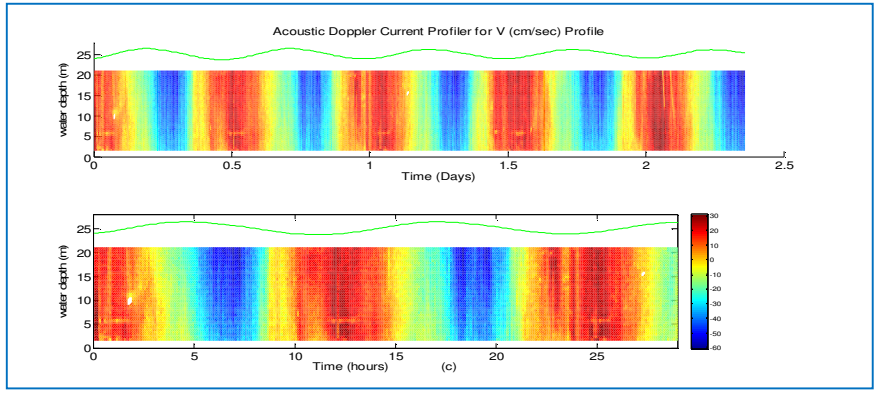

(c)

Figure 4.14.a, b, c The spring period of the ADCP No.2260 measurements positioned in Loch Linnhe as spotted in (a) that shows the tidal current with tidal waves in (b) and the contour of the tidal current *U* and *V* components profiles in (c).

4.4 Tidal current profiles for spring and neap for a daily tidal wave period

The Loch Linnhe tide is semidiurnal, having two peaks and two troughs every 24 hours. The spring and neap tidal wave periods recognized in pervious Figure 4.8 was picked to investigate the nature of the vertical tidal current profiles. The ADCP No.6358 data was focused on due to the fact that it is relatively far away from the artificial reef and the tidal vertical velocity will not be significantly affected by reef. The daily spring is shown in Figure 4.15.a and neap tidal is spotted in Figure 4.15.b. Their waves record were subdivided into 12 points over the 24 hours tide cycle with each pair of corresponding points being represented by their average at the picked tide time during the daily cycle. Note that averaging was chosen because of unsymmetrical tidal wave patterns existing in the Loch Linnhe site as demonstrated in Figure 4.15.a, b. The figure illustrates an example of the pair-wise averaging at the first point of the spring and neap tidal wave, and it presents the positions of all other points on the spring and neap tidal waves for the tidal current profiles taken from the ADCP No.6358 data records. The tidal current profile curves taken from the processed data that was recorded by the ADCP have a zigzag pattern. Therefore, the moving average technique was implemented to smooth the tidal current profiles, for the first profile of spring presented in Figure 4.16.a with neap tidal current profiles demonstrated in Figure 4.16.b. As can be seen the tidal current profile was averaged between the two points of the recorded vertical velocity denoted by the dashed blue line. The blue averaged line representing the tidal current profile which was further smoothed by three points averaging method as represented by the solid green line in Figure 4.16.a, b.

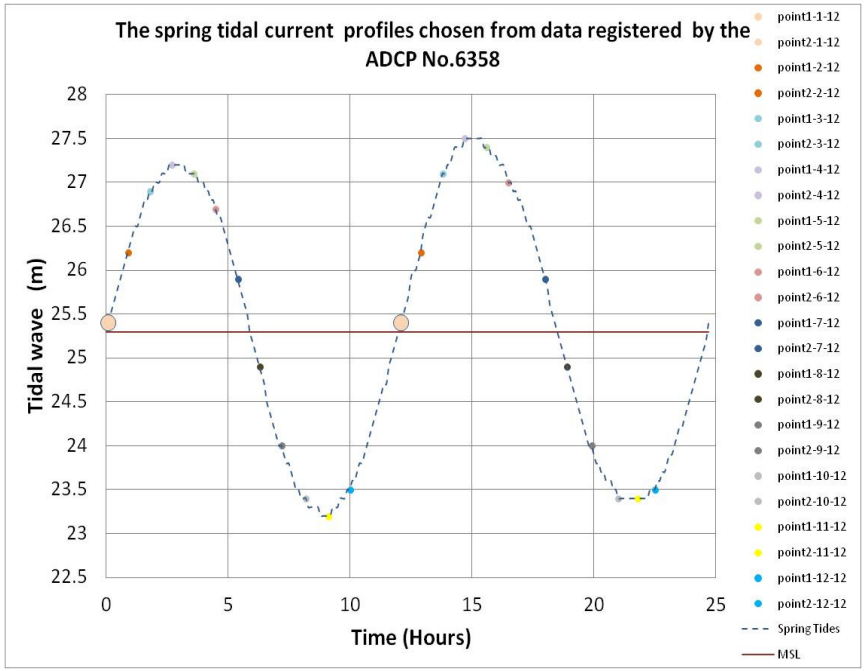

(a)

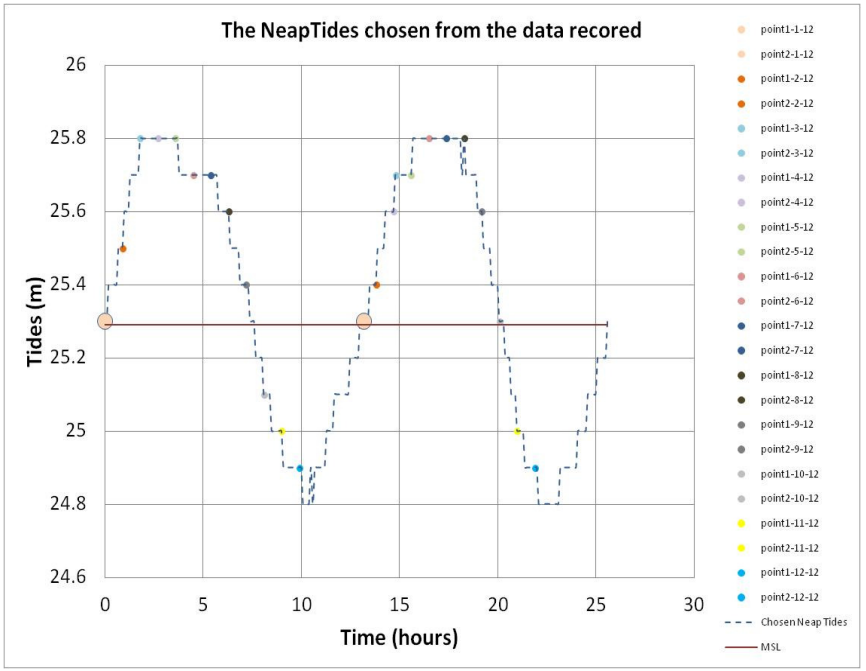

(b)

Figure 4.15.a, b The point's position of tidal current profiles selected on the tides wave of spring cycle viewed in (a) and neap cycle seen in (b) which was taken from ADCPNo.6358 measurements. Note that the spring cycle tidal wave indicates unsymmetrical pattern as recorded by the ADCP instrument.

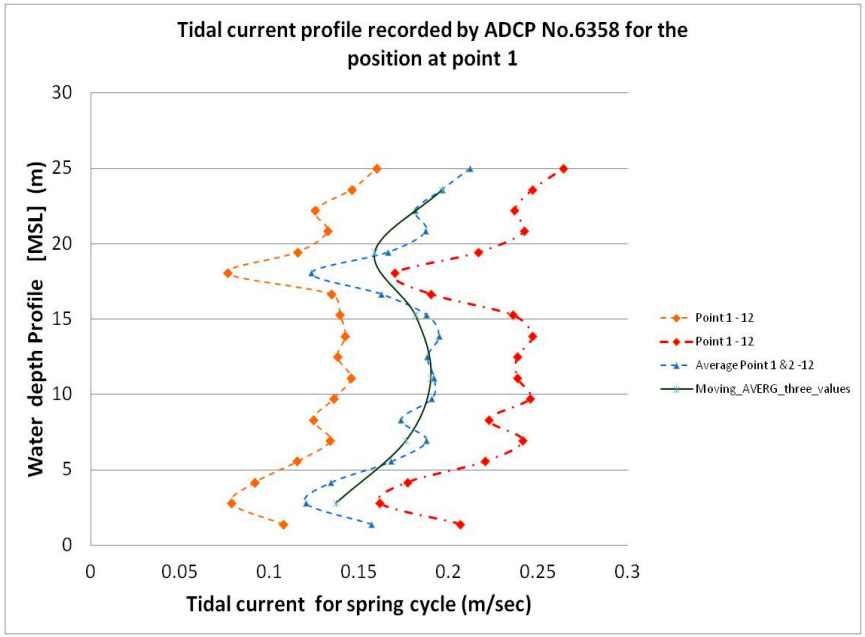

(a)

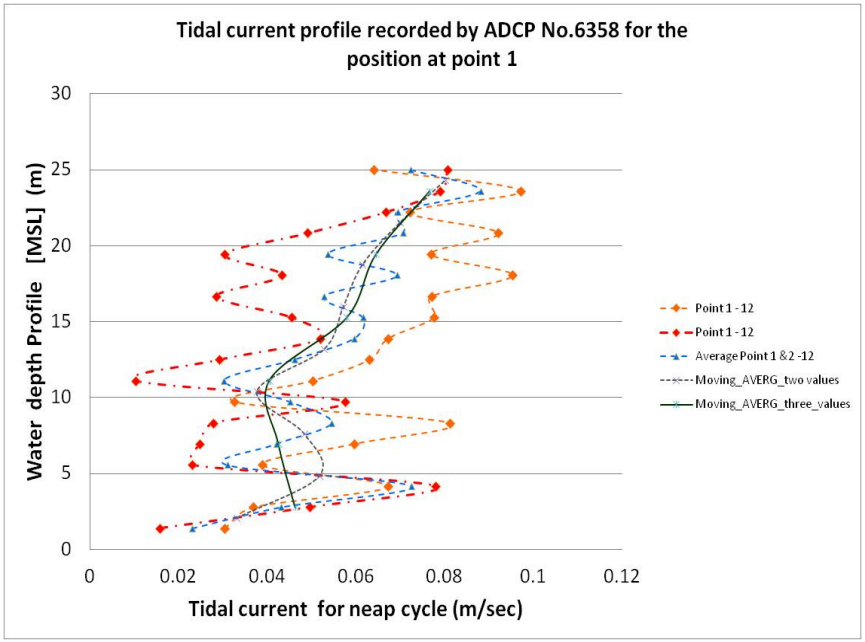

(b)

Figure 4.16.a, b The process of smoothing the tidal current profiles by implementing the three point moving average technique to the tidal current profiles of the spring and neap tidal wave periods. As the figure indicates the pair-wise velocity profiles in spring cycle are dissimilar due to the unsymmetrical tidal wave pattern existed in the Loch Linnhe as demonstrated in Figure 4.15.a, b.

This method was applied to all tidal current profiles points demonstrated in Figure 4.15.a, b above to represent the vertical tidal current as a smooth curve for modelling purposes. The objective of smoothing the tidal current profiles was to simplify the vertical velocity so it can be easily and realistically input in the FLUENT software that has been applied in the present work to simulate the detailed 3D flow around the artificial reef.

The first point of the tidal current profiles of the spring and neap periods is represented in Figure 4.17 for spring tidal current profile and Figure 4.18 for neap tidal current profile. The tidal current has been presented with the tidal current denoted as *C*, and with the two components *U* and *V* that indicating the direction of the tidal flow as it varies between the flood and ebb cycles. Note that the water depth was taken as the still water level (Mean Sea Level) with 25 m as displayed in the figures. Other eleven tidal current profiles processed during the spring and neap periods with the three point averaging method are calculated and exhibited in appendix (B).

The field measurement data taken from ADCP instruments can be used for validation of the two-dimensional numerical model. In the following chapter, the simulation of the Loch Linnhe tidal wave using the Finite Volume Method numerical model was carried out. The data record was compared with the numerical results to verify the accuracy and ability of the numerical model as will be seen in the next chapter.

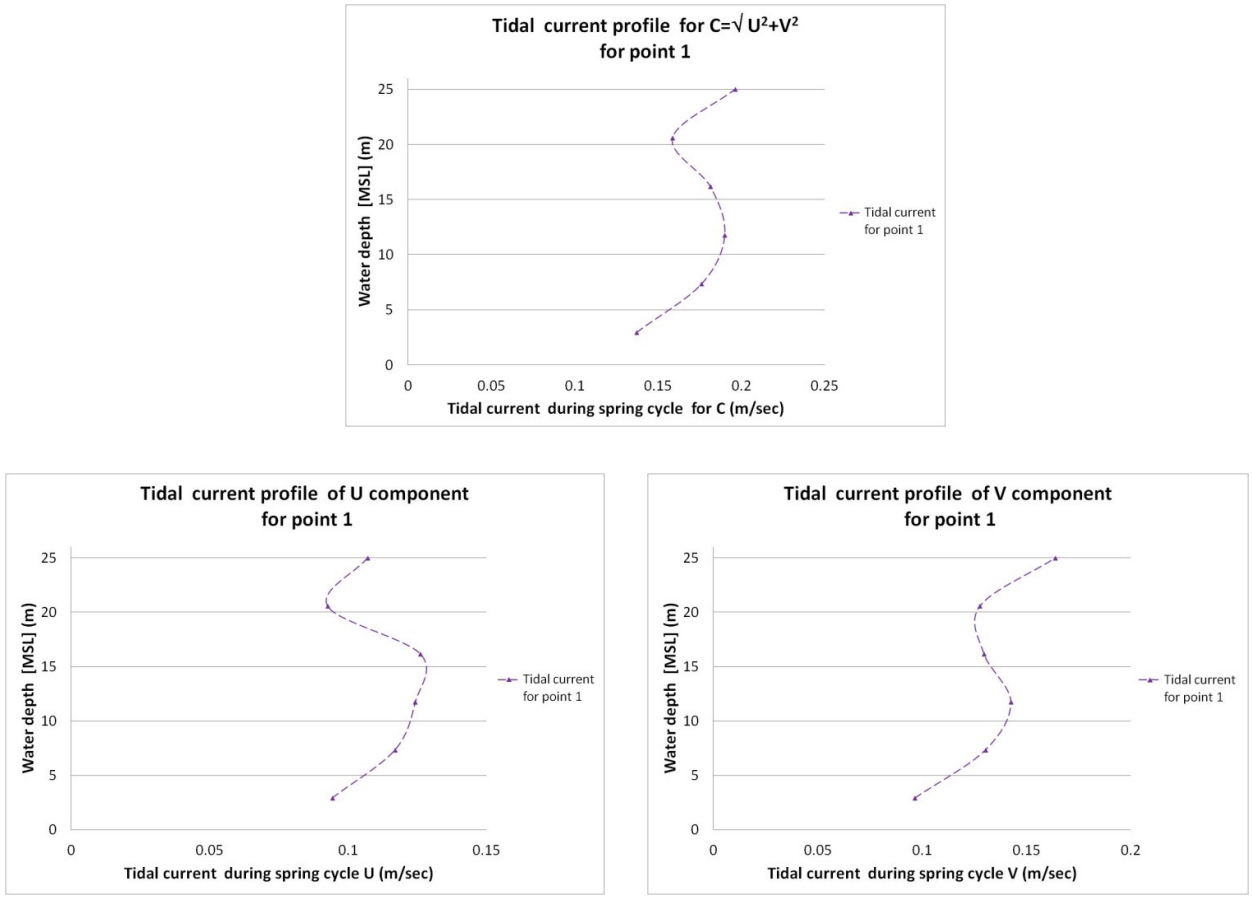

Figure 4.17 The spring tidal current profiles for the first point as represented in the previous Figure 4.15.a, b.

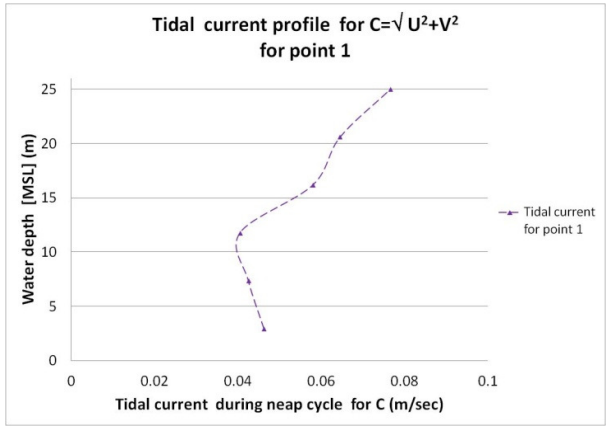

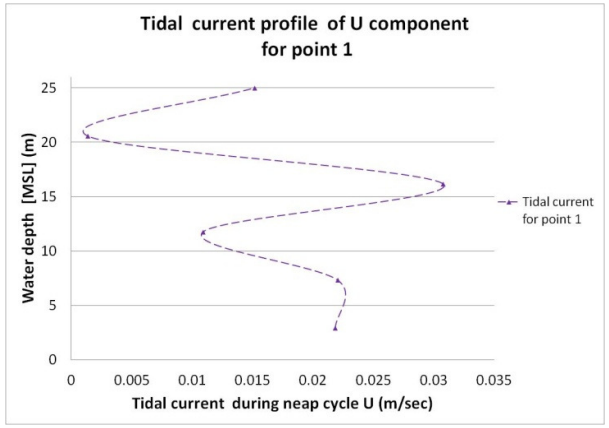

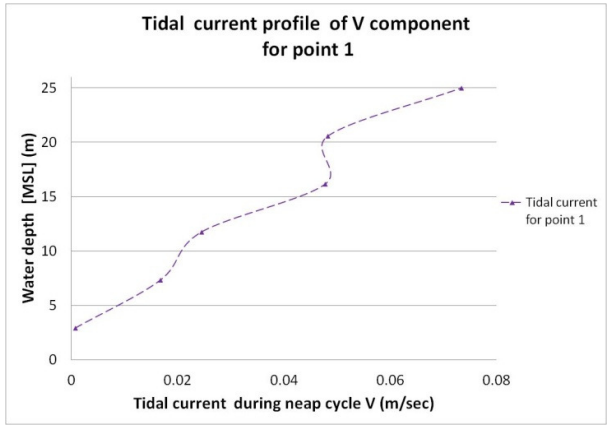

Figure 4.18 The neap tidal current profiles for the first point as shown in the previous Figure 4.15.a, b.

Chapter 5. The numerical modelling of Loch Linnhe tidal dynamics applying the 2D shallow water equations

5. Introduction

The Godunov-type Finite Volume numerical method has been tested by simulating various benchmark tests and realistic 1D-tidal flow and two-dimensional Cook Strait tidal flow in New Zealand problems, as seen in the previous chapter three. This numerical technique has received considerable attention recently due to its ability to simulate complex coastal flow problems. Therefore, the Godunov-type Finite Volume numerical method has been implemented to simulate the tidal dynamics in Loch Linnhe. The tidal flows of Loch Linnhe, lying on the West Coast of Scotland have been modelled to assess their influence on the marine environment with particular reference to, an artificial reef structure that was submerged to enhance the marine life in the Loch. However, the Loch Linnhe has a complicated topology that presents a challenge to any numerical modelling of the tides. In addition, the deployment of an irregular artificial reef structure increases the complexities of the seabed and increases the difficulties in the modelling Loch. The present model will describe the fluid dynamics of the tidal flow in the Loch and is intended to assist in understanding the complex interaction of physical parameters, such as tidal currents, and the marine habitat. In fact, fluid dynamics plays a role in settling, nutrients, oxygen and colonization of marine life, as seen in chapter two.

The shallow water equations were solved using a Cartesian coordinate system. Thus, maps that were used in the numerical modelling had to be converted from WGS84 GPS (Global Positioning System) format to a Cartesian system, A MATLAB Geodetic toolbox provided from MATLAB central for file exchange (Craymer, 20111, see references for website) has been used to convert the WGS84 coordinate system to Cartesian coordinate system. In this chapter, the Loch Linnhe tidal dynamics was simulated for daily cycle, and for a half monthly cycle, for a period of 13 days. This time duration represents the phenomenon of the tidal dynamics during the neap and spring tides. The comparison between the numerical results and measurements data was satisfactory.

5.1 The Loch Linnhe tidal dynamics simulation

A sea loch on the West Coast of Scotland, known as Loch Linnhe, has been used for the application of the Finite Volume Method numerical model. The Loch has a potentially important role to play in the sea fishing industry but the tidal flow pattern in the Loch have not been studied in detail yet. At the southern end of the loch, near an island called Lismore, lies an artificial reef system that was constructed in the period of 2001-2006 (Beaumont, 2006) with an area size of 1Km × 1 Km as seen from Admiralty charts, Figure 5.1.a. Its purpose is to provide a site for studying artificial reefs for enhancing, protecting and restoring fisheries, as defined in chapter two.

A numerical section zone was created to simulate the tidal dynamics on the Loch that include the artificial reef area as shown from an image of Google earth Figure 5.1.b. The bathymetry of Loch Linnhe was digitized from an Admiralty chart (Admiralty chart, 2010), as Figure 5.1.a indicates. A numerical grid was constructed for numerical tidal wave simulation as shown in Figure 5.2.a with longitude, latitude in degrees and seabed in meter. Note, the characteristic of the Finite Volume Method model with reference to its ability to work in wet-dry process was explained in the previous chapter three. Thus, the coastal boundary dry cells were defined as large positive elevations see Figure 5.2.a.

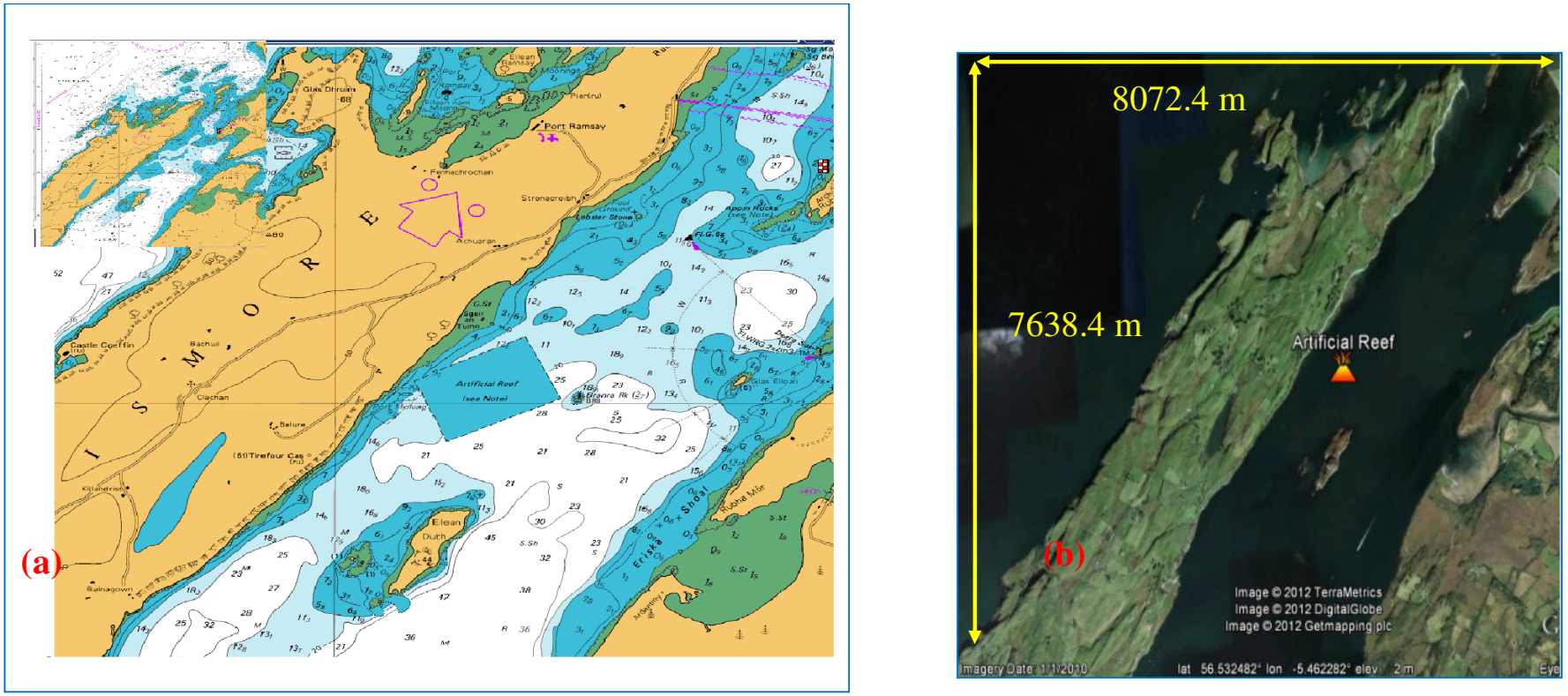

Figure 5.1.a, b The selected areas of Loch Linnhe with the artificial reef zone as seen from the Admiralty chart with the reefs are near Lismore Island.

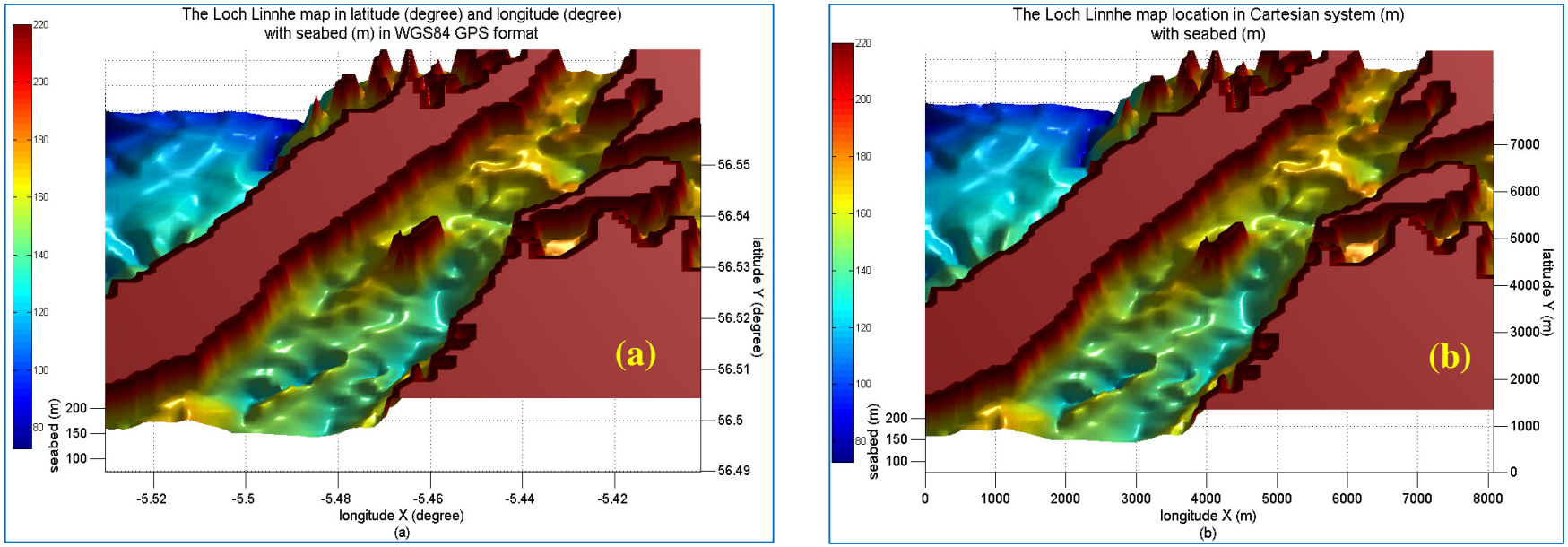

Figure 5.2.a, b The focused zone displayed in GIS foramt as seen in (a) and Cartesian coordinate system as presented in (b).

The Loch Linnhe numerical domain was converted to a Cartesian system using the previous information of map construction which was represented in the above Figure 5.2.b.

5.2 Model configuration

The Loch Linnhe water depth varies from 1m to 181m which implies that wetting and drying may occur, which can be dealt with by the present numerical model. The amplitude of the tidal range of the Loch varies from 1 to 2.5 m during a lunar month (Hydrographic Office, 2011). However, the tidal currents are moving from an open sea with a low speed range in the order of cm/sec and passing through a channel with a complicated bathymetry, such as Straits, or between Islands and shallow water zones where the tidal current gains power. Indeed, the powerful tidal currents exist in these specific sites where the tidal flow may increase in strength with tidal currents having peak velocities in the range of 2-3 m/sec (4-6 knots) or more during the monthly rhythms of spring-neap cycles (Fraenkel, 2002). At the Loch Linnhe shallow water region, with two exits zones near the port of Appin and near the Loch of Creran, a tidal current of approximately 4 knots in springs and 2.75 knots in neaps is indicated from seafarer's navigation information, Figure 5.3. The numerical domain has been centred about the region with the artificial reef site, and zones not required in the tidal wave simulation have been blocked with dry cells, as shown in Figure 5.4. The Cartesian coordinate grids were defined by several matrixes to study the mesh convergence as will be demonstrated in the convergence curve section. A sample grid size of 94 × 89 cells with a dimensional size of 8072.4 m × 7638.4 m is presented in Figure 5.4 that gives a size of each 2D cell with 86 m × 86 m. The maximum water depth of new blocked region is about 60.5 m. Therefore, the coastal boundary dry cells height was set to 80 m. Nevertheless, the field measurement time duration was in the variation of winter-spring seasons which indicates seasonal high winds blowing on the Loch Linnhe region.

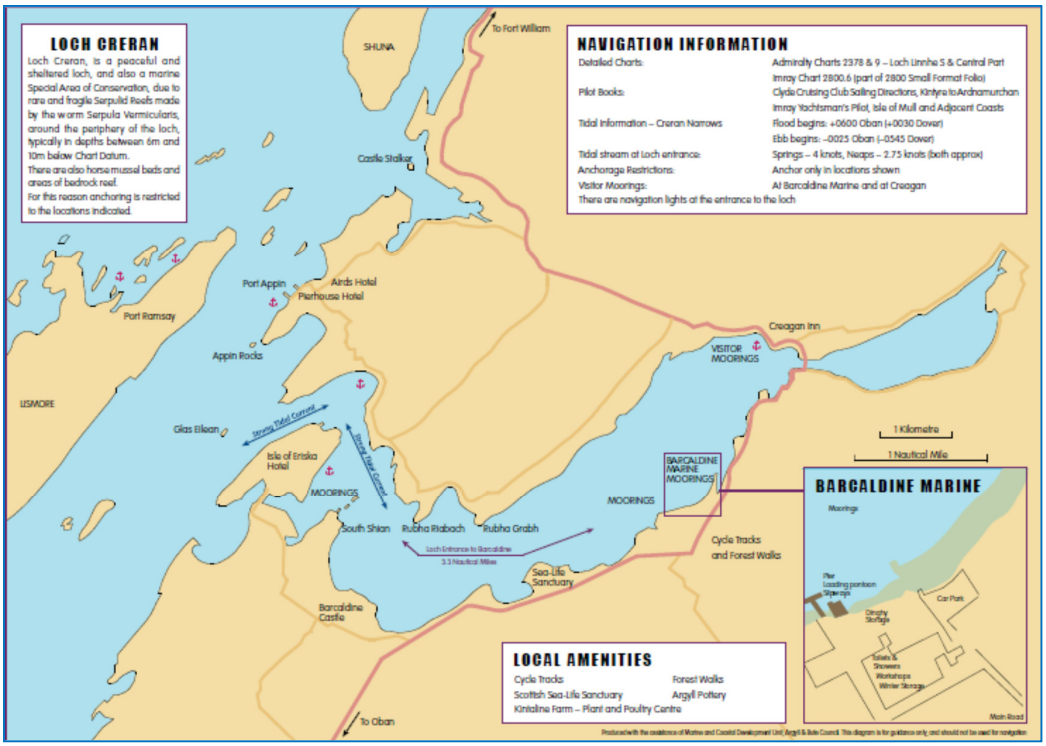

Figure 5.3 The tidal strength at the interaction between the Loch Linnhe and Loch Creran from the seafarer's navigation information.

The wind stress can affect the tidal current structure magnitude as demonstrated by previous studies such as Matsuura and Cannon (1996). Therefore, wind stress effect has been included in the Finite Volume numerical model which was calculated from (Stewart, 2008):

$$W_s = \rho_a C_D U_{10}^2 \qquad (5.1)$$

$$C_D = (0.8 + 0.065\, U_{10}) \times 10^{-3} \qquad (5.2)$$

Here ρ_a is air density, C_D is the drag coefficient that was estimated applying the formula proposed by Wu (1982) as identified in equation (5.2). U_{10} is expressing the wind velocity measurement at 10 m above the mean sea surface. A data collection of wind speed and direction was taken from the meteorological station sited on the Eilean Dubh as presented in Figure 5.4.

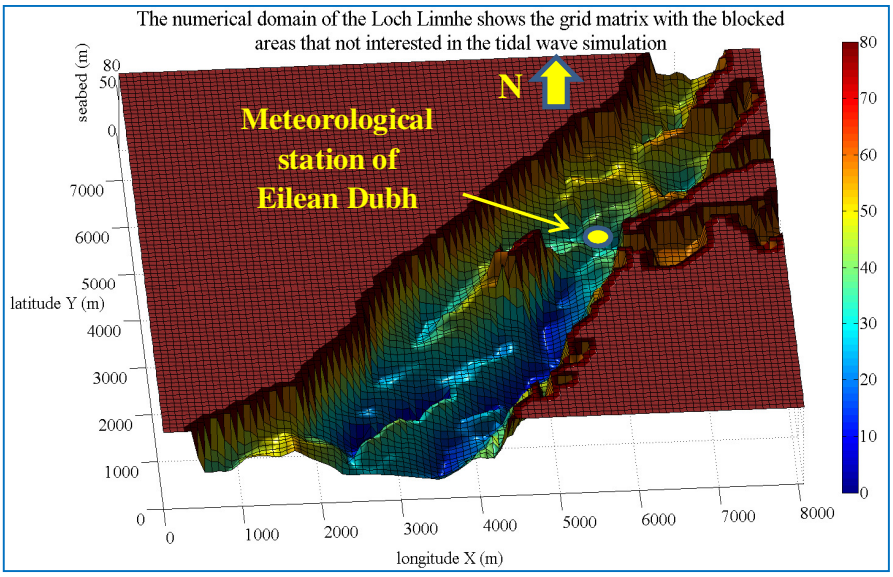

Figure 5.4 The sample of a matrix of grid cells (94 × 89) of Longitude and Latitude in the Cartesian system with the blocked dry cells and the location of the weather station as displayed.

A summary of the wind conditions during the field measurement is displayed in Figure 5.5.a, b in wind rose form. The hourly mean wind (m/sec) is presented in Figure 5.5.a whereas the maximum gust (m/sec) within each one-hour sample interval is exposed in Figure 5.5.b. The wind speed varies between 1.3 m/sec to gust that reach about 25 m/sec as established in Figure 5.5.a, b. The wind velocity has been considered in the Finite Volume numerical model calculation to investigate the effect of wind stress on the tidal current structure magnitude.

However, very large wave lengths compared with the water depth is one of the characteristics of the shallow water wave. In fact, in a typical continental shelf with an average depth of 100 m and tidal period of 12 hours, a quarter wavelength shelves can reach a width of about 300 Km (Defant, 1961). Therefore, two tidal gauge stations were selected in the research to control the south inflow and the north outflow boundaries as spotted in Figure 5.6.

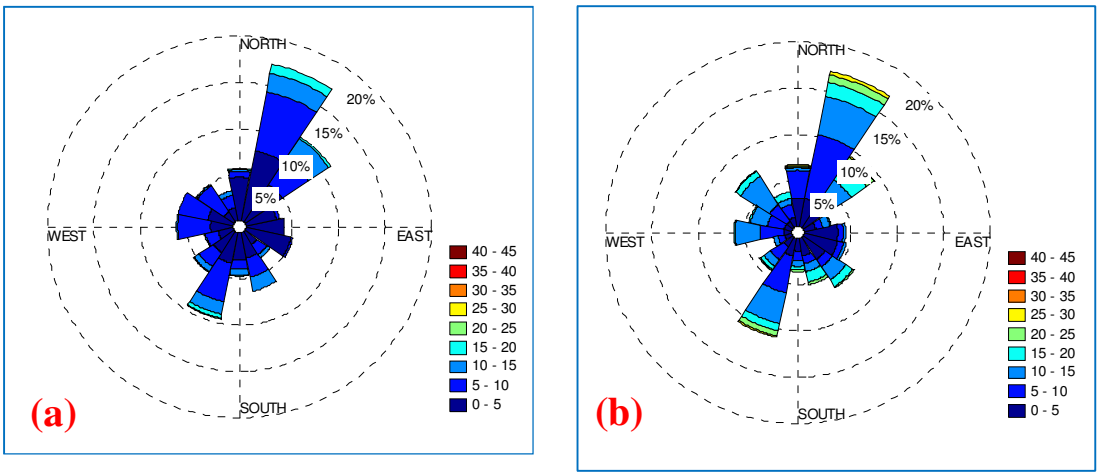

Figure 5.5.a, b The wind roses during the full deployment period demonstrating the frequency and the amplitude (m/sec) distrubtion of hourly mean winds presnted in (a) and the maximum gust winds within each one houre sample interval in (b). It has been notice that dominant winds were approximatley aligned with the axis of the Loch Linnhe.

Figure 5.6 The location of the stations required to control the inflow and outflow boundaries.

The east outflow boundaries in the numerical domain were restrained with a tidal predication analysed by the UK Hydrographic Office for Pier of Barcaldine seen overhead in Figure 5.6, while the west side boundary is forced by the Lismore Island as noticed in Figure 5.4. The tidal record was gathered from the UK Hydrographic Office (2011) for the two tidal gauge stations at the Port of Oban and the Port of Appin, as the stations location revealed in Figure 5.6. The duration of the two station tides recorded was for 13 days to include the spring and neap tides in the Loch. In addition, data records were taken for the same lunar dates to synchronize the inflow with the outflow boundary. On the other hand, tides predicted for Pier of Barcaldine were also synchronized according to the lunar month dates in a spring-neap pattern cycle as in the two tidal gauge stations data record.

5.3 The Loch Linnhe harmonic analysis

As described in chapter three the tidal wave can be analysed applying the harmonic analysis. The ultimate objective of the harmonic analysis was to model tidal variability and identifies semi-annual periods, or any well-defined cyclic oscillation, (as defined by Emery and Thomson, 2001) at a global scale in the vicinity of the artificial reef, the spring-neap tidal period was analysed to obtain the harmonic constituents that represent the tidal wave lunar cycle. The Least Squares method was applied to analyse the tides records of the two stations to solve the best fitting curve Figure 5.7 shows the Port of Oban 13 day's tides regression curve compared with the measured data, which also presents their residual. The tidal record with same time duration for the Port of Appin was analysed to solve the constituents of the astronomical tidal forces as shown in Figure 5.8. The selection of the constituents related to tidal amplitude depends on the tidal time period. In general, the number of constituent's increases with the length of the period of the tides data (Pugh, 1996). In the present case the choice of the harmonic constituents was based on the analysis of tides data in the North-West European Shelf, as described by Pugh (1996).

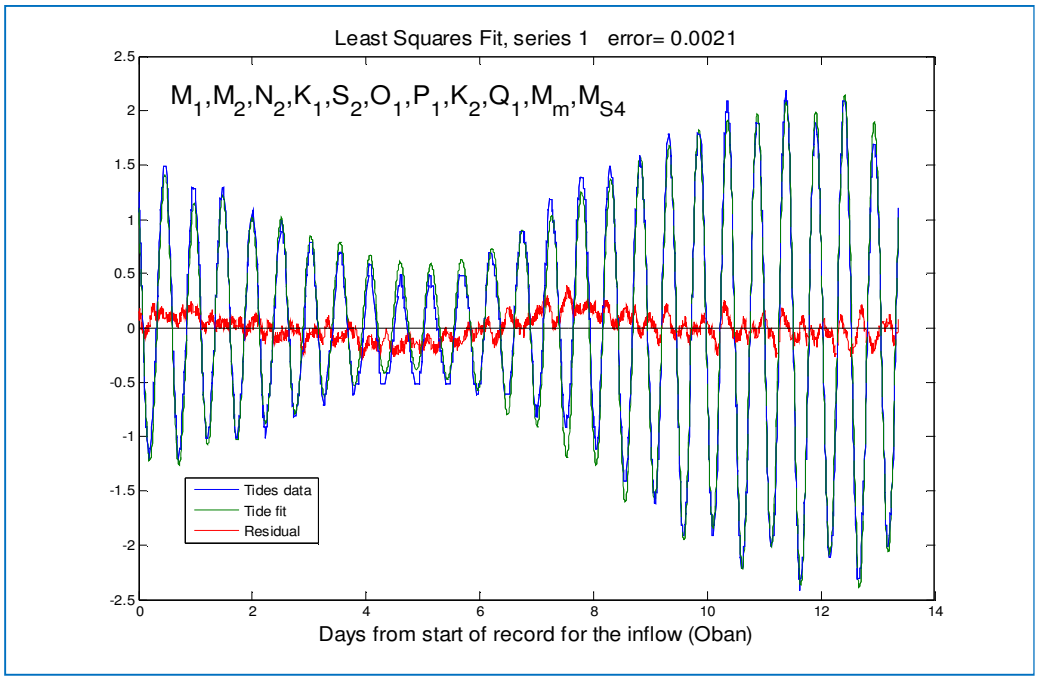

Figure 5.7 The harmonic analysis for Port of Oban compared with the measured tides data.

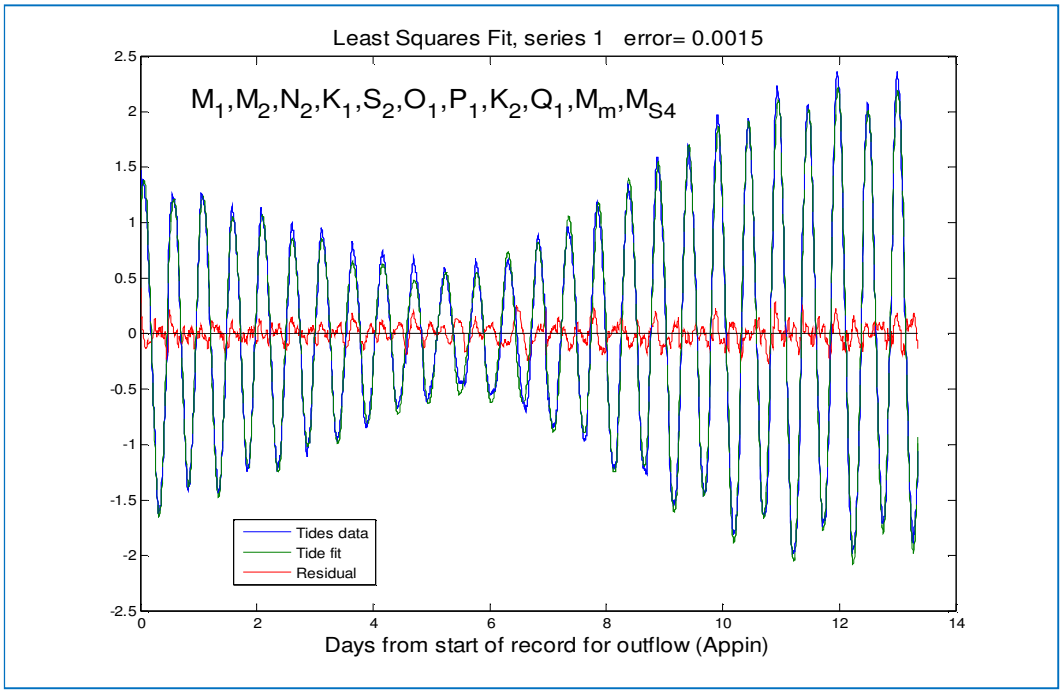

Figure 5.8 The harmonic analysis for Port of Appin compared with the measured tides data.

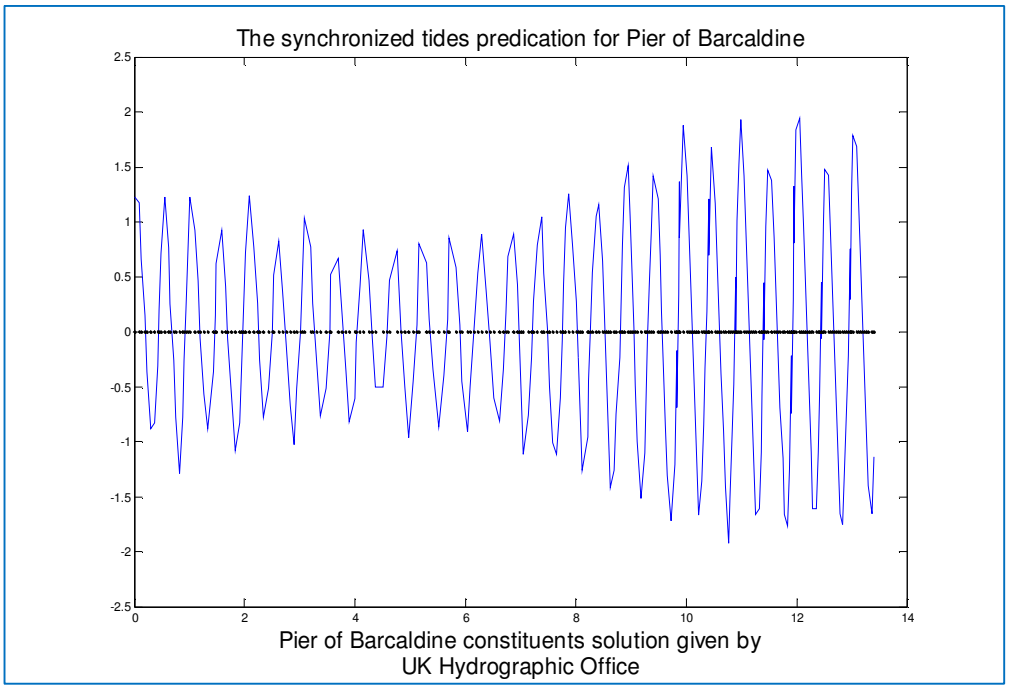

Figure 5.9 The tidal wave constituent's solution given by UK Hydrographic Office for Pier of Barcaldine.

Additionally, the analysed tidal wave for Pier of Barcaldine taken from UK Hydrographic Office is presented in Figure 5.9. Note that the predication of tides seen in Pier of Barcaldine is actually analysis of tides data applying mathematical method such as Least Squares method, but the tides data couldn't be hold. Besides, it's crucial to restrict the east outflow boundaries and the tides analysis given by the UK Hydrographic Office will be preferred.

5.4 The initial and boundary conditions for Loch Linnhe

The initial condition of the Loch Linnhe water elevation (η=h_s+z_b) was set to 60.5 m, as exhibited in Figure 5.10. The tidal series of the harmonic constituents solved for Port of Oban was applied to the inflow boundary and north outlet boundary conditions was controlled by the tidal solution of harmonic constituents for Port of Appin as shown in Figure 5.10. Whereas, toward the east outflow boundaries the tidal wave analysis for Pier of Barcaldine was adopted to command it.

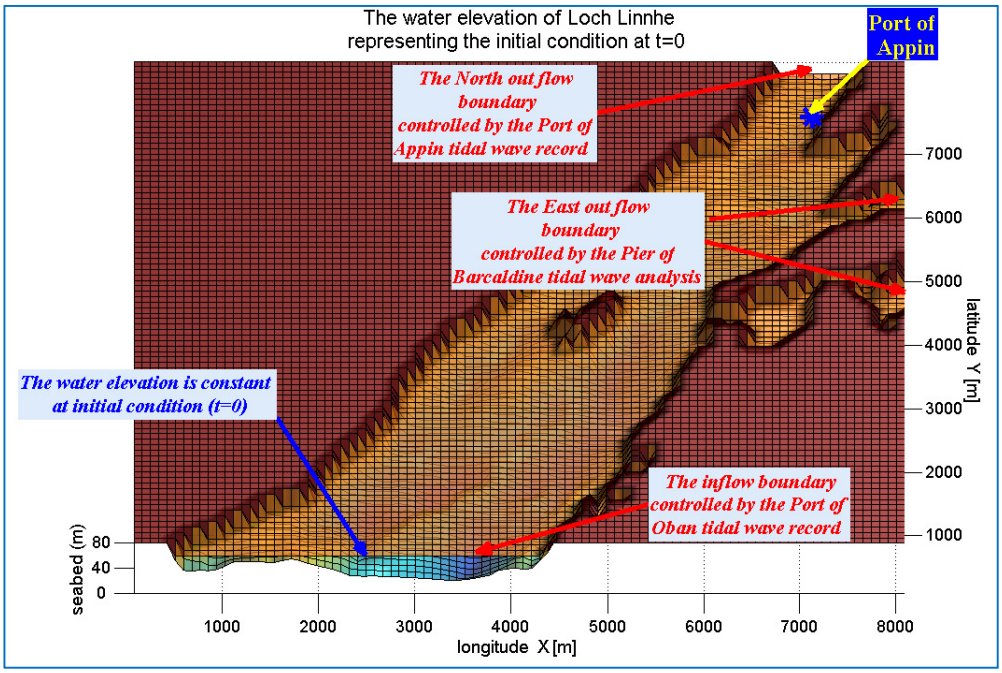

Figure 5.10 The still water level at t=0 in the Loch Linnhe with the inflow and outflow boundaries as presented by the numerical model.

The numerical domain was monitored with a long-section of cells, as shown by Figure 5.11, so that it could be checked at from the initial condition and during the tides dynamics simulation. The water elevation (η) was taken as still during t=0 as Figure 5.11 established.

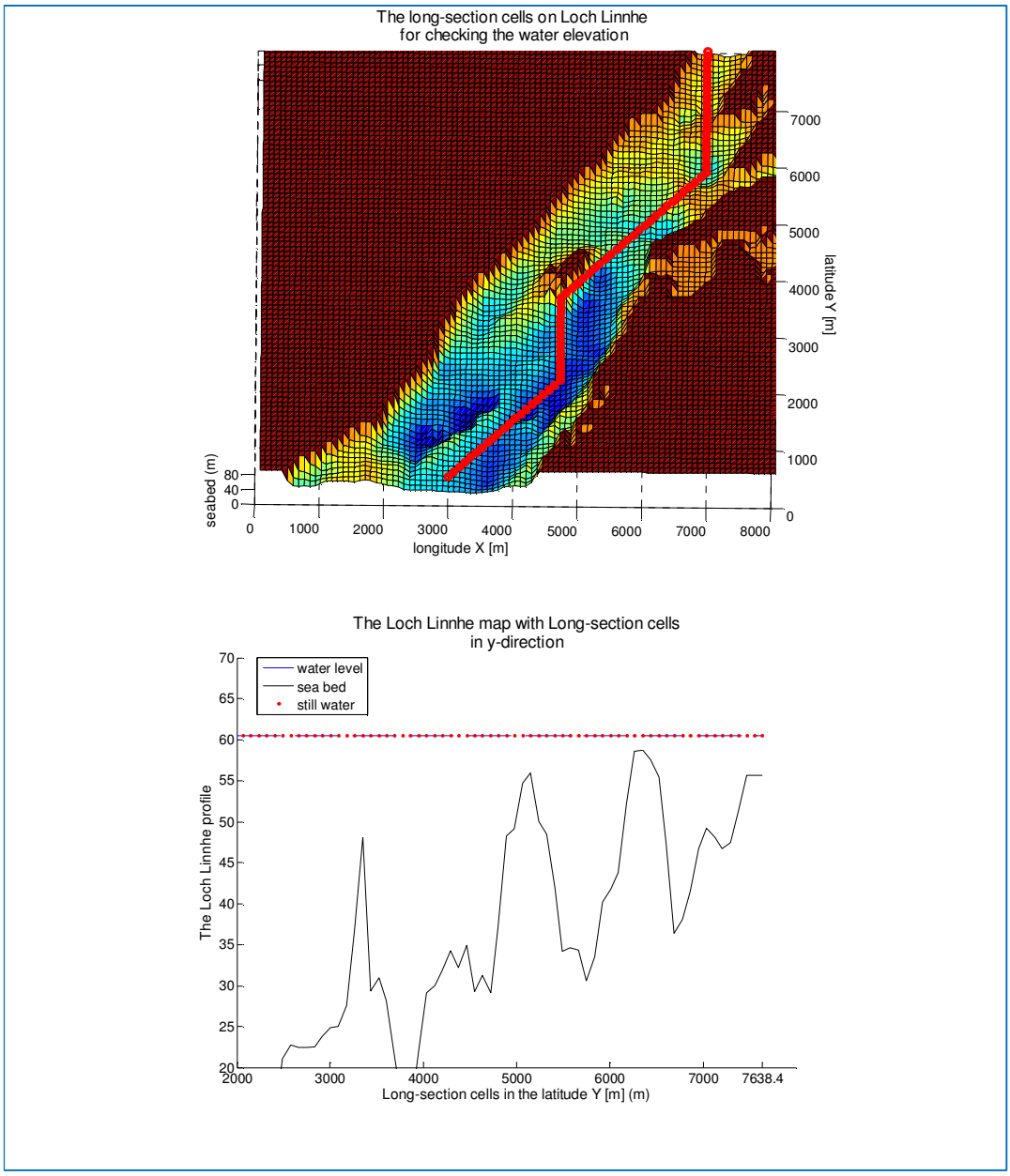

Figure 5.11 The long-section was implemented for checking the water elevation of Loch Linnhe tidal dynamics simulation.

5.5 The Loch Linnhe tidal analysis results

The tidal wave simulation of the Loch was computed during a daily spring-neap tides cycles as well as for a 13 day's spring-neap tides lunar cycle, the water elevation in the location of the artificial reef with tidal current components was computed. Two ADCP (Acoustic Doppler Current Profiler) instruments were deployed in positions near the artificial reef to gather tidal measurements of the water elevation and velocity components over time duration of 57 days to detect the spring-neap lunar

cycle. The results of the ADCP were described in the previous chapter four. The locations of the ADCPs instruments are presented in Figure 5.12. The water elevation and velocity components, *U* and *V,* were recorded by the ADCPs during the required period. The location of seafarer's navigation information that will be used for comparing the numerical tidal current speed with tidal current given by it, as shown in Figure 5.12. The tide gauge data taken from Port of Appin was used as a checking location for the numerical modelling. The grid size and numerical accuracy of numerical model was investigated to demonstrate the efficiency and the accuracy of the present numerical model as well be seen in the following section.

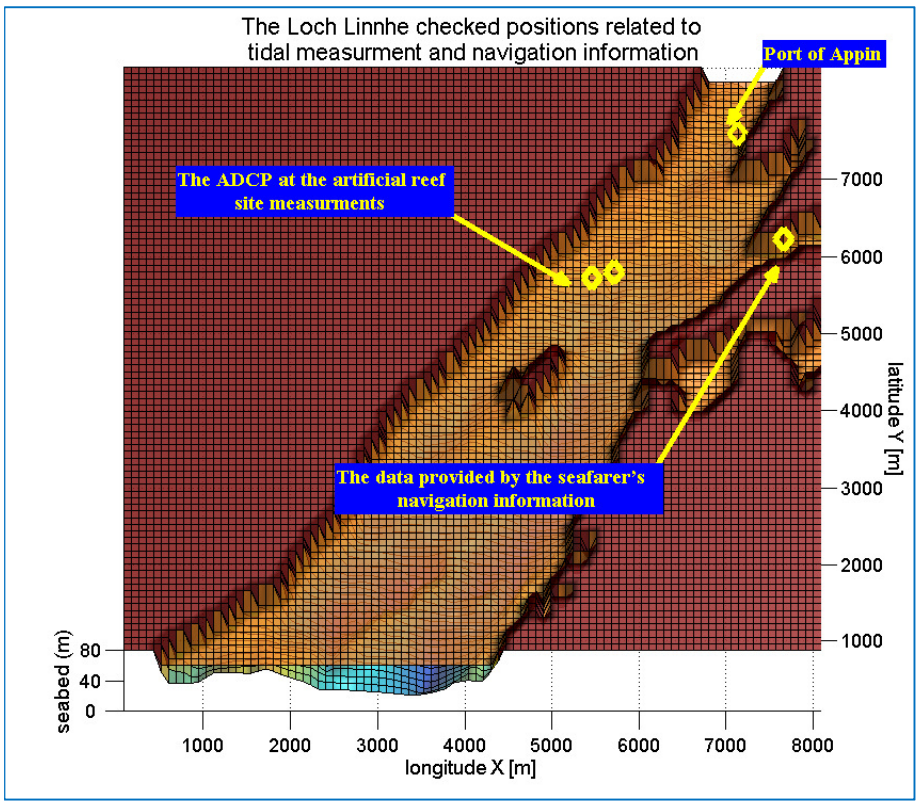

Figure 5.12 The montoring cells in the Loch Linnhe during the tidal wave simulation.

5.5.1 *The convergence curve of the Finite Volume Method numerical model*

The effect of computational meshes on numerical accuracy and efficiency was investigated by applying four grid cell sizes. These grid cell sizes are constructed in regular square mesh size that increases with mesh density in the two-dimensional that has a resolution of $\Delta x, \Delta y$ =173.6, 86.8, 63.3 and 43.3 m. As shown in Figure 5.13.a, b the different grid resolutions of the U and V components for the numerical predictions

correlated with the ADCP measured at the artificial reef site for the U and V components represented in a daily cycle. The numerical model predicted the U and V components with good accuracy as shown in Figure 5.13.a, b. The convergence of the mean tidal wave elevation during the 13 day's simulation time was checked as can be seen in Figure 5.14. The numerical model solution implies that as the mesh is refined the numerical results are more accurate. In fact, the comparison between the measured and the fine mesh grid size mean tidal wave is actually very small. In addition, the mean tidal current during the simulation time was investigated to obtain the convergence curve for the mesh refinement. As indicated from both Figure 5.14 and Figure 5.15 the numerical solution is converged in $\Delta x, \Delta y = 43.3$ m grid cell size, since the numerical solution has a negligible change in the results compared with other mesh sizes. As presented in chapter three the numerical model calculate the fitted time step according to the CFL criterion, for further details see appendix A. The preferred time steps estimated by CFL criterion for each mesh refinement are displayed in Figure 5.16. It has been observed that the time steps decreases as the mesh density increases. As experienced from the mesh convergence study finer grid cell size 43.3 m is giving good accurate mathematical solution and it can be said that grid independent solution has been achieved. All the results of the Finite Volume Method numerical model will be presented in the converged grid cell size 43.3 m.

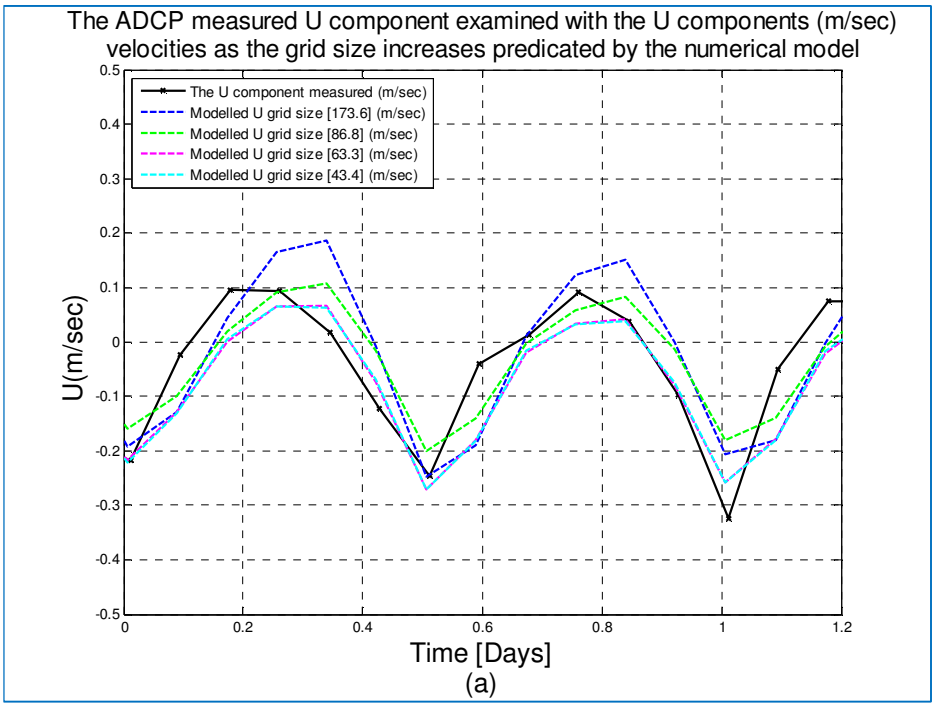

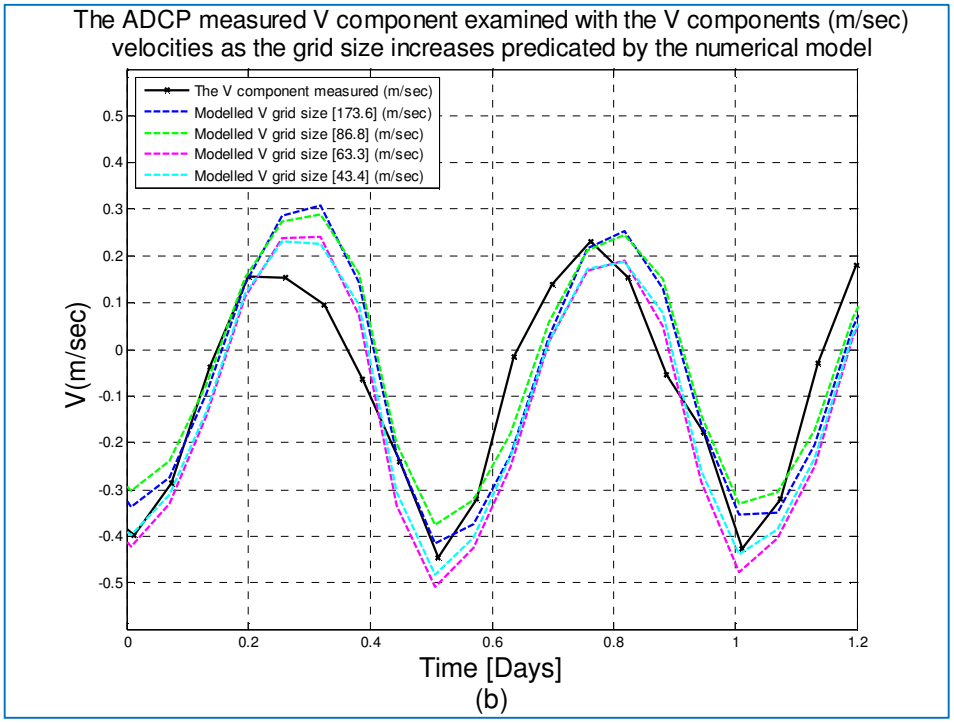

Figure 5.13.a, b The U and V velocities components of the different mesh grid sizes correlated with the ADCP field measurement for one day cycle.

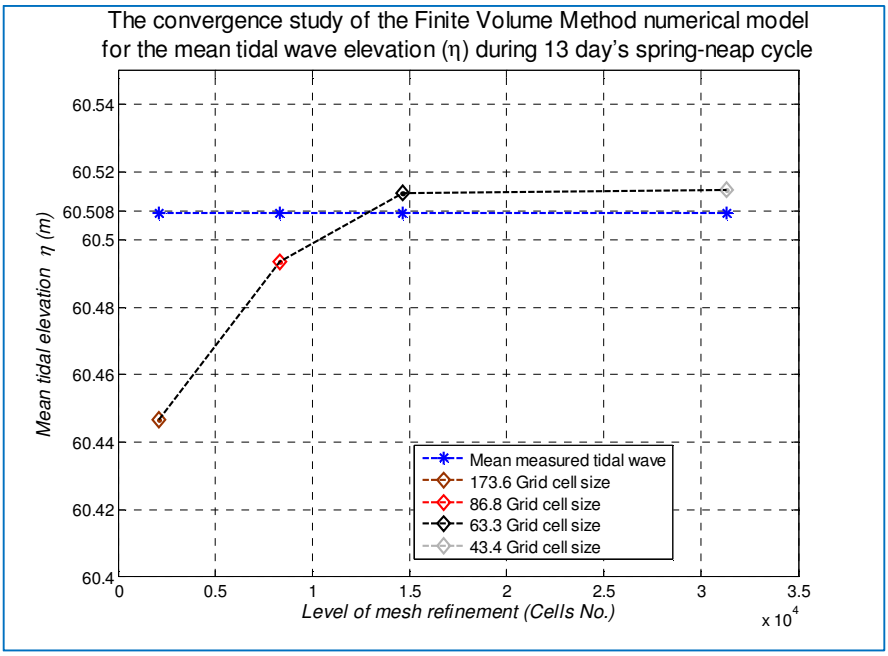

Figure 5.14 The Finite Volume Method convergence curve was performed to judge an adequate fine mesh grid size that provides an accurate numerical solution for mean tidal wave elevation.

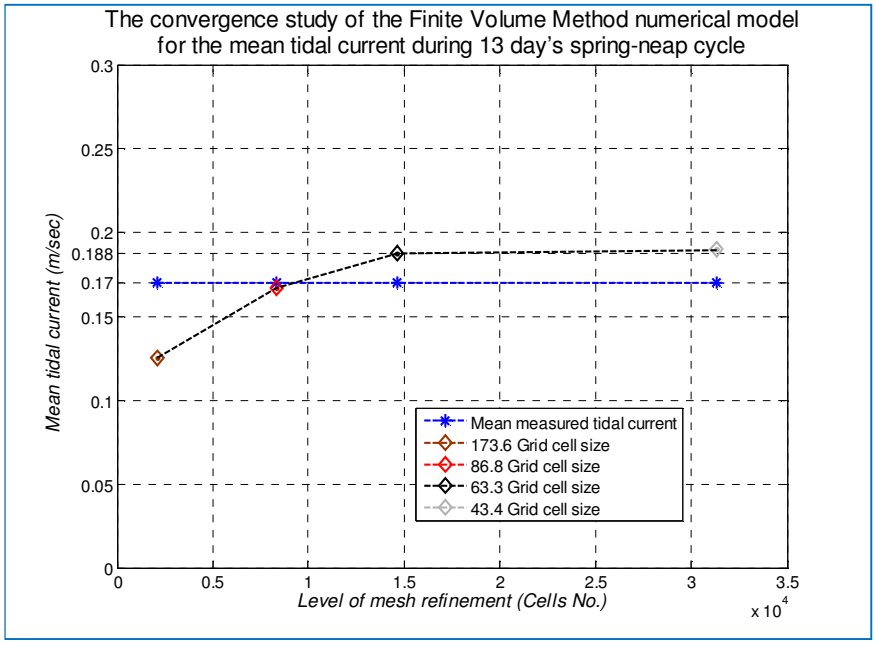

Figure 5.15 The sufficiently refined mesh was converged in the grid cell size of 43.3 m which give a good numerical accuracy for the mean tidal current.

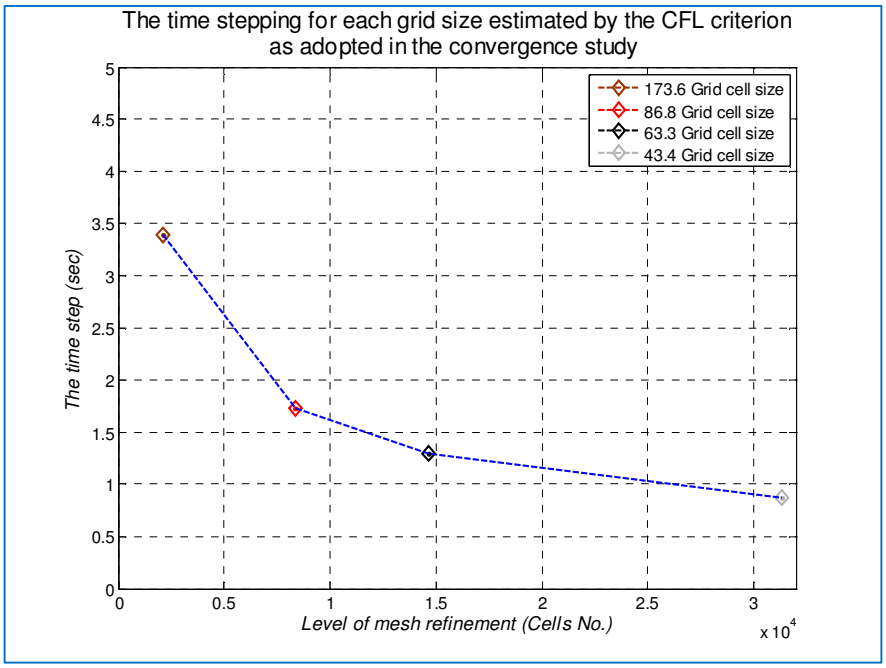

Figure 5.16 The CFL criterion calculation provides the numerical model with a suitable time step for mesh refinement during the convergence study.

5.5.2 *The daily tidal wave of the Loch Linnhe for spring and neap cycles*

The daily spring tidal wave cycle was applied as an input into the Finite Volume Method numerical model to simulate the tidal wave daily cycle over the whole computational domain with the adopted fine grid cell size 43.3 m. The outcome of the water elevation tidal wave is shown in Figure 5.17.a where it is compared with the measured values from the ADCP. The peaks of the modelled spring tidal wave on the artificial reef sites are nearly match the ADCP observations, as exhibited by Figure 5.17.a. In similar pattern, the daily neap tidal wave period was simulated and the numerical results were compared with the ADCP data tidal wave records as presented in Figure 5.17.b. The neap tide's oscillation of both ADCP and numerical model agreed well with each other as illustrated in Figure 5.17.b. Note, the mean still water elevation is shown in both figures to indicate the tidal wave range.

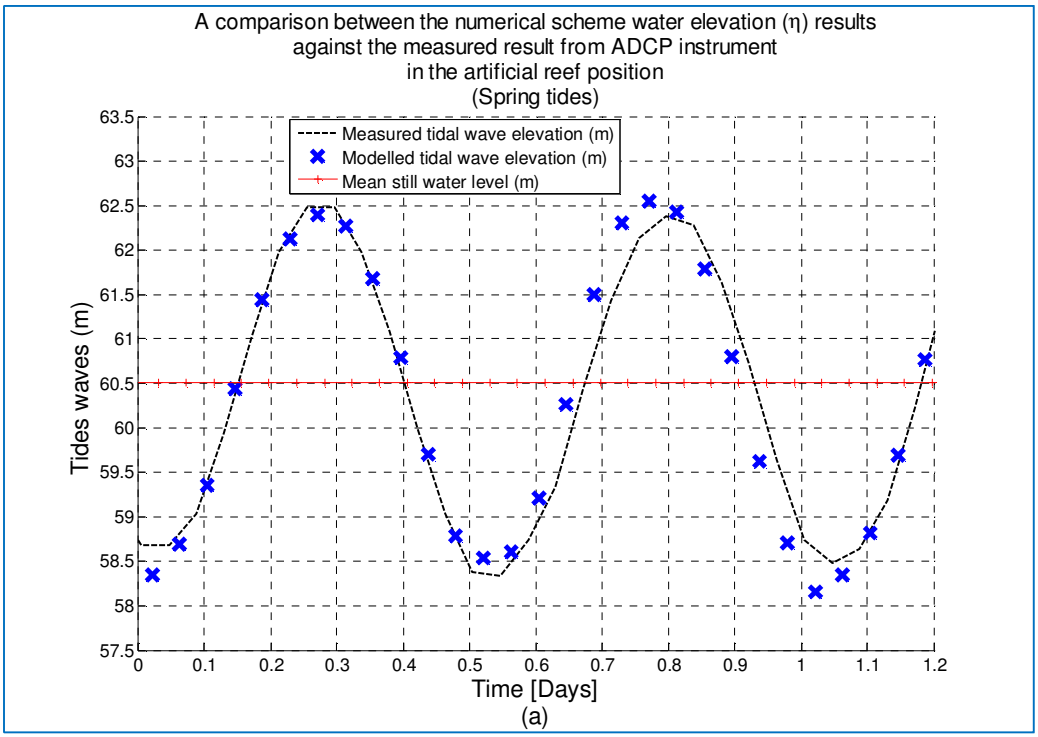

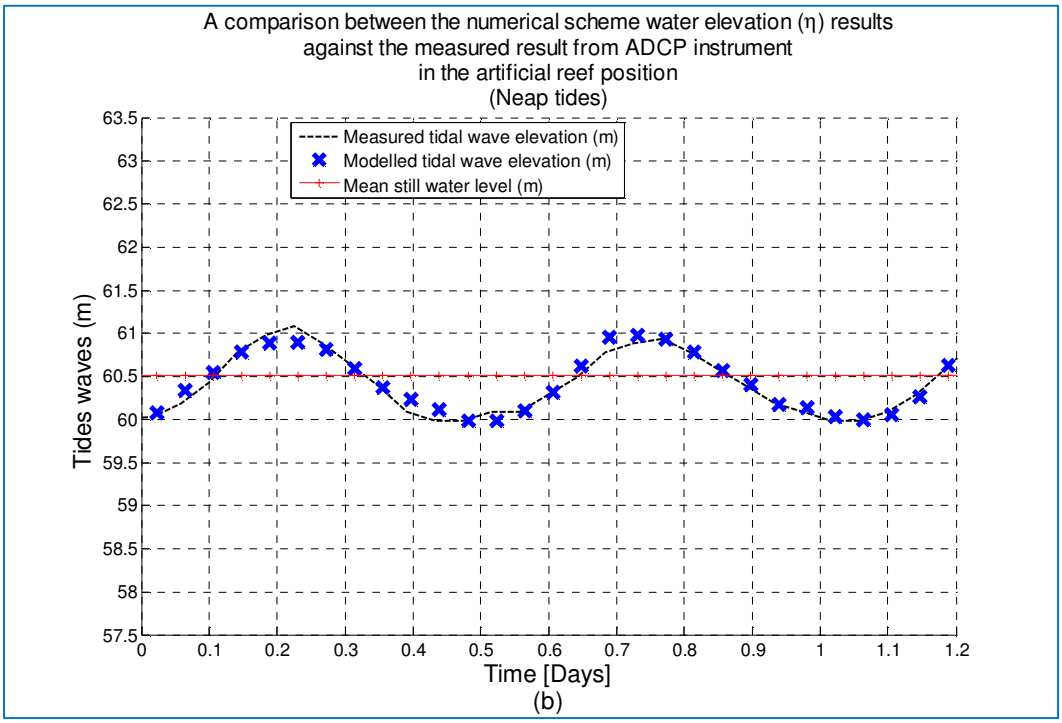

Figure 5.17.a, b The tidal wave elevation for both numerical modelling results and the tides data measurment in a dialy spring(a)-neap(b) tide cycle.

Furthermore, the daily spring and neap tidal wave cycles of numerical conclusion were analysed against tides gauge data taken from Hydrographic Office. The

comparison of the numerical daily spring tidal wave cycle against the tidal wave data at the Port of Appin is exhibited in Figure 5.18.a. The modelled tidal wave is differed slightly from the tide gauge data taken from Hydrographic Office, but it has same harmony with values are approximately equal. Note that, the seabed is produced from admiralty charts which indicate sensible conclusion given by the numerical model, since the accuracy of the seabed is important in this wet-dry numerical model. In resemblance, the lowest astronomical tides wave recorded at Port Appin was compared with the numerical neap cycle outcome. A similarity of tides wave pattern is found between the numerical calculation and tidal gauge data as exposed by Figure 5.18.b. There is a small deviation in the tidal wave values between the numerical conclusion and measured tides data, but it is in an acceptable error range in the seabed accuracy provided. In fact, the numerical tidal results are approximately matching the tidal wave records from the tide gauges observed at Port of Appin. The Finite Volume Method numerical model delivers a very good prediction for the daily tidal wave during spring and neap tides cycles with a reasonable differences and good agreement between the numerical and the measured results.

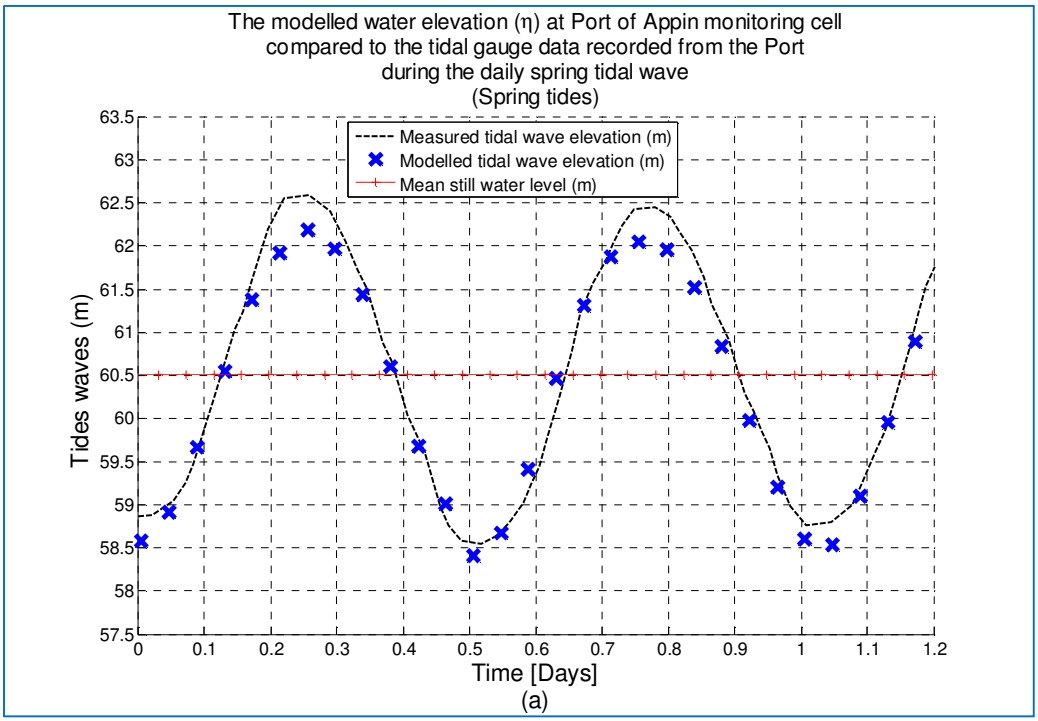

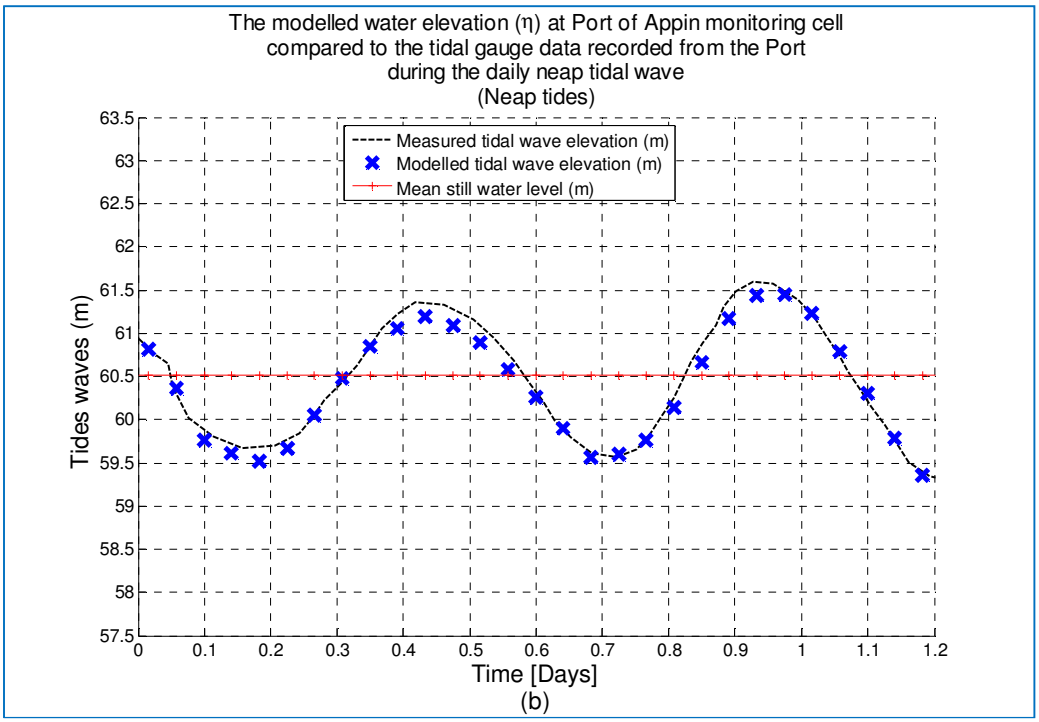

Figure 5.18.a, b The numerical monitoring cell at the Port of Appin shown in Figure 5.12 compared with the tides observation taken from Hydrographic Office during a selected daily spring-neap tidal wave cycle.

However, the numerical model results were inspected every three hours during the tidal dynamics simulation by monitoring the Long-section cells as seen above in Figure 5.11 during the tidal wave propagation. In Figure 5.19 the tidal wave is presented as it travels inside the computational domain of the Loch Linnhe region. A relationship exists between the vertical rise and fall of the tides and the horizontal motion of the water created by the tides. This relationship is complicated but it can be related to time and the phase of the motion (NOAA, 2012).

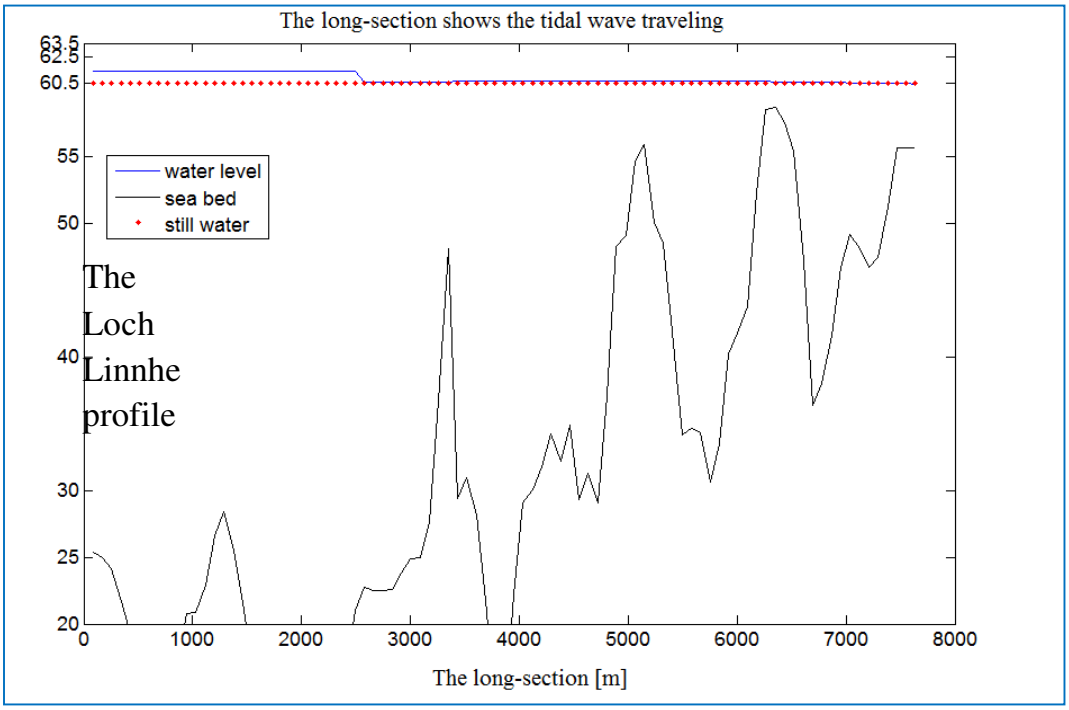

Figure 5.19 The long-section cells checker in the Loch Linnhe seen above during the simulation time which indicates the tidal wave traveling in the Loch Linnhe region.

There is a phase relationship between the times of high/low water tide and the times of the flood/ebb. The correlation of the tides and tidal currents can be classified according to three base case conditions. The Standing tidal wave is considered the first case in which the times of slack water have nearly the same time as the high and low tide conditions, but the maximum flood and ebb currents take place half way through the high and low tides, see Figure 5.20. The Standing tidal wave conditions are familiarly at the head of larger bays and harbours. The second condition is a Progressive tidal wave where the peaks of flood and ebb match the high and low tides as presented in

Figure 5.20. The Progressive tidal wave condition can be seen at the oceanic entrance such as Loch Linnhe region.

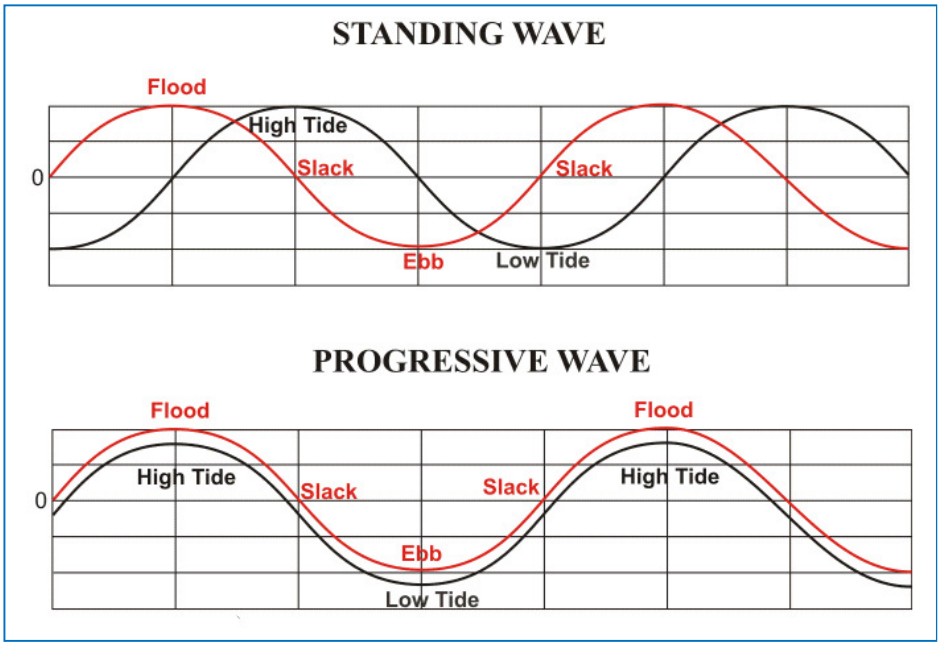

Figure 5.20 The tides and tidal current time relationship conditons (NOAA, 2012).

A rare third case condition is known as a Hydraulic current that is created due to the contrariness in the height of the tides within two sites connected by a water path (NOAA, 2012). The peaks of flood and ebb currents occur as the variations of the tides heights are building up and the differences in the two tides heights are the greatest. This tides condition appears in finite number locations like Chesapeake and Delaware Canal that connects both bays together. The characteristic of tides and tidal currents of the Loch Linnhe are delineated in Figure 5.21. As seen from Figure 5.21 the tidal wave in the Loch Linnhe has similar characteristics to the Progressive tidal wave as expected since it lies in oceanic entrance, a matching pattern of tides peaks and tidal currents is displayed in Figure 5.21.

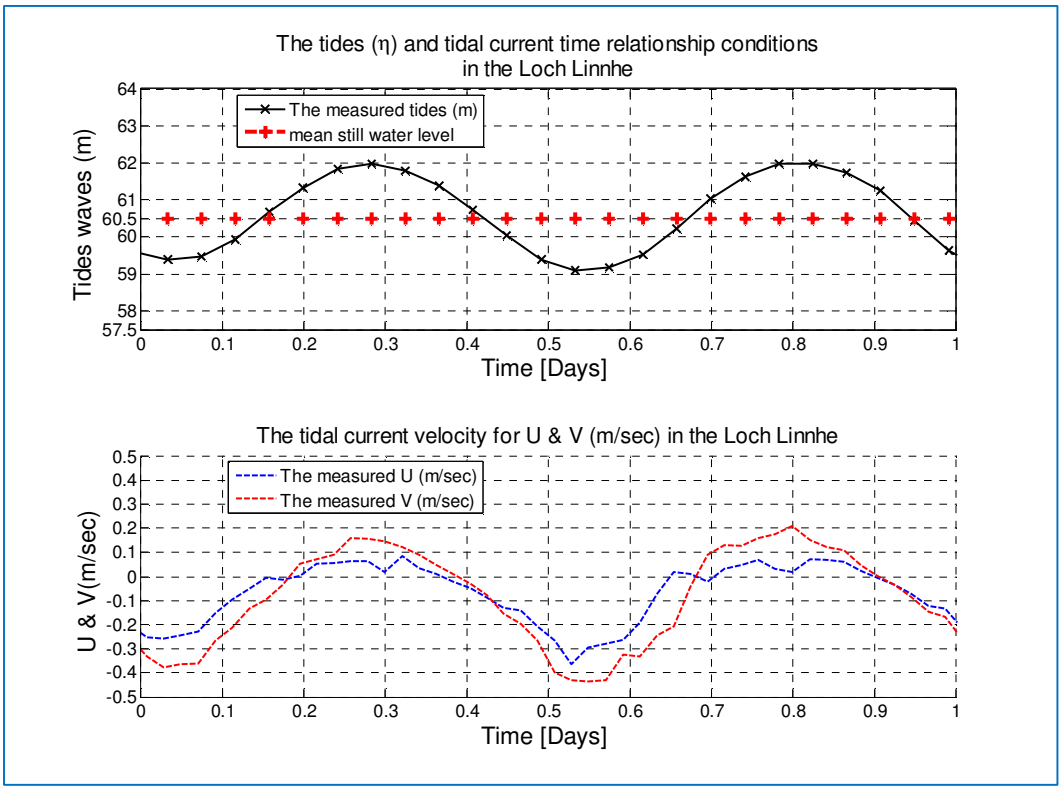

Figure 5.21 The relationship between tides and tidal currents in Loch Linnhe.

Note that, the tides and tidal current is demonstrated in a daily spring tide as recorded by the ADCP instrument at the artificial reef site.

Neverthless, a comprsion between values of the *U* velocity component of the numerical model in the fine grid cell size 43.3 m and the measured ADCP data from the reef site is shown in Figure 5.22.a that demonstrates the differences of the *U* component values during the spring tides for a daily cycle. The tidal current pattern of both values are similar as seen in the Figure 5.22.a, the oscillation in the quantity in the measured ADCP data may occur due to the interaction between short frequency wave with the tidal current. Note that, the measured ADCP data actually is the average of the 48 ADCP bins, it represents the *U* and *V* components of the field measurement tidal current which indicate surface gravity wave can be included.

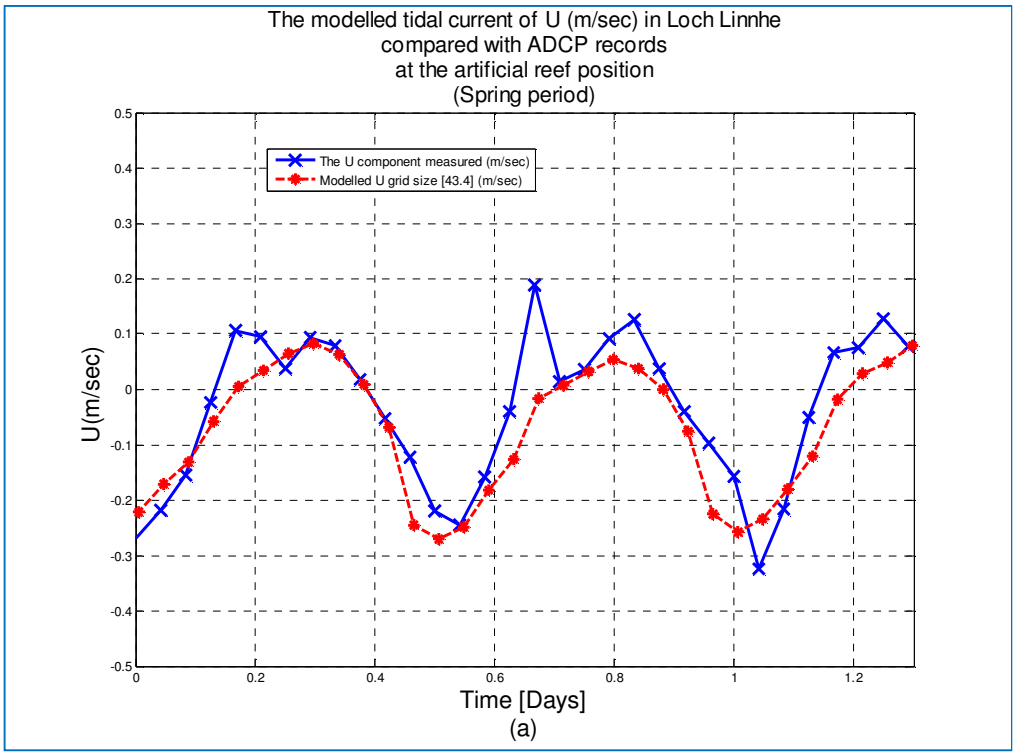

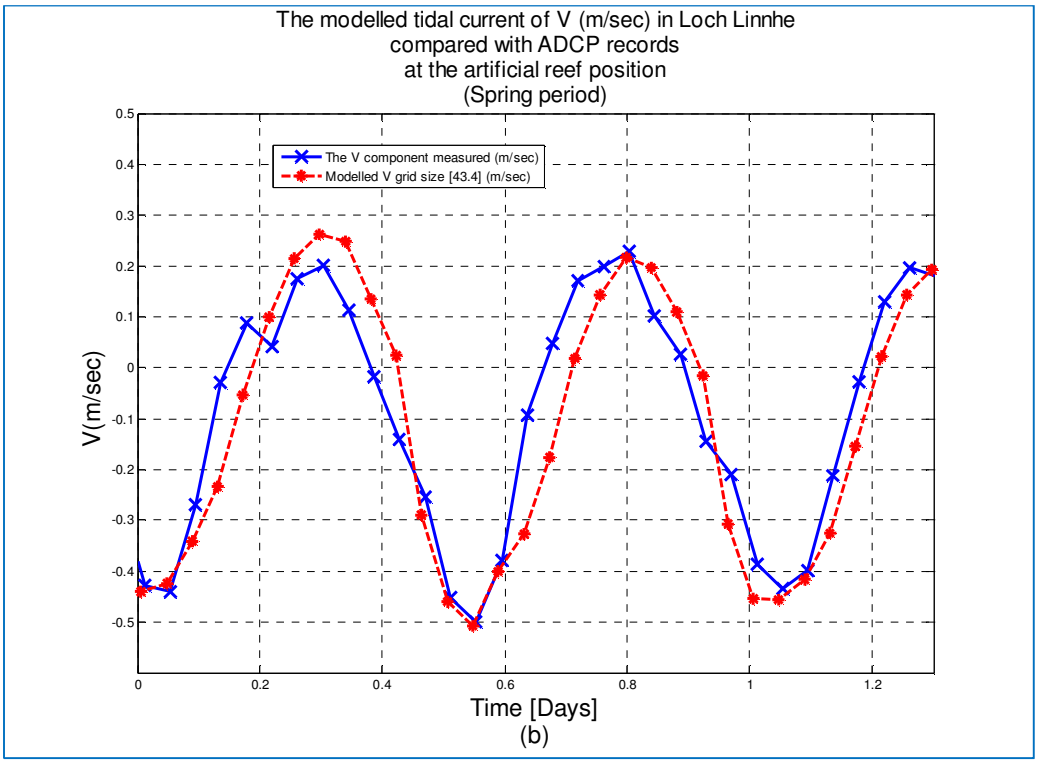

Figure 5.22.a, b The numerical tidal current *U* and *V* components against the ADCP measured *U* and *V* components at the reef location for spring daily period.

The wave and current interaction is a very difficult issue to investigate due to the scale differences both spatially and temporally. It was concluded from previous studies such as Wolf et al. (1988), Janssen (1989) along with Wolf and Prandle (1999) that the surface gravity waves have a significant effect on the tidal current especially for higher wave amplitudes. In addition, the ADCP instrument measure the velocities in the bins of the water column in the z-direction which indicates it can measure the three-dimensional physical features such as stratification condition that may cause internal waves, which in turn can affect the value of mean tidal current. Further details of the internal wave effect on tidal current can be found in Lee et al. (2011) and Tsimplis (2012). The *V* component of the ADCP data was examined with the numerical model conclusion as seen in Figure 5.22.b above. A similarity in the tidal current pattern exists where the quantities of both *V* components are approximately in agreement, but the impact of the surface gravity waves and stratification condition on the measured ADCP data may be seen in the Figure 5.22.b. The lowest astronomical tides cycle was inspected for both numerical and measured *U* component values as spoted in Figure 5.23.a. Moreover, the *V* component of measured data at the artificial reef site was checked against the numerical *V* component outcome as presented in Figure 5.23.b. The previous comparison of the daily neap tidal current values of the *U* and *V* components may indicate the impact of surface gravity waves on both ADCP data measured quantities because of a high wind speed. In fact, the weather station recorded high speed winds during the neap cycle as demonstrated in Figure 5.24. The figure presents the *U* and *V* components of the tidal current in cm/sec against the *U* and *V* components of the mean wind speed in m/sec which implies the relationship between the wind speed and tidal current.

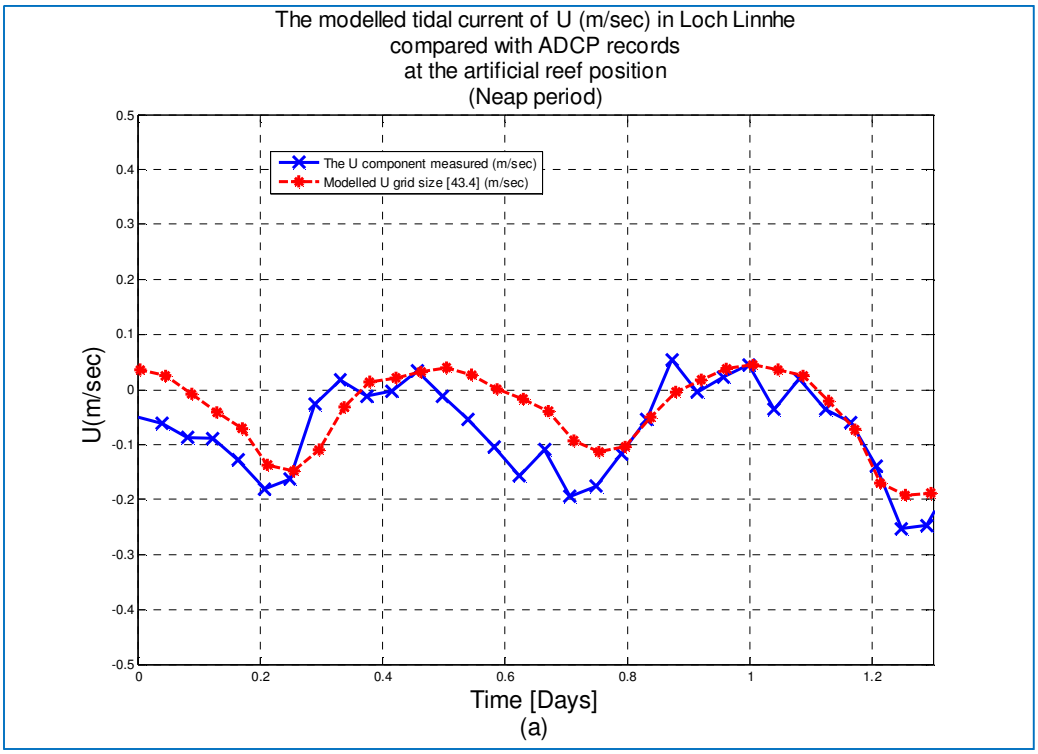

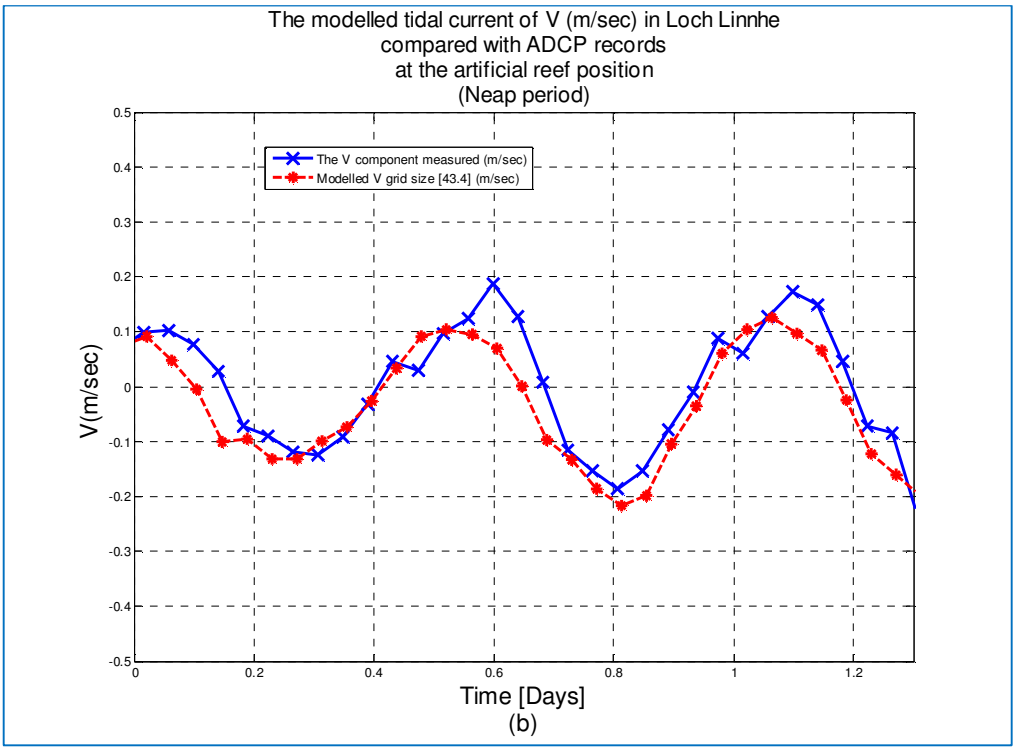

Figure 5.23.a, b The *U* and *V* components for the daily neap tidal current cycle of both the numerical model and the ADCP record in the reef position.

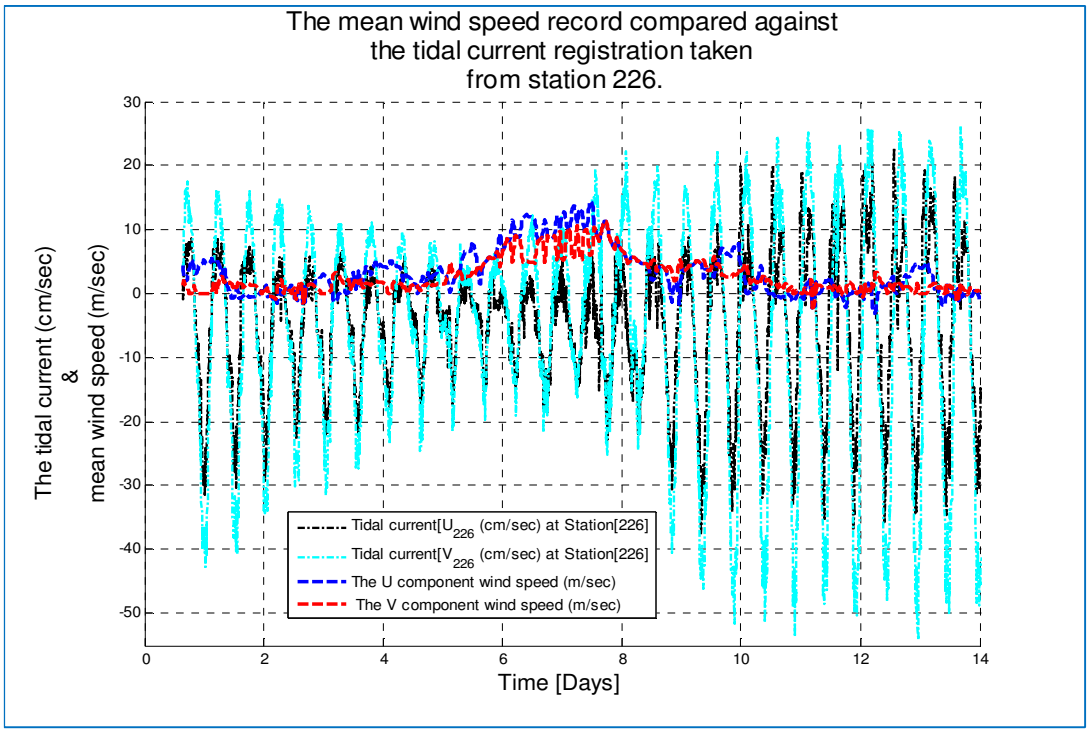

Figure 5.24 The *U* and *V* components of the tidal current record at station 226 near the artificial reef with the mean wind speed data during the filed measurement.

The Loch of Creran entrance was also investigated during the daily spring-neap cycles to compare with the seafarer's navigation information as shown in Figure 5.25.

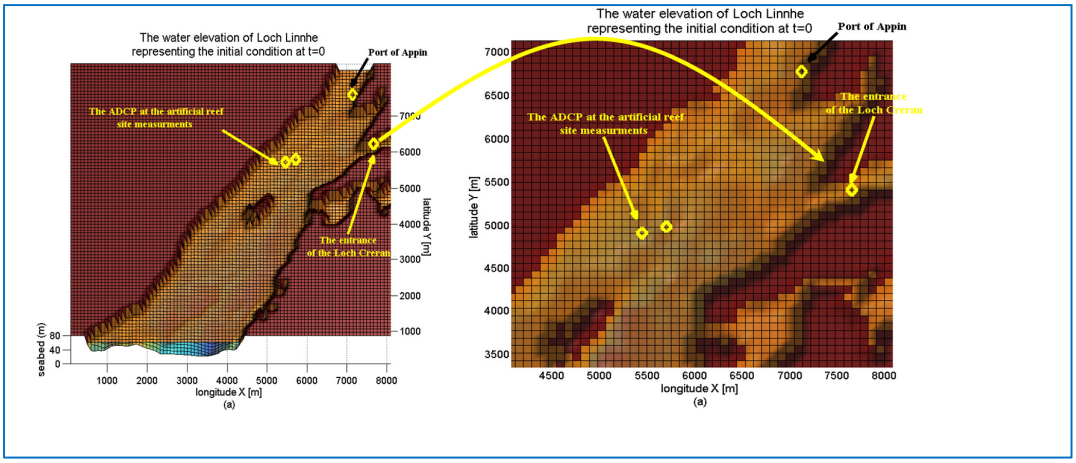

Figure 5.25 The Loch Creran inlet inspection cell and the comparison of the numerical results against the seafarer's navigation information.

The *U* and *V* components that represent the tidal current for the daily spring cycle at the Loch of Creran inlet are demonstrated in Figure 5.26.a.

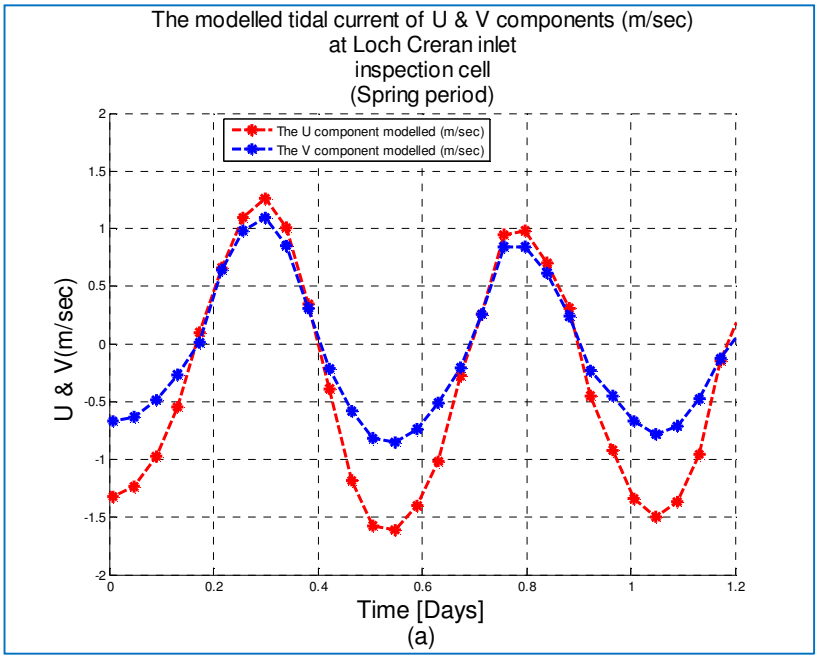

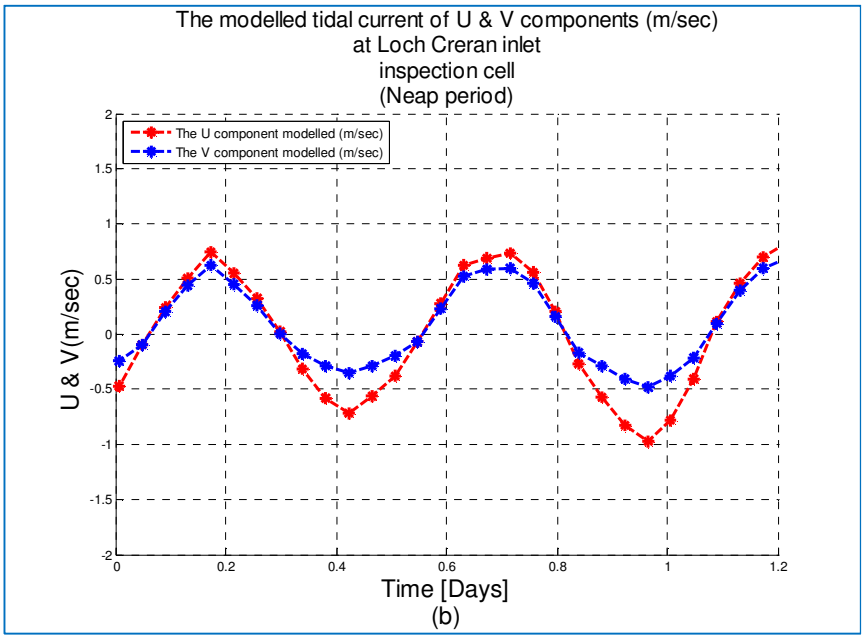

Figure 5.26.a, b The *U* and *V* components of the numerical model at the entrance of Loch Creran for the daily spring-neap tidal current cycles as registered by the monitored cell.

The resultant of both *U* and *V* components daily spring cycle gives a maximum value of 1.96 m/sec (3.809 knots) which is approximately equal to the observed value of 4 knots

in spring tides as seen previously from seafarer's navigation information. The neap tides were verified with the navigation observation for the same monitoring cell and the result is presented in Figure 5.26.b above. The maximum value recorded in the numerical results of the neap tidal current is 1.08 m/sec (2.099 knots). Whereas, the registered value from seafarer's navigation information was 2.75 knots which is near to the numerical result. The Godunov-type Finite Volume numerical method did capture reasonable values of the tidal current at the entrance of Loch Creran which indicate the efficiency and numerical accuracy of the present model.

5.5.3 ***The tidal wave dynamics of the Loch Linnhe during a lunar cycle***

The tidal wave was simulated for a lunar spring-neap cycle with duration of 13 days to study the performance of the Finite Volume Method during long time periods. The tidal wave elevation of these periods is produced as seen in Figure 5.27.a, b. The sequence of the numerical model results was compared with data records from the ADCP measurements at the artificial reef location as shown in Figure 5.27.a. The water elevation of both numerical conclusion and measured ADCP data match together. In addition, the port of Appin tides elevation data was validated against the numerical model results at the port Appin position. Figure 5.27.b indicates a correspondence between the two values that show the present numerical model with tides elevation data at the port of Appin which demonstrate a very good performance for the studied numerical model, the differences are seen in the peaks of tidal waves elevation data, it can be related to the seabed accuracy applied in the numerical simulation since seabed created from admiralty chats, but the result is still very good.

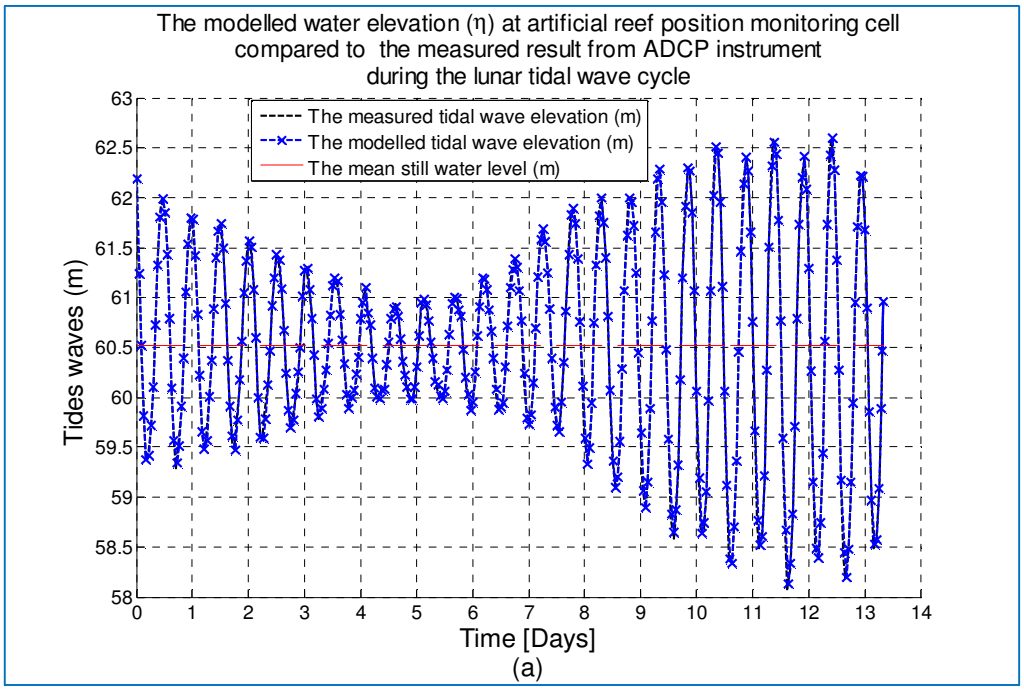

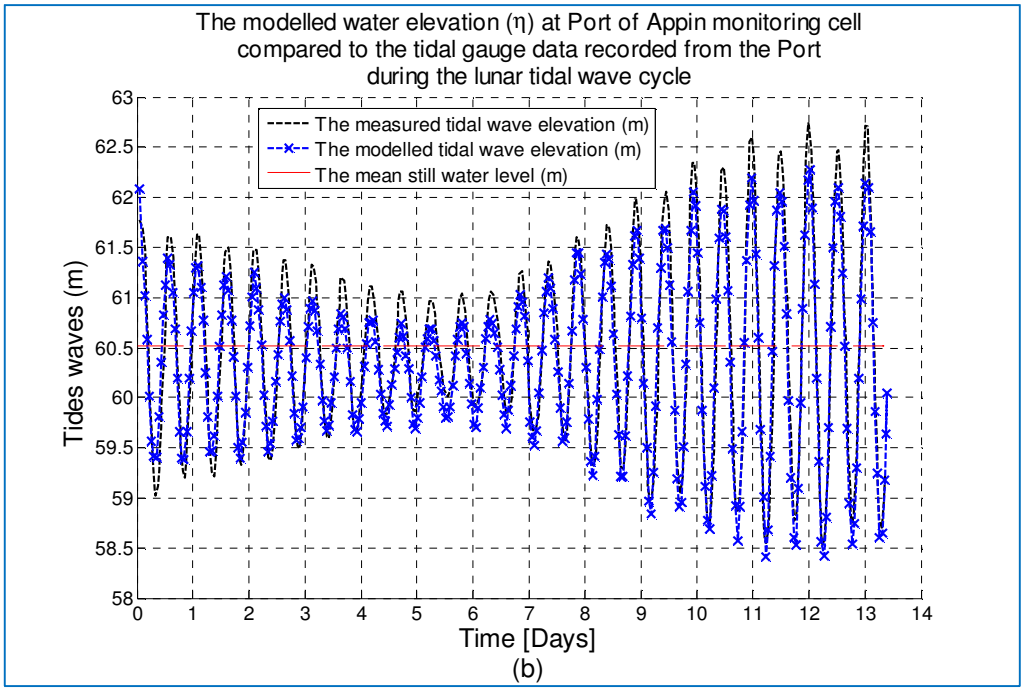

Figure 5.27.a, b The tidal waves for numerical results with ADCP measurements comparison during a period of 13 day's time duration in (a). The tidal wave data was taken from the tides gauge station at port of Appin site against the numerical conclusion in (b).

Nevertheless, these results give confidence in the capability of the numerical model in handling the tidal hydrodynamics over a complex topology such as that exhibited by Loch Linnhe. However, the tidal wave current *U* and *V* components were compared with the measurements of the ADCP instruments. The measured values of the velocity components is exposed in Figure 5.28.a, b, it was taken from the averaging of the ADCP 48 bins data, as defined in the ADCP measurement chapter four. The results for the *U* velocity component from the numerical Finite Volume Method model were plotted opposed to the ADCP data record in Figure 5.28.a. The *U* component phase agreement between the numerical results and the ADCP records are clearly shown in Figure 5.28.a. The magnitude of the *U* component of the computed velocity displayed in magenta colour agrees well with the measured component in the black colour. Indeed, it is almost match each other. The small differences between both quantities that found in ADCP measured data, it can be related to the effect of surface gravity wave since the variation occur in the short frequency period. On the other hand, the phase between the computed results presented in red colour and measured *V* component seen in the black colour is identical whereas the magnitude of the *V* components are very well agreed with small differences due to seabed accuracy and surface gravity wave impact. In the numerical model it is critical to control the outflow boundary at the entrance of the Loch Creran on the East coast of the computational domain by applying the tidal wave constituent's solution for Pier of Barcaldine. In addition, the impact of wind stress on the sea surface plays a role in the numerical model solution. In Figure 5.28.a, b the green colour line on both *U* and *V* component indicates the tidal current numerical results without controlling the outflow east boundary by tidal wave constituent's solution for Pier of Barcaldine and neglecting the wind stress. Whereas, the magenta colour for *U* component and red colour for the *V* component in the numerical solution that agree more accurately with ADCP measured data, it shows the important role of both parameters in the numerical solution.

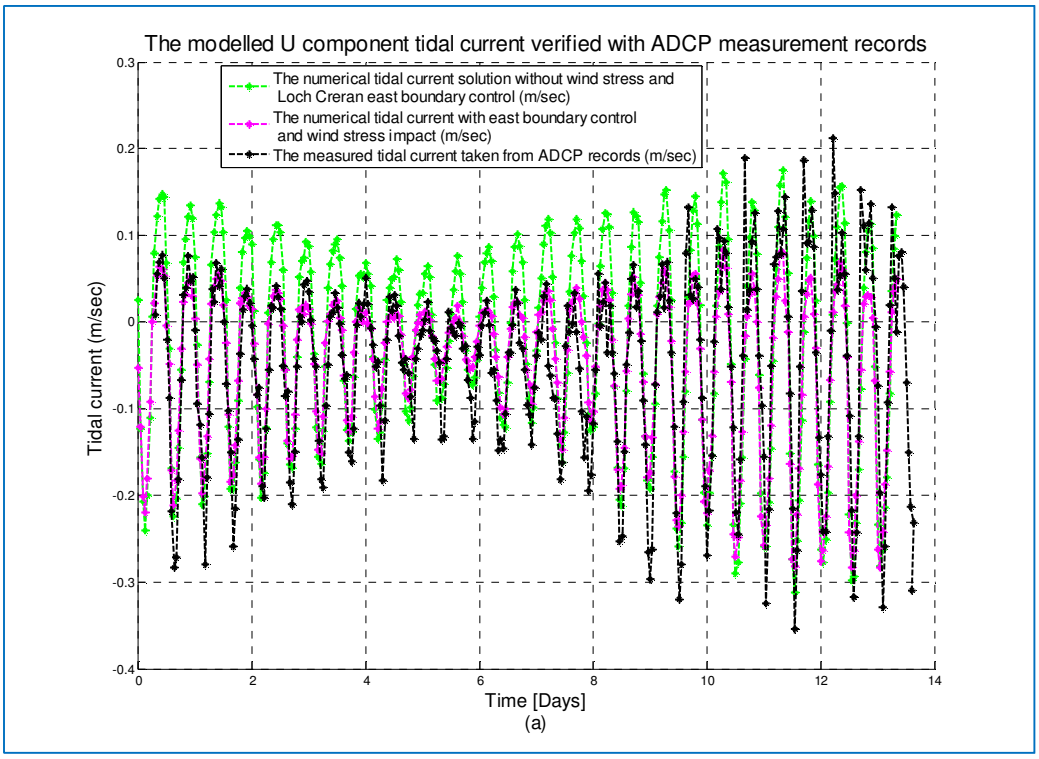

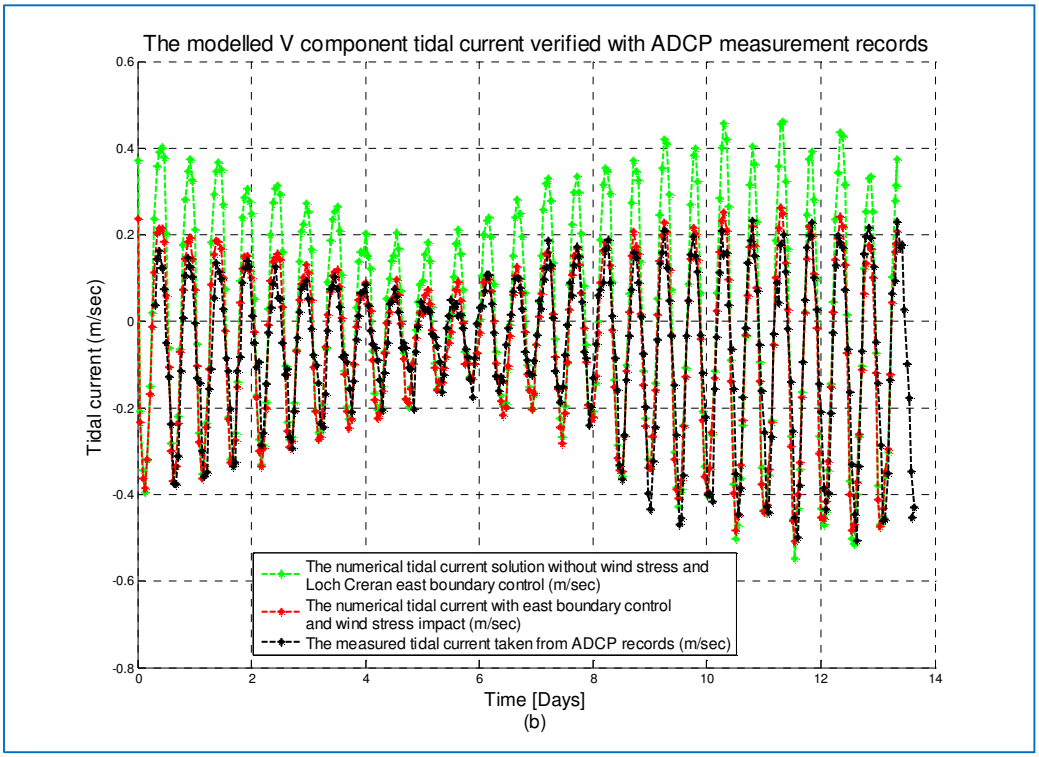

Figure 5.28.a, b The comparison of *U* and *V* tidal current components between the numerical calculation results and ADCP measured data quantification.

The tidal velocity vectors over the whole solution numerical domain presented on the finer grid cell size 43.3 m as the incoming tide propagates through Loch Linnhe are presented in Figure 5.29. The velocity vectors near the outlet rise due to the narrow cross section of the outlet and shallow topology as seen from Figure 5.30 that present the complexity of the Loch Linnhe seabed. The reverse tidal wave cycle is demonstrated in Figure 5.31 which is representing the velocity vectors in the reverse mode with high speed in the narrow region and low speed in the wider region. The flow is consistent with complicated Loch topology which leads to acceleration in regions where the water depth decreases or the channel narrows. The measurements are focused on the reefs site and there are no detailed measurements of the tidal flow away from it. The numerical model behaves as would be expected as presented from previous results.

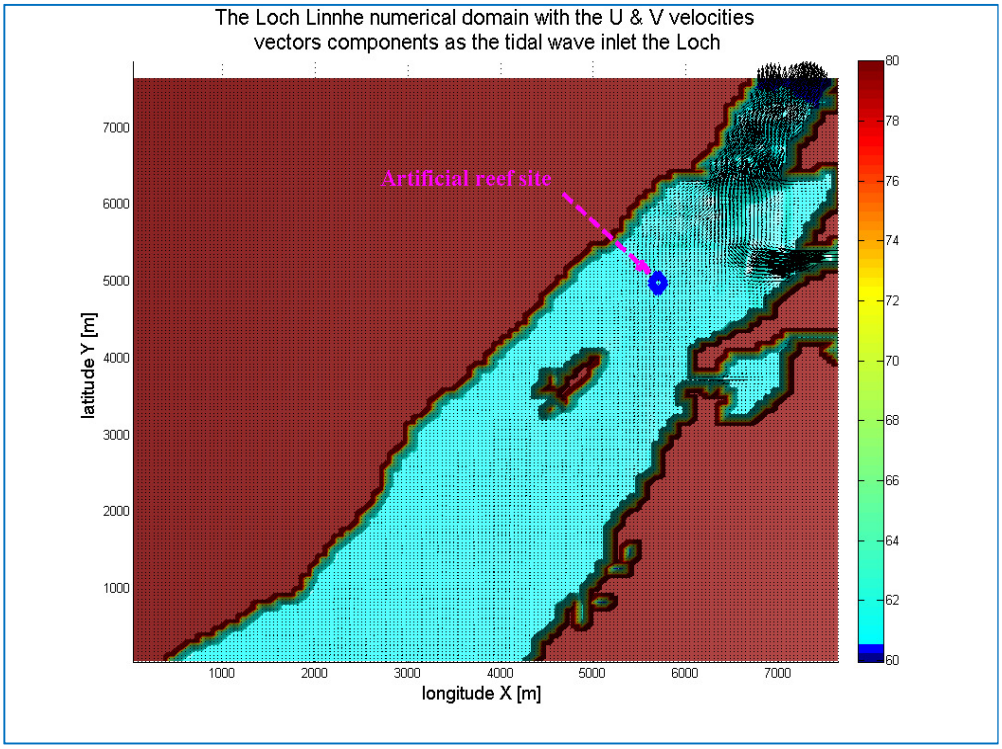

Figure 5.29 The velocity vector of a positive tidal wave propagating in the Loch Linnhe. The position of the artificial reef is represented by the diamond marker.

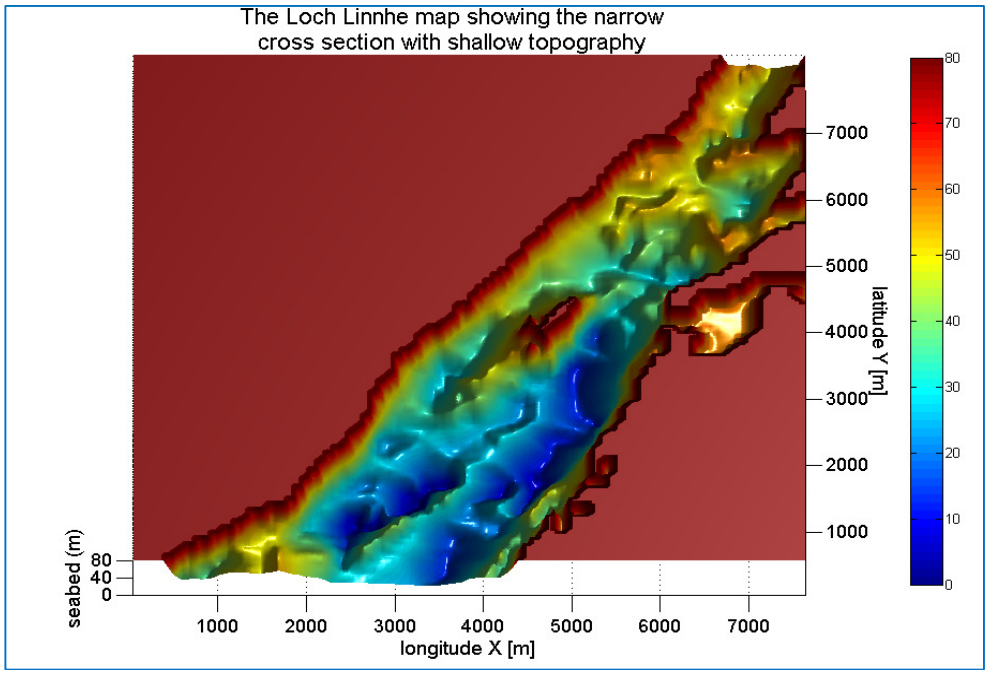

Figure 5.30 The Loch Linnhe complex topology with the indication of the narrow outlet that has shallower seabed compared with other region in the Loch.

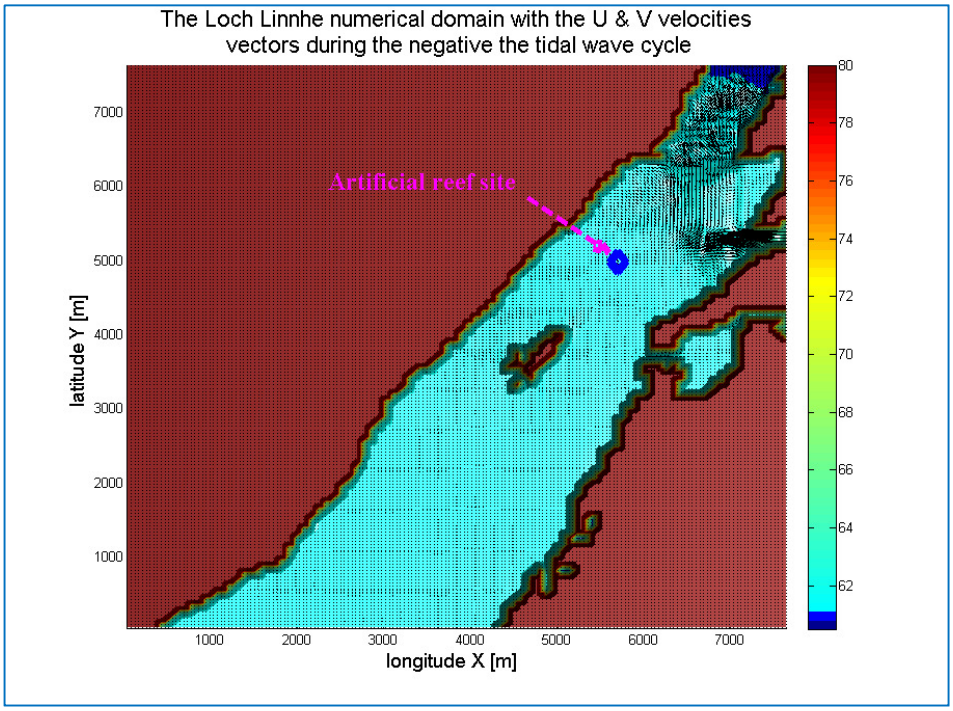

Figure 5.31 The velocity vectors of a tidal wave in the negative cycle with a marker for the reef site.

In conclusions, The Godunov-type shallow water flow model has been implemented to simulate tidal flow hydrodynamics in the Cook Straits, New Zealand as presented in chapter three, for validation of the model before applying it to the unknown case of Loch Linnhe, off the West Coast of Scotland. The numerical results from both tidal dynamics simulations were compared with measurements. In general, a good agreement between the predicted and measured values (where available) was obtained. These results demonstrate a good performance of the numerical model when it is applied for tidal dynamics simulation. A relatively small disparity in the magnitudes of the numerical and measured velocities is found in some instances and the reasons for this are complex. It may be simply due to the use of the shallow water equations for a complicated three-dimensional domain. The measurements from ADCP may have been reflecting the influence of local features (e.g. the reefs themselves. 140 m away) on the global flow. The results of the 2D shallow water simulation have been published in the ISOPE (International Offshore and Polar Engineering Conference) Conference Proceedings for 2012, see appendix C.

In the next chapter a 3D model will be implemented for investigating the details of the local flow about the reef, and this will be followed by matching the local 3D flow to the global 2D flow by using output from the shallow water equation analysis as input to the 3D numerical model.

Chapter 6. The three-dimensional artificial reef flow modelling

6. Introduction

Attention has recently focused on artificial reefs due to the decline of marine fishery resources. The development of artificial reefs has increased rapidly around the world, particularly in countries such as Japan and the USA, but, there are still many unresolved problems regarding the hydrodynamics of artificial reefs from the design point of view. In addition, the artificial reef stability and structural integrity, which are important issues from an engineering perspective, are concerned with the prevention of reef failure under current conditions causing excessive drag on the reef structure or sediment erosion on the seabed at its base. For these reasons calculating and analysing the hydrodynamic capabilities of an artificial reef under ocean field conditions is a very important resource to have available. Researchers to date have largely adopted an experimental approach to studying the reef fluid dynamics phenomenon. For example, Liu et al. (2009) have conducted wind tunnel experiments on artificial reef elements represented by different shapes, including pyramids, triangular prisms and cubes, for comparison with a modelled flow field obtained by a numerical simulation method. Other experimental methods, such as particle image velocimetry (PIV), have been adopted by Su et al. (2007) to investigate the flow patterns within and surrounding an artificial reef, which have also been compared with the results from numerical simulation.

However, the study of artificial reef flow patterns by conducting experiments in the laboratory or making in-situ observations have been time consuming and expensive. In principle, numerical modelling can obtain detailed flow patterns around artificial reefs without having to recourse too expensive and time consuming experiments. An understanding of the hydrodynamic capabilities of an artificial reef can be gained using computational fluid dynamics software such as FLUENT 12.0. This proprietary code has been employed in the present study for a three-dimensional numerical simulation of the detailed flow around an artificial reef using built-in unstructured tetrahedral grids to solve the three-dimensional incompressible Reynolds Averaged Navier-Stokes equations over the numerical domain. The k-ε renormalization group (RNG) was implemented in a Navier-Stokes solver to investigate the turbulent flow pattern around the selected reef. A number of case studies have been undertaken using the code including a comparison between a case with the initial conditions based on output from

the two-dimensional code described in previous chapter five, and a case with the initial conditions taken from experimental measurements of the flow profiles.

6.1 The k-ε turbulence model

The two-equations k - ε model has been applied in many practical engineering turbulent flow modelling problems due to its accuracy and reliability in a wide class of flows. An enhancement to the k - ε turbulence model was developed to give an improved version known as the renormalization group (RNG) k - ε model. The RNG based on the k - ε turbulence model has been developed for significant improvements in the accuracy for rapidly strained flow, and enhanced accuracy for the effect of swirling flows on turbulence. The RNG model gives improved flow prediction at low Reynolds number near wall flows due the analytically-derived differential formula for effective viscosity adopted (ANSYS FLUENT 12.0, 2009). The RNG k - ε model transport equations can be written in many ways but if it is assumed that the flow is fully turbulent and the effect of molecular viscosity is neglected the RNG transport equations can be simply represented as follows:

For k equation:

$$\frac{\partial}{\partial t}(\rho k) + \frac{\partial}{\partial x_i}(\rho k \bar{u}_i) = \frac{\partial}{\partial x_j}(\alpha_k \mu_{eff} \frac{\partial k}{\partial x_j}) + G_k - \rho\varepsilon \qquad (6.1)$$

For ε equation:

$$\frac{\partial}{\partial t}(\rho\varepsilon) + \frac{\partial}{\partial x_i}(\rho\varepsilon \bar{u}_i) = \frac{\partial}{\partial x_j}(\alpha_\varepsilon \mu_{eff} \frac{\partial \varepsilon}{\partial x_j}) + C_{1\varepsilon}\frac{\varepsilon}{k}G_k - C_{2\varepsilon}\rho\frac{\varepsilon^2}{k} - R_\varepsilon \qquad (6.2)$$

In these equations G_k terms represent the generation of turbulent kinetic energy due to the gradient of the mean velocity: the α_k and α_ε quantities represent the inverse effective Prandtl numbers for k and ε respectively; the $C_{1\varepsilon}$, $C_{2\varepsilon}$ terms are constant given values of 1.42 and 1.68 respectively. The term μ_{eff} is the turbulent (or eddy) viscosity that can be computed from the kinetic energy k and dispassion rate ε as follows:

$$\mu_{eff} = \rho C_{\mu} \frac{k^2}{\varepsilon}) \qquad (6.3)$$

Here C_{μ} is a constant given value of 0.09 and there is an additional term, R_{ε} ,which is the major difference between the standard k-ε and the RNG k-ε models. This term improves the accuracy for high strain rate and large degree high turbulent flows, and it is given by the formula:

$$R_{\varepsilon} = \frac{C_{\mu}\rho\theta^3(1-\theta/\theta_0)}{1+\beta\theta^3}\frac{\varepsilon^2}{k} \qquad (6.4)$$

Where, $\theta = St\, k/\varepsilon$ and $St = (2St_{ij}St_{ij})^{1/2}$ with the turbulent viscosity computed as in the standard k-ε model with $\theta_0 = 4.38$ *and* $\beta = 0.012$. A complete mathematical background to turbulence modelling is beyond the scope of this thesis but more comprehensive description of RNG theory and its application to turbulence modelling can be seen in Orszag et al. (1993). In the present study, the water is assumed to have a constant density and temperature, and the usual assumptions of an incompressible, viscous and Newtonian fluid with isothermal flows and no heat exchange have been adopted.

6.2 Test case of a Backward Facing Step

In order to gain experience with the FLUENT with the renormalization group (RNG) k -ε model and confidence in its capabilities with respect to modelling separated recirculating flows, the challenging case of flow past a backward-facing step was computed. This flow is a good example of the flow separation of a boundary layer which is followed downstream by reattachment of the separated layer. The effect of Reynolds number on the separation and attachment points as briefly explained in appendix (D) which gives more details of these test cases. The test cases were run for two different Reynolds numbers, Re= 5100 and Re=44,000 as given in appendix (D). The numerical domain is seen in Figure 6.1.a. The numerical results at a Re of 5100 was compared with the experimental results presented by Jovic and Driver (1994), who found that the reattachment length (L_r) varied between 6.0H and 6.1H where H is the step height. The stream-wise velocity contours of the Re=5100 is displayed in Figure 6.1.b. The computational results are displayed with the experimental results in

Figure 6.2.a, b, c, d that indicates good agreement of the stream-wise velocities with (a) x/H=4 and (b) x/H=6 with slightly less good agreement for (c) x/H=10 and (d) x/H=19. The major characteristic of the flow is the recirculation zone that forms at the back of the step, as seen in Figure 6.1.b. This is a challenging flow to compute and is often used as a classic example for validating numerical models. Other tests have been considered as presented in Appendix (D).

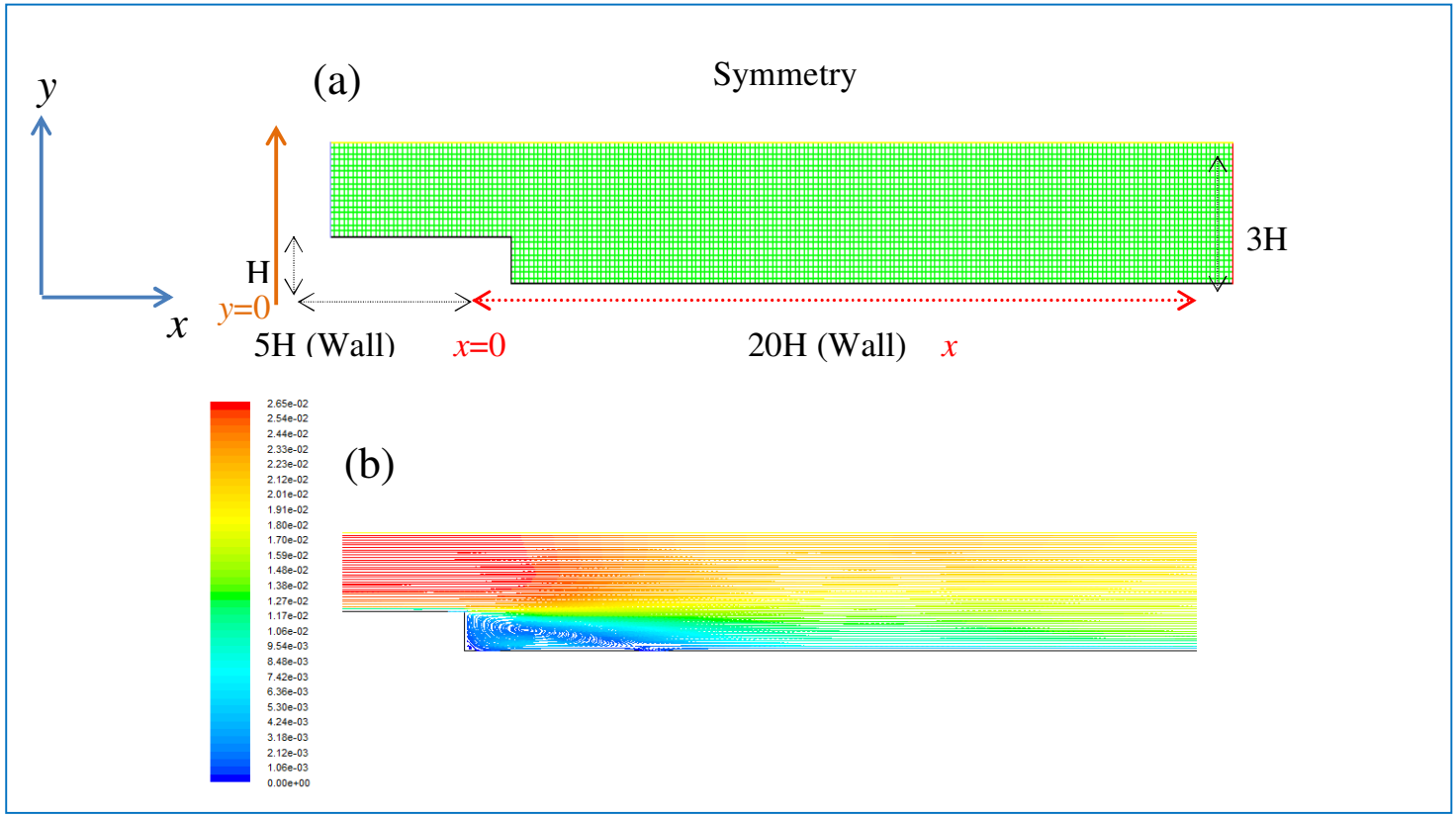

Figure 6.1.a, b The numerical domain of the test case for Re=5100 is exhibited in (a) and the stream-wise velocity contour is spotted in (b).

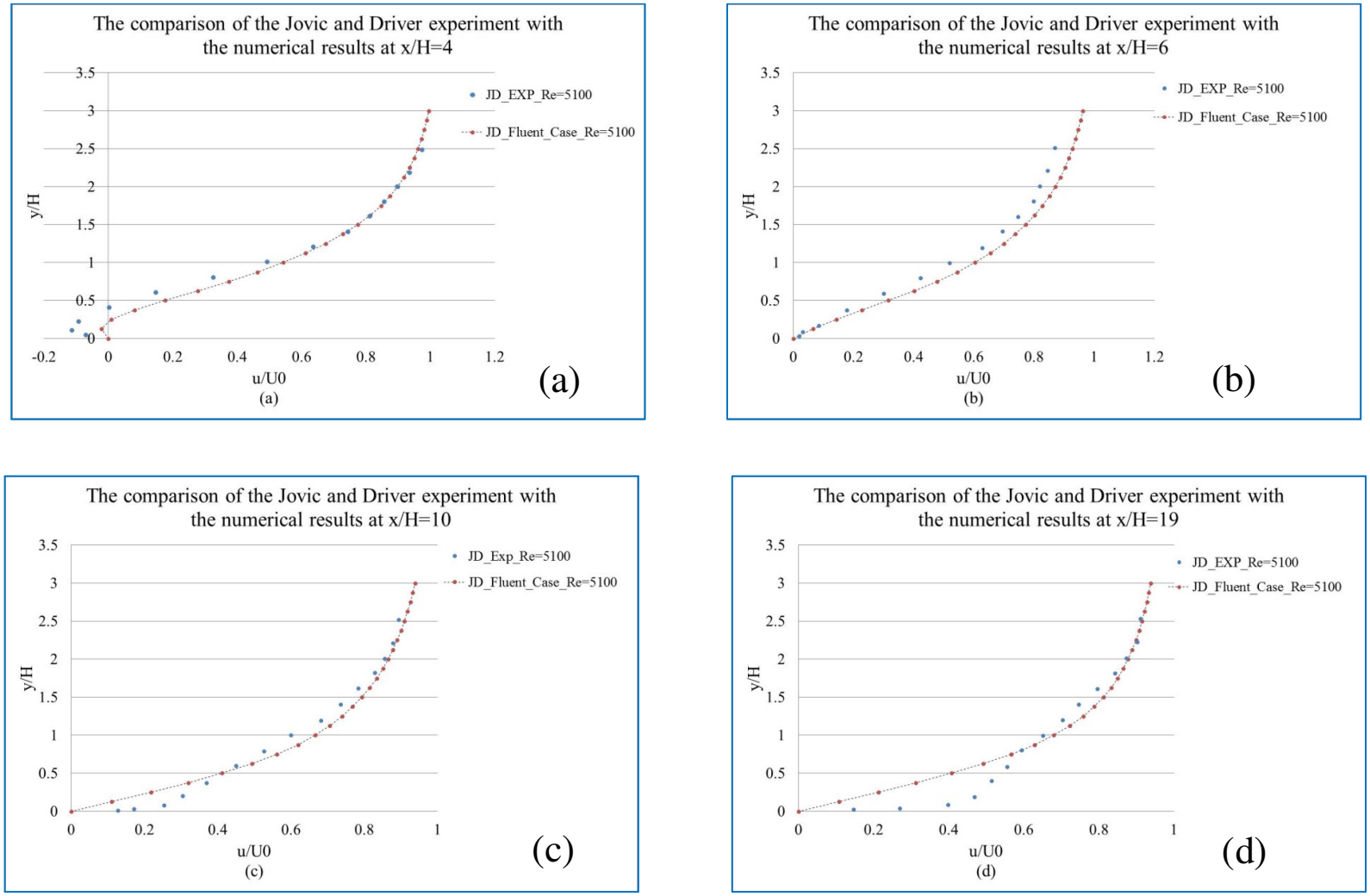

Figure 6.2.a, b, c, d The comparison of the stream-wise velocity at Re=5100 at (a) x/H=4, (b) x/H=6, (c) x/H=10 and (d) x/H=19.

6.3 The artificial reef with initial conditions of the tidal velocity flow profile

The spring tidal cycle represented in Chapter four was selected due to the high speed of the tidal current compared with a neap cycle. The spring tidal current profile chosen has a high tidal current strength as shown in Figure 6.3. However, it difficult to explain the vertical structure of the tidal current since the upper layer is affected by surface boundary layer process such as stratification. The stratified condition can create internal waves which cause interfacial disturbance along with a vertical shear of the tidal current. In fact, these conditions have been detected in the M_2 tidal current Yellow Sea as discussed by Lee et al. (2011). In addition, the vertical structure of tidal current was observed to be parabolic in Guaymas Bay (Mexico) due to these surface boundary layer processes (Gómez-Valdés et al., 2012). The tidal current velocity profile was adopted to be set as a tidal current flow study case. The tidal velocity profile was set as an initial condition at the inlet face to investigate the tidal current flow pattern surrounding the artificial reef over a period of one hour on the grounds that the flow varies relatively slowly over the tidal cycle.

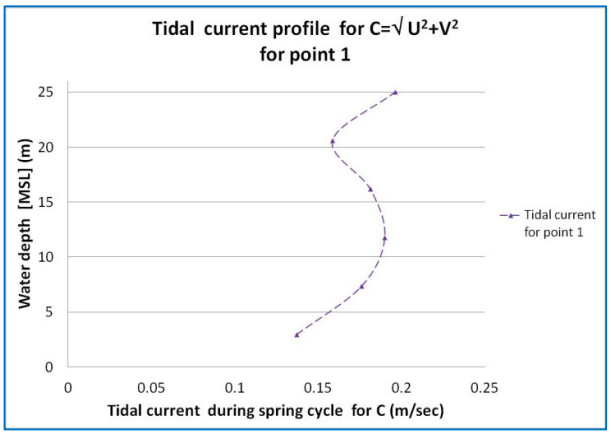

Figure 6.3 The chosen velocity profile for reef hydrodynamics investigation. The point one refer to selected hour time as described in previous chapter four.

6.3.1 *The numerical method and model configuration*

The numerical method adopted for the calculations is embedded in the FLUENT software which discretises the 3D- incompressible Navier-Stokers equations. The software implements a pressure-based solver in a first order implicit unsteady formulation. The gradients are estimated by the Least Squares cell based method. The SIMPLE scheme algorithm was applied to solve the pressure and velocity coupling in

each time step. The discrete formats of the momentum, turbulent kinetic energy and turbulent dissipation rate were formulated in a second order upwind scheme. The solution convergence is controlled by the residuals. The residuals summarize the differences between the current and past states of the numerical solution which is done every time the solver iterate. Therefore, residuals indicate the degree to which the numerical solver is satisfied. Further details information of the residuals calculation for the conservation equation is found in theory guide in ANSYS-FLUENT 12.0 (April 2009). In the present work the convergence was obtained if all residuals fell below 10^{-3} every time step as suggested by theory guide manual. The numerical domain adopted for the modelling is generated in tetrahedral unstructured cells due to the irregularity of the object required for simulation. The numerical domain grid size is 3,605,318 tetrahedral cells applied in the present work since, the actual reef is composed of a mound of concrete blocks dropped randomly onto the sea bed. The roughness applied in the calculation is based on results presented by Rose (2005) as will be demonstrated. The numerical domain and boundaries are defined as specified in Figure 6.4.a as inflow (velocity-inlet), outflow (pressure-outlet), symmetry (top and both sides) and two wall boundaries on the seafloor. The height of the domain was set to the still water depth as seen from figure. The walls were set with no-slip boundary conditions. As discussed in a previous chapter two the artificial reef itself was made from concrete blocks and has been individually set as a wall. In fact, the density of the concrete blocks making up the reef is high due to the randomly deployment, and it was considered that a solid structure would give a good approximation of the fluid/structure interaction. The wall roughness required for the computation was estimated from the roughness height of the artificial reef. The artificial reef structure complexity was studied by Rose (2005) and the roughness height has been adopted from data presented in his PhD thesis and shown in Figure 6.4.b, having a relative roughness, k_r /D, of 0.0190 where k_r is the roughness height and D is a reef length scale taken as the diameter of the base of the reef. The tidal current velocity profile of the inflow was set by applying a UDF (User Define function) formulated in a subroutine written in C code (see the ANSYS-FLUENT 12.0) and based on the measured values for the velocity. The outflow was set as a pressure-outlet that is allowed to change as the hydrodynamics pressure at all the boundaries is calculated from known values inside the computational domain.

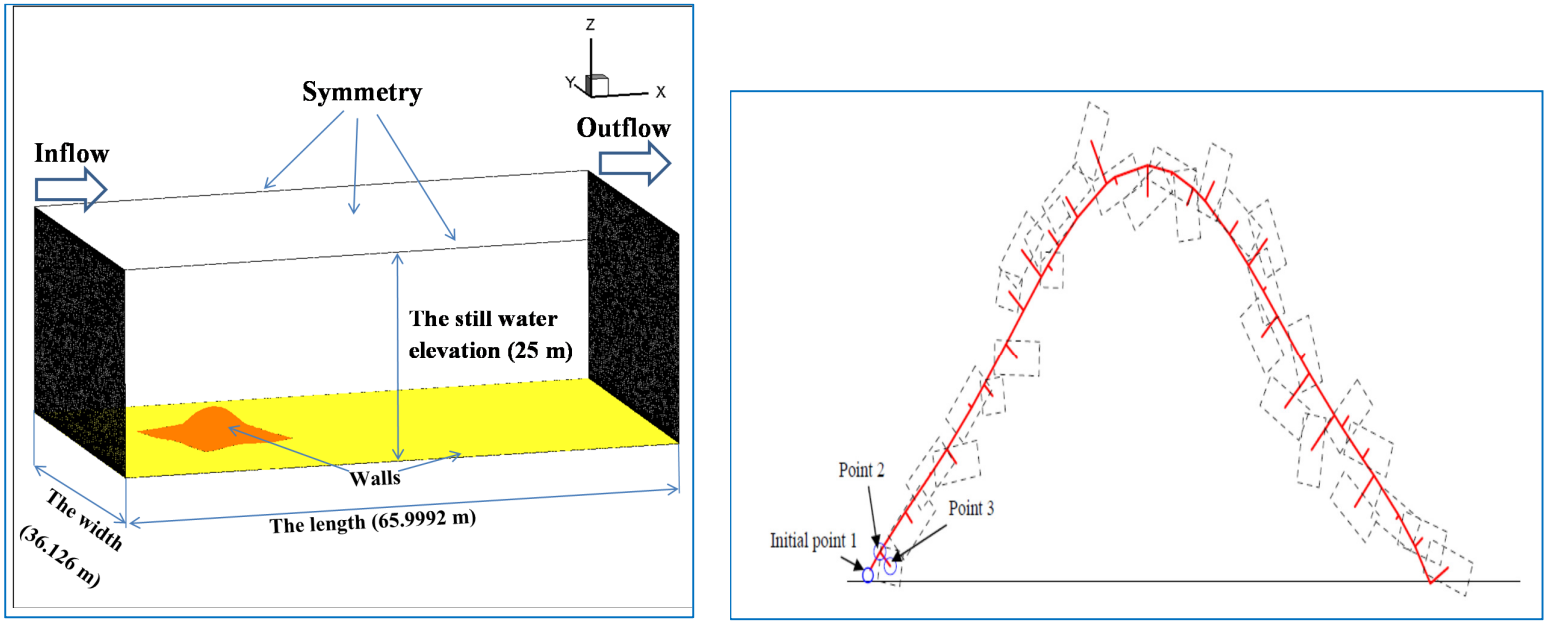

(a) (b)

Figure 6.4.a, b The numerical domain adopted in the numerical simulation with indication of the boundary condition applied during the simulation (a), whereas, (b) shows the wall roughness complexity in the randomly deployment of concrete blocks that creates the artificial reef as discussed in Rose (2005).

6.3.2 *The results of the tidal current flow profile*

The tidal flow cycle was considered to be relatively slowly varying and well represented by dividing it up into a series of twelve different steady flows of one hour duration as described in chapter four. This assumption was subsequently tested by computing an actual unsteady flow over the same time duration. The execution time of each of the numerical simulations of the flow patterns surrounding the artificial reef was therefore set to correspond to one-hour of flow time. The results of the computational domain were output every 100 s of the flow time with a total duration of 3600 s. In this chapter, selective results will be displayed every 600 s in a time frame beginning from 145 s after tidal current profile entered the computational domain and ending after the flow has propagated around the artificial reef over a time simulation of 3600 s. The results are presented as sections of the Y-Z plane, the X-Z plane and the X-Y plane through the artificial reef, together with the seafloor as will be seen in all of the figures.

The tidal current velocity profile at the inlet with the artificial reef is shown in Figure 6.7.a. The first time of 145 s frame contour of the tidal current velocity in the *x*-direction with the turbulent kinetic energy in the Y-Z plane is shown in Figure 6.8.a & 6.8.c, X-Z plane viewed in Figure 6.9.a & 6.9.c and X-Y plane displayed in Figure 6.10.a & 6.10.c. The results show the early stage of the interaction of the artificial reef with the tidal current profiles and turbulent kinetic energy production which is low as the figures indicates. Finally, the seabed characteristic regarding the tidal velocity and kinetic energy production is presented in Figure 6.11.a & 6.11.c).

The middle time flow frame at 1345 s will be demonstrated in a similar format as in the previous time step. Figure 6.12.a & 6.12.c represent the Y-Z plane section of the tidal current at the same distance of 20 m from the inlet as presented for the previous time step. The X-Z plane is spotted in Figure 6.13.a & 6.13.c which indicates the changes in the velocity profile as well as the kinetic energy production. Figure 6.14.a &6.14.c presents the tidal current profile and the kinetic energy of turbulence in X-Y plane. In general, the tidal current profile has interacted with the artificial reef and created a turbulent region with an increased turbulent kinetic energy seen clearly in the X-Z plane and the X-Y plane. The seabed velocity and turbulent kinetic energy have been computed because of their possible effect on sediment transport problems, and are demonstrated in Figure 6.15.a & 6.15.c.

Finally, the results for the flow at 3600 s are presented in the same format as before in Figure 6.16.a & 6.16.c for the Y-Z plane, Figure 6.17.a & 6.17.c for the X-Z plane and Figure 6.18.a & 6.18.c for the X-Y plane. The impact of the tidal current on the seafloor can be assessed by considering the velocity effect in the *x*-direction and the turbulent kinetic energy as displayed in Figure 6.19.a & 6.19.c. In summary, the flow is separating from the artificial reef and creating a recirculating flow, or vortex, on its downstream face leading to an increase in the turbulent kinetic energy during the tidal current propagation as realized from Figure 6.20.a & 6.20.c that exhibit the a recirculating flow caused by the artificial reef.

However, the nature of the sediment transport on the marine organism that live on the artificial reef is a key factor for reef life productivity (Bacchiocchi and Airoldi, 2003) and it is determined by the wall shear stress and skin friction coefficients in the near vicinity. The wall shear stress and the skin friction coefficient are calculated from the formulas:

$$\tau_w = \mu\left(\frac{\partial u}{\partial y_D}\right)_{y_D=0} \tag{6.5}$$

$$C_{SKf} = \frac{\tau_w}{\frac{1}{2}\rho U_\infty^2} \tag{6.6}$$

The wall shear stress (τ_w) is estimated by equation (6.5), note that y_D here represents the water depth, u is the free stream velocity and μ is the dynamics viscosity. The skin friction coefficient (C_{SKf}) is calculated from equation (6.6). In here, ρ is the water density, τ_w is the wall shear stress and the free stream velocity U_∞. The results of the wall shear stress and the skin friction coefficient is given in Figure 6.21.a and Figure 6.22.a. The seafloor wall cells estimation is seen in black whereas the artificial reef wall cells are shown in the red colour. The shear stress has a maximum value of 0.35 Pascal on the reef at its peak as illustrated in Figure 6.21.a. The skin friction arises from the interaction between the fluid and the surface of the artificial reef body which gives peak values of the skin friction coefficient of 0.0225. These higher numbers of the shear stress and the skin friction coefficient on the artificial reef (as opposed to the sea bed) can be seen as red dots in both of Figure 6.21.a & 6.22.a. Note that in the present research, the aim is to indicate the magnitude of the shear stress and the sediment erosion is not focused on this study.

Another parameter has been investigated is the drag coefficient, which is a measure of the resistance of an object in a fluid flow field. Since, the Loch Linnhe reef was constructed from concrete blocks, the drag coefficient plays an important role in calculations relating to its structure stability. The drag coefficient rises at early stage of time simulation and decreases to almost a fixed value about 0.027 as shown in Figure 6.23.a and which is characteristic of impulsively started flows.

6.4 A comparison between flows based on numerically and empirically derived starting conditions

One of the objectives of this study was to assess the viability of computing realistic three-dimensional flows about a reef, taking the output of a two-dimensional global model of the wider region as a starting point. To investigate this, a logarithmic velocity profile was developed from the mean velocity output from the shallow water equation solver in the vicinity of the reef. The velocity profile so derived was then used to formulate the initial conditions (input velocities) for the three-dimensional analysis. The results obtained were compared with the output from the three-dimensional software using experimental measurements of the velocity profile to define the initial conditions. If the method is viable, it follows that the two sets of results should be similar.

A selected average tidal current gained from the two-dimensional simulation described in Chapter five was simulated and compared with the modelled field measurement tidal current profile adopted in the previous section. The chosen average tidal current of 0.2284 m/sec calculated from the adopted tidal numerical model was transformed to a logarithmic profile as schemed by Figure 6.5 according to the formula (6.7) and on the basis that the integral of the mean velocity through the water column is equal to the integral of the measured velocity profile over the same limits. The logarithmic velocity profile derived from the average tidal current profile with the following equation (6.7) can be seen in Figure 6.6.

$$\frac{U(z)}{U^*} = \frac{1}{\kappa} ln \frac{Z}{Z_0} \qquad (6.7)$$

Whereas, *U (z)* is velocity function of *Z*, *U** is friction velocity yield to a value of 2.5 cm/sec as investigated by Sanford and Lien (1999) which is almost equal to the typical value suggested by Marchuk and Kagan (1989) with a value of 3 cm/sec, κ is

von Kármán's constant that equal to 0.41, Z is still water height and Z_0 frequently termed a roughness length (Perlin et al., 2005).

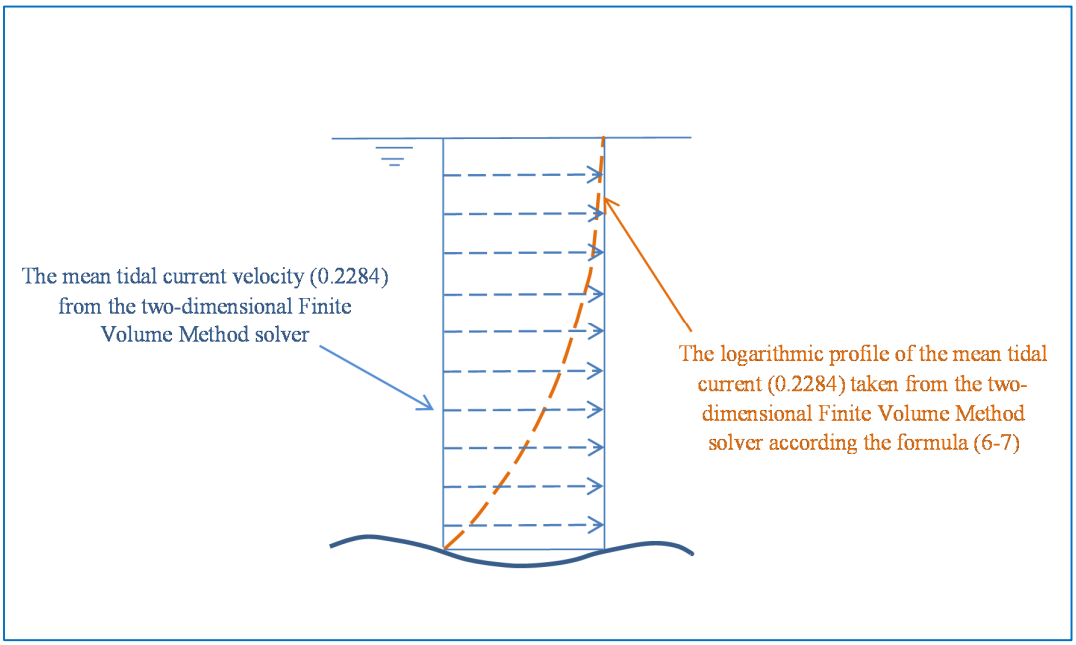

Figure 6.5 The transformation of mean tidal current for the two-dimensional depth averaged uniform velocity profile gained from Finite Volume Method numerical model changed to a logarithmic profile that adopted as inlet in the present investigation.

The initial conditions using the average tidal current profile were set along similar to those adopted in the numerical method and model configuration detailed in pervious section 6.3.1 and the results of the measured tidal current profile with logarithmic tidal current profile were positioned opposite to each other.

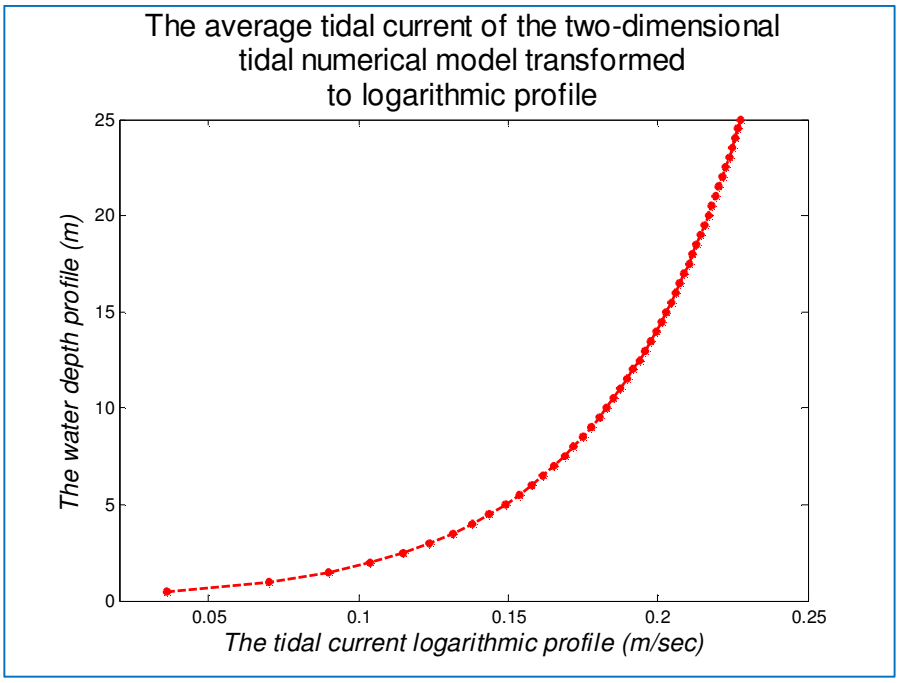

Figure 6.6 The average tidal current gained from the two-dimensional tidal numerical model in the logarithmic profile.

The output from the separate models based on the two tidal current profiles will be compared in the same frame times for the results as adopted in the previous case study. Both tidal current profiles are spotted in Figure 6.7.a, b.

The model using the measured tidal current profiles viewed in Figure 6.7.a with its distinct feature of the effect of both surface and bottom boundary layers impact on the profile, the upper layer of the tidal current suffers from the surface boundary layer process that cause a reduction in the tidal current. Further, information can be found in Lee et al. (2011) and Tsimplis (2012). On other hand, the bottom friction is affecting the bottom layer of the tidal current. The second model using the logarithmic tidal current profile displayed in Figure 6.7.b. The two profiles were run for one hour to produce the velocity profile in the *x*-direction and the production of turbulent kinetic energy presented in the three-plane sections (X-Y plane, X-Z plane and X-Y planes) in the near vicinity of the reef.

The comparison of results indicates similarity in the Y-Z plane and seafloor contour of both tidal current profiles with some minor differences with the other two planes even though the, X-Z plane and the X-Y planes give similar distributions of turbulence in the wake of the reef. The logarithmic profile has a higher velocity near the

surface whose influence doesn't extend significantly down to the reef. Therefore, the measured tidal current with the higher speed over the peak on the artificial reef than logarithmic tidal current, as seen from all figures, creates more turbulent kinetic energy than the logarithmic one. In addition, the vortices/recirculating flow created by both profiles have similar in velocity fields in magnitude and location. In Figure 6.20.a, b the velocity vector profiles are seen for both measured tidal current and logarithmic one in the X-Z plane. The turbulent circulation of the measured profile is wider than the logarithmic one. In fact, the logarithmic profile creates a vortex with almost circle shape whereas the measured vortex has an elliptical shape. The phenomenon is presented clearly in the X-Y plane which intimate to wider turbulent occur in the measured tidal profile than logarithmic one as demonstrated from Figure 6.20.c, d. This effect may be explained due to the higher velocity seen in the measured profile as shown in Figure 6.17.a compared to lower velocity found in logarithmic velocity profile seen in the Figure 6.17.b. Therefore, the effect of the both tidal current profiles on the turbulent kinetic energy production is recognized in Figure 6.17.c, d due to the differences in the tidal current profiles. The shear stresses produced by both tidal current profiles indicates a higher wall shear stress for the measured profile (with 0.35 Pascal) compared to the logarithmic profile (with 0.25 Pascal) as presented in Figure 6.21.a, b.

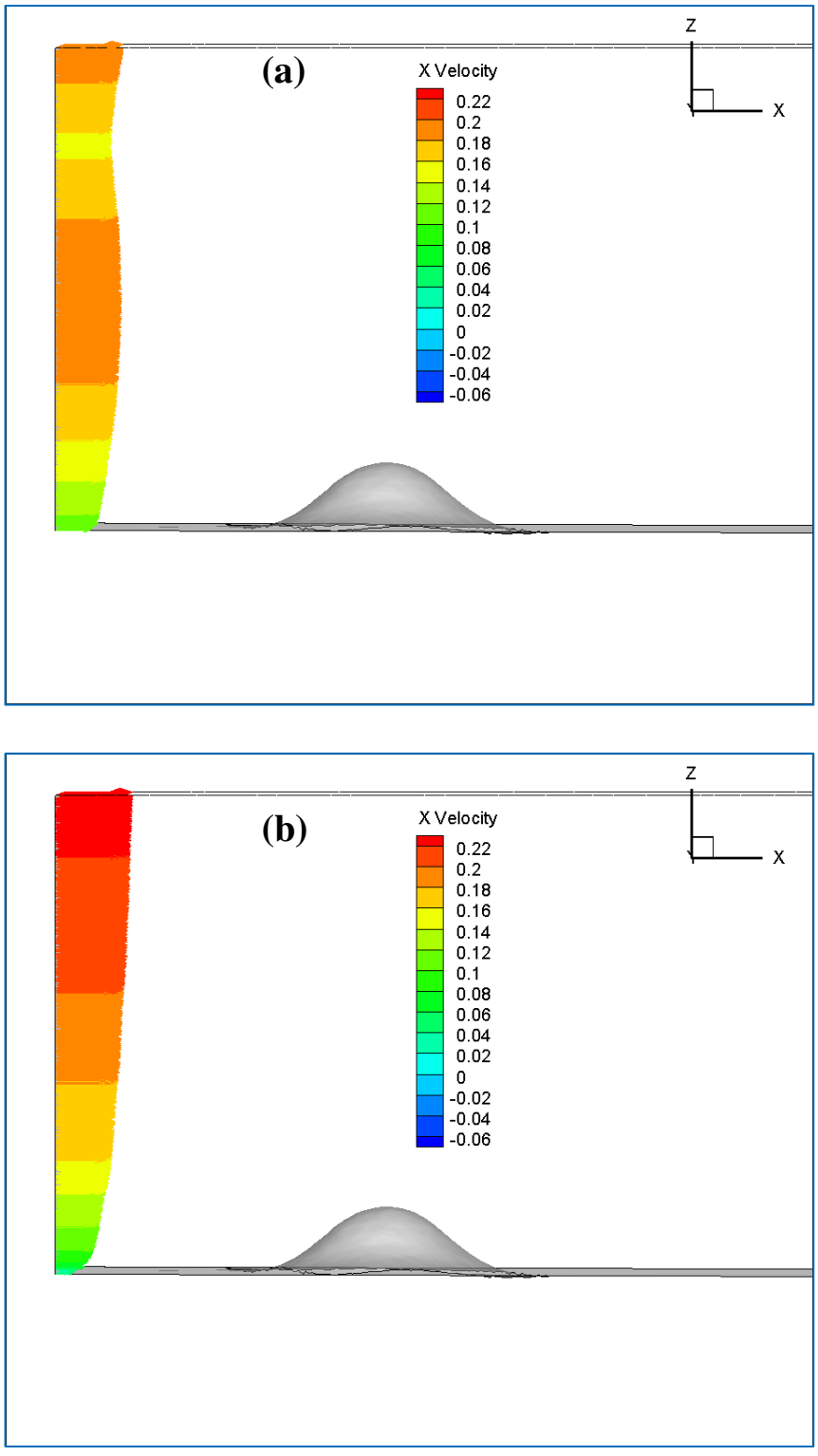

Figure 6.7.a, b The tidal current measured is spotted in (a) with it distinct feature due to the effect of surface and bottom boundary layers and numerical averaged tidal current with the logarithmic profile presented in (b).

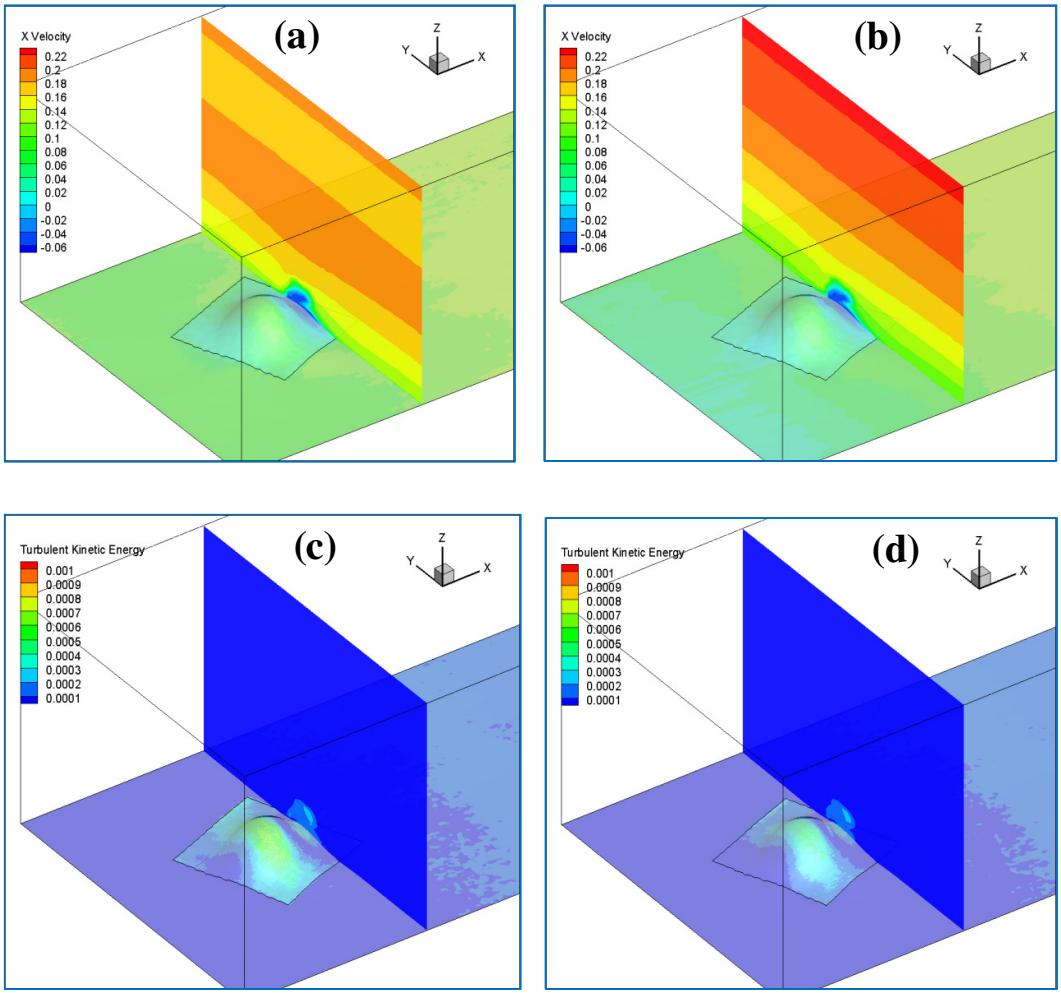

Figure 6.8.a, b, c, d The tidal current at frame time 145 s in Y-Z plane section. The measured tidal current profile is shown in (a) and numerical average tdial current is seen in (b).The turbulent kinetic energy in the same plane for the tidal current measured is spotted in (c) and numerical averaged tidal current is presented in (d).

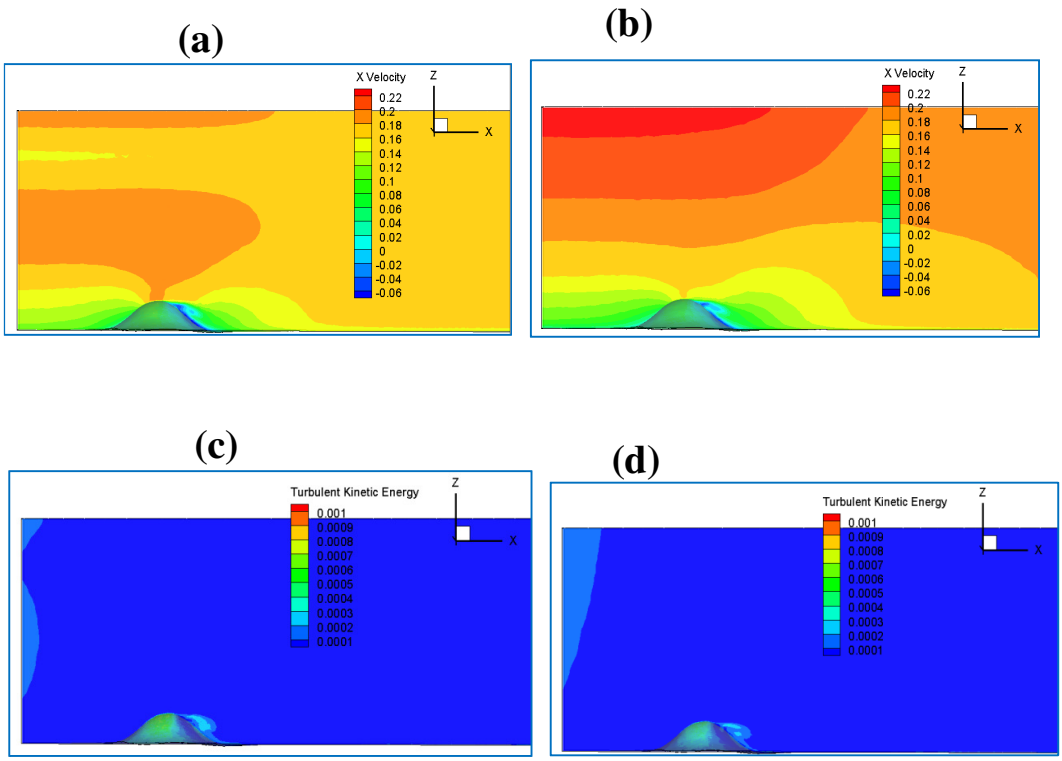

Figure 6.9.a, b, c, d The tidal current in the X-Z plane for the tidal current measured is exhibited in (a) and numerical averaged tidal current exposed in (b). The turbulent kinetic energy for the tidal current measured is displayed in (c) and numerical averaged tidal current is viewed in (d).

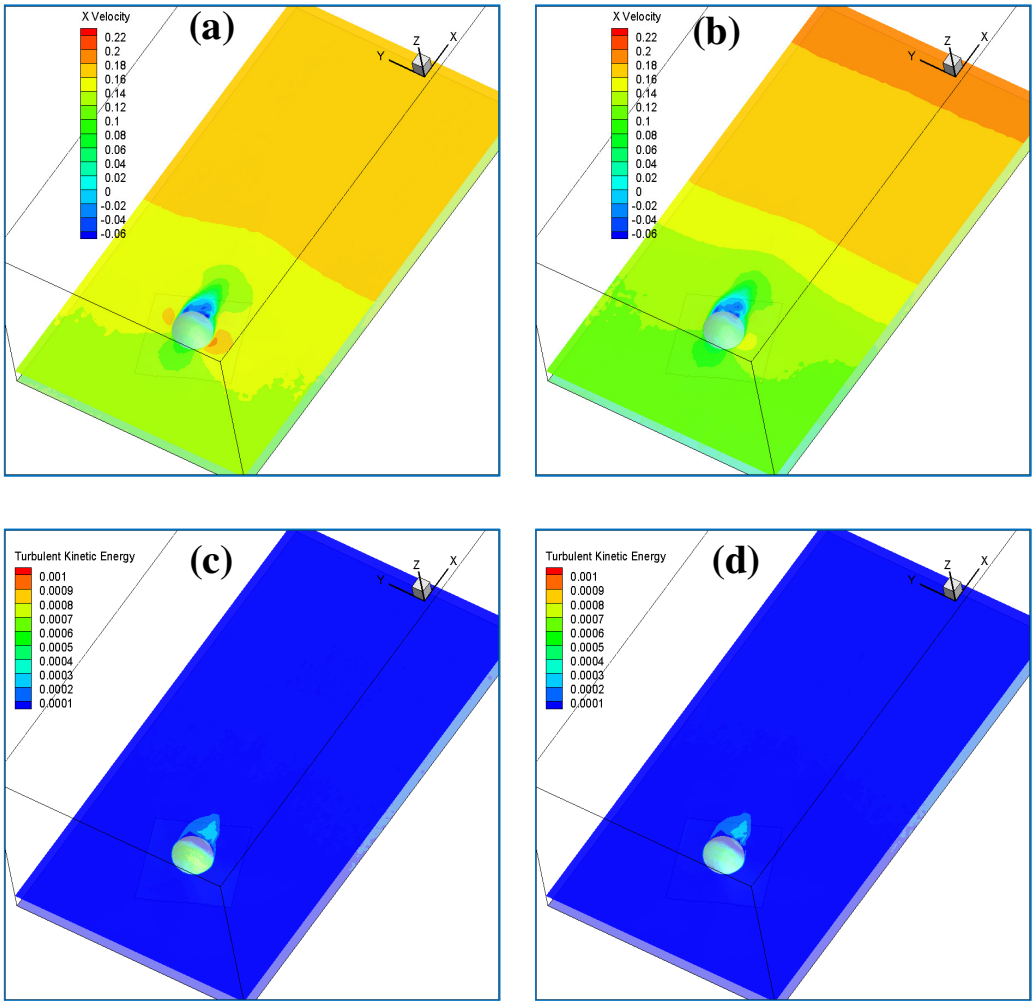

Figure 6.10.a, b, c, d The X-Y plane of tidal current velocity of the measured is demonstrated in (a) and numerical averaged tidal current is exposed in (b).The turbulent kinetic energy of the measured is displayed in (c) and numerical averaged tidal current is seen in (d).

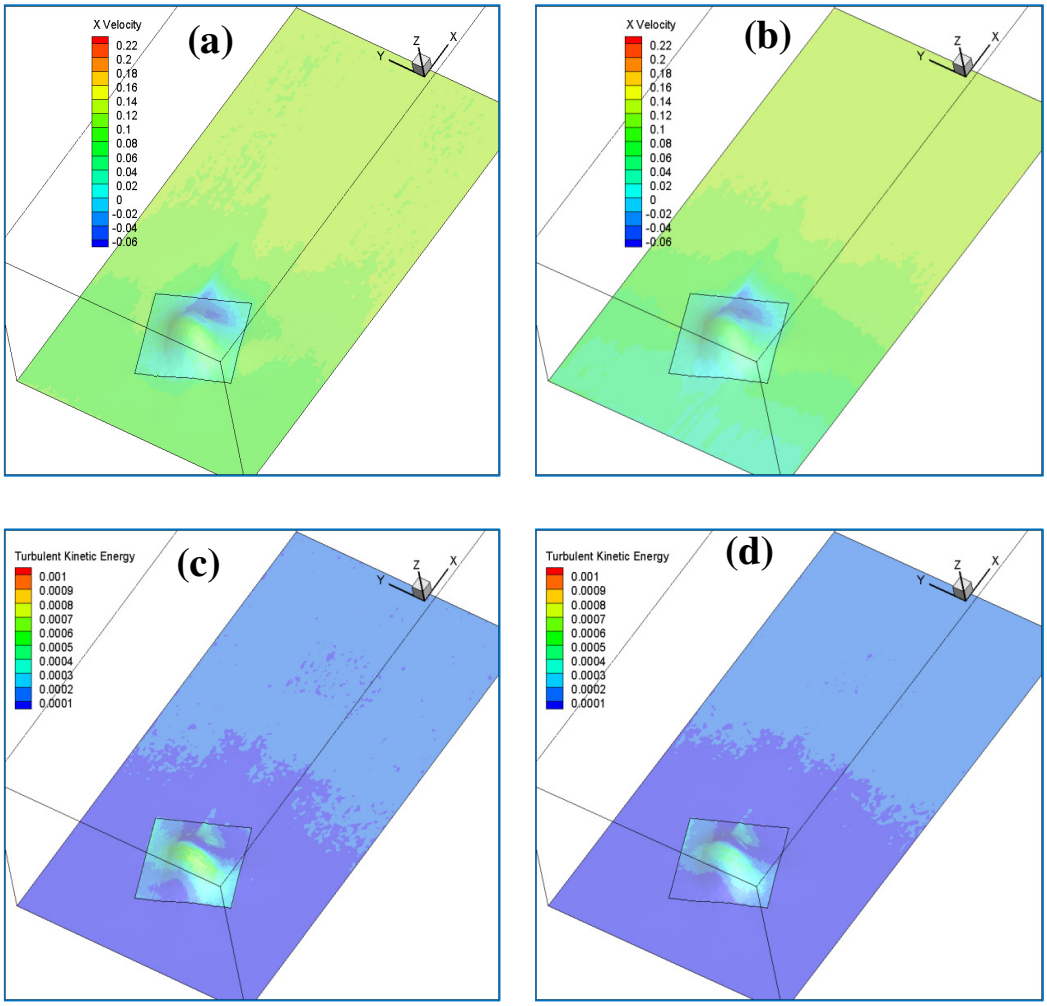

Figure 6.11.a, b, c, d The seafloor tidal current profile of both (a) the measured tidal current and numerical averaged tidal current is presented in (b). The seafloor turbulent kinetic energy for both (c) the measured tidal current and numerical averaged tidal current is spotted in (d).

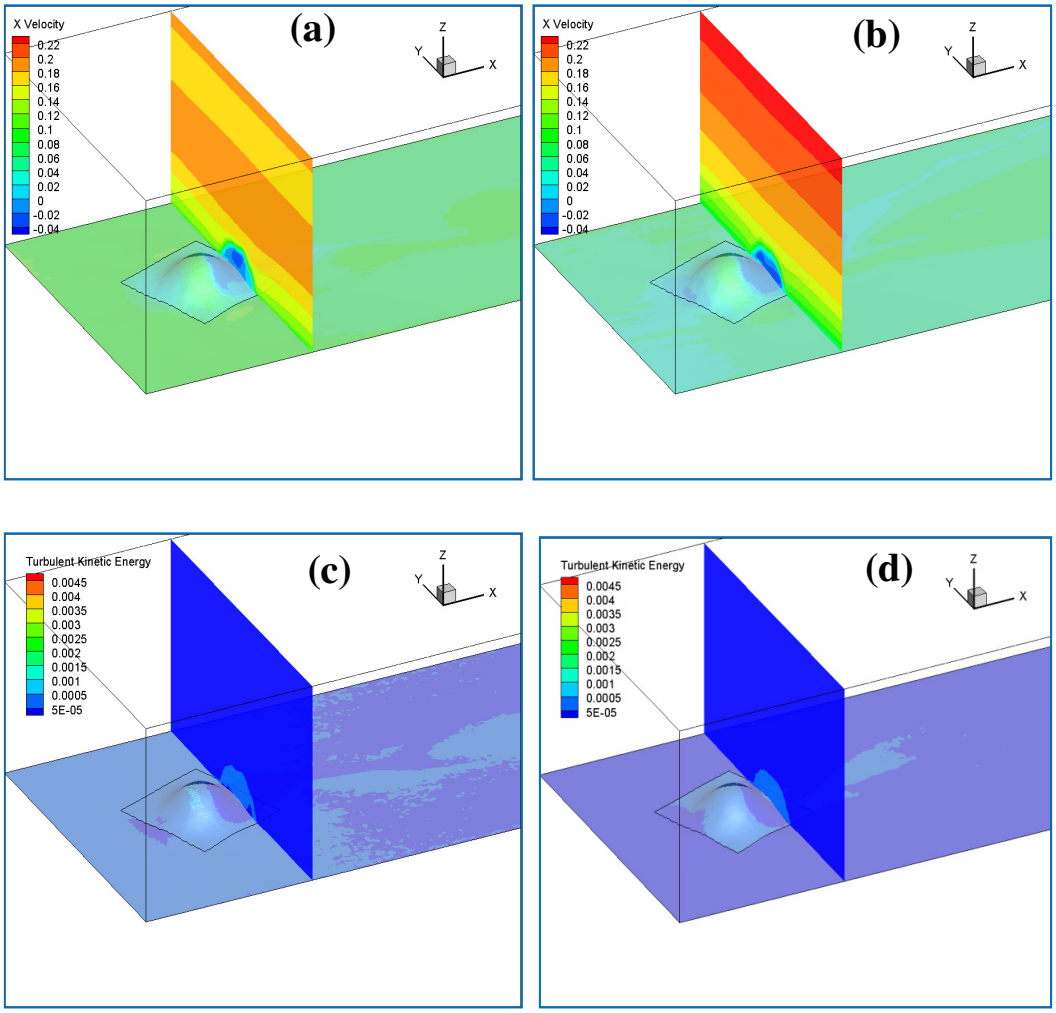

Figure 6.12.a, b, c, d The tidal current velocity of the measured profile is seen in (a) and for logarithmic profile is viewed in (b) as shown from the Y-Z plane (1345 s). The production of the turbulent kinetic energy for the measured current is displayed in (c) and for logarithmic profile is presented in (d).

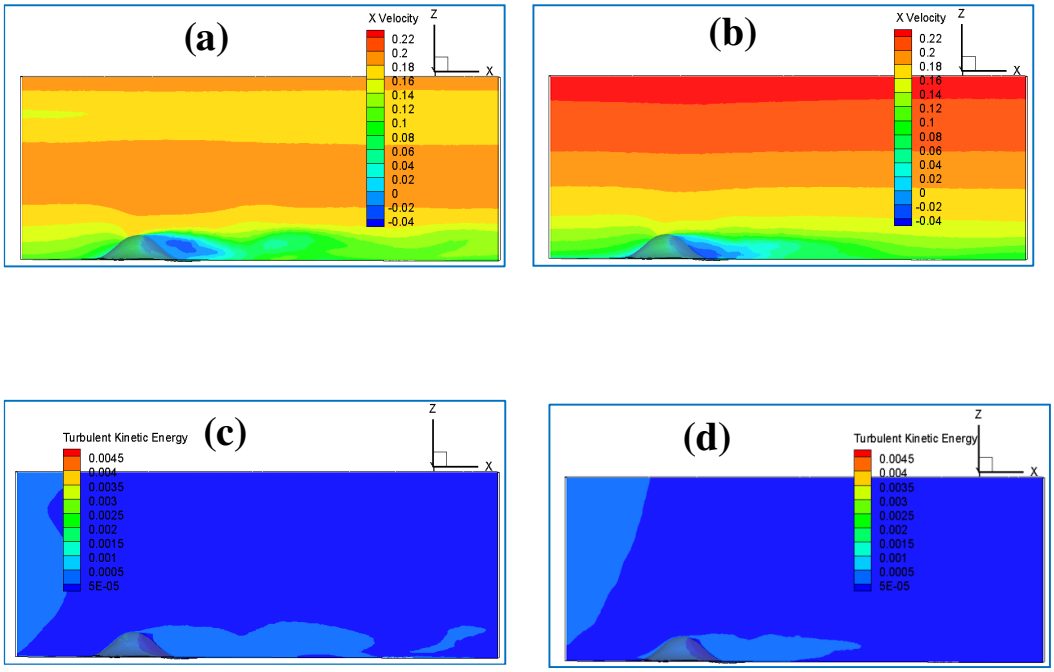

Figure 6.13.a, b, c, d The tidal current profile in *x*-direction for measured profile from X-Z plane is exposed in (a) and logarithmic tidal current profile is exhibited in (b). The tidal current produce a turbulent kinetic energy for the inflow measured profile is spotted in (c) and logarithmic profile is viewed in (d).

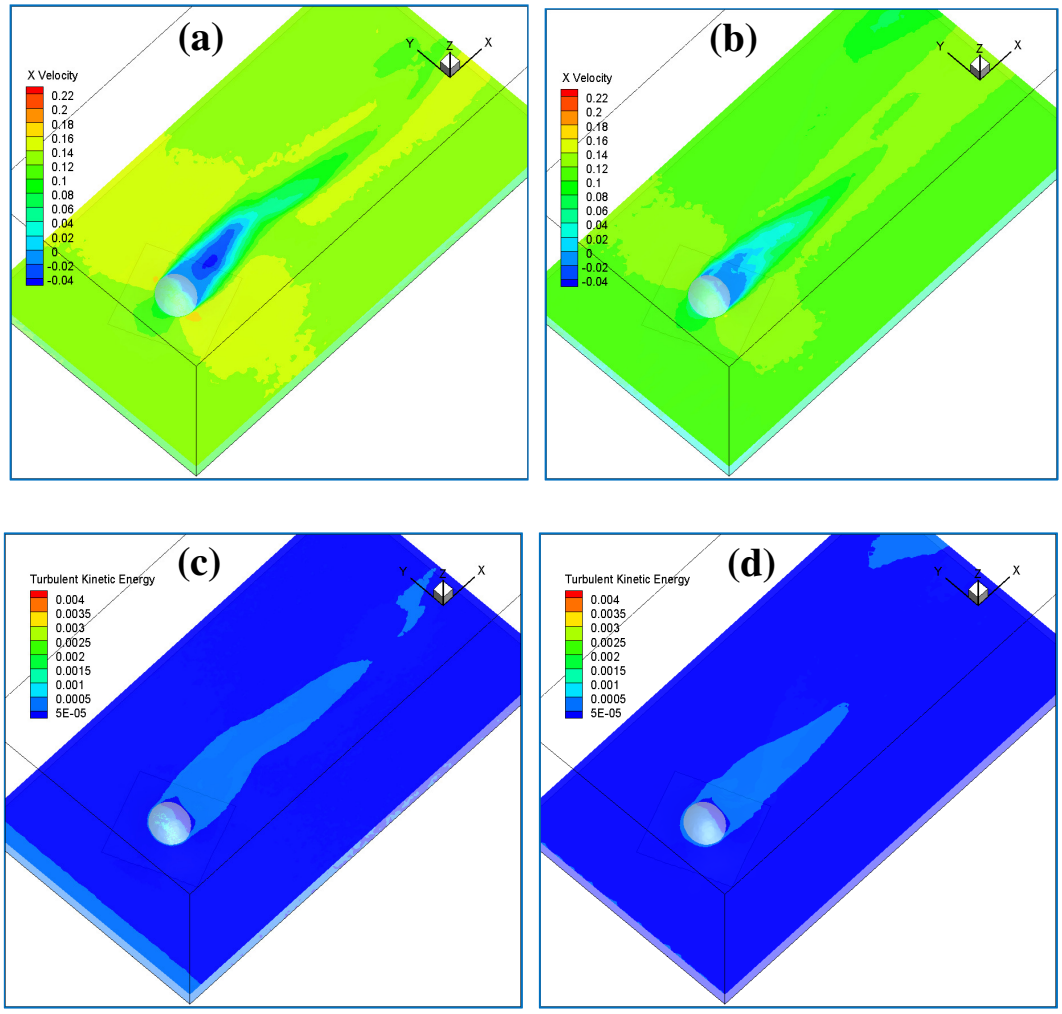

Figure 6.14.a, b, c, d The tidal current for measured current as pass the reef in *x*-direction is demonstrated in (a) and logarithmic current profile is presented in the X-Y plane on 50% of the reef height. The turbulent kinetic energy produced by the inflow measured current is exhibited in (c). The logarithmic inlet effect on the turbulent is seen in (d).

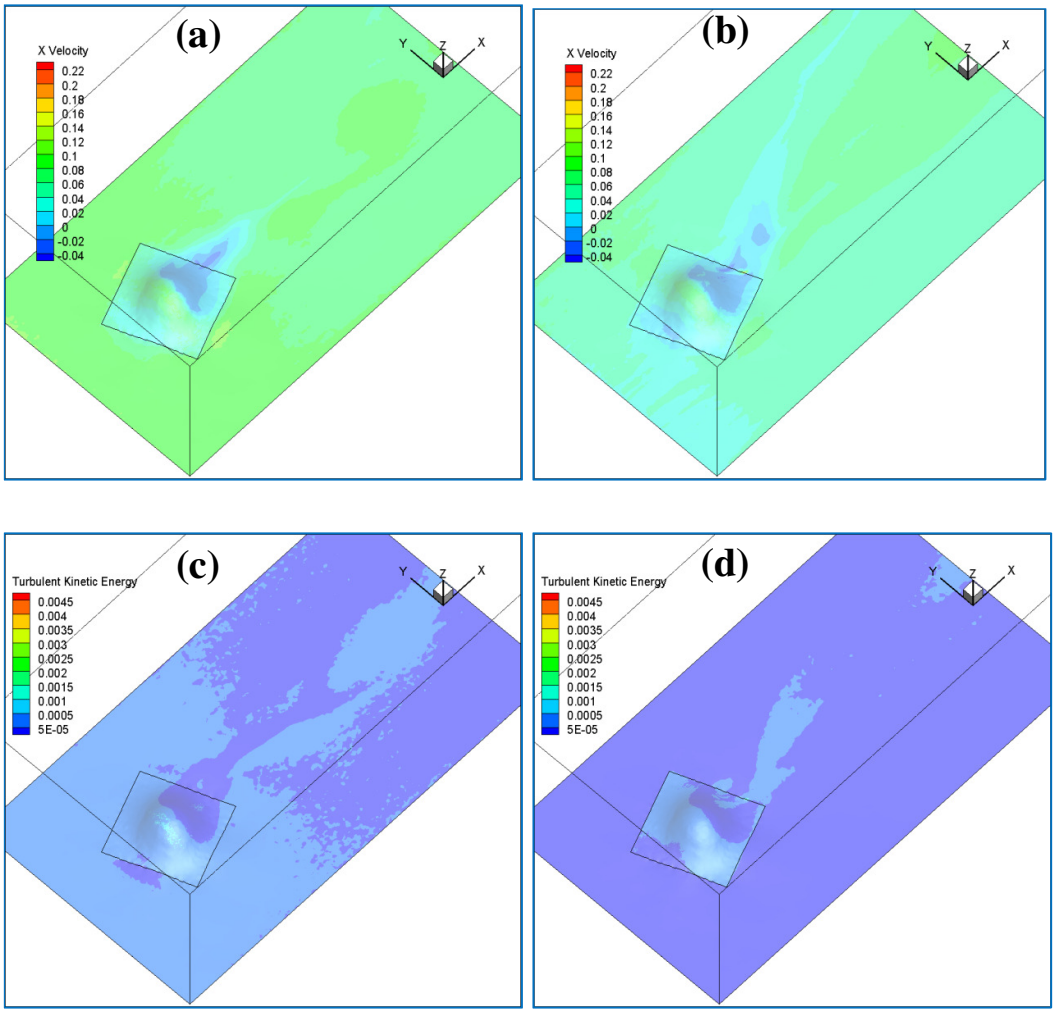

Figure 6.15.a, b, c, d The seafloor velocity contour in x-direction for measured current is displayed in (a) and for logarithmic current is viewed in (b). The seafloor turbulent kinetic energy with (c) the measured tidal current and logarithmic tidal current energy production as presented in (d).

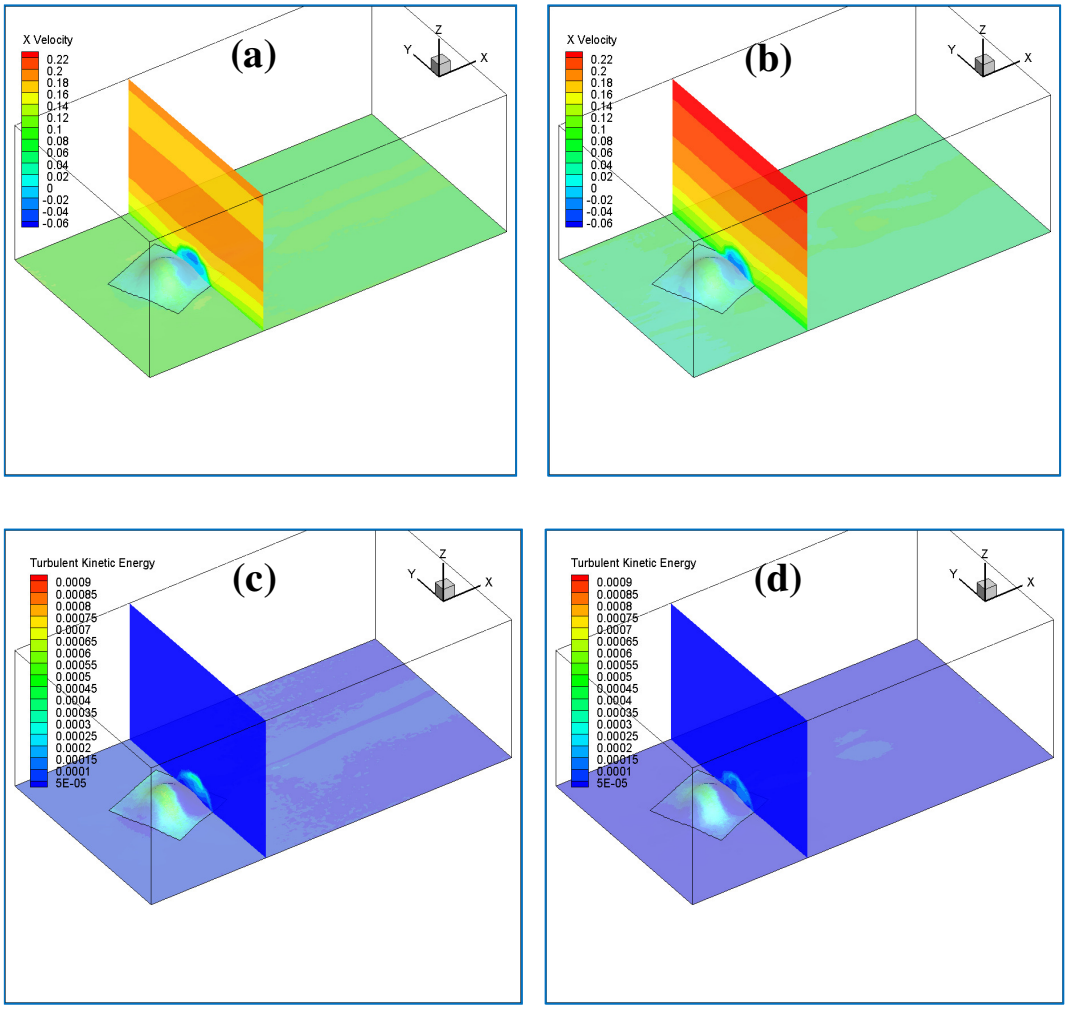

Figure 6.16.a, b, c, d The Y-Z plane on cross section position for measured profile in (a) and logarithmic profile in (b). The turbulent energy production of both measured profile (c) and logarithmic profile in (d) has a similarly pattern of the energy production (3600 s).

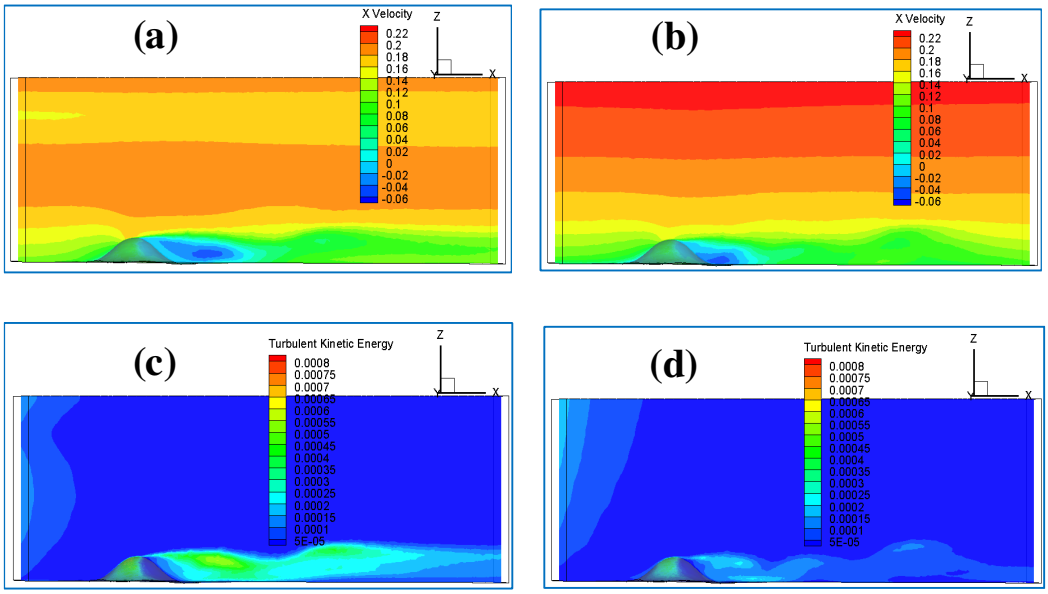

Figure 6.17.a, b, c, d The measured velocity profile is shown (a) for the X-Z plane and the logarithmic profile is presented in (b). Turbulent kinetic energy production for both tidal current profiles (c) measured profile and (d) logarithmic profile. Note that, the higher turbulent kinetic energy viewed in the measured one due to the high velocity at the peak of the artificial reef as demonstrated from the velocity profiles figures.

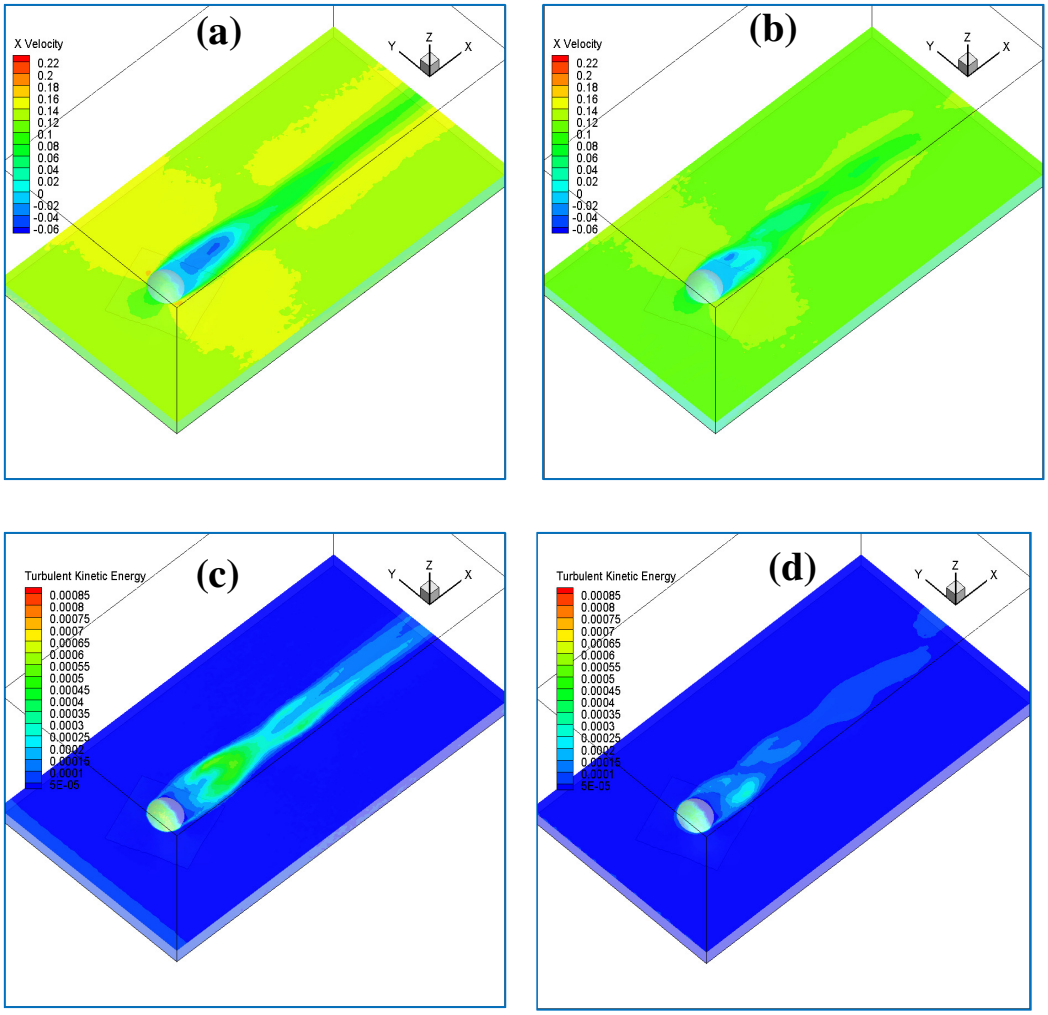

Figure 6.18.a, b, c, d The velocity in the *x*-direction of (a) measured tidal current profile and logarithmic tidal current profile in (b). The turbulent kinetic energy production for the measured profile current is seen in (c) has higher value as the velocity is higher than the logarithmic tidal current shown in (d).

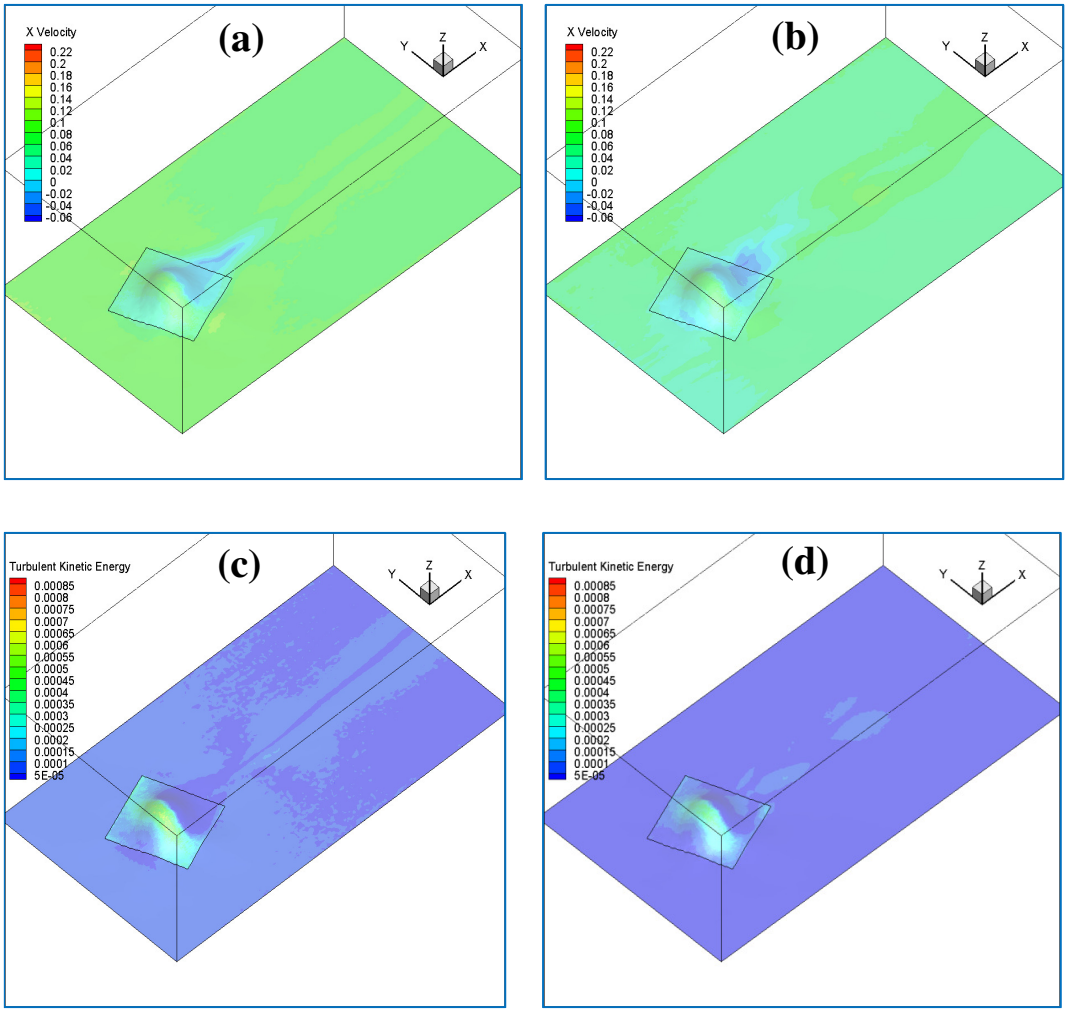

Figure 6.19.a, b, c, d The velocity on the seafloor has similarity values and location as presented for measured tidal current profile in (a) and logarithmic profile one in (b). The positions of higher turbulent kinetic energy are the same in both figures of measured tidal current profile (c) and logarithmic profile current on (d).

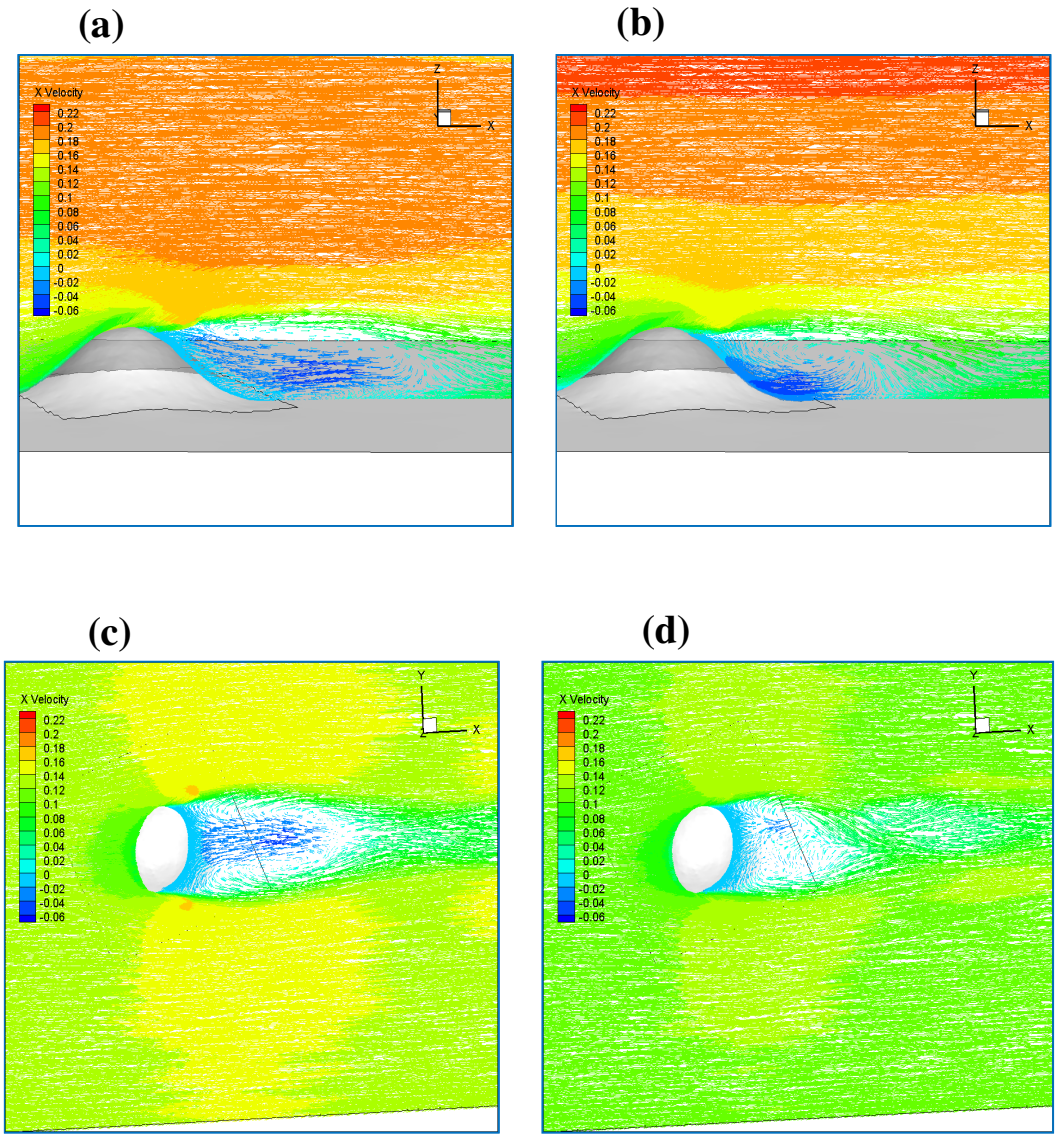

Figure 6.20.a, b, c, d The velocity vectors of both measured profile in (a) and logarithmic profile in (b) in the X-Y plane. The vectors velocity of both measured profile in (c) and logarithmic in (d) in the X-Y plane. It indicates the wake region in both profiles which demonstrates the different size of the created wake region.

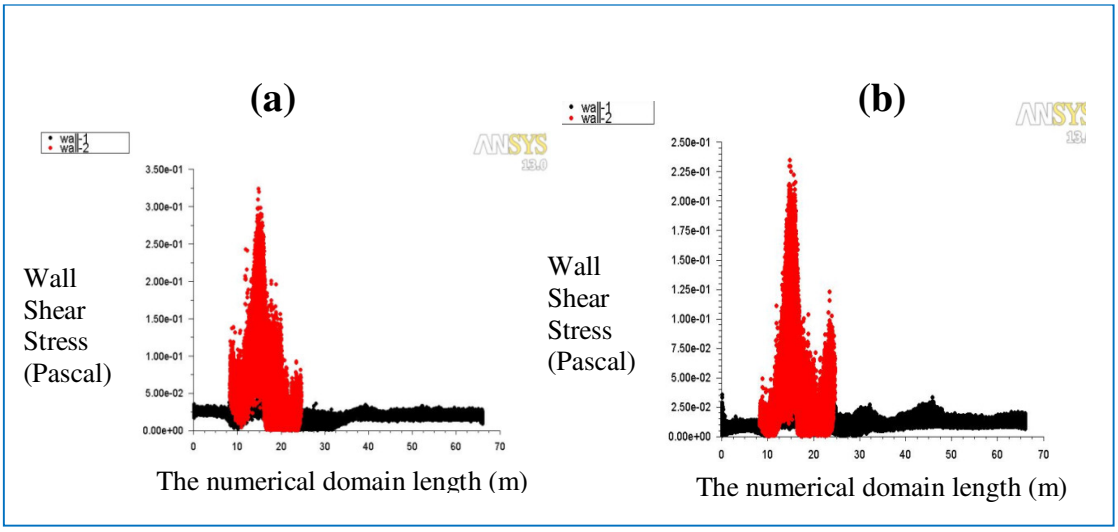

Figure 6.21.a, b The shear stress of measured tidal current profile on the artifice reef is seen in (a) whereas, the shear stress of the logarithmic profile is shown in (b). Note that red dot for artificial reef wall and black dot for seafloor.

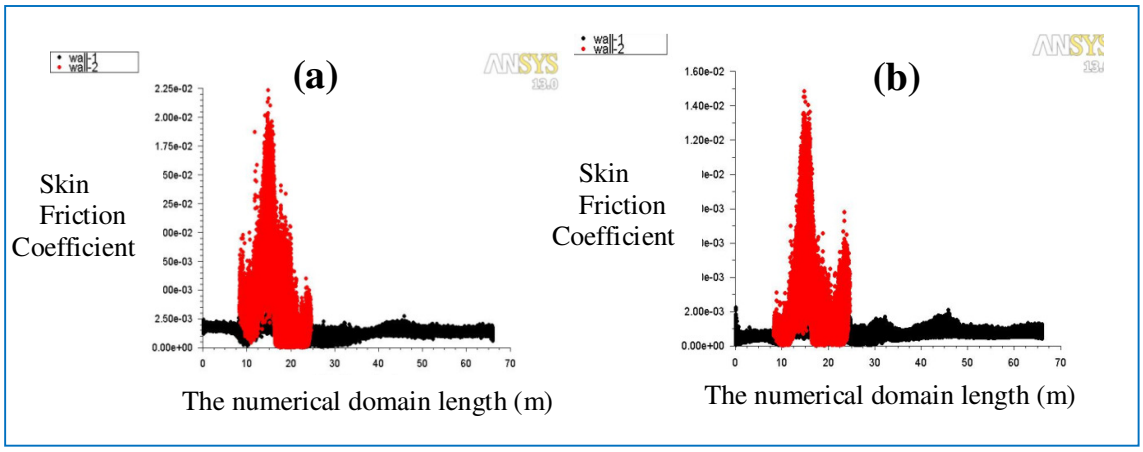

Figure 6.22.a, b The skin friction coefficient of the artificial reef as tidal current profile of measured data propagate the reef is presented in (a) along with the logarithmic profile tidal current cause a skin friction coefficient that is demonstrated in (b). Note that red dot for artificial reef wall and black dot for seafloor.

Similarly, as would be expected, the skin friction coefficient achieved a greater value for the measured tidal current profile than for the logarithmic profile as demonstrated in Figure 6.22.a, b above.

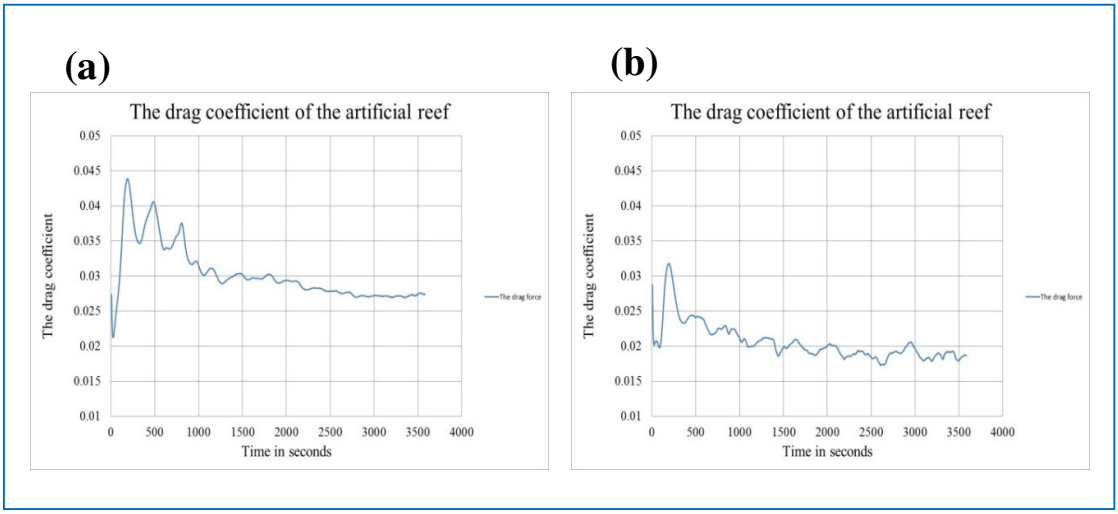

Figure 6.23.a, b The drag coefficient caused by both tidal current on the artificial reef is presented in (a) for measured tidal current profile and (b) for the logarithmic tidal current profile.

The drag force on artificial reef was investigated for both tidal current profiles to reflect the relative impact of the drag forces on the structure integrity of the reef as is presented in Figure 6.23.a, b. Again, as would be expected, the measured tidal current profile shows a higher drag coefficient due to the higher velocity near the artificial reef compared to logarithmic tidal current profile.

6.5 The artificial reef under varying tidal current profiles

In the methods described in the previous sections the assumption has been made that the tidal cycle can be divided into twelve intervals points and the tidal variation can be represented by a corresponding series of step changes with each one having steady inlet conditions. This assumption is tested in the work described in the present section in which the inlet conditions are varied continuously over the hourly time interval. The measured data for the spring tidal current demonstrated in Chapter four was adopted for the exercise by selecting two points of the twelve described in the previous Chapter, the two profiles represents a variation of a one hour time duration that will define the inlet conditions with a similar numerical domain to the one viewed in Figure 6.4.a, b. The inlet was controlled as before using a UDF subroutine written to interpolate in time between two measured tidal current profiles. The two tidal current profiles adopted for the interpolation of a one hour time period can be seen in Figure 6.24.a, b which represents a tidal current similar to the natural ocean conditions and shows the input conditions at the beginning tidal current profile (point 7) and end of the interval represented by tidal current profile (point 8). Note that, the points refer to the twelve intervals points selected from the spring tidal cycle as explained in Chapter four.

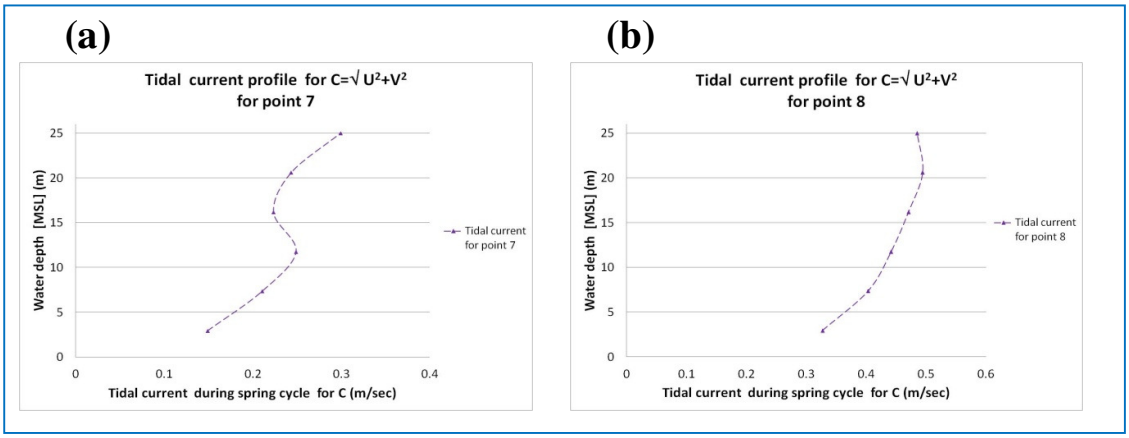

Figure 6.24.a, b The chosen two profiles selected from the tidal spring cycle as illustrated in Chapter four. These were interpolated to create unsteady condition similar to what the artificial reef affected under the normal ocean condition.

The measured tidal current profiles were solved with the same numerical method and model configurations as presented in section 6.3.1 except the inlet conditions are varies with time. The data was output every 200 s during the time of flow to investigate its hydrodynamics as it propagates over the artificial reef. The results displayed in this section will be presented for three time frames of 574 sec, 1790 s and 3600 s shown in three section plans (Y-Z plane, X-Z plane, X-Y plane) as well as the seafloor contours for both the velocity and the turbulent energy in the following figures.

The figures of the Y-Z plane of the unsteady flow a rise in the tidal current velocity profiles from 0.25 m/sec to 0.45 m/sec as viewed from Figure 6.25.a, b, c consistent with the unsteady inlet flow. Similarly, the turbulent kinetic energy increases as the tidal current speed surge and this energy is distributed around the artificial reef as spotted in Figure 6.26.a, b, c. The results for the X-Z plane reveal a similarity in behaviour to those of the Y-Z plane for the velocity tidal current profiles and turbulent kinetic energy. It can be witnessed that flow separation from the reef occurs leading to re-circulating flow and a growing vertical wake that boost as the velocity profiles increases as exhibited in Figure 6.27.a, b, c. A vector plot of the velocity field is delineated in Figure 6.28.a, b, c. It can be observed that the turbulent kinetic energy production rises with the growing region of high speed recirculating flow as viewed in the plot for the turbulent kinetic energy in Figure 6.29.a, b, c. In fact, the initial stages of vortex shedding from the artificial reef can be clearly identified from the X-Y plane, which was taken at a 2.0 m height above the seabed which is about 50 % of the artificial reef height as noticed by Figure 6.30.a, b, c. The tidal current velocity and turbulent

kinetic energy continue to increase in the last time frame due to the gain of speed in the tidal current. Note that, asymmetrical flow seen in Figure 6.30.a, b, c is due to the slope of the seafloor reinforced by effects due to the turbulent nature of the flow. The impact of the tidal current on the seabed is represented in the velocity contour and the production of the turbulent kinetic energy is laid out in Figure 6.32.a, b, c and Figure 6.33.a, b, c respectively.

The computed flow presented in this section is characterised by flow separation and the formation a vertical recirculating flow in the wake region of the artificial reef.

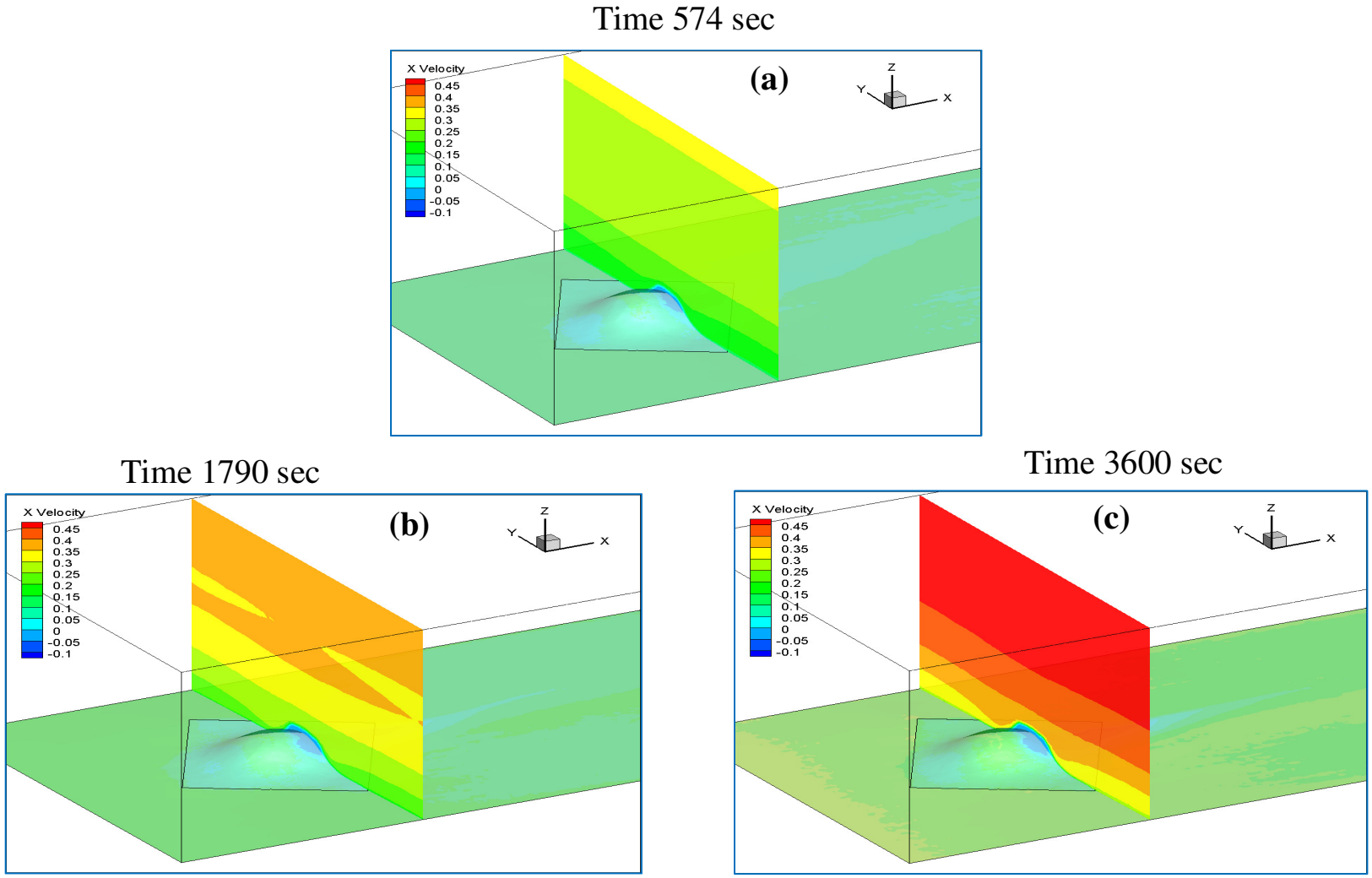

Figure 6.25.a, b, c The velocity in the Y-Z plane of chosen time frames that inidcate the rises of the tidal current profile during unsteady flow conditions.

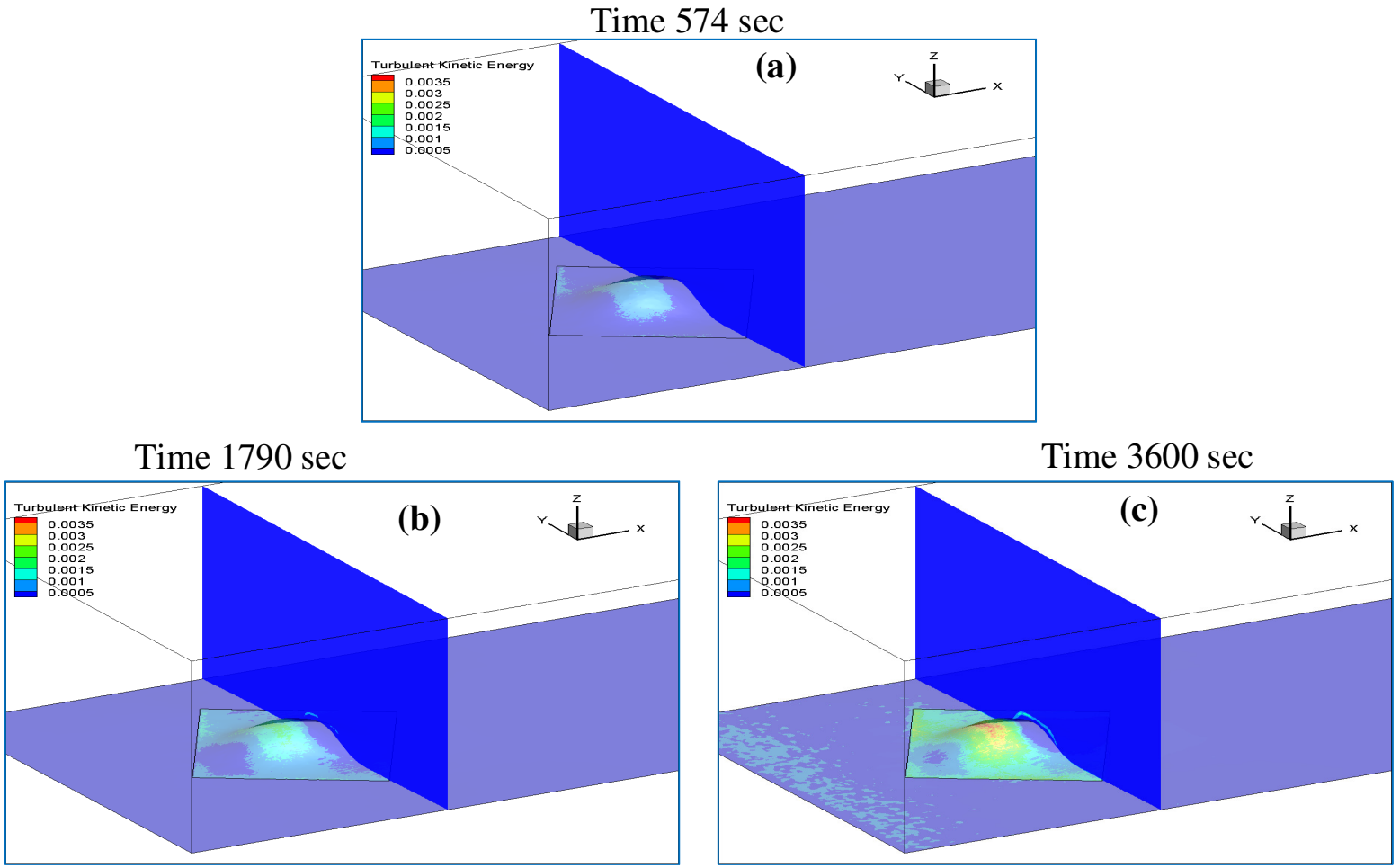

Figure 6.26.a, b, c The turbulent kinetic energy production of the time dependent inlet conditions flow is seen in section Y-Z plane.

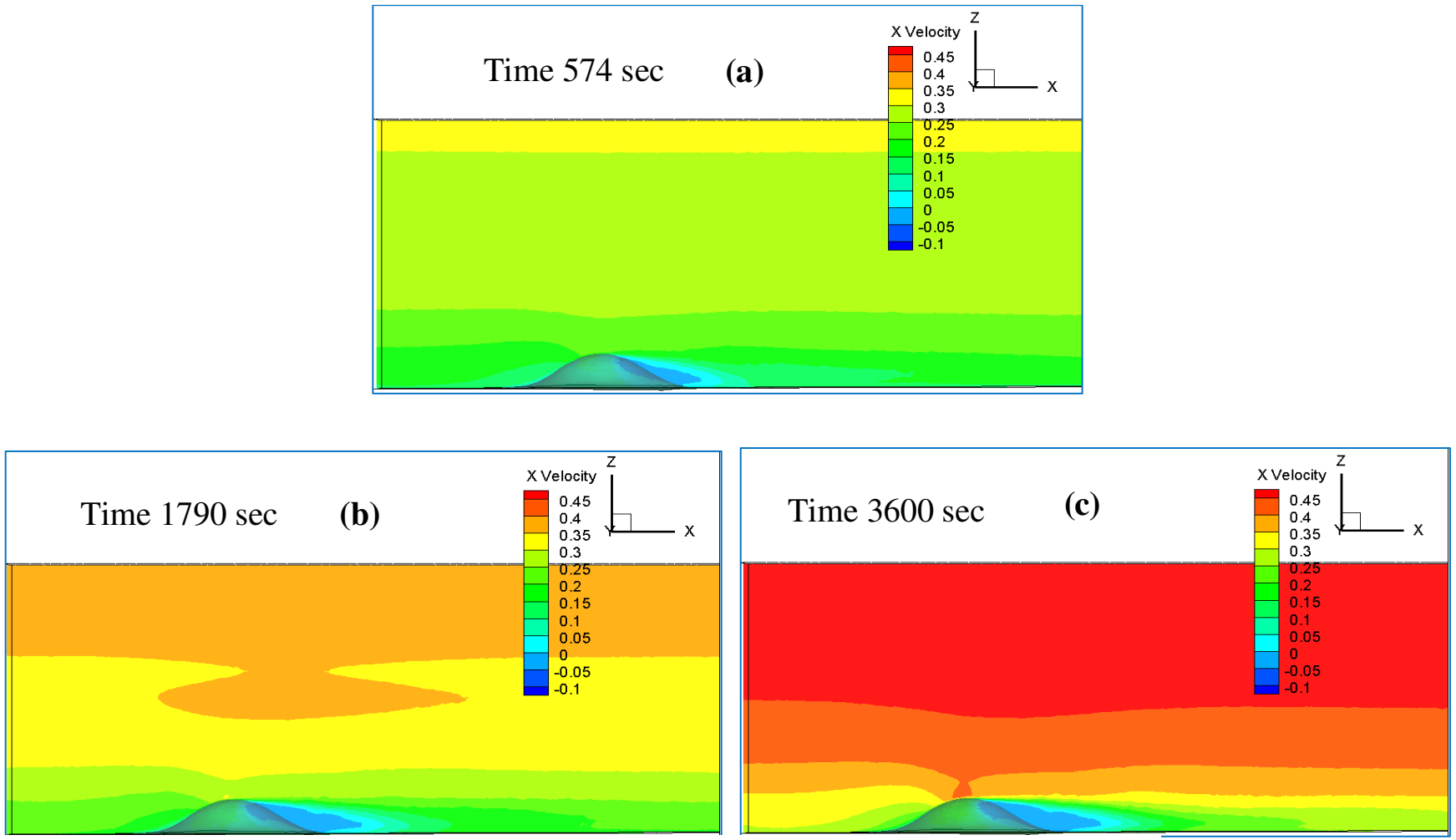

Figure 6.27.a, b, c The X-Z plane velocity contour in the *x*-direction which indicates the increases in of the tidal current profiles as inlet interpolate between the two profiles spotted in Figure 6.24.a, b.

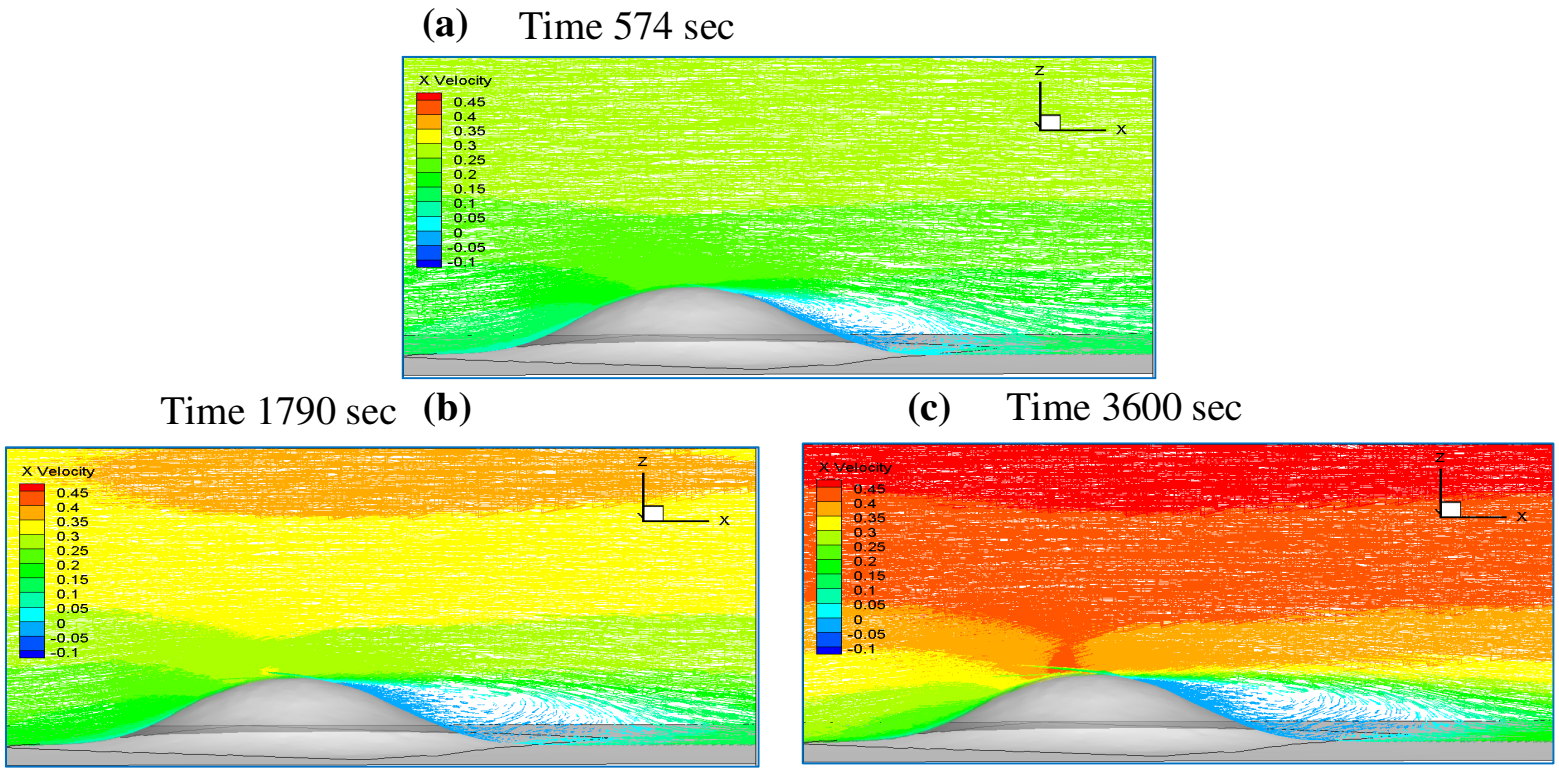

Figure 6.28.a, b, c The vectors of the velocity profiles time frames displaying the development of vortex caused by the artificial reef during the simulation.

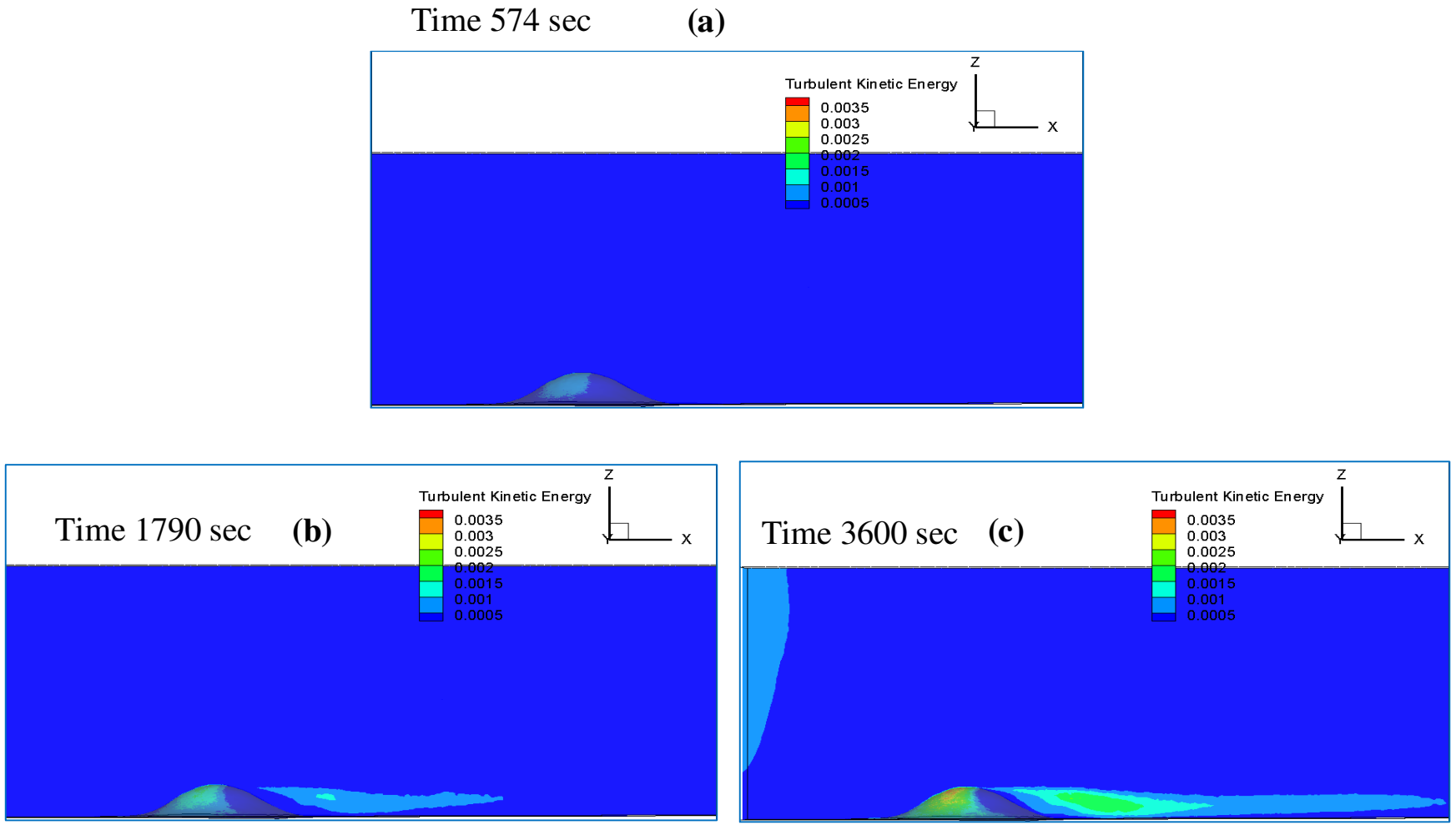

Figure 6.29.a, b, c The turbulent kinetic energy as it generate during the unsteady flow modelling in a one hour time period.

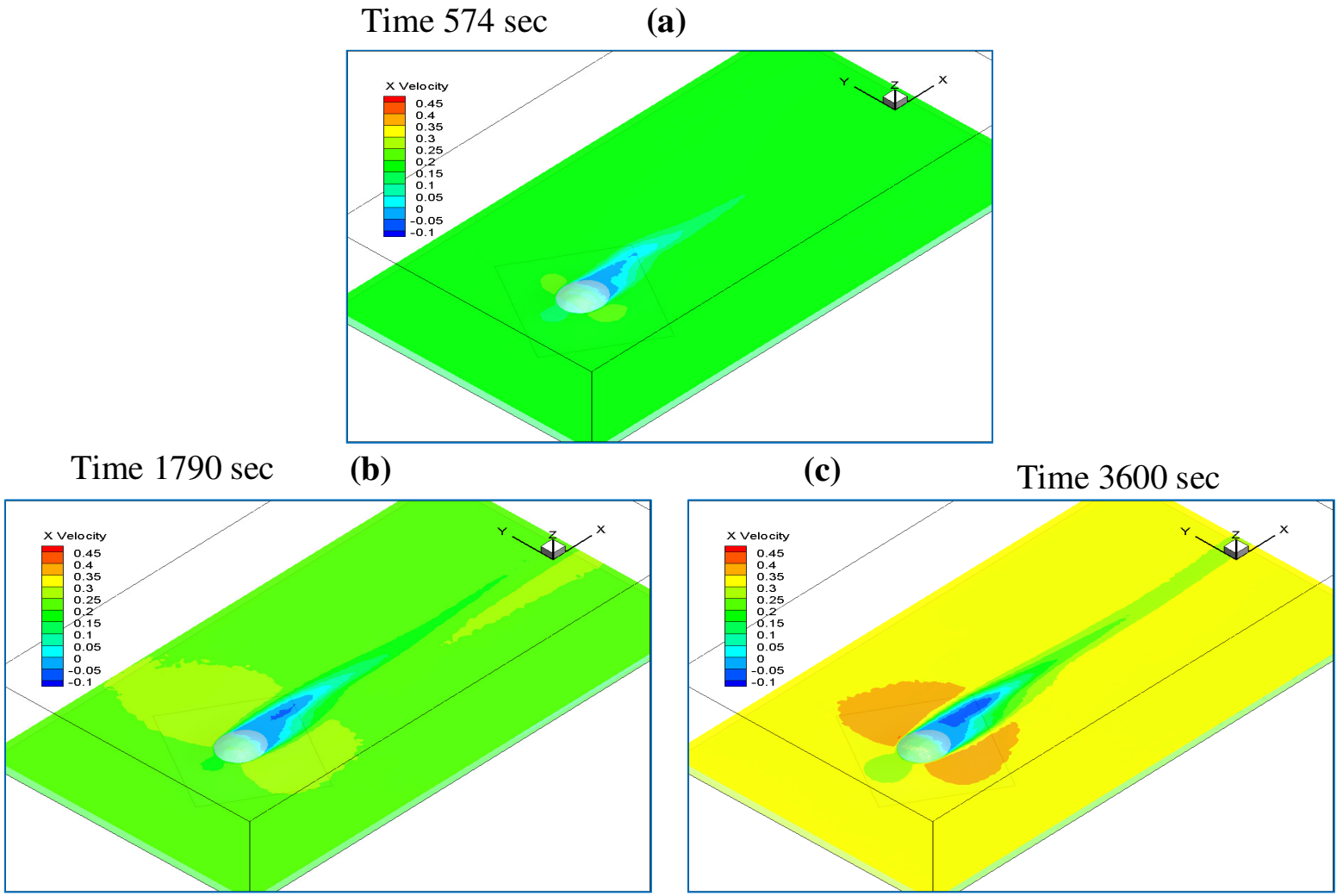

Figure 6.30.a, b, c The X-Y plane of the tidal current velocity contour at the half about 50% of the artificial reef height presenting the turbulent occur on the reef due to the unsteady flow.

Time 574 sec **(a)**

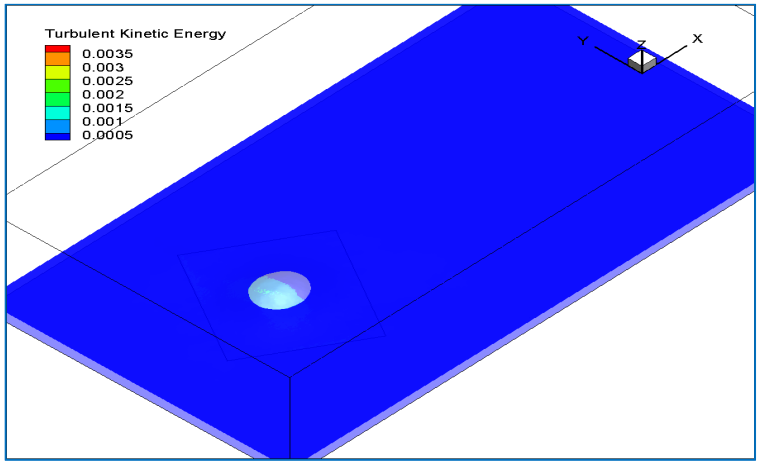

Time 1790 sec **(b)**

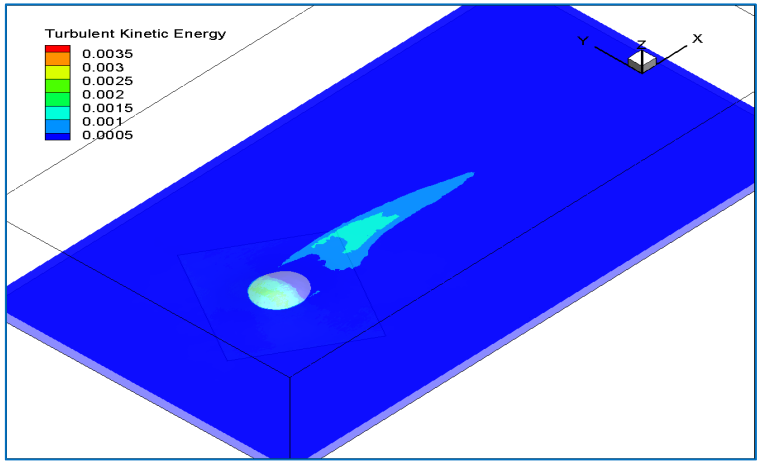

(c) Time 3600 sec

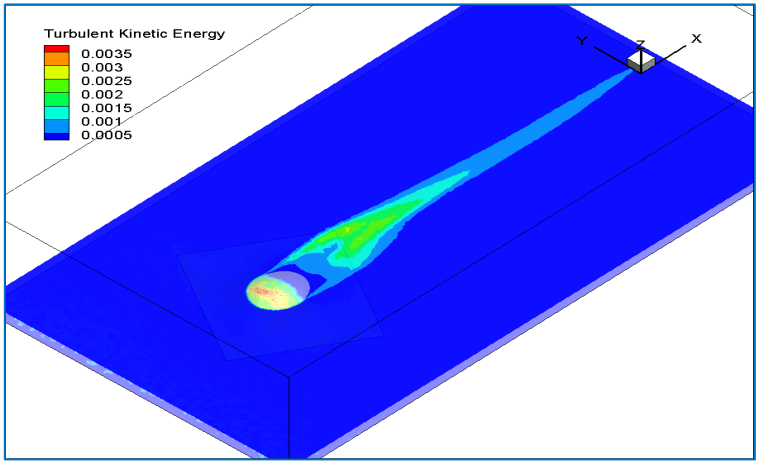

Figure 6.31.a, b, c The production of turbulent kinetic energy due to the unsteady tidal current as presented in the X-Y plane viewed in time frames.

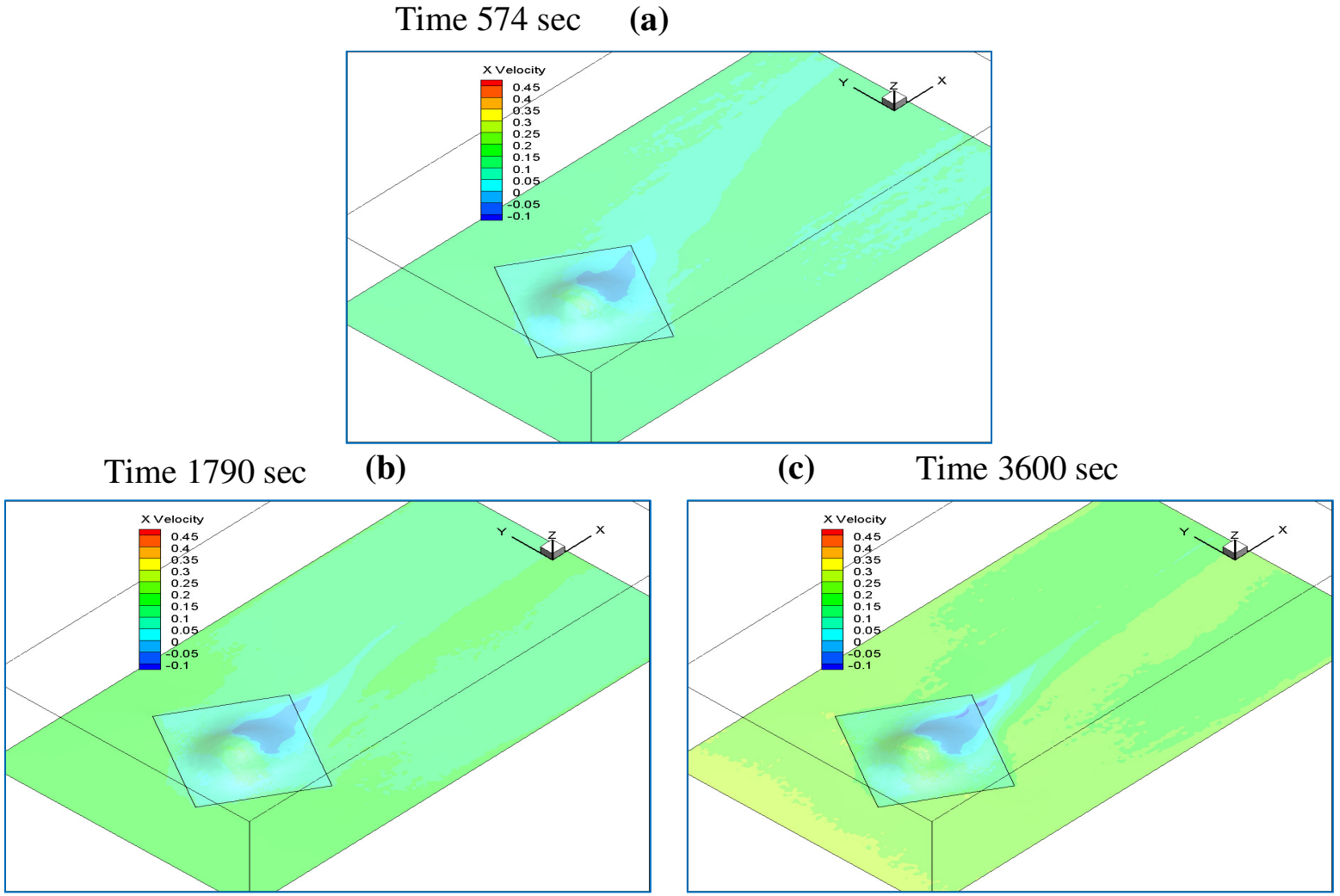

Figure 6.32.a, b, c The effect of velocity contour on the seabed that indicate an increase of the outcome as the tidal current interpolated between the two adopted profile seen in Figure 6.24.a, b increases.

Time 574 sec **(a)**

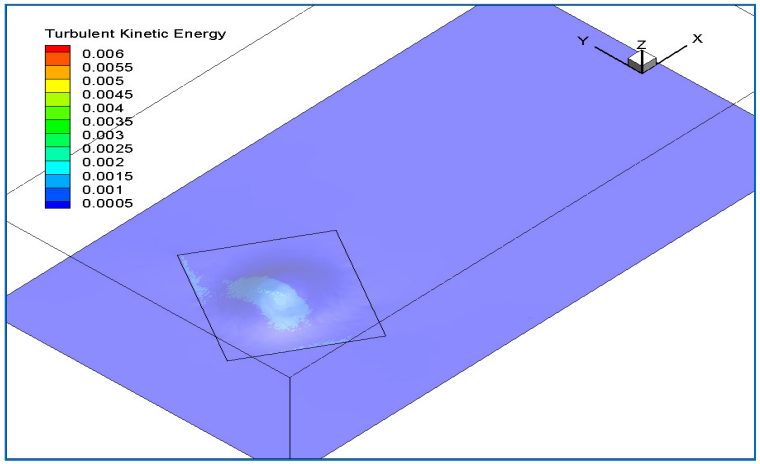

Time 1790 sec **(b)**

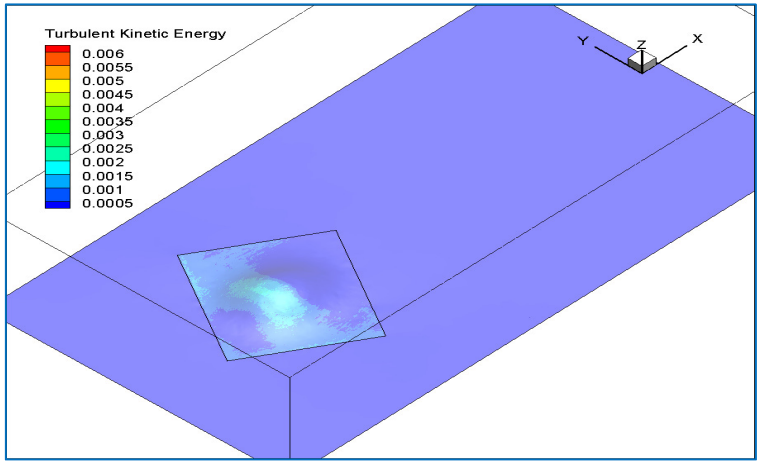

(c) Time 3600 sec

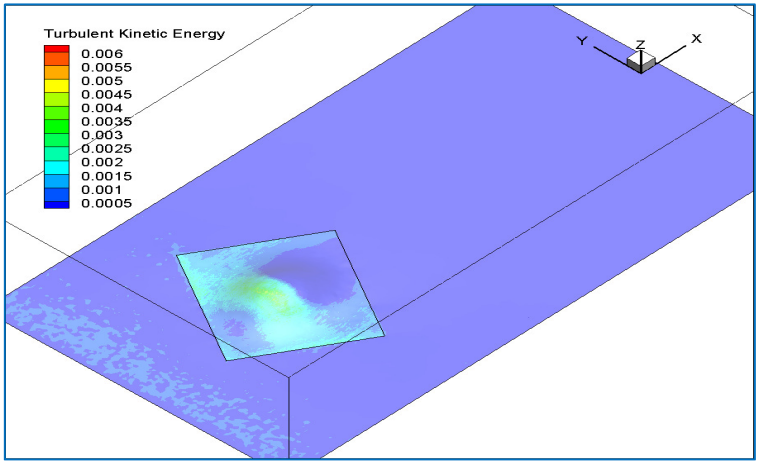

Figure 6.33.a, b, c The X-Y plane the turbulent kinetic energy production on the reef increases as the speed of the tidal current rises due to the interpolation between the two adopted profiles for the unsteady condition.

Chapter 7. Discussion and Conclusions

In recent decades, marine resources have suffered a decline over the whole world due to intensive fishing and the retreat of the shelter and attraction regions like natural reefs. In consequence, members of the fishing industry in several countries have adopted artificial reefs to aggregate and increase total biomass production of fishes. Fluid hydrodynamics has an important influence on a number of aspects of artificial reef functionality and operability. For example, hydrodynamic forces from energetic complex flows can have an impact on the artificial reef stability (threatened by soil erosion at its base) and structural integrity (caused by removal of reef structural elements, such as blocks, by high drag forces). In addition, recent studies have postulated the importance of the role of the flow field in its influence on the artificial reef marine habitats in aquatic systems.

The overall aim of the study, as stated in Chapter 1, is to develop a methodology, and provide the tools for its implementation, for the determination of the detailed hydrodynamic characteristics of an artificial reef with a specified topology at a given location defined only by its bathymetry and tidal information from Admiralty charts, or their equivalent. It was chosen to carry out the study using the artificial reef in Loch Linnhe as an example. From there it followed that the overall objective of the study is divided into three major parts. The first part is related to modelling Loch Linnhe at large scale (global) by analysing the tides' hydrodynamics affecting the Loch. The second part involves small scale (local) modelling aimed at determining the detailed hydrodynamics of the flow surrounding the artificial reef as determined from the global flow. The third major element of the overall objectives involved obtaining measured data for the hydrodynamic characteristics of the artificial reef site from ADCP instruments deployed in its vicinity for refining and validating the numerical models. The overall objectives have all been met and the necessary numerical modelling for achieving the aim of the project has been achieved. Observations and conclusions arising from the work involved are made in the following sections.

7.1 The tides hydrodynamics on the Loch Linnhe

A two-dimensional numerical model solving the shallow water equations (Liang and Borthwick, 2009) was adopted in the present work and implemented to quantify the tidal (global) hydrodynamics on the Loch. Initially, the numerical model itself was intensively examined for fitness for purpose using a variety of benchmark tests in one-dimension. It was also implemented to model the flow through the New Zealand Strait, having similar execution aspects to Loch Linnhe, and the results were compared with the numerical model results presented by Msadek (2005). The adopted numerical model gave very accurate results compared with the standard benchmark tests and found an acceptable accuracy between its results and those of Msadek (2005) in numerically modelling tides. The preliminary numerical tests demonstrated the accuracy of the method and its suitability for modelling tidal hydrodynamics.

The model was then used to simulate the global marine environmental conditions in Loch Linnhe. Implementing the computational domain based on the correct bathymetry and marine environmental conditions required extensive data mining and mesh development. The output from the model was compared with the measured output from instruments deployed around the chosen artificial reef, and with data from Admiralty charts. The model again gave acceptable accuracy and demonstrated its suitability for modelling the global flow in the Loch.

7.2 The detailed hydrodynamics about the reef

The three-dimensional modelling was focused in the present work on the detailed hydrodynamics, such as the velocity field and the turbulent intensity, arising from the interaction of the tidal flow with the artificial reef. The three-dimensional numerical modelling was into three test cases. Case one involved applying the measured data taken from the instrument deployed near the artificial reef to develop the inlet conditions for the 3D-simulation. The only difference in Case two is that the initial/inlet conditions were derived from the output from the Global Analysis (shallow water equations) so that the whole analysis was based on numerical modelling without empirical input. The inlet conditions were based on a velocity profile created by converting the global tidal average current (2D quantity) to a 3D logarithmic profile

with depth. The results from the two cases of the measured data tidal current profile and the logarithmic profile were compared to examine the degree of similarity between the two conditions. As seen in Figure 6.7.a, b to Figure 6.20.a, b the output from the two cases is nearly the same and it can be concluded on the basis of these results that a good representation of the detailed reef dynamics can be achieved solely through numerical modelling, ie by computing a global flow using the shallow water equations and matching it at a point of interest to a local flow computed using a Navier Stokes solver with a turbulence model.

In Case three the computational domain remains the same, but the inlet conditions vary continuously over the period of computation. The unsteady inlet conditions were developed from one hour tidal current profiles taken from the measured data recorded by ADCP instruments. It can be seen from Figure 6.24.a, b to Figure 6.33.a, b that the results from Case three are nearly similar in the turbulent production to those of Case one. From this it can be concluded that the tidal cycle can be modelled as a slowly varying process with a stepped-constant inlet flow distribution, as discussed in Chapter six.

The results of all cases illustrate a bluff body flow regime around the artificial reef characterised by flow separation and a recirculating turbulent wake. There are some minor differences between the flows of Case One and Case Two but these are caused by differences in the vertical velocity distribution of the different velocity profiles. The measured profiles in the case study tend to have a higher velocity near reef than the logarithmic profile, which itself has a higher velocity nearer the free surface. The consequence is observed in the phasing of the development of the recirculating flow in the wake of the reef rather than in a difference in the qualitative nature of the flow. There is evidence that a steady vortex shedding process would develop if the steady inlet conditions were allowed to run for a long enough time duration, however this is constrained by the cyclic nature of the tidal flow.

7.3 The ecological effect of hydrodynamics on the artificial reef habitats

The role of reef hydrodynamics has been considered by several researchers such as Lin and Zhang (2006). The flows characterized by flow turbulence have been focused

on due to it's impact on water quality. For example, eddy and upwelling current fields generated on the upstream and downstream faces of artificial reefs enhances the marine life productivity as found by Zhang and Sun (2001). In addition, one of the reasons that fish aggregate on artificial reefs is because of marine organisms such as plankton on which the fish feed. The concentration of the plankton may be affected by the flow or the current interacting with the artificial reef.

An artificial reef generates a weak stream in the wake region that can be seen in the down-current area from the artificial reef. The wake region can flow in a counter-direction with a weak flow and many eddies of varying in scale (Mann and Lazier, 1996). The plankton that can be found in this region attracts fish to the artificial reef along with the shelter the reef provides. In addition, it has been found that turbulence on the edge of the weak region attracts a kind of marine pelagic species (Seaman and Jensen, 2000). Also, Kakimoto (1983) found that fishes are attracted to the contour flow regions on the down current side of the artificial reef due to the increase of zoolplankton concentration. Therefore, wake zone size is one parameter that affects the performance of the artificial reef (Gun Oh et al., 2011). The region of high turbulence for the present artificial reef is found in its wake, which indicates a likely region of fish attraction due to the high concentration of plankton likely to be found there. In addition, it is known that current affects the settlement and growth of Epifaunal organisms, which also has an impact on reef performance from biological productivity. The wake zones can be the perfect spot for this kind of marine organisms to settle. It has also been noticed that fish swim in turbulent zones and avoid laminar flow to save energy (Godoy et al., 2002).

7.4 Concluding comments

It has been concluded by various authors and in this thesis that the hydrodynamics of artificial reefs is a key factor in their successful design and operation. It is therefore of importance in the early design phase to be able predict the hydrodynamics of a prototype design in a given locality with the best possible reliability and accuracy with the minimum effort and expense. This study has demonstrated that this objective can be achieved by solving the shallow water equations in the general locality of the proposed reef and using its output to define initial/boundary conditions

for a detailed hydrodynamic analysis of the reef near vicinity using a three-dimensional Navier Stokes solver with a turbulence model.

The study was focussed on a reef element in Loch Linnhe, and numerical descriptions of the marine (hydrodynamic) environment have been generated. The data displays special distributions of velocity fields and turbulent intensity on the reef and the study indicates correlations between the hydrodynamic reef characteristics and issues of marine biological interest. In addition some measured data has also been presented for the marine (hydrodynamic) environment in the vicinity of the reef.

7.5 Suggestions for future work

The study has focussed on the Loch Linnhe reef, which is an existing reef that was designed subject to specific constraints and without the benefit of the 'design tools' developed in this study. An interesting piece of work would be to investigate the hydrodynamic characteristics of a variety of reef geometries.

It was not possible within the scope of this study to investigate the detailed relationship between reef hydrodynamics and its stability and structural integrity as touched upon in the thesis.

There is a great deal of work that could be carried out on the correlation between reef hydrodynamics and its environmental impact in both the physical and the marine biological aspects of the subject.

Finally, useful work could be carried out in developing explicit purpose made design tools similar to those proposed in principal in the thesis to facilitate the design of economic and effective artificial reefs.

Appendix (A). The shallow water equations solver

The two-dimensional non-linear shallow water equations (SWE) in its conservation law form can be written as:

$$\frac{\partial \mathrm{u}}{\partial t} + \frac{\partial \mathrm{f}}{\partial x} + \frac{\partial \mathrm{g}}{\partial y} = \mathrm{S} \qquad \text{(A.1)}$$

where x and y are Cartesian coordinates in space, t denote time and **u, f,** g, and S are the vectors respectively representing the conserved variables, fluxes in the two Cartesian directions and source terms. The Coriolis effect has been neglected due to the relatively small horizontal scale of the numerical domain here. Further neglecting the viscous terms and surface stresses, the vector terms are given as follows:

$$\mathrm{u} = \begin{bmatrix} \eta \\ uh \\ vh \end{bmatrix} \quad \mathrm{f} = \begin{bmatrix} uh \\ u^2h + \frac{1}{2}g(\eta^2 - 2\eta z_b) \\ uvh \end{bmatrix} \quad \mathrm{g} = \begin{bmatrix} vh \\ uvh \\ v^2h + \frac{1}{2}g(\eta^2 - 2\eta z_b) \end{bmatrix} \quad \mathrm{S} = \begin{bmatrix} 0 \\ -\frac{\tau_{bx}}{\rho} - g\eta\frac{\partial z_b}{\partial x} \\ -\frac{\tau_{by}}{\rho} - g\eta\frac{\partial z_b}{\partial y} \end{bmatrix} \qquad \text{(A.2)}$$

Herein $h = \eta - z_b$ defines the total water depth, with η and z_b representing the water surface elevation and bed elevation above datum. u and v are the depth-averaged velocity components in the x and y directions, respectively. g is the gravity acceleration. ρ is the water density. $-\frac{\partial z_b}{\partial x}$ and $-\frac{\partial z_b}{\partial y}$ represent the bed slope in the two Cartesian directions and τ_{bx}, τ_{by} are the bed friction stresses which indicate the effect of bed roughness on the flow and it can be calculated by following empirical formulae:

$$\tau_{bx} = \rho C_f u\sqrt{u^2 + v^2} \quad \textit{and} \quad \tau_{by} = \rho C_f v\sqrt{u^2 + v^2} \qquad \text{(A.3)}$$

The bed roughness coefficient C_f can be calculated by $C_f = gn^2 / h^{1/3}$, where n is the Manning coefficient. By adopting water surface elevation as one of the flow variables, the above shallow water equations were specifically derived to preserve the

solution of lake at rest problem, which is an essential condition for stable and accurate simulation of shallow flow over non-uniform bed profile (Liang and Borthwick 2009).

A.2 Numerical model

The equations (A.1) and (A.2) are discretized using an explicit finite volume Godunov-type scheme with the HLLC approximate Riemann solver chosen to calculate fluxes across a cell interface. The flow variables are updated to a new time step using the following time-marching formula:

$$\mathbf{u}_i^{n+1} = \mathbf{u}_i^n - \frac{\Delta t}{\Delta x}\left(\mathbf{f}_E - \mathbf{f}_w\right) - \frac{\Delta t}{\Delta y}\left(\mathbf{g}_N - \mathbf{g}_S\right) + \Delta t \mathbf{S}_i \tag{A.4}$$

Here, superscript n denote the time level, subscript i is the cell index, Δt is the time step, $\mathbf{f}_w$ and $\mathbf{f}_E$ are the fluxes through the west and east cell interfaces and $\mathbf{g}_S$ with $\mathbf{g}_N$ are the fluxes through the south and north cell interfaces. These fluxes are calculated by solving local Riemann problems defined at the corresponding cell interfaces using an appropriate Riemann solver and an HLLC approximate Riemann solver (Toro et al., 1994) is employed in this work. Taking the east interface flux $\mathbf{f}_E$ as an example, it can be computed as follows:

$$\mathbf{f}_E = \begin{cases} \mathbf{f}_L & \text{if } 0 \le S_L \\ \mathbf{f}_{*L} & \text{if } S_L \le 0 \le S_M \\ \mathbf{f}_{*\mathrm{R}} & \text{if } S_M \le 0 \le S_R \\ \mathbf{f}_\mathrm{R} & \text{if } 0 \ge S_R \end{cases} \tag{A.5}$$

Here $\mathbf{f}_L = \mathbf{f}(\mathbf{u}_L)$ and $\mathbf{f}_R = \mathbf{f}(\mathbf{u}_R)$ are estimated from the left and right Riemann states $\mathbf{u}_L$ and $\mathbf{u}_R$ defining the local Riemann problem. The Riemann states $\mathbf{u}_L$ and $\mathbf{u}_R$ are reconstructed from the central values of the flow variables by applying a piece-wise linear approach that leads to second-order accuracy in space. $\mathbf{f}_{*\mathbf{L}}$ and $\mathbf{f}_{*\mathbf{R}}$ are the numerical fluxes in the left and right sides of the middle (contact) wave of the Riemann solution. S_L, S_M and S_R are the estimated speeds of the left, middle (contact) and right waves. of the HLLC Riemann solution structure. $\mathbf{f}_{*L}$ and $\mathbf{f}_{*R}$ are calculated from:

$$\mathbf{f}_{*\mathbf{L}} = \begin{bmatrix} \mathbf{f}_{*1} \\ \mathbf{f}_{*2} \\ \mathbf{v}_{\mathbf{L}}\mathbf{f}_{*1} \end{bmatrix} \quad \text{and} \quad \mathbf{f}_{*\mathbf{R}} = \begin{bmatrix} \mathbf{f}_{*1} \\ \mathbf{f}_{*2} \\ \mathbf{v}_{\mathbf{R}}\mathbf{f}_{*1} \end{bmatrix} \tag{A.6}$$

In here, v_L and v_R are the tangential velocity components of the left and right hand side of the Riemann states. The first $\mathbf{f}_{*1}$ and second $\mathbf{f}_{*2}$ entries of the flux vector $\mathbf{f}_*$ in the middle region can be calculated by the HLL formula proposed by Harten et al. (1983).

$$\mathbf{f}_* = \frac{S_R\mathbf{f}_L - S_L\mathbf{f}_R + S_R S_L(\mathbf{u}_R - \mathbf{u}_L)}{S_R - S_L} \tag{A.7}$$

To apply the HLLC scheme for solving the shallow water equations, it require an identification of the correct left, middle and right wave speed, S_L, S_M and S_R. Fraccarollo and Toro (1995) suggested using a two-rarefaction approximate Riemann solver and S_L and S_R can be calculated using the following formulae:

$$\mathrm{S_L} = \begin{cases} \mathrm{u_R} - 2\sqrt{\mathrm{gh_R}} & \text{if } \mathrm{h_L} = 0 \\ \min(\mathrm{u_L} - \sqrt{\mathrm{gh_L}}, \mathrm{u_*} - \sqrt{\mathrm{gh_*}}) & \text{if } \mathrm{h_L} > 0 \end{cases} \tag{A.8}$$

$$\mathrm{S_R} = \begin{cases} \mathrm{u_L} + 2\sqrt{\mathrm{gh_L}} & \text{if } \mathrm{h_R} = 0 \\ \max(\mathrm{u_R} + \sqrt{\mathrm{gh_R}}, \mathrm{u_*} + \sqrt{\mathrm{gh_*}}) & \text{if } \mathrm{h_R} > 0 \end{cases} \tag{A.9}$$

Here, u_L, u_R, h_L and h_R are left and right initial values for a local Riemann problem, u_* and h_* are evaluated as follows:

$$u_* = \tfrac{1}{2}(u_L + u_R) + \sqrt{gh_L} - \sqrt{gh_R} \tag{A.10}$$

$$h_* = \frac{1}{g}\left[\frac{1}{2}(\sqrt{gh_L} + \sqrt{gh_R}) + \frac{1}{4}(u_L - u_R)\right]^2 \tag{A.11}$$

The middle wave speed S_M can be calculated as Toro (2001) recommended:

$$S_M = \frac{S_L h_R(u_R - S_R) - S_R h_L(u_L - S_L)}{h_R(u_R - S_R) - h_L(u_L - S_L)} \tag{A.12}$$

This scheme is used for computing the east interface flux and similar formula is applied to calculate the other cell interfaces.

In order to update the flow variables to a new time step, it is also necessary to properly evaluate the source terms. Due to the use of the pre-balanced shallow water equations as given in (A.1) and (A.2), the bed slope source terms can be simply evaluated using a central-differencing scheme at the cell centre. For example, the source terms in the *x*-direction are discretized as:

$$-\frac{\tau_{bx}}{\rho} - g\eta\frac{\partial z_b}{\partial x} = -\left(\frac{\tau_{bx}}{\rho}\right)_i^n - g\eta_i^n\left(\frac{z_{bE}-z_{bW}}{\Delta x}\right) \tag{A.13}$$

where z_{bE} and z_{bW} are the bed elevation at the mid-point of the east-west interfaces of cell i. To maintain better numerical stability for simulations involving wetting and drying, the friction source terms are calculated separately using a point-wise implicit scheme as proposed in Liang (2010). The above numerical scheme is only first-order accurate in time and second-order accuracy can be achieved using the MUSCL-Hancock method (refer to Liang and Borthwick (2009) for detailed implementation of this scheme).

The current numerical scheme is overall explicit and its numerical stability is governed by the Courant-Friedrichs-Lewy (CFL) criterion. The appropriate time step Δt will be decided by the following expression:

$$\Delta t = C\min(\Delta t_x, \Delta t_y) \text{ In which } \quad \Delta t_x = \min\frac{\Delta x_i}{|u_i| + \sqrt{gh_i}} \text{ and } \Delta t_y = \min\frac{\Delta y_i}{|v_i| + \sqrt{gh_i}} \tag{A.14}$$

Here, Δx_i and Δy_i are the cell dimensions, u_i and v_i are the depth-averaged velocity components at the cell centre. The Courant number C is in the range of $(0 < C \le 1)$. In the present study the Courant number applied is equal to 0.5.

A.2.1 *Boundary conditions*

The numerical model has reflective slip and normal transmissive open boundary conditions. In the x-direction the boundary condition can be imposed as follows

At slip boundary boundaries

$$h_B = h_I, \quad \hat{u}_B = 0, \quad \hat{v}_B = \hat{v}_I \tag{A.15}$$

At open boundary conditions which are implemented based on Riemann invariants according to the local Froude number as shown below

1. $Fr < 1$ (Subcritical flow)

$$\hat{u}_B = \hat{u}_I \pm 2\sqrt{g}(\sqrt{h_I} - \sqrt{h_B}), \ \hat{v}_B = \hat{v}_I, \tag{A.16}$$

In which h_B is prescribed.

Or

$$\hat{h}_B = \left(\sqrt{h_I} \pm \frac{1}{2\sqrt{g}}(\hat{u}_I - \hat{u}_B) \right), \quad \hat{v}_B = \hat{v}_I, \tag{A.17}$$

In which $\hat{u}_B$ is prescribed.

The sign dependent on the flow direction inflow (–) ; outflow (+)

3. $Fr > 1$ (Supercritical flow)

For inflow, the variables $h_B, \hat{u}_B$ and $\hat{v}_B$ are prescribed and for outflow

$h_B = h_I, \quad \hat{u}_B = \hat{u}_I, \quad \hat{v}_B = \hat{v}_I$

Note that $\hat{u}$ and $\hat{v}$ are the depth-averaged velocity components in normal and tangential directions to the boundary and the subscripts B and I represent the positions at the ghost boundary (next to the boundary) and inner boundary cells.

Appendix (B). The ADCP data registered for springs and neaps tidal current profiles.

B.1. Tidal current profiles for neap tidal wave period

The investigation of the neap period tidal current profiles showed the maximum tidal current profiles can rise to about 0.14 m/sec whereas most of the values are actually below this maximum. The investigation of tidal current profiles of the neap period begins from Figure B.1 to Figure B.6. The majority of the tidal current profiles indicate negative direction as can be seen from Figure B.3 at point 5 towered Figure B.6 at point 12.

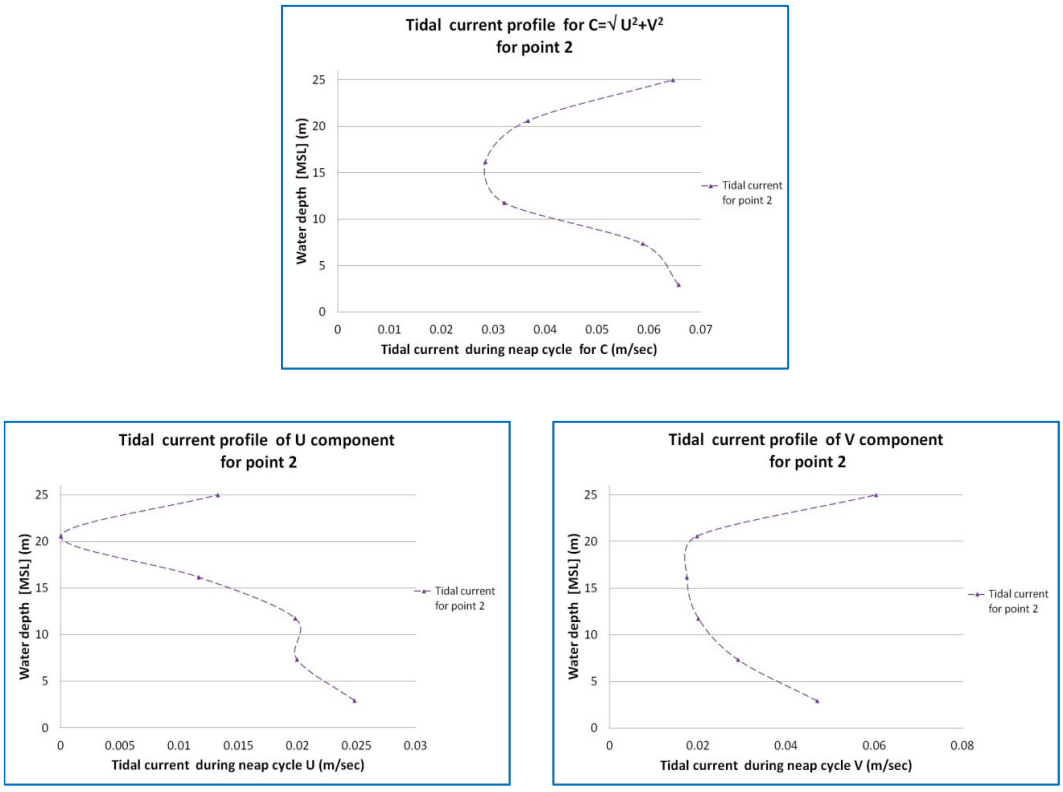

Figure B.1 The tidal current profiles of the point 2 that presents the tidal current *C* and the two *U* and *V* components during the neap period.

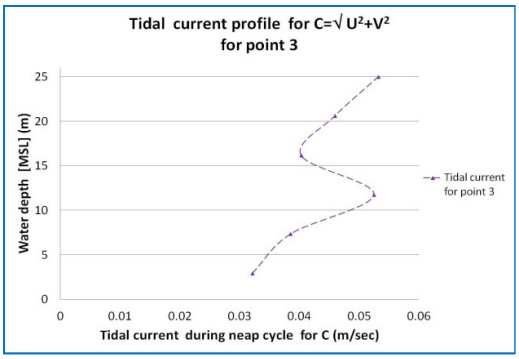

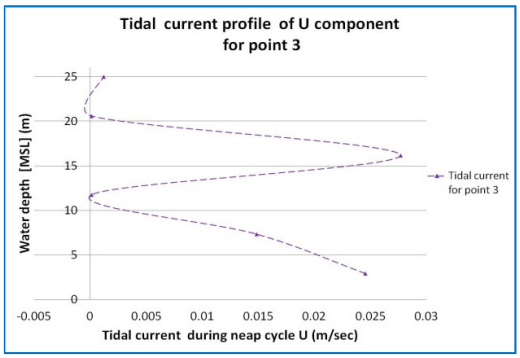

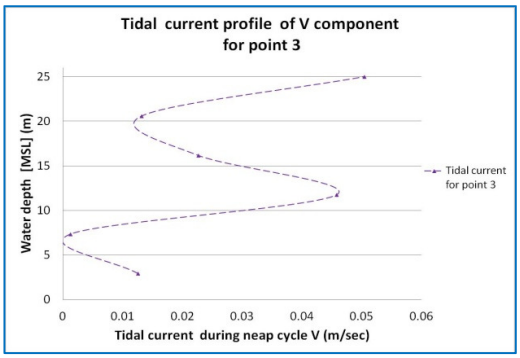

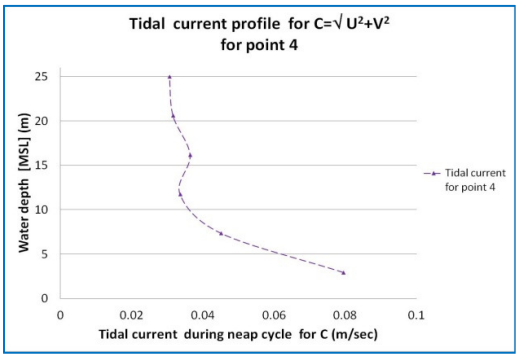

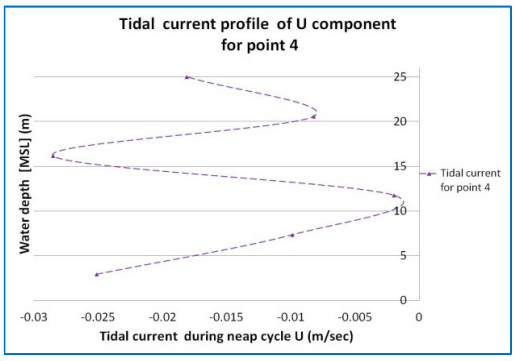

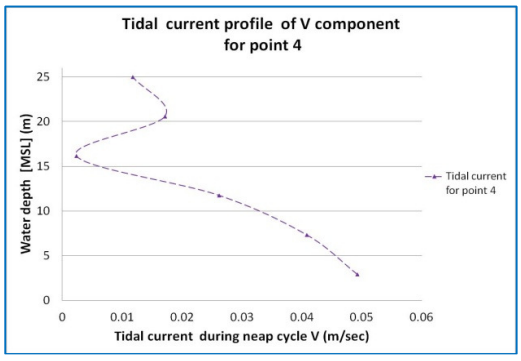

Figure B.2 The tidal current profiles for the two points of 3 and 4 that show the tidal current *C* and the two *U* and *V* components in the neap cycle.

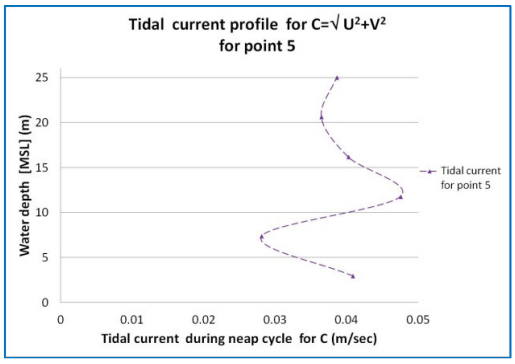

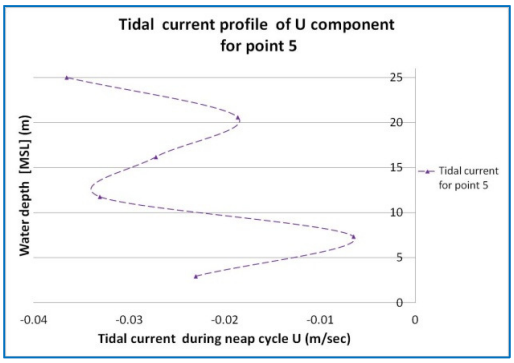

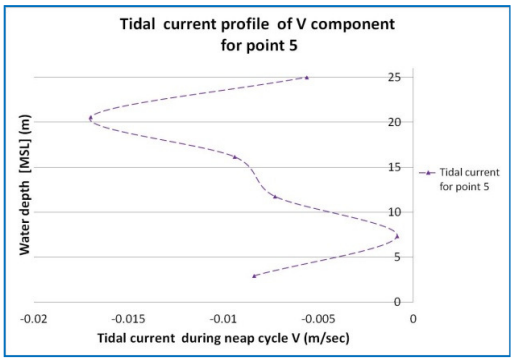

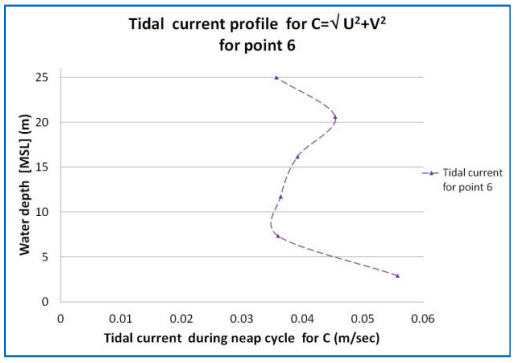

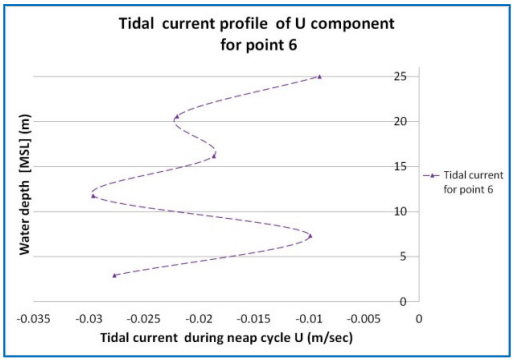

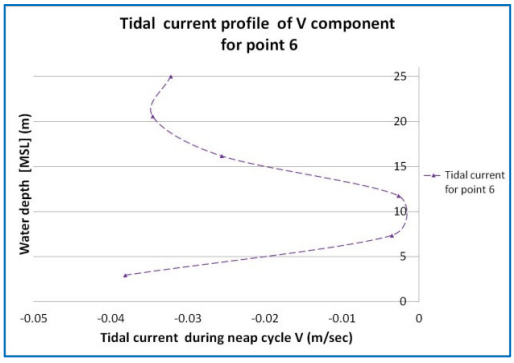

Figure B.3 The tidal current profiles of the two points of 5 and 6 that demonstrate the tidal current *C* with the two *U* and *V* components of neap period.

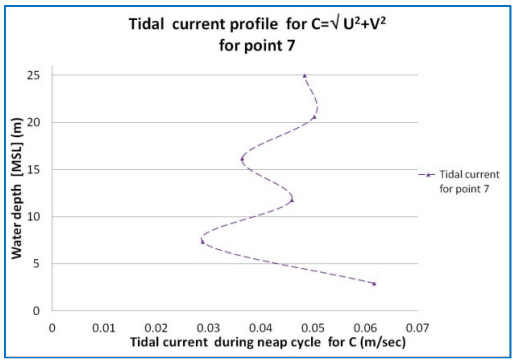

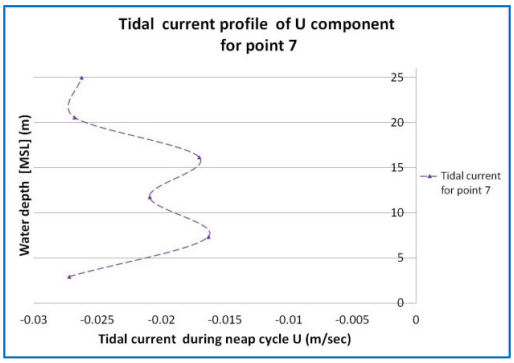

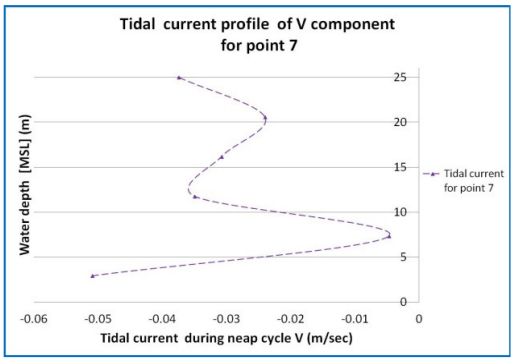

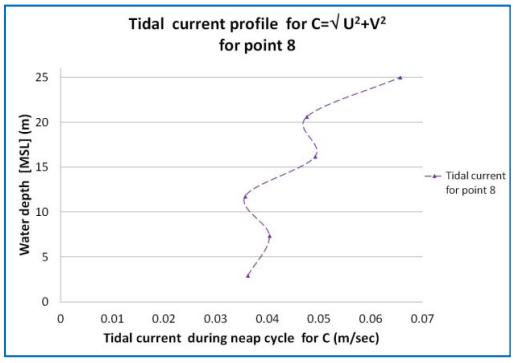

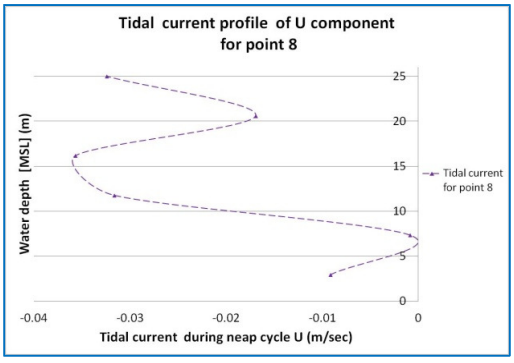

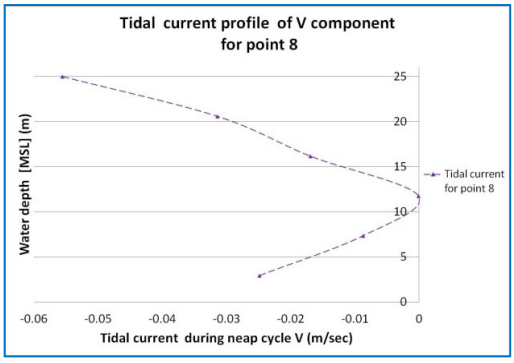

Figure B.4 The neap period tidal current profiles of the two positions of 7 and 8 that exhibited the tidal current *C* and the two *U* and *V* components.

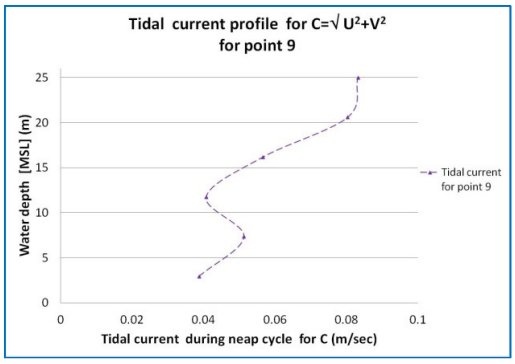

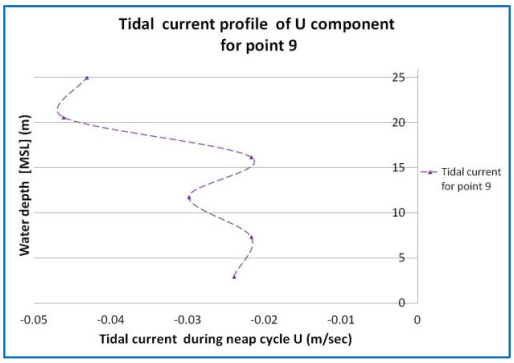

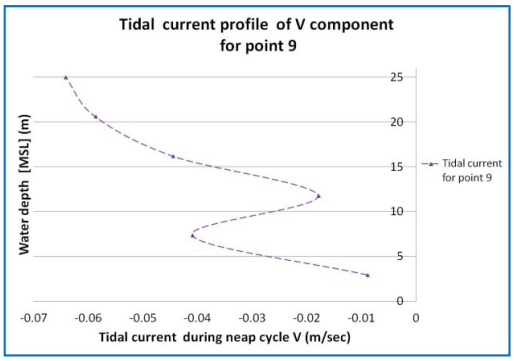

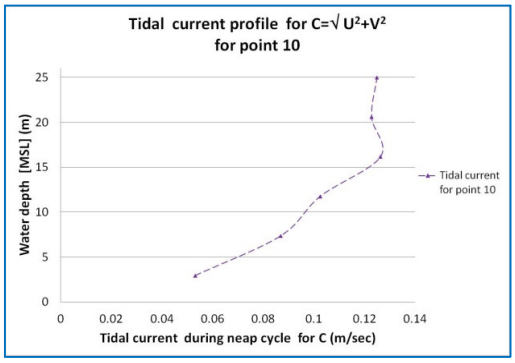

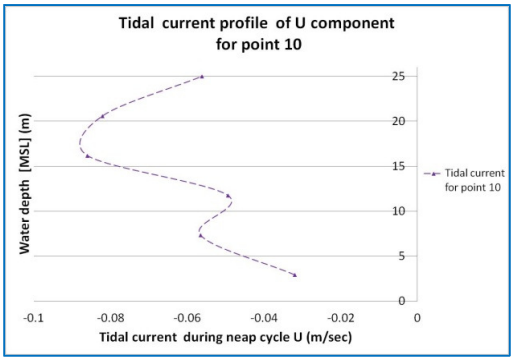

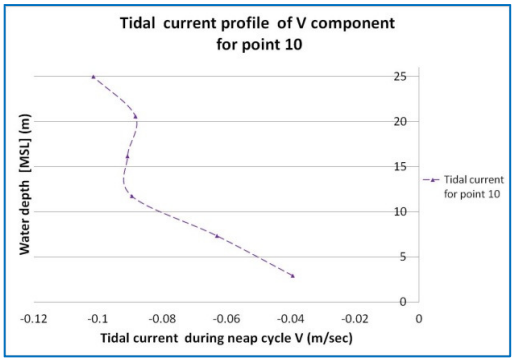

Figure B.5 The tidal current profiles of the two positions of 9 and 10 which present the tidal current *C* and the two *U* and *V* components within the neap cycle.

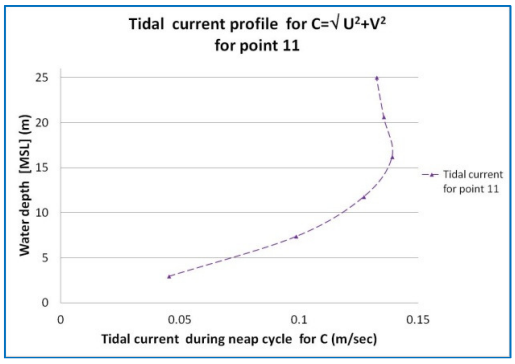

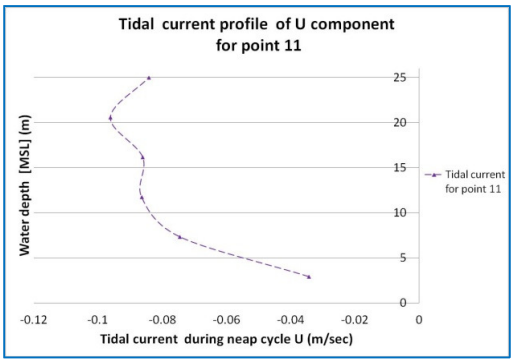

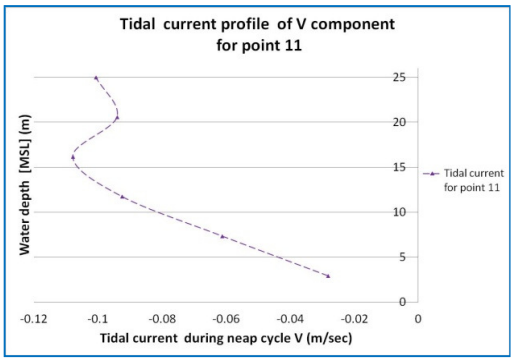

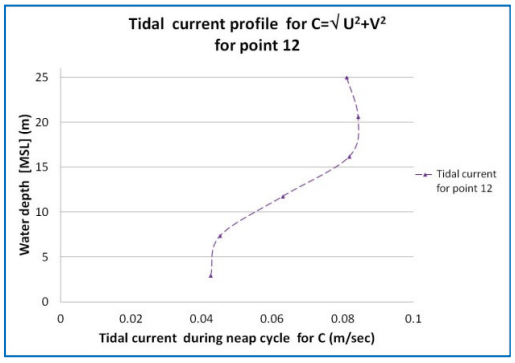

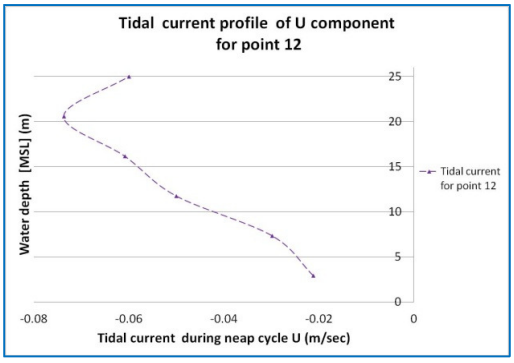

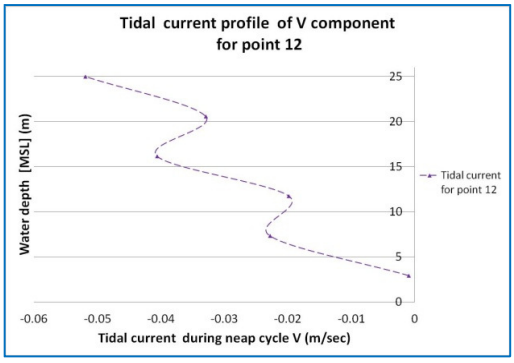

Figure B.6 The tidal current profiles of the two positions of 11 and 12 which are showing the tidal current *C* and the two *U* and *V* components during the neap cycle.

B.2.Tidal current profiles for spring tidal wave period

The spring tidal wave has been processed using a similar method to that used for the neap period. The tidal current data from the ADCP instrument was taken in the hour's time duration as described in chapter four. In similarly process to the neap cycle the tidal current profiles was tender by applying the three moving average values that result a smooth curve that can applied as an input for three-dimensional turbulent simulation.

However, there are twelve tidal current profiles within the spring cycle that was adopted with the method of three rolling average and the tidal current profiles of the eleven profiles are shown from Figure B.7 to Figure B.12. Note that, the first tidal current profile is already presented in chapter four. The tidal current *C* was displayed with the two components *U* and *V* which can indicates the tides cycle as it change between the flood and ebb cycles. The maximum tidal current profile seen in the figures was in the Figure B.10 with peak value reach 0.5 m/sec which was as expected from previous investigation of the ADCP data record that indicates the higher values are in the ebb cycle.

Most of the high velocity tidal current profiles are in the ebb cycle as was found with the neap period but, since the tidal wave is in the spring period, the currents collected are of a higher speed than those found in the neap cycle.

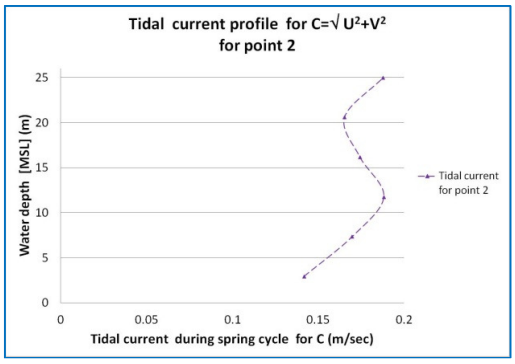

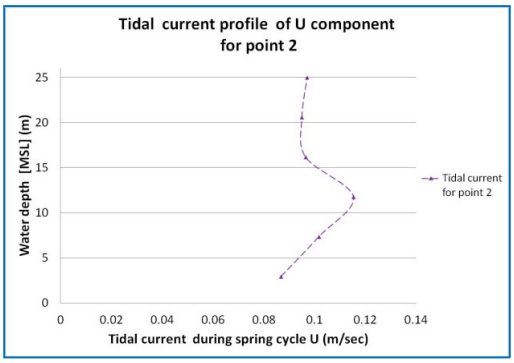

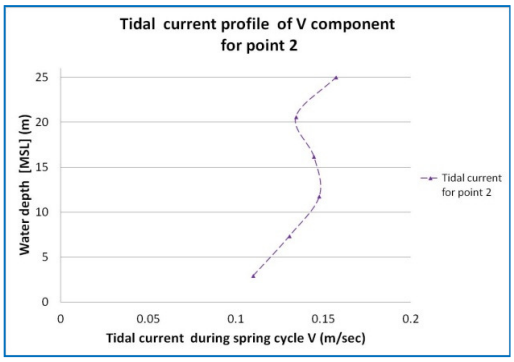

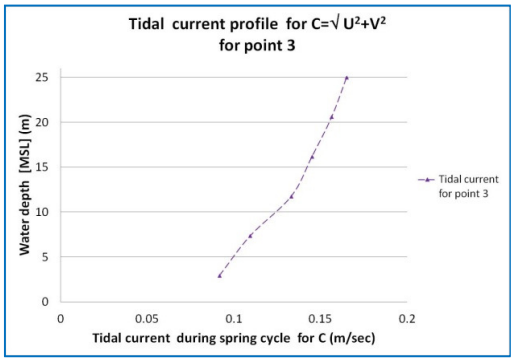

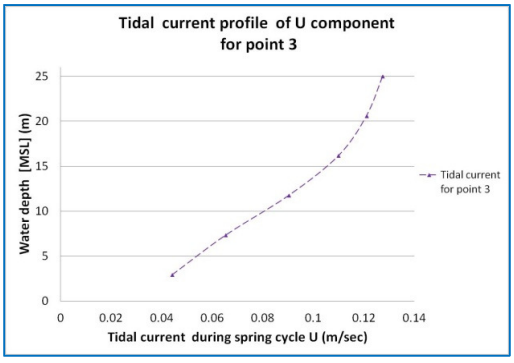

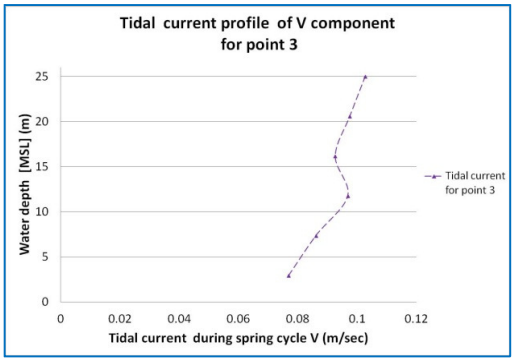

Figure B.7 The tidal current profiles of tidal flow *C* and the two *U* and *V* components at the two point positions of 2 and 3 within the spring period.

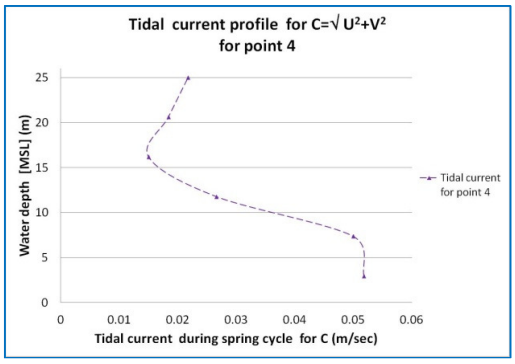

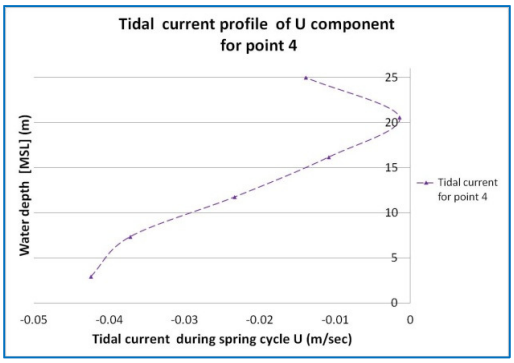

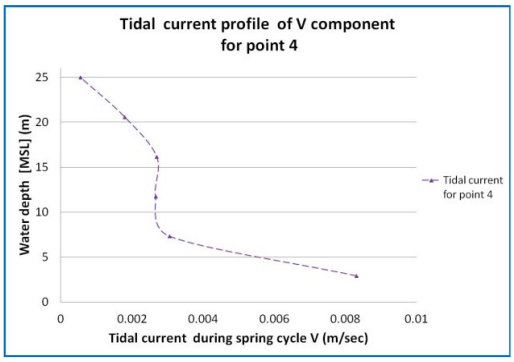

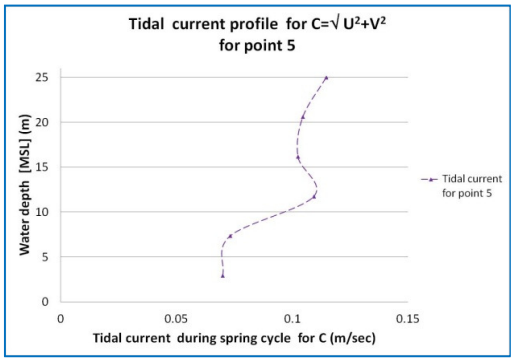

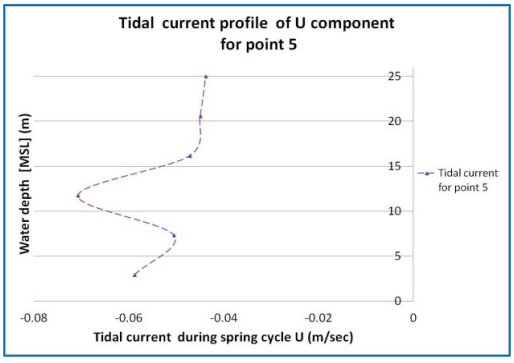

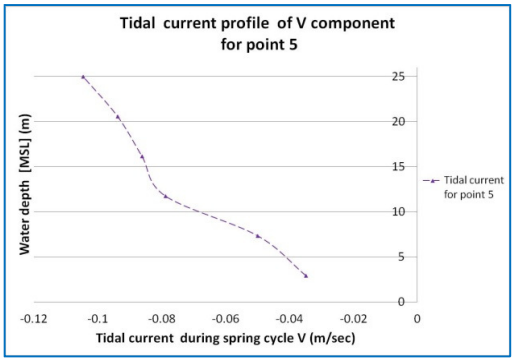

Figure B.8 The two positions of 4 and 5 that show the tidal current profiles *C* and the two *U* and *V* components in the spring period.

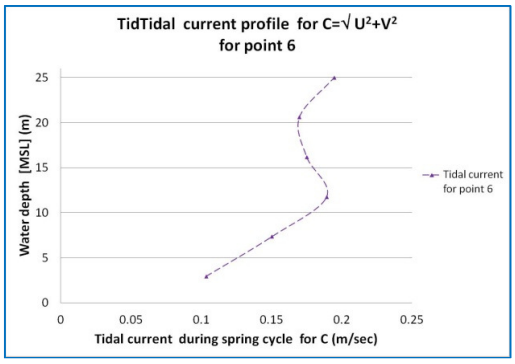

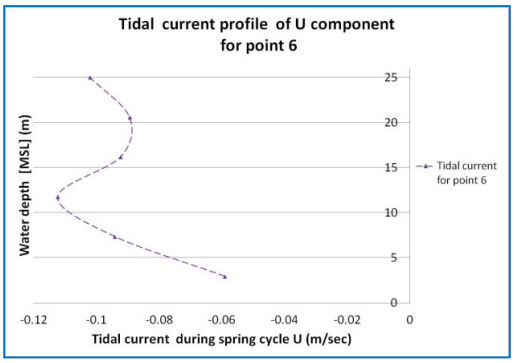

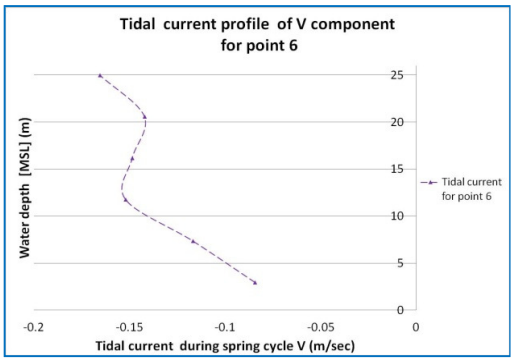

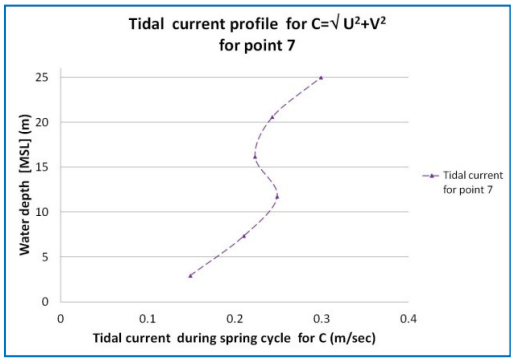

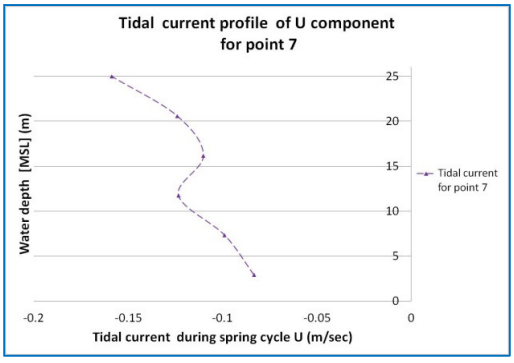

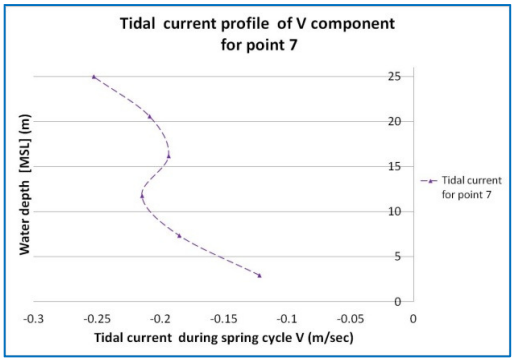

Figure B.9 The tidal current profiles for the two positions of 6 and 7 as the tidal current *C* and the two *U* and *V* components are demonstrated in the spring duration.

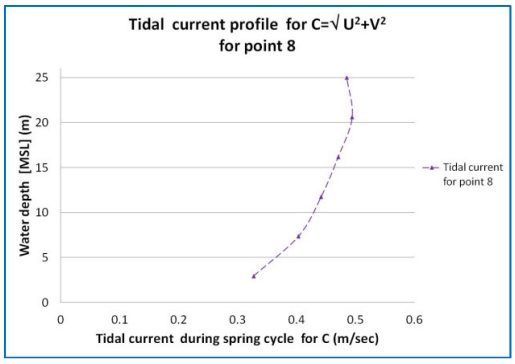

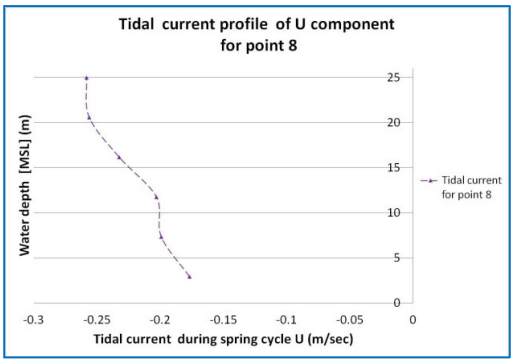

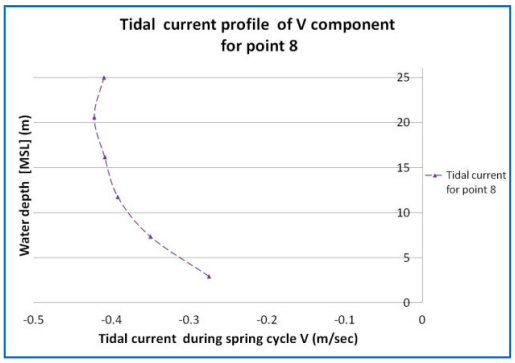

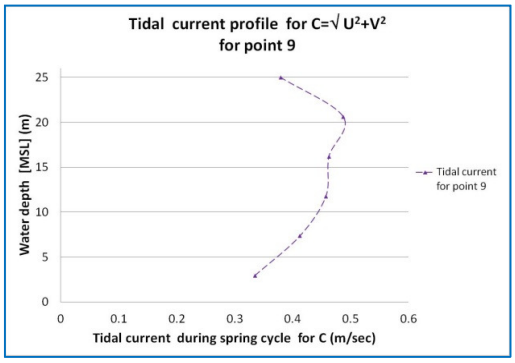

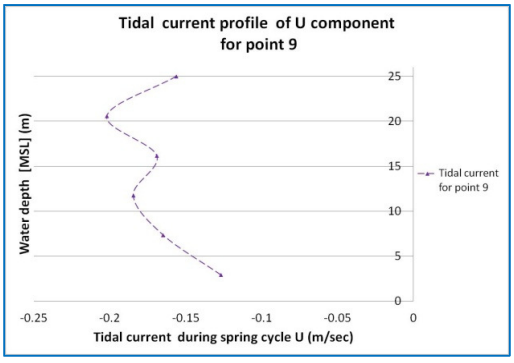

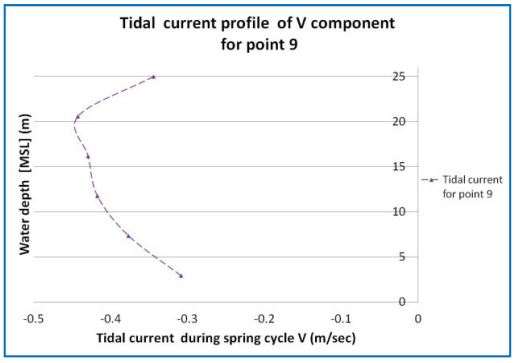

Figure B.10 The spring period tidal current profiles of the two point positions of 8 and 9 that exhibited the tidal current *C* and the two *U* and *V* components.

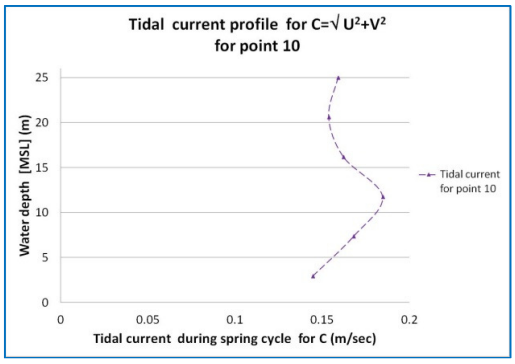

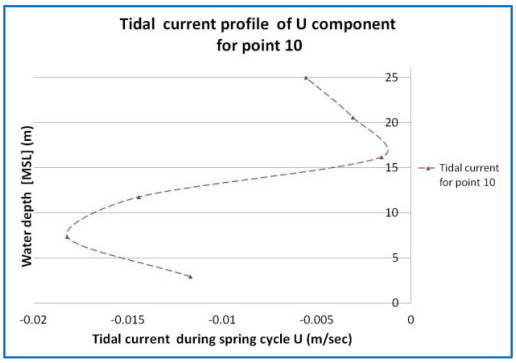

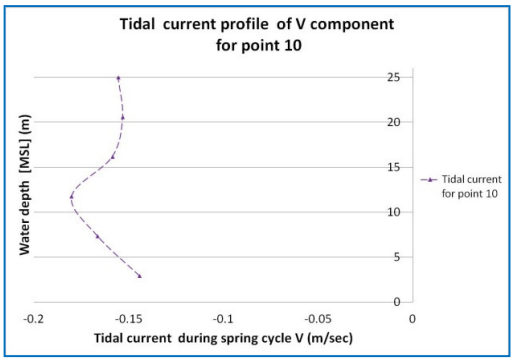

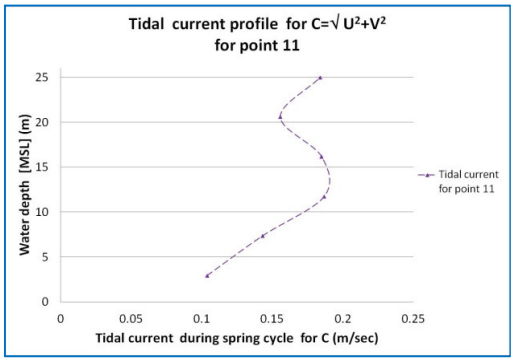

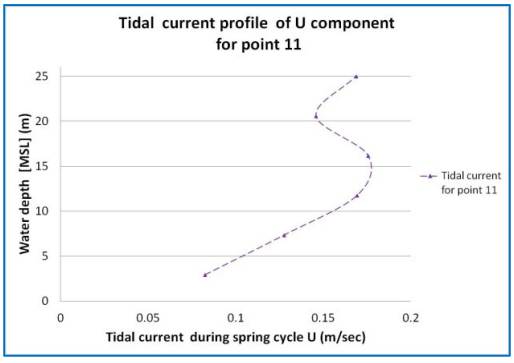

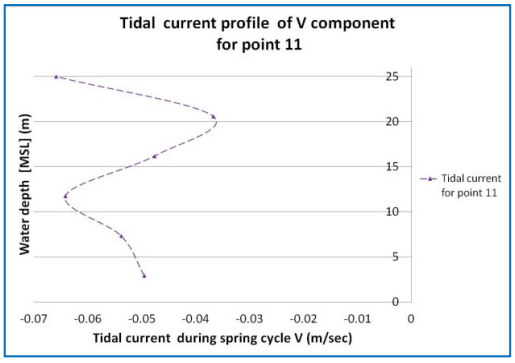

Figure B.11 The two positions of 10 and 11 which represent the tidal current profiles of *C* and the two *U* and *V* components within the spring cycle.

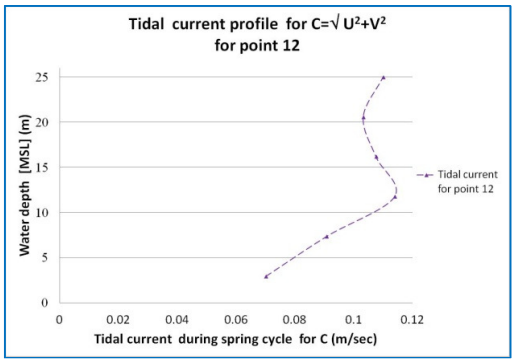

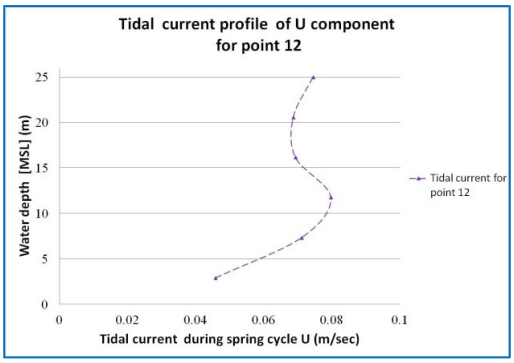

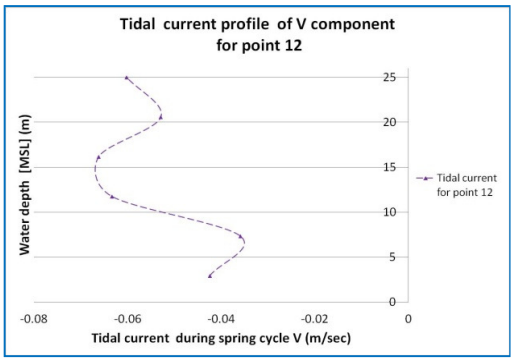

Figure B.12 The final tidal current profile for the tidal current *C* and the two *U* and *V* components of the point position 12 during the spring period.

Appendix (C).

The paper published in ISOP (International Offshore and Polar Engineering Conference-2012)

Proceedings of the Twenty-second (2012) International Offshore and Polar Engineering Conference
Rhodes, Greece, June 17–22, 2012

ISBN 978-1-880653-94-4 (Set); ISSN 1098-6189 (Set)

www.isope.org

Tidal Simulation in Loch Linnhe Using a Finite Volume Shallow Flow Model

Yassir Al-Bourae[1]; Qiuhua Liang[2] and Martin Downie[1]
[1] School of Marine Science and Technology, Newcastle University
[2] School of Civil Engineering and Geosciences, Newcastle University
Newcastle upon Tyne, England, UK

ABSTRACT

Tidal flow hydrodynamics near coastlines can be very complex due to the presence of complicated bottom topographies and irregular boundaries. The model described in this paper has been developed for the prediction of tidal flows on a global scale to inform further detailed modeling on a local scale using 3-D methods. This work presents the numerical simulation of tidal flow in Loch Linnhe on the west coast of Scotland. The numerical model adopted solves the two-dimensional shallow water equations using a finite volume Godunov-type scheme directly applied to the complex, but idealized, flow hydrodynamics involved in the different regimes treated. The results are in good agreement with field measurements, which indicates that the model is able to represent the complex tidal conditions in this area convincingly.

KEY WORDS: 2D shallow water equations; finite volume Method Godunov-type scheme; tidal flow modeling; Loch Linnhe.

INTRODUCTION

Researchers and engineers are interested in tidal flow hydrodynamics for many reasons. In recent years, tidal flow hydrodynamics has been studied for the mitigation of any adverse impacts on those people living near coastal areas. In fact, much of the world's shorelines are subject to severe coastal flooding and serious coastal erosion in the event of storm surges and extreme high tides (e.g. Wolf 2009; Ozer et al. 2000; Ding and Wang 2005). In the context of ongoing climate change, this type of extreme event is becoming more frequent. Another area of application involves the concept of sustainable fisheries, which has also revived the interest in artificial reefs as an alternative solution to marine ecosystem recovery.

In the present instance, the authors are concerned with investigating the flow about artificial reefs that have been installed on the sea bed of Loch Linnhe off the West coast of Scotland. The model described in the following sections concerns the large scale prediction of tidal flows in Loch Linnhe. Further detailed study of the flow about the reefs will be described in a subsequent paper.

LITERATURE REVIEW

Today, an important way of understanding tidal flow hydrodynamics involves the use of computer modeling. There are many models available to evaluate tidal flow based on different numerical methods, such as the Finite Different Method (FDM) (e.g. Garcia and Kahawitha 1986; Fennema and Chaudhry 1989 and 1990), the Finite Element Method (FEM) (e.g. Akanbi and Katopodes 1988), the Discontinuous Galerkin Finite Element Method (DG FEM) as described by Aizinger and Dawson (2002) as well as Yu and Kyozuka (2004), the Finite Volume Method (e.g. Zhao et al. 1994), and the Lattice Boltzmann Method (LBM) (e.g. Chen and Doolen 1998; Zhou 2002; Banda et al. 2009). Specifically, The FVM has the same advantages of simplicity as the FDM and the same flexibility in handling complex domain geometry as for the FEM, and it can be implemented on both structured and unstructured meshes (Aghajanloo et al. 2011).

The FDM has been the most commonly used method so far in tidal flow simulations. The Princeton ocean model (POM) (Casulli and Cheng 1992) used the FDM to solve the primitive three-dimensional flow equations (assuming the hydrostatic pressure distribution in the vertical direction) and has been applied to simulate flooding and drying of tidal mud-flats. Another well-known finite difference tidal flow model has been developed by the Marine Environmental Committee (MEC) in Japan (Yang et al. 2008), which has been widely used by the Japanese Society of Naval Architects and Ocean Engineering to study changes in the water level of the Caspian Sea. Although the finite difference models may predict accurate results for applications where the solution is smooth they are less well adapted for coping with more complex flow hydrodynamics that involve flow discontinuities (Yu and Kyozuka 2004). The FEM based models have also been applied to tidal flow modeling. For example, Walters (1989) compared two finite element models in predicting the North Sea Tides in English Channel. As a finite element based shallow flow model, TELEMAC has been widely applied in coastal simulations (e.g. Jones and Davies 2006; Hervouet 2007). However, similar to the finite difference models, the finite element codes encounter the same obstacles when applied to flow problems. In recent years, the DG FEM has gained popularity in solving the shallow water equations. Although it is less popular, the DG

FEM based shallow water flow models have also been employed in simulating tidal flows (e.g. Aizinger and Dawson 2002). and have produced promising results (Krivodonova et al. 2004). However, the DG type models are generally computationally much more demanding. Another type of shallow water flow model that has been used in tidal flow modeling is based on the finite volume Godunov-type scheme. For example, Chippada et al. (1998) used such a model to simulate tidal waves in Galveston Bay in USA. Compared with the aforementioned approaches, the finite volume Godunov-type models automatically accept complex flow conditions such as flow discontinuities and are computationally much more efficient than the DE FEM codes. In this work, a finite volume model is adopted to investigate the complex tidal hydrodynamics in Loch Linnhe caused by its complicated seabed and meandering coastline. The present model solves the non-linear shallow water equations using a Godunov-type numerical scheme combined with an HLLC approximate Riemann solver on a Cartesian uniform grid (Liang 2010). The model has been intensively tested for fluvial flood modeling (Liang 2010) but has not been applied in modeling tidal flow hydrodynamics.

NUMERICAL MODEL

Tidal flows may be mathematically described by the 2D shallow water equations (SWEs) that are derived from the 3D Reynolds averaged Navier-Stokes equations by assuming a hydrostatic pressure distribution. Ignoring the Coriolis effects, viscous terms and surface stresses, the non-linear SWEs may be written a matrix form as:

$$\frac{\partial \mathbf{u}}{\partial t}+\frac{\partial \mathbf{f}}{\partial x}+\frac{\partial \mathbf{g}}{\partial y}=\mathrm{S} \qquad (1)$$

where x and y are the Cartesian coordinates, t denotes time and **u**, **f**, **g** and S are the vectors containing the flow variables, x- and y-direction fluxes and source terms. The vectors may be given as follows (Liang and Borthwick 2009)

$$\mathbf{u}=\begin{bmatrix}\eta\\ uh\\ vh\end{bmatrix} \quad \mathbf{f}=\begin{bmatrix}uh\\ u^2h+\frac{1}{2}g(\eta^2-2\eta z_b)\\ uvh\end{bmatrix}$$

$$\mathbf{g}=\begin{bmatrix}vh\\ uvh\\ v^2h+\frac{1}{2}g(\eta^2-2\eta z_b)\end{bmatrix} \quad \mathrm{S}=\begin{bmatrix}0\\ -\frac{\tau_{bx}}{\rho}-g\eta\frac{\partial z_b}{\partial x}\\ -\frac{\tau_{by}}{\rho}-g\eta\frac{\partial z_b}{\partial y}\end{bmatrix} \qquad (2)$$

where u and v are depth-averaged velocity components in the x- and y-directions, respectively, η is the water level, $h = \eta - z_b$ is the total water depth with z_b being the bed elevation above the datum, g is the gravity acceleration, ρ is the water density, $\partial z_b/\partial x$ and $\partial z_b/\partial y$ are defined as the bed slope in the two Cartesian directions, and τ_{bx} and τ_{by} are the bed friction stresses that can be calculated by the following empirical formulas:

$$\tau_{bx}=\rho C_f u\sqrt{u^2+v^2} \quad \text{and} \quad \tau_{by}=\rho C_f v\sqrt{u^2+v^2} \qquad (3)$$

where $C_f = gn^2/h^{1/3}$ is the bed roughness coefficient with n being the Manning coefficient.

The model employed in this work solves the above SWEs using an explicit finite volume Godunov-type scheme, which was originally developed for flood simulations. Details of the model may be found in Liang (2010). Finite volume Godunov-type scheme is applicable for predicting a variety complex flow hydrodynamics and is well-suited for handling complex tidal flow phenomena that are considered in this work.

CASE STUDY TOPOLOGY

The site chosen for the case study is the artificial reef site in Loch Linnhe located on the West Coast of Scotland as shown in Fig.1. The reef was deployed by under the direction of Dunstaffnage Marine Laboratory in 2001 (Sayer and Wilding 2002). It was designed by the fishing industry to promote the economic potential of reef-based fisheries such as that of the European Lobster (*Homarus gammarus* (L.)). The size of the reef site equates to about 50 football pitches (Beaumont 2007). There are 42 artificial reefs of two different types of reef module and 25,000 tons of concrete blocks have been used to create each one of them, see Fig.2. The reefs are intended to alter the biological habitat of the area. Moreover, it may affect the original tidal current profile due to the change of seabed (Wilding and Sayer 2002).

The water depth varies from 1m to 181 m in Loch Linnhe and so wetting and drying process may be involved. The UK Hydrographic Office recorded a tidal range of the Loch varies from 1 – 2.5 m in a lunar month (Hydrographic Office 2011). According to the Marine Resource Center, a tidal flow between 4 - 6 knots at spring tides has been noticed in this coastal area (Marine Resource Center 2011). Simulation of these conditions requires a numerical model that can handle complex flows with a good accuracy.

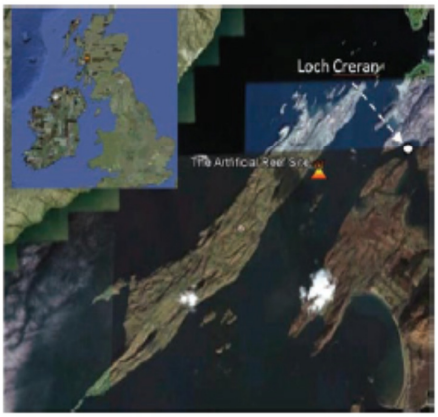

Fig. 1 Loch Linnhe artificial reef site.

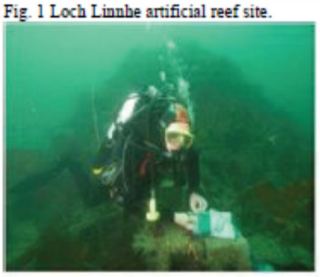
Fig. 2 The artificial Reef made from concrete blocks.

FIELD MEASUREMENT

The bathymetry of the Loch Linnhe was digitized from an Admiralty Chart (Admiralty Chart 2010) giving water depth and the coastline boundary cells (dry) which were raised to 220 m as indicated in Fig. 3. The map has been converted from GPS system format to Cartesian Coordinates grid matrix equal to (94 × 89 cells) as seen from Fig. 3. The field measurements were carried out using ADCP (Acoustic Doppler Current Profiler) instruments. These instruments were deployed in positions near the Artificial Reefs to record the tidal elevation and current used for setting initial conditions and validating the numerical model. The location of the ADCP instruments is shown in Fig. 3.

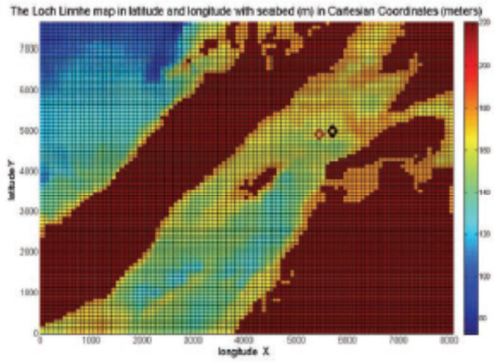

Fig. 3 The Loch in Cartesian Coordinate system with the positions of ADCP instruments in the Loch Linnhe.

The ADCP is a sonar system that is capable of measuring water current velocities for a range of water depths, as illustrated in Fig. 4. The duration of the measurements was 57 days, which includes the spring and neap tides. The ADCP was equipped with a pressure sensor to check the tidal elevation.

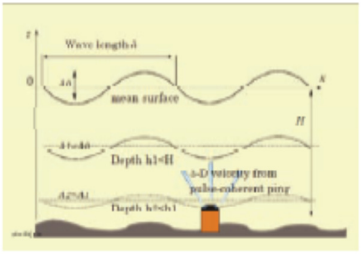

Fig. 4 The ADCP measuring the water velocities in Bin Layers.

The ADCP measured data were investigated and analyzed to show how the velocity components varied over a two cycles of tide wave period and a four cycles of tide wave period, as shown in Fig. 5. The tidal elevation is represented by the green curves in the figures, which also show the U and V components of the velocity profiles of tidal current (cm/sec) for periods of 24 hours and about two and half days. The tidal velocity component U varies between -30 – 10 cm/sec in the *West–East* direction whereas V component varies between -40 – 20 cm/sec in the *South-North* direction in tides cycles as shown in Fig. 5. The ADCP velocity data is unrealistic near the seabed due to reflections of the sound which contaminate the acoustic signals. It is advised to extract %15 of the velocity data from the bottom (Aubrey and Friedrichs 1992). A similar phenomenon occurs at the free surface and the readings for the first 4m depth and the last 3m were discarded in Fig.5.

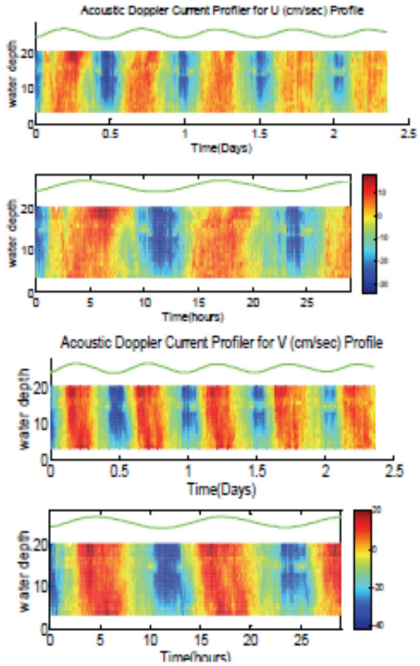

Fig. 5 The tidal current components U and V for about 24 Hours and 2.5 Days.

NUMERICAL SIMULATION

The 8072.4 m × 7638.4 m solution domain used in the numerical simulation is discretized into a 94 × 89 mesh as shown in Fig. 3. This gives the size of each 2D cell as 86 m × 86 m. In order to save computational time, those regions that are dry or not of interest are blocked and classified as solid cells (dry bed), as shown in Fig. 6. Obviously the computational domain is only part of the region as presented in Fig. 3. As seen from Fig. 6 after constraining certain areas in the problem domain the maximum water depth in the new region is about 62.5 m. Thus, the topographical height of the new coastal boundary solid cells (dry bed) becomes 80 m see Fig. 6.

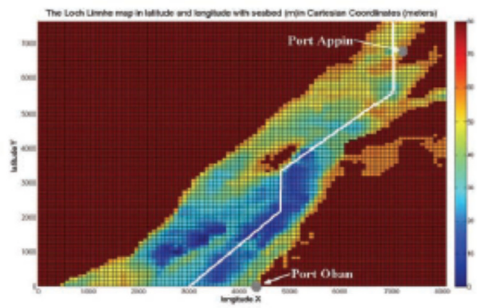

Fig. 6 The 2D modeled area with blocked solid cells (dry cells).

The initial still water level in the Loch is set to be 62.5 m. The water level (η) is defined as the surface elevation above datum, as sketched in Fig. 7.

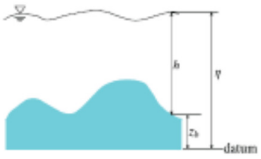

Fig. 7 Definition of relevant variables.

During the simulation, the boundary conditions of inflow and outflow are imposed using tidal records obtained from the UK Hydrographic Office (Hydrographic Office 2011) in the locations as indicated in Fig. 6. The tidal records at Oban, which are added to still water level of 62.5 m to set the tidal hydrodynamics at the inlet boundary, are shown in Fig. 9. Duration of 14 days is taken to investigate the spring and neap tides in the Loch. Tidal records for the same dates were obtained from the Hydrographic Office for Port Appin see Fig. 10. The tidal series has been adopted as the outlet boundary conditions.

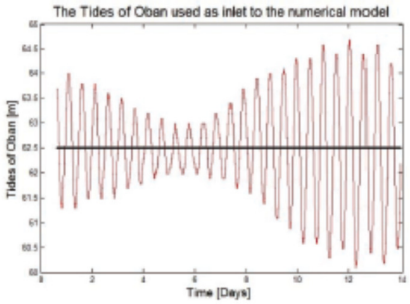

Fig. 9 The Oban tides used as at the inflow boundary in the numerical model.

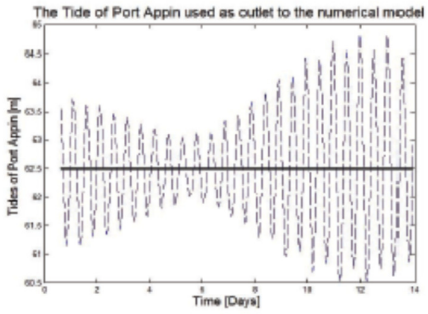

Fig. 10 Port Appin tides used at the outflow boundary in the numerical model.

RESULTS AND DISCUSSION

The numerical model was checked first for initial setup. The seabed topography is presented in Fig. 6, where a long cross-section is made to check the initial still water profile at t = 0, as shown Fig.11-a. During the 14-day simulation, the water surface profile along the long section is checked every 15 minutes and Fig. 12 shows the profile at t =15.35 hour as the tidal wave propagates through the Loch. The numerical results for the water level (i.e. surface elevation above lowest point of seabed), which agree closely with the ADCP measurement with only small differences in the spring tides are shown in Fig. 13. These results give confidence in the capability of the numerical model in handling the complex tidal hydrodynamics in Loch Linnhe. Note that the mean sea level (MSL) is set to 62.5 m which gives a tidal range of spring and neap that agree with Hydrographic record (Hydrographic Office UK 2011).

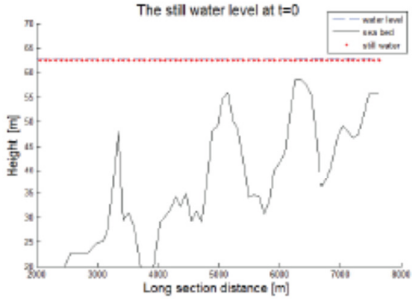

Fig.11-a The water elevation in the numerical domain for initial condition as seen from the long section cells.

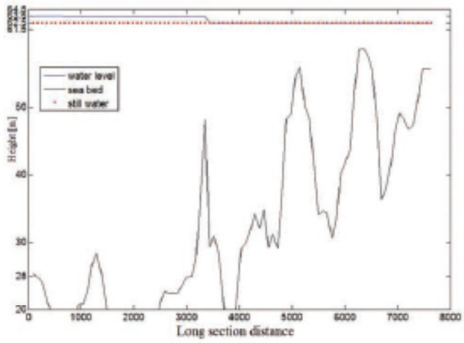

Fig.12 The tidal wave as it propagates in the Loch along the long section.

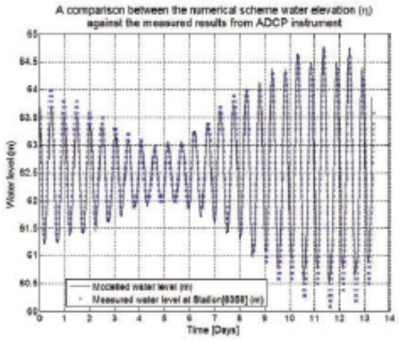

Fig.13 Numerical water elevation compared with measurements.

The calculated U and V velocity components are also presented and compared with the measured data in Fig. 14. The measured values of the velocity components shown in Fig. 4 were taken from one of the ADCP 'bins' in the middle third of the water column (Epler 2010). The numerically predicted U velocity component is compared with the measured one in Fig.14-a. and the V component is compared with the measured values in Fig.14-b. Both components show a similar behavior. The phase of both the U and V components of tidal flow computed by the numerical model is in good agreement with the measured values. The magnitude of the U component of the computed velocity agrees reasonably well with the measured component. The agreement of the V component is less good. In the model, inflow from Loch Car (Fig. 1) on the East coast of the computational domain was assumed to have a negligible effect on the flow in the vicinity of the artificial reefs (near the location of the ADCPs). In the event, it may be a factor in the discrepancy in the results, and this will be addressed in future studies.

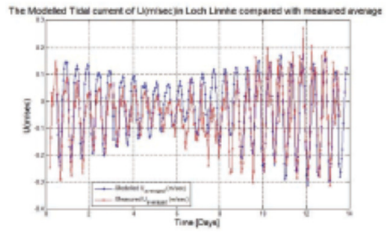

Fig.14-a. The x-direction component U (m/sec) compared with measured values from the ADCP at Loch Linnhe Artificial Reef site.

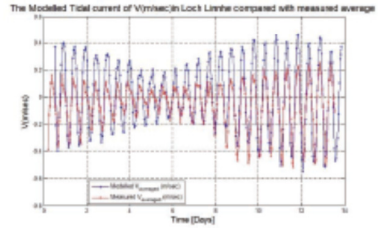

Fig. 14-b. The y-direction component V(m/sec) compared with measured values from the ADCP at Loch Linnhe Artificial Reef site.

The tidal velocity vectors over the whole solution domain with an 'incoming' tide are shown in Fig.15. The vectors achieved on flow reversal are shown in Fig. 16, which also shows the corresponding water level at that state of the tide along a section across the Loch outlet. Similar results have been generated every 15 minutes over the tidal cycle but no further results are presented here in the interests of brevity. There are no detailed measurements of the tidal flow away from the reefs, but the model behaves as would be expected. The flow is consistent with the complex Loch topology and accelerates in regions where the depth decreases or the channel narrows. The numerical model has shown the ability to predict the water elevation over the whole tidal cycle, as shown in Fig.16. Finally, the numerical model has been tested in flood simulation, as mentioned by Liang (2010), and it has displayed the ability to model tides and the average of tidal current with acceptable results.

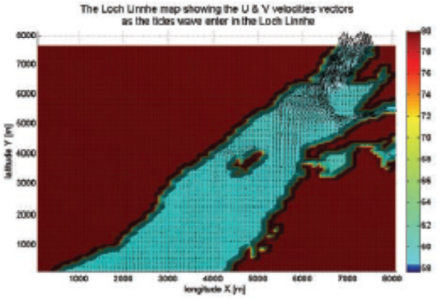

Fig.15 The velocity vector of the tidal current with an 'incoming' tide

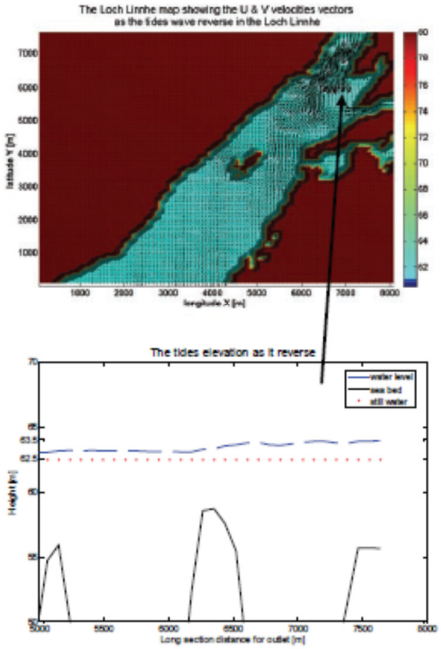

Fig.16 The velocity vectors as the tide reverses, together with the water level over a section across the Loch outlet

CONCLUSIONS

In this paper, a Godunov-type shallow water flow model has been applied to investigate the tidal flow hydrodynamics in Loch Linnhe. Numerical results have been compared with field data and good agreement between the predicted and measured water surface elevations was observed. There is a disparity in the magnitudes of the predicted and measured velocities. The reasons for this are complex. It could be simply the use of the shallow water equations for a complicated three-dimensional domain, or it could relate to second order assumptions concerning inflow into the Loch. The ADCP measurements may have been reflecting the influence of local features (e.g the reefs themselves, 140m away) on the global flow.

The purpose of the current work is to use the 2D numerical model to approximate the global flow field in the vicinity of the reef, which will then be fed into a fully 3D model, to investigate the detailed hydrodynamics around the reefs. In this context, the numerical model provides acceptable results although further work is required on the relationship between the 2D computed velocity field and the physical vertical velocity profiles.

ACKNOWLEDGEMENTS

The authors would like to thank Dr. Tom Wilding from the Scottish Association for Marine Science for his assistance in installing the ADCP instruments and his useful discussion on the Loch Linnhe tide patterns.

REFERENCES

Admiralty Chart – *"1860 admiralty chart2814a"*

Aghajanloo, A, Pirouz, M-D, and Namin, M-M (2011). "Numerical Simulation of Tidal Currents in Persian Gulf." *World Academy of Science, Engineering and Technology* Vol 58 pp793-800.

Akanbi, A, and Katopodes N (1988). "Model for flood propagation on initially dry land." *Journal of Hydraulic Engineering* Vol 114 pp 689-706.

Aizinger, V, and Dawson, C (2002). "A discontinuous Galerkin method for two-dimensional flow and transport in shallow water." *Advances in Water Resources* Vol 25 pp 67–84.

Aubrey, DG, and Friedrichs, CT, (1992). "Buoyancy Effects on Coastal and Estuarine Dynamics (Coastal and Estuarine Sciences). " *Augusta-Margaret River Shire, W. A.) International Conference on Physics of Estuaries and Coastal Seas* edition 6th.

Epler, J, (2010). "Tidal Resource Characterization from Acoustic Doppler Current Profilers" MSc. thesis University of Washington

Banda, M, Seaoid, Y-M, and Thoommes, G (2009). "Lattice Boltzmann Simulation of Dispersion in Two-Dimensional Tidal Flows." *International Journal for Numerical Methods in Engineering* Vol 77, pp878-900.

Beaumont, J, (2007). "Concrete ideas for inshore fisheries." *Planet Earth online Environmental research news* issue 21 May 2007.

Casulli, V, and Cheng, R, (1992) "Semi-Implicit Finite Difference Methods for Three-Dimensional Shallow Water Flow." *Int J Numer Methods Fluids* Vol 15 pp 629-48.

Chen, S, and Doolen, G-D (1998). "Lattice Boltzmann method for fluid flows." *Ann. Rev. Fluid Mech.* Vol 30 pp329–364.

Chippada, S, Dawson, C-N, Martinez, M-L, and Wheeler, M.F., (1998). "A Godunov-type finite volume method for the system of Shallow Water Equations." *Comput. Methods Appl. Mech. Engrg.*, Vol 151 pp105129.Ding, Y, and Wang, S (2005). "Development and Validation of Integrated Coastal Process Models for Simulating Hydrodynamics and Morphological Processes." *US-China Workshop On Advanced Computational Modelling In Hydroscience And Engineering"* pp19-21.

Fennema, R-J, and Chaudhry, M-H (1989). "Implicit methods for two-dimensional unsteady free-surface flows." *J. Hydraulic Res.* Vol 27 pp 321–332.

Fennema, R-J, and Chaudhry, M-H (1990). "Explicit methods for 2-D transient free-surface flows." *J. Hydraulic Eng. ASCE* Vol 116 (8) pp1013–1034.

Garcia, R, and Kahawitha, R (1986). "Numerical solution of the St. Venant equations with the Mac Cormack finite difference scheme." *International Journal for Numerical Methods in Fluids* Vol 6(5) pp 259–274.

Hervouet, J-M (2007). "Hydrodynamics of Free Surface Flows: Modelling with the finite element method." *John Wiley and Sons, Ltd* pp 341.

Hydrographic office UK "*http://www.ukho.gov.uk*" tides gauge records.

Jones, J-E, and Davies, A-M (2006). "Application of a finite element model (TELEMAC) to computing the wind induced response of the Irish Sea." *Continental Shelf Research* Vol 26 pp1519–1541.

Krivodonova, L, Xin, J, Remade, J-F, Chevaugeon, N, and Flaherty, J-E, (2004)."Shock Detection and Limiting with Discontinuous Galerkin Methods for Hyperbolic Conservation Laws." *Applied Numerical Mathematics* Vol 48 pp 323-338.

Liang, Q, Borthwick, AGL, and Stelling, G (2004). "Simulation of Dam and Dyke-Break Hydrodynamics on Dynamically Adaptive Quadtree Grids." *International Journal for Numerical Methods in Fluids* Vol 46 pp127-62.

Liang, Q (2008). "Simulation of shallow flows in Nonuniform open channels." *Journal of Fluids Engineering, Transactions of the ASME* Vol 130(1) pp 0112051-0112059.

Liang, Q, and Borthwick, AGL, (2009). "Adaptive quadtree simulation of shallow flows with wet–dry fronts over complex topography." *Computers and Fluids* Vol 38 pp 221-234.

Liang, Q (2010) . " Flood Simulation Using a Well-Balanced Shallow Flow Model" *Journal of Hydraulic Engineering* Vol 136(9) pp669-675.

Marine resource centre *"http://www.marineresourcecentre.co.uk"*

Ozer, J, Padilla-Hernandez, R, Monbaliu, R, Alvarez Fanjul, E, Carlos Carretero Albiach, J, and Osuna, P, Yu, JCS, and Wolf, J (2000). "A coupling module for tides, surges and waves." *Coastal Engineering"* Vol 41 pp 95-124.

Sayer, MDJ, and Wilding, TA, (2002). "Planning, Licensing, and Stakeholder Consultation in an Artificial Reef Development: The Loch Linnhe Reef, a Case Study." *ICES JOURNAL OF MARINE SCIENCE* Vol 59 pp178-85.

Walters, Roy-A (1989) "A Comparison of Two Finite Element Models of Tidal Hydrodynamics Using a North Sea Data Set." *Advances in Water Resources* Vol 12 pp184-93.

Wilding, TA, and Sayer, MDJ, (2002). "Evaluating artificial reef performance: approaches to pre- and post-deployment research." *ICES JOURNAL OF MARINE SCIENCE* Vol 59 pp1S222-S230.

Wolf, J (2009). "Coastal flooding: impacts of coupled wave–surge–tide models." *Natural Hazards* Vol 49(2) pp 241-260.

Yang, J, Kitazawa, D, and Yamanaka, R (2008). "Numerical Study on the Hydrological Change Due to Water Level Rising in the Caspian Sea " *OCEANS 2008 - MTS/IEEE Kobe Techno-Ocean*, no. 8-11 April pp1 - 5.

Yu, Z, and Kyozuka, Y (2004). "A Discontinuous Galerkin Finite Element Shallow Water Model in Simulating Tidal Flows." *OCEANS '04. MTTS/IEEE TECHNO-OCEAN '04* Vol 3(9-12 Nov. 2004) pp 1526 – 1531.

Zhao, D-H, Shen, H-W, Tabios, G-Q, Lai, J-S, and Tan, W-Y (1994). *J. Hydraul. Eng.* Vol 120 pp 863-883.

Zhou, J-G (2002). "A lattice Boltzmann model for the shallow water equations." *Comput. Methods Appl. Mech. Engrg.* Vol 191 pp3527–3539.

Appendix (D). The backward face step flow literature reviews

The separations of the flow and its reattachment to solid surface occur in many engineering systems which are considered to be important theoretical and practically as shown in Figure D.1. The shear layer separates from the step and then it reattaches itself to the floor of the channel on further downstream as demonstrated in by Figure D.1. Therefore, it was stressed in many publications such as Abbott and Kline (1962) and Goldstein et al. (1970). In fact, the turbulent flow over backward facing step was widely applied as a benchmark problem test to analyse the performance of the turbulent models in the prediction of flow separation. The flow is known to be in the turbulent condition when the inertial forces of the fluid are higher than the viscous forces that create chaotic fluctuations in the flow. Thus, a ratio of the inertial forces to the viscous forces that characterized with non-dimensional form called the Reynolds number (Re) represented by the formula:

$$\mathrm{Re} = \frac{L_R U_R}{\nu}, \qquad \nu = \frac{\mu}{\rho} \qquad \text{(D.1)}$$

Here ρ is the density of the fluid, ν is the kinematic viscosity, μ is the dynamic viscosity L_R is the characteristic length scale of the flow and U_R is the fluid velocity. In the present study a computation of the flow over a backward facing step by solving the Navier-Stokes equations with the RNG turbulence model to investigated the turbulence characteristic of the case. It was based on two different Reynolds numbers Re=5100 and Re=44,000. The first test case is displayed in Chapter 6. Another, two-dimensional numerical domain was built in uniform rectangular mesh for Re=44,000 as presented in Figure D.2. The numerical results were compared with experimental results that have similar flow configuration. The results of the numerical test case with Reynolds number equal to 44,000 and the numerical stream-wise profiles which was compared with the experimentally observed by Jovic and Driver (1994) and Kim et al. (1980).

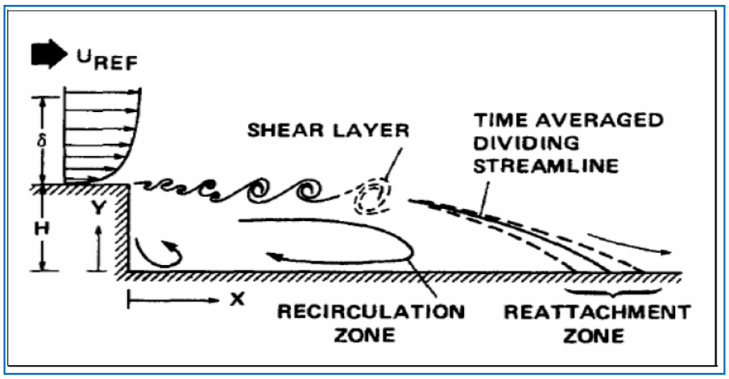

Figure D.1 The schematic of the backward-facing step turbulent phenomenon (Simpson, 1996).

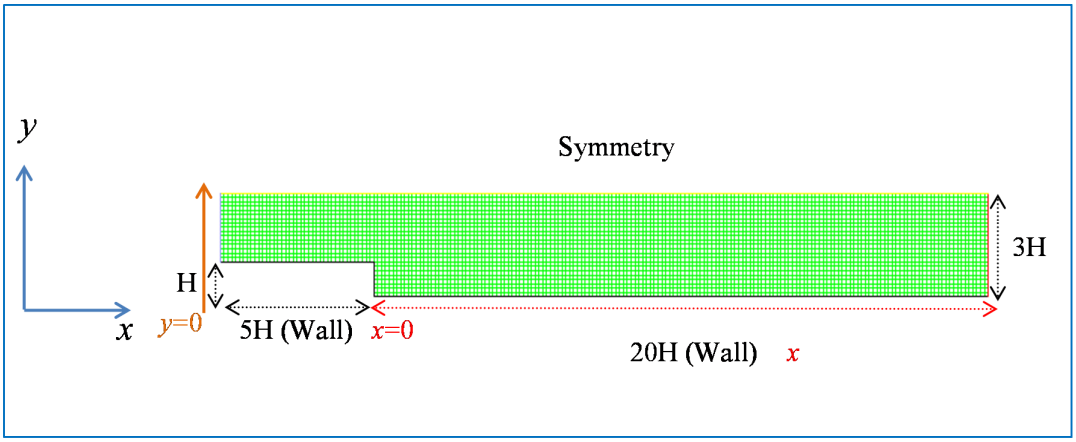

Figure D.2 The dimension of backward-face step for Re=44,000.

The observation results made by Jovic and Driver are seen in Figure D.3 compared with the numerical computation that represents the velocity profile at two different positions (a) x/H=1.33 and (b) x/H=2.66 along the channel. The good agreement is spotted at Figure D.3 it shows the FLUENT RNG turbulence model numerical ability. The velocity profile with Re=44,000 has been numerical investigated and compared with an experimentally data done by Kim et al. (1980) in various positions on the channel at (a) x/H=1.33, (b) x/H=2.667, (c) x/H=6.22 and (d) x/H=8 seen in both Figure D.3 and Figure D.4. There are good agreement between the numerical and the experiment measurement done by Kim et al. (1980) that indicate the numerical accuracy for the RNG turbulence model. This numerical model was adopted in the present study for the three-dimensional simulation.

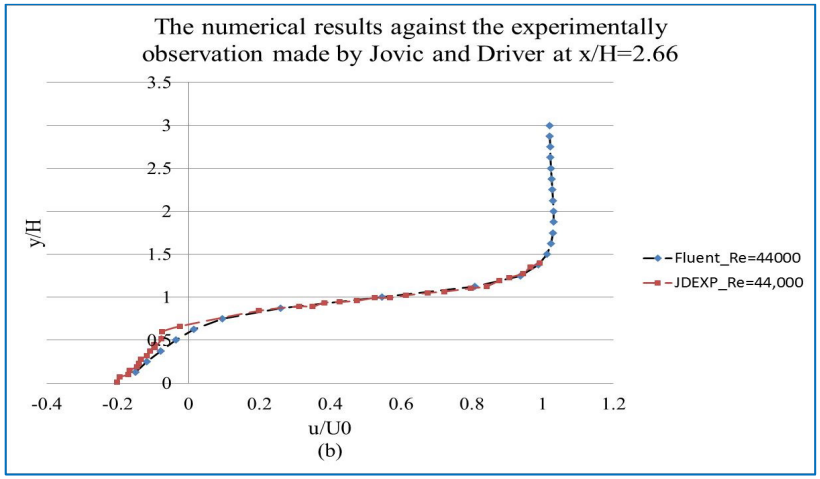

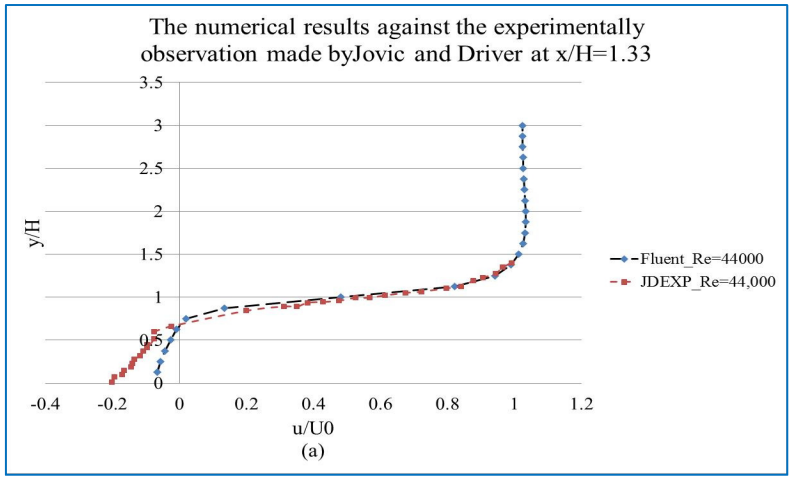

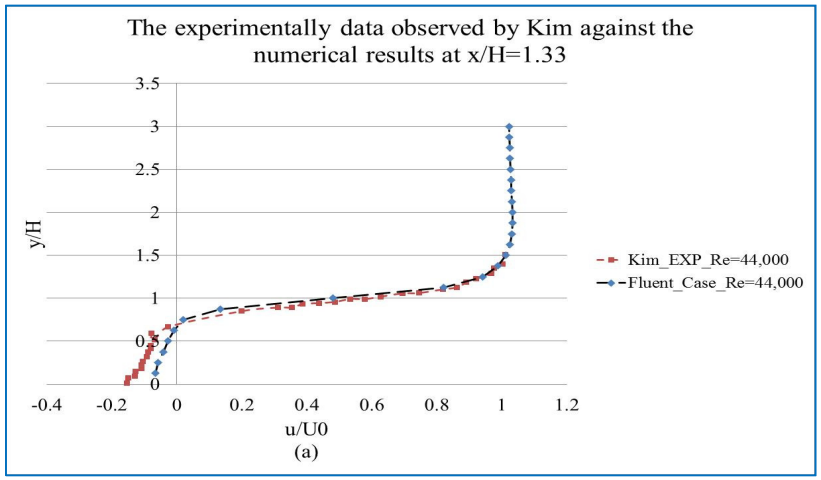

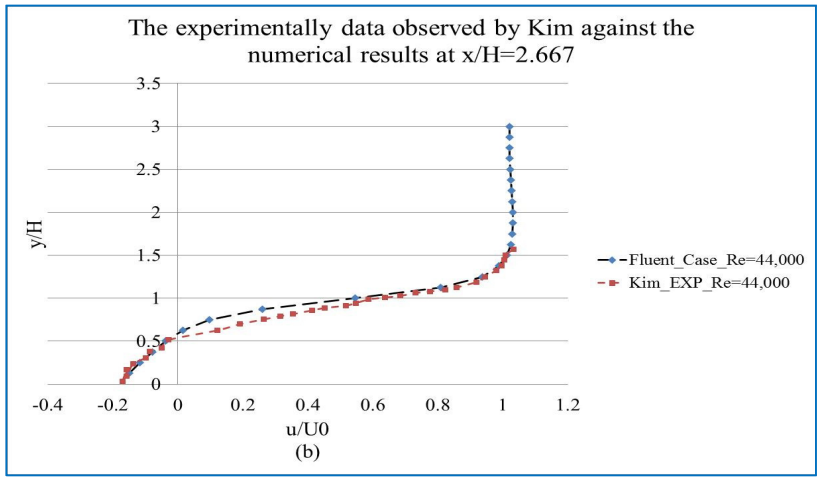

Figure D.3 The Jovic and Driver experimental data compared with the numerical results is presented in the upper figure and the Kim experimental results differentiate with numerical ones is seen in the below.

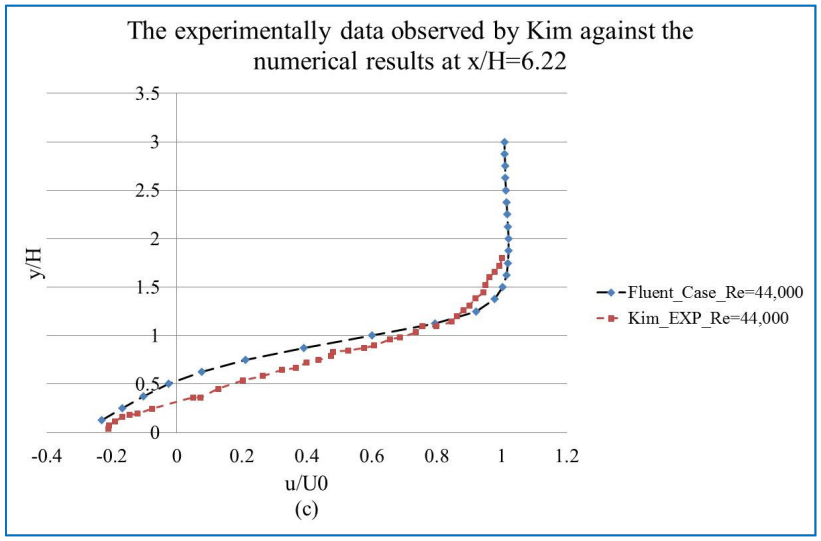

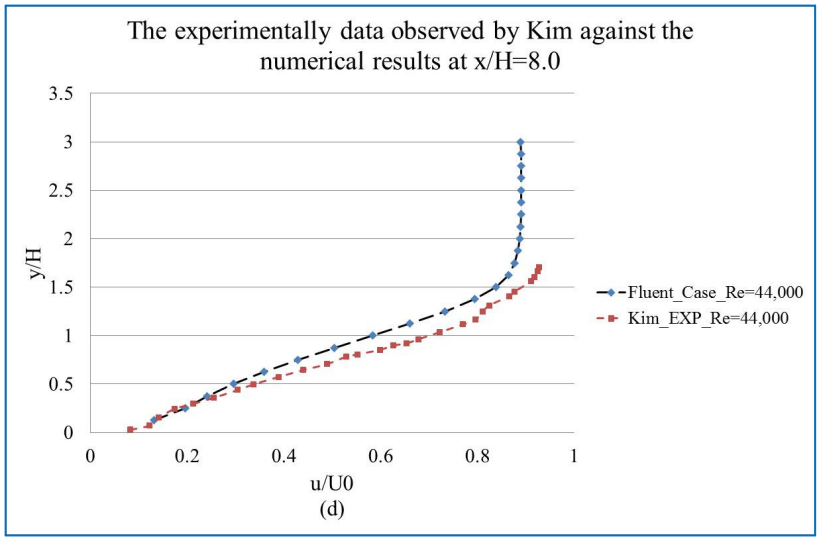

Figure D.4 The Kim experimental measurements compared with the FLUENT RNG turbulence model numerical results at different position in the channel.

References

12.0, A. F. (April 2009) 'Theory Guide for ANSYS FLUENT 12.0'.

Abbot, D. E., and Kline, S. J. (1962) 'Experimental investigations of subsonic turbulent bow over single and double backward-facing steps', *ASME Journal of Basic Engineering*, Vol.84, pp.317-325.

Abbot, D. E., and Kline, S. J. (1962) 'Experimental investigations of subsonic turbulent bow over single and double backward-facing steps', *ASME Journal of Basic Engineering*, Vol.84, pp.317-325.

Abelson, A., and Shlesinger, Y. (2002) 'Comparison of the development of coral and fish communities on rock-aggregated artificial reefs in Eilat, Red Sea', *ICES Journal of Marine Science*, Vol.59, pp.S122-S126.

Admiralty chart (2010) (http://www.ukho.gov.uk/ProductsandServices/Pages/Home.aspx).

Aghajanloo, A., Pirouz, M. D., and Namin, M. M. (2011) 'Numerical Simulation of Tidal Currents in Persian Gulf', *World Academy of Science, Engineering and Technology*, 58, pp.793-800.

Aizinger, V., and Dawson, C. (2002) 'A discontinuous Galerkin method for two-dimensional flow and transport in shallow water', *Advances in Water Resources*, 25, pp.67–84.

Akanbi, A. A., and Katopodes, N. (1988) 'Model for flood propagation on initially dry land', *Journal of Hydraulic Engineering*, Vol 114, pp. 689-706.

Angel, D. L., and Spanier, E. (2002) 'An application of artificial reefs to reduce organic enrichment caused by net-cage fish farming: preliminary results', *ICES Journal of Marine Science*, Vol.59, pp.S324-S329.

Anon (1998) 'OSPAR Decision 98/3 on the disposal of disused offshore installations. ', *Ministerial Meeting of the OSPAR Commission*, Vol.July 1998, pp.22-23.

Antsulevich, A., Laihonen, P., and Vuorinen, I. (2000) 'Employment of artificial reefs for environmental maintenance in the Gulf of Finland. In: Jensen A.C., Collins K.J., Lockwood A.P.M.', *(eds) Artificial Reefs in European Seas. Kluwer Academic Publishers, Dordrecht,*, pp.319-329.

Audusse, E., and Bristeau, Marie-Odile. (2007) 'Finite Volume solvers for a multilayer saint-venant system', *international applied mathematics and computer science*, Vol.17(3), pp.311-320.

Bacchiocchi, F., and Airoldi, L. (2003) 'Distribution and dynamics of epibiota on hard structures for coastal protection', *Estuarine, Coastal and Shelf Science*, Vol.56, pp.1157–1166.

Baine, M. (2001) 'Artificial reefs: a review of their design, application, management and performance', *Ocean and Coastal Management*, Vol.44(3-4), pp.241-259.

Banda, M., Seaidy M., and Th¨ommes, G. (2009) 'Lattice Boltzmann Simulation of Dispersion in Two-Dimensional Tidal Flows', *International Journal for Numerical Methods in Engineering*, Vol.77(6), pp.878-900.

Barros, F., Underwood, A. J., and Lindegarth, M. (2001) 'The influence of rocky reefs on structure of benthic macrofauna in nearby soft-sediments', *Estuarine Coastal and Shelf Science*, Vol.52(2), pp. 191-199.

Barton, B. (June 2006) 'formerly North Hoyle but now Crown Estate, pers. comm.'.
Baynes, T. W., and Szmant, A. M. (1989) 'Effect of Current on the Sessile Benthic Community Structure of an Artificial Reef.', *Bulletin of Marine Science*, Vol.44, pp.545-566.

Beaumont, J. (2006) 'Quantifying biotic interactions with inshore subtidal structures: comparisons between artificial and natural reefs', *PhD thesis - Scottish Association for Marine Science*.

Beaumont, J. (2007) 'Concrete ideas for inshore fisheries', *Planet Earth online Environmental research news* 21 May 2007 (http://planetearth.nerc.ac.uk/features/story.aspx?id=111).

Begg, J. G., and Johnston, M.R. (2000) 'Geology of the wellington area', *Institute of Geological & Nuclear Sciences Limited Lower Hutt, New Zealand*.

Benkhaldoun, F., Elmahi, I., and Monthe L.A. (1999) 'Positivity preserving finite volume Roe schemes for transportdiffusion equations', *Computer Methods in Applied Mechanics and Engineering*, Vol.178, pp.215-232.

Bermudez, A., Rodrfguez, C. and Vilar, M.A. (1991) 'Solving Shallow Water Equations by a Mixed Implicit Finite Element Method', *IMA Journal of Numerical Analysis*, Vol.11, pp.79-97.

Bermúdez, A. a. V., M. E. (1994) 'Upwind methods for hyperbolic conservation laws with source terms', *Comput. Fluids*, Vol.23, pp.1049.

Biber, P. D. (2007) 'Hydrodynamic transport of drifting macroalgae through a tidal cut', *Estuarine, Coastal and Shelf Science*, 74, pp.565-569.

Blockley, D. J., and Chapman, M. G (2006) 'Recruitment determines differences between assemblages on shaded or unshaded seawalls', *Marine Ecology-Progress Series*, Vol.327, pp.27-36.

Blumberg, A. F., and Mellor, G.L. (1987) 'A description of a three-dimensional coastal ocean circulation model. In: Three-Dimensional Coastal Ocean Models (edited by N. Heaps)', *Amer. Geophys. Union, Washington D.C.*, pp. 1-16.

Bohnsack, J. (1989) 'Are high densities of fishes at artificial reefs the result of habitat limitation or behavioural preference?', *Bulletin of Marine Science*, Vol.44, pp. 631-645.

Bohnsack, J., Johnson, D., and Ambrose, R. (1991) 'Ecology of artificial reef habitats and fishes. In: W.J. Seaman and L.M.E. Sprague (Editors), Artificial Habitats for Marine and Freshwater', *Academic Press, Inc., San Diego, California.*, pp. 61-99.

Bohnsack, J. A. (1991) 'Habitat structure and the design of artificial reefs', *Chapman and Hall, New York*.

Bohnsack, J. a. S., DL (1985) 'Artificial reef research: a review with recommendations for future priorities', *Bulletin of Marine Science*, Vol.37, pp. 11-39.

Bombace, G., Fabi, G., and Fiorentini L. (2000) 'Artificial reefs in the Adriatic Sea. In: Jensen AC, Collins KJ, Lockwood APM (eds) Artificial reefs in European seas.', *Kluwer Academic Publishers, Dordrecht,*, pp. 31-63.

Borrero, J. C., and Nelsen, C. (2003) 'Results of a comprehensive monitoring program at Pratte's Reef', *3rd International Surfing Reef Symposium, Raglan, New Zealand,*, pp.83-98.

Bortone, S. A., Martin, T., and Bundrick, C.M. (1994) 'Factors affecting fish assemblage development on a modular artificial reef in a northern Gulf of Mexico estuary.', *Bull. Mar. Sci.*, Vol.55(2-3), pp. 319-332.

Branden, K. L., Pollard, D., A. and Reimers, H. A. (1994) 'A review of recent artificial reef developments in Australia', *Bulletin of Marine Science*, Vol.55 (2-3), pp.982-994.

Brock, R. E., and Kam, A. K. H. (1994) 'Focusing the recruitment of juvenile fishes on coral-reefs', *Bulletin of Marine Science*, Vol.55(2-3), pp. 623-630.

Brown, C. J. (2005) 'Epifaunal colonization of the Loch Linnhe artificial reef: Influence of substratum on epifaunal assemblage structure', *Biofouling*, Vol.21, pp. 73-85.

Brufau, P., Vázquez-Cendón, E., and Garcia-Navarro, P. (2002) 'A numerical model for the flooding and drying of irregular domains', *Int. Journal for Numerical Methods in Fluids*, Vol.39, pp. 247-275.

Bruno, M. S. (1993) 'Laboratory testing of an artificial reef erosion control device. Coastal zone 93.', *Proc. Symp. Coastal and Ocean Management. American Society of Civil Engineers*, (2), pp. 2147–2154.

Bryan, K. (1969) 'A numerical model for the study of the circulation of the world oceans', *J. Comput. Phys.*, Vol.4, pp. 347-359.

Bulleri, F., Chapman, M.G., and Underwood, A.J. (2005) 'Intertidal assemblages on seawalls and vertical rocky shores in Sydney Harbour, Australia', *Austral Ecology*, Vol.30, pp. 655-667.

Bye, J. A. T., and Heath, R.A. (1975) 'The New Zealand semi-diurnal tide', *Journal of Marine Research*, Vol.33, pp.423-442.

Callow, M. E., and Callow, J. A. (2002) 'Marine biofouling: a sticky problem', *Bioologist* Vol.49(1), pp.1-5.

Caselle, J. E., Love, M.S., Fusaro, C., and Schroeder, D. (2002) 'Trash or habitat? Fish assemblages on offshore oilfield seafloor debris in the Santa Barbara Channel, California', *ICES Journal of Marine Science*, Vol.59, pp. S258-S265.

Casulli, V., and Cheng, R. (1992) 'Semi-implicit finite difference methods for three-dimensional shallow water flow', *Int J Numer Methods Fluids*, 15, pp. 629-648.

Causon, D. M., Mingham, C.G., and Ingram, D.M. (1999) 'Advances in Calculation Methods for Supercritical Flow in Spillway Channels ', *J. Hydraul. Eng.* , Vol.125(10), pp.1039-1050.

Chang, K. H., and Shao, K.T. (1988) 'The sea farming projects in Taiwan', *ACTA OCEANOGRAPHICA TAIWANICA*, Vol.19, pp. 52-59.

Chapman, M. G., and Clynick, B.G. (2006) 'Experiments testing the use of waste material in estuaries as habitat for subtidal organisms', *Journal of Experimental Marine Biology and Ecology*, Vol.338, pp. 164-178.

Chapman, M. G. (2006) 'Intertidal seawalls as habitats for molluscs', *Journal of Molluscan Studies*, Vol.72, pp. 247-257.

Chen, S., and Chen, S.H. (1957) 'Preliminary report of artificial reefs at Linbien, Pington, China', *Fish. Monthly*, Vol.51, pp. 7-8.

Chen, S., and Doolen, G.D. (1998) 'Lattice Boltzmann method for fluid flows', *Ann. Rev. Fluid Mech*, Vol.30, pp. 329–364.

Cheng-Hai, W., and Osamu, S. (1986) 'Hydrodynamic Characteristics in Simplified Components of Artificial Reef Structures', *Bull. Fac. Fish. Hokkaido University*, Vol.37(3), pp.190-206.

Chippada, S., Dawson, C.N., Martinez, M.L., and Wheeler, M.F. (1998) 'A Godunov-type finite volume method for the system of Shallow Water Equations', *Comput. Methods Appl. Mech. Engrg.*, Vol.151, pp. 105-129.

Chou, L. M. (1997) 'Artificial reefs of Southeast Asia - do they enhance or degrade the marine environment.', *Environmental Monitoring and Assessment*, Vol.44, pp. 45-52.

Chu, P. C., and Fan, C. (1997) 'Sixth-order difference scheme for sigma coordinate ocean models', *J. Phys. Oceanogr.*, Vol.27, pp. 2064-2071.

Chu, P. C., and Fan, C. (2002) 'Finite Volume Ocean Circulation Model', *The OCEANS 2002 MTS/IEEE Conference Proceedings, St. Petersburg, FL, Oct 29-31,*, pp. 1-8.

Clark, L. (2008) 'Benign tides', *Energy NZ*, Vol.6, pp. 1-2.

Clark, S., and Edwards, A.J. (1999) 'An evaluating of artificial reef structures as tools for marine habitat rehabilitation in the Maldives', *Aquatic Conservation: Marine and Freshwater Ecosystems*, Vol.9, pp.5-21.

Collins, K., Jensen, A., and Smith, I.P. (2000) 'Artificial Reef Technology. In Man-Made Objects on the Sea Floor 2000', *Ed. by Sut. The Society for Underwater Technology, London*, pp. 5-11.

Collins, K. J., Jensen, A.C., Mallinson, J.J., Roenelle, V., and Smith, I.P. (2002) 'Environmental impact assessment of a scrap tyre artificial reef', *ICES Journalof Marine Science*, Vol.59, pp. S243-S249.

Craymer, M. (2011) 'Geodetic toolbox ', *MATLAB central for file exchange (http://www.mathworks.com/matlabcentral/fileexchange/15285-geodetic-toolbox)*
Davies, S. F. (1988) 'Simplified second-order godunov-type methods', *SIAM Journal on Scientific Computing*, Vol.9, pp. 445-473.

Davis, A. (1995) 'Marine BioFouling: a sticky problem. ', *NERC News (http://www.biosciences.bham.ac.uk/external/biofoulnet).*

Dean, L. (1983) 'Undersea oases made by man: artificial reefs create new fishing grounds', *Oceans*, Vol.16, pp. 27-33.

Defant, A. (1961) 'Introduction to Physical Oceanography, Vol. II ', *Oxford Pergamon Press*, pp.598.

Department of Energy and Climate Change website (2011) (*http://www.berr.gov.uk/energy/ sources/renewables/index.html*).

Dethier, M. N., and Schoch, G.C. (2005) 'The consequences of scale: assessing the distribution of benthic populations in a complex estuarine fjord', *Estuarine Coastal and Shelf Science*, Vol.62, pp. 253-270.

Dewees, C. M., and Gotshall, D.W. (1974) 'An experimental artificial reef in Humboldt Bay, California', *California Fish and Game*, Vol.60, pp. 109-127.

Diplock, J. (2008) 'Artificial reefs in Australia an overview', *report*, pp. 1-12.

Ditton, R. B., Osburn, H.R., Baker, T.L., and Thailing, C.E. (2002) 'Demographics, attitudes, and reef management preferences of sport divers in offshore Texas waters', *ICES Journal of Marine Science*, Vol.59, pp.S186-S191.

Duedall, I. W., and Champ, M.A. (1991) 'Artificial reefs: Emerging science and technology.', *Oceans*, Vol. 34(1), pp. 94-101.

Einfeldt, B. (1988) 'On godunov-type method for gas dynamics', *SIAM Journal on Numerical Analysis,*, Vol.25, pp. 294-318.

Emery, W. J., and Thomson, R.E. (2003) *Data Analysis Methods in Physical Oceanography Elsevier Inc -84 Theobalds Road London WC1X RR UK.*

Fabi, G., and Fiorentini, L. (1997) 'Molluscan aquaculture on reefs. In European Artificial Reef Research', *Proceedings of the 1st EARRN conference, Ancona, Italy, March 1996*, pp.123-140.

Falace, A., and Bressan, G. (2002) 'A qualitative-quantitative analysis of the evolution of macroalgal vegetation on an artificial reef with antigrazing nets (Loano – Ligurian Sea).', *ICES J. Mar. Sci.*, Vol.59, pp. 150–156.

Falconer, R. A. (1993) 'An introduction to nearly horizontal flows In: Abbott MB, Price WA, Editors, Coastal, Estuarial and Harbour Engineer's reference book. London: Chapman and Hall:1993', pp.29-36.

Fennema, R. J., and Chaudhry, M.H. (1989) 'Implicit methods for two-dimensional unsteady free-surface flows', *J. Hydraulic Res.*, Vol.27, pp. 321–332.

Fennema, R. T., and Chaudhry, M.H. (1990) 'Explicit methods for 2D transient free-surface flows', *Journal of Hydraulic Engineering*, Vol.116, pp.1003-1014.

Forrester, W. D. (1983) 'Canadian Tidal Manual. Department of Fisheries and Oceans, Ottawa', pp.138.

Forster, S., Huettel, M. and Ziebis, W. (1996) 'Impact of boundary layer flow velocity on oxygen utilisation in coastal sediments', *Marine Ecology Progress Series*, Vol.143, pp. 173-185.

Fortunato, A. B., Baptista, A.M., and Luettich, R.A. (1997) 'A three dimensional model of tidal currents in the mouth of the Tagus estuary', *Continental Shelf Research*, Vol.17, pp. 1689-1714.

Fortunato, A. B., Oliviera, A., and Baptista, A.M. (1999) 'On the effect of tidal flats on the hydrodynamics of the Tagus estuary', *Oceanologica Acta*, Vol.22, pp. 31-44.

Fraccarollo, L., and Toro, E.F. (1995) 'Experimental and numerical assessment of the shallow water model for two dimensional dam-break type problems', *Journal of Hydraulic Research*, Vol.33(6), pp. 843-864.

Fraenkel, P. L. (2002) 'Power from marine turbines', *Proc I Mech E, Part A*, Vol.216, pp. 1-15.

Freitag, H. P., McPhaden, M.J. and. Pullen, P.E (26-29 October 1992) 'Fish-induced bias in acoustic Doppler current profiler data.', *Proceedings of Oceans '92, Mastering the Oceans Through Technology, Newport, RI*, pp. 712-717.

Garcia, R., and Kahawitha, R. (1986) 'Numerical solution of the St. Venant equations with the Mac Cormack finite difference scheme', *International Journal for Numerical Methods in Fluids*, 6(5), pp. 259–274.

Gardner, J., Hamer, B., and Runcie, R. (1996) 'Physical protection of the seabed and coasts by artificial reefs', *Proceedings of the First European Artificial Reef Research Network Conference, Ancona, Italy*, pp. 17-37.

Gary, J. M. (1973) 'Estimate of truncation error in transformed coordinate primitive equation atmospheric models', *J. Atmos. Sci.*, Vol.30, pp.223–233.

Glasby, T. M., and Connell, S.D. (1999) 'Urban structures as marine habitats', *Ambio*, Vol.28, pp. 595-598.

Glasby, T. M. (2000) 'Surface composition and orientation interact to affect subtidal epibiota', *Journal of Experimental Marine Biology and Ecology*, Vol.248, pp. 177-190.

Godoy, E. A. S., Almeida, T.C. M., and Zalmon, I.R. (2002) 'Fish assemblages and environmental variables on an artificial reef north of Rio de Janeiro, Brazil', *ICES Journal of Marine Science*, Vol.59, pp. S138-S143.

Godunov, S. K. (1959) 'A difference method for numerical calculation of discontinuous solutions of the equations of hydrodynamics.', *Matem. Sbornik* Vol.47, pp. 271-306.

Golstein, R. J., Eriksen, V.L., Olson, R.M., and Eckert, E.R.G. (1970) 'Laminar separation, reattachment and transition of the bow over a downstream-facing step', *ASME Journal of Basic Engineering*, Vol.92, pp. 732-741.

Gómez-Valdés, J., Dworak, J. A., Vázquez, H. J., and Paz, M. (2012) 'Vertical structure of tidal flows at the entrance to Guaymas Bay, Mexico', *Geofísica Internacional*, Vol.51(3), pp. 271-279.

Goring, D. (1995) 'Primary M2 Tide for New Zealand', *National Institute of Water and Atmosperic Research Ltd*.

Goring, D. (2001) 'Computer Models Define Tide Variability', *The Industrial Physicist - American Institute of Physics*, pp. 14-17.

Goutal, N. a. M., F. (1997) 'Proceedings of the 2nd workshop on dam-break wave simulation', *HE 43/97/016/B, Départment Laboratoire National d''Hydraulique, Groupe Hydraulique Fluviale Electricité de France, France.*

Gratwicke, B., and Speight, M.R. (2005) 'Effects of habitat complexity on Caribbean marine fish assemblages', *Marine Ecology Progress Series*, Vol.292, pp. 301-310.

Greilach, P., You, Z., Black, K., and Gorman, R. (1997) 'Port Phillip Bay Environmental Study: Sediment Characteristics in Port Phillip Bay', *Marine and Freshwater Resources Institute, Queenscliff, Victoria, Australia.*

Grove, R. S., Sonu, C.J., and Nakamura, M. (1991) *Design and Engineering of Manufactured Habitats for Fisheries Enhancement. In: W.J. Seaman and L.M.E. Sprague (Editors), Artificial Habitats for Marine and Freshwater Fisheries. Academic Press, Inc., San Diego, California.* pp.109-149.

Grove, R. S., Nakamura, M., Kakimoto, H. and Sonu, C. J. (1994) 'Aquatic habitat technology innovation in Japan', *Bulletin of Marine Science*, Vol. 55(2-3), pp. 276-294.

Guichard, F., Bourget, E., and Robert, J.L. (2001) 'Scaling the influence of topographic heterogeneity on intertidal benthic communities: alternate trajectories mediated by hydrodynamics and shading', *Marine Ecology Progress Series*, Vol.217, pp. 27-41.

Guinot, V. (2003) *Godunov-type schemes, An introduction for engineers. Elsevier Science, Elsevier*.

Gun Oh, T., Otake, S., and Ock Lee, M. (2011) 'Estimating the Effective Wake Region (Current Shadow) of Artificial Reefs', *Artificial reef in Fisheries Management* pp. 279-295.

Hamer, B., Hayman, S.J., Elsdon, P.A., and Fleming, C.A. (1998) *Happisburg to Winterton Sea Defences: Stage Two. In Coastlines, structures and breakwaters.Ed. by N. W. H. Allsop. Thomas Telford Publishing, London.* pp.119-134.

Hammar, L., Andersson, S. and Rosenberg, R. (2010) *Adapting offshore wind power foundations to local environment, translated by Dimming, A., Vindval report 6367, (Broma).*

Harten, A., Lax, P.D., and van Leer, B. (1983) 'On upstream differencing and godunov-type schemes for hyperbolic conservation laws.', *SIAM Review*, Vol.25, pp.35-61.

Heath, R. A. (1978) 'Semidiurnal tides in Cook Strait', *New Zealand Journal of Marine and Freshwater Research*, Vol.12, pp. 87-97.

Heath, R. A. (1985) 'A review of the physical oceanography of the seas around New Zealand — 1982', *New Zealand Journal of Marine and Freshwater Research*, Vol.19(1), pp. 79-124.

Hermeline, F. (2000) 'A finite volume method for the approximation of diffusion operators on distorted meshes', *J. Comput. Phys.*, Vol.160, pp. 481-499.

Hervouet, J. M., and Bates, P. (2000) 'The TELEMAC modelling system', *special issue. Hydrol. Process*, Vol.14(13), pp. 2207-2363.

Hervouet, J. M. (2007) *Hydrodynamics of Free Surface Flows: Modelling with the finite element method.Copyright © 2007 John Wiley & Sons, Ltd*. pp.341.

Hervoueta, J. M., Hubertb, J.L., Janinc, J.M., Lepeintrec, F., and Peltierc, E. (2010) 'The computation of free surface flows with TELEMAC: an example of evolution towards hydroinformatics', *Journal of Hydraulic Research*, Vol.32(1), pp. 45-64.

Hicks, S. D. (2006) *UNDERSTANDING TIDES-Center for Operational Oceanographic Products and Services National Oceanic and Atmospheric Administration National Ocean Service (NOAA).*

Hinrichsen, D. (1997) 'Coral reefs in crisis - An overview of these vanishing ecosystems, the problems that plague them, and the means for saving them', *Biosciences*, Vol.47, pp. 554-558.

Hirsch, C. (1990) 'Numerical computation of internal and external flows', *Volume 2,Computational methods for inviscid and viscous flows. New York: Wiley.*

Hoffmans, G. J. C. M., and Pilarczyk, K.W. (1995) 'Local Scour Downstream of Hydraulic Structures', *Journal of Hydraulic Engineering*, Vol.121(4), pp. 326-340.

Hoffmans, G. J. C. M., and Verheij, H. J. (1997) *Scour manual. Rotterdam: Balkema*.

Hu, K., Mingham, C.G., and Causon, D.M. (1999) 'A bore-capturing finite volume method for open-channel flows', *International Journal for Numerical Methods in Fluids*, Vol.28(8), pp.1241-1261.

Hu, K., Mingham, C.G., and Causon, D.M. (2000) 'Numerical simulation of wave vertopping of coastal structures using the non-linear shallow water equations', *Coastal Engineering*, Vol.41(4), pp. 433-465.

Hydrographic Office - UK (2011) *tides gauge records* – (*http://www.ukho.gov.uk/easytide/EasyTide/index.aspx*.)

Ino, T. (1974) 'Historical review of artificial reef activities in Japan.', *Proc. Int. Conf. Art. Reefs (Houston, Texas), com.*, Vol.75-10786, pp. 21-33.

Janssen, P. A. E. M. (1989) 'Wave-induced stress and the drag of air-flow over sea waves', *Journal of Physical Oceanography*, Vol.19, pp.745-754.

Jensen, A., and Collins, K. (1997) 'The use of artificial reefs in crustacean fisheries enhancement. In European Artificial Reef Research', *Proceedings of the 1st EARRN conference, Ancona, Italy, March 1996*, Ed. by A. C. Jensen. Southampton Oceanography Centre, pp.115-121.

Jensen, A., Collins, K. and Lockwood, P. (2000) 'Introduction and background to 'Artificial Reefs in European Seas'.', *In: Jensen AC, Collins KJ, Lockwood APM (eds) Artificial Reefs in European Seas. Kluwer, Dordrecht*, pp. ix-xii.

Jones, J. E. (2002) 'coastal and shelf-sea modelling in the european context ', *Oceanography and Marine Biology, An Annual Review*, Vol.40, pp. 37-141.

Jones, J. E., and Davies, A.M. (2006) 'Application of a finite element model (TELEMAC) to computing the wind induced response of the Irish Sea', *Continental Shelf Research*, Vol.26, pp. 1519–1541.

Jonsson, P. R., Berntsson, K.M., and Larsson, A.I. (2004) 'Linking larval supply to recruitment: flow-mediated control of inital adhesion of barnacle larvae.', *Ecology*, Vol.85, pp. 2850-2859.

Jovic, S., and Driver, D. (1994) *Backward-facing step measurements at low Reynolds number-NASA Ames Research Center.*

Kakimoto, H. (1983) 'Study on the distribution of zoo plankton at artificial reefs', *Journal of Japanese Society of Fisheries Engineering*, Vol.19(2), pp. 21-28.

Karnofsky, E. B., Atema, J., and Elgin, R.H. (1989) 'Natural dynamics of population structure and habitat use of the lobster, Homarus americanus', *Biological Bulletin*, Vol.176, pp. 239-246.

Keough, M. J., and Downes, B.J. (1982) 'Recruitment of marine invertebrates: the role of active larval choices and early mortality', *Oecologia*, Vol.54, pp. 348-352.

Kim, C. G. (2001) 'Artificial reefs in Korea', *Fisheries*, Vol.26(12), pp. 15-18.

Kim, J., Kline, S.J., and Johnston, J.P. (1980) 'Investigation of a reattaching turbulent shear layer: flow over a backward facing step', *ASME Journal of Fluids Engineering*, Vol.102, pp. 302-308.

Kobayashi, M. H. (1999) 'On a class of Pade finite volume methods', *J. Comput. Phys.*, Vol.156, pp.137-180.

Kodama, T., and Kawahara, M. (1994) 'FINITE ELEMENT TIDAL CURRENT ANALYSIS WITH AN OPEN BOUNDARY CONDITION', *ENGINEERING COMPUTATIONS*, Vol.11, pp. 3-24.

Kress, N., Tom, M., and Spanier, E. (2001) 'The use of coal fly ash in concrete for marine artificial reefs in the Southeastern Mediterranean: compressive strength, sessile biota and chemical composition', *ICES Journal of Marine Science*, Vol.59, pp.S231-S237.

Krivodonova, L., Xin, J., Remade, J.F., Chevaugeon, N., and Flaherty, J.E. (2004) 'Shock Detection and Limiting with Discontinuous Galerkin Methods for Hyperbolic Conservation Laws', *Applied Numerical Mathematics*, Vol 48, pp. 323-338.

Le Provost, C., Genco, M.L., Lyard, F., Vincent, P., and Canceil, P. (1994) 'Spectroscopy of the world ocean tides from a finite element hydrodynamic model', *Journal of Geophysical Research*, Vol.99, pp. 24,777-24,797.

Lee, S., Lie, Heung-Jae., Cho, Cheol-Ho., Kang, S. K., Teague, W. J., Chang, Kyung-Il., Song, Kyu-Min., and Oh, Kyung-Hee. (2011) 'Vertical Structure of the M2 Tidal Current in the Yellow Sea', *Ocean Science Journal*, Vol.46(2), pp. 73-84.

Leupi, C., Miglio,E., Altinakar, M, Quarteroni, A. and Deville, M.O. (2009) 'A 3D finite element model for free-surface flows', *Computers & Fluids*, Vol.38, pp. 1903-1916.

LeVeque, R. J. (1992) *Numerical Methods for Conservation laws-Birkhauser Verlag*.

LeVeque, R. J. (2002) *Finite Volume Methods For Hyperbolic Problems-Cambridge Texts in Applied Mathematics. Cambridge University Press, Cambridge, United Kingdom*.

Li, L., Zuo, J.C. and Li, P.L. (2003) 'Tidal Simulation in the East China Sea with Finite Element Method', *Proceedings of TheThirteenth (2003) International Offshoreand Polar Engineering Conference Honolulu, Hawaii,USA,May25–30, 2003*, pp. 802-808.

Liang, Q., Borthwick, A.G.L. and Stelling, G. (2004) 'Simulation of dam-and dyke-break hydrodynamics on dynamically adaptive quadtree grid', *international Journal for Numerical Methods in Fluids*, Vol.46, pp. 127-162.

Liang, Q. (2008) 'Simulation of shallow flows in Nonuniform open channels', *Journal of Fluids Engineering, Transactions of the ASME* Vol.130(1), pp. 12051-12059.

Liang, Q., and Borthwick, A.G.L. (2009) 'Adaptive quadtree simulation of shallow flows with wet-dry fronts over complex topography', *Computers and Fluids*, Vol.38(2), pp.221-234.

Liang, Q. (2010) 'Flood Simulation Using a Well-Balanced Shallow Flow Model', *Journal of Hydraulic Engineering*, Vol.136((9)), pp.669-675.

Limpsaichol, P., Khokiattiwong, S., and N. Bussarawit (1994) 'Water conditions and nutrient content at the artificial reef sites in Ranong Province, Thailand', *In The effect of artifical reef installation on the biosocioeconomics of small-scale fisheries in Ranong Province, Thailand ,Madras (India) Bay of Bengal programme*, pp. 9-5.

Lin, J., and Zhang, S.Y. (2006) 'Research advances on physical stability and ecological effects of artificial reef', *Marine Fisheries*, Vol.28(3), pp. 257-262.

Lin, J. C., and Su, W.C. (1994) 'Early phase of fish habitation around a new artificial reef off southwestern Taiwan', *Bulletin of Marine Science*, Vol.55(2-3), pp.1112-1121.

Linley, E. A. S., Wilding, T.A., Black, K.D., Hawkins, A.J.S., and Mangi, S. (2007) *Review of the reef effects of offshore wind farm structures and potential for enhancement and mitigation-Report from PML Applications Ltd. to the Department of Trade and Industry Contract no. RFCA/005/0029P.*

Liu, H. S., MA, X., Zhang, S., Lin, J., Yu, H., and Huang, H. (2009) 'Validation and comparison between wind tunnel experiments and numerical simulation of flow field around artificial reefs', *Journal Fishery Sciences of China*, Vol.16(3), pp. 365-371.

Lomax, H., Pulliam, T.H. and Zingg, D.W. (1999) *Fundamentals of Computational Fluid Dynamics-Springer (2011).*

Lovas, S. M., and Torum, A. (2001) 'Effect of the kelp Laminaria hyperborea upon sand dune erosion and water particle velocities', *Coastal Engineering*, Vol.44, pp. 37-63.

Mann, K. H., and Lazier, J.R.N. (1996) 'Dynamics of marine ecosystems: Biological-physical interactions in the oceans', *Blackwell Science (Boston)*, (2nd edition), pp.394.

Manoukian, S., Fabi, G., and Naar, D.F. (2011) 'Multibeam investigation of an artificial reef settlement in the adriatic sea (Italy) 33 years after its deployment', *BRAZILIAN JOURNAL OF OCEANOGRAPHY*, Vol.59, pp. 145-153.

Marchuk, G. I., and Kagan, B.A. (1989) 'dynamics of ocean tides', *Oceanographic Sciences Library*, Vol.3, pp. 266-267.

Marmer, H. A. (1954) 'Tides and sea level in the Gulf of Mexico ', *Fishery Bull. Fish. Wildl. Serv. U.S.*, Vol.55, pp.101-118.

Massel, S. R. (1999) *Fluid Mechanics for Marine Ecologists-Springer-Verlag, Berlin-* pp.566.

Mathews, H. (1985) 'Physical and geological aspects of artificial reef site selection. In: F.M.E. D'Itri (Editor), Artificial Reefs: Marine and Freshwater Applications', *Lewis Publishers, Inc., Chelsea., Michigan.*, pp. 141-148.

Matsuura, H., and Cannon, G. A. (1997) 'Wind Effects on Sub-Tidal Currents in Puget Sound', *Journal of Oceanography*, Vol.53, pp. 53-66.

Maughan, B. C. (2001) 'The effects of sedimentation and light on recruitment and development of a temperate, subtidal, epifaunal community', *Journal of Experimental Marine Biology and Ecology*, Vol.256, pp. 59-71.

McCalpin, J. D. (1994) 'A comparison of second-order and fourthorder pressure gradient algorithms in a sigma-coordinate ocean model', *Int. J. Numer. Methods Fluids*, Vol.18, pp.361-383.

McGurrin, J. M., Stone, R.B. and Sousa, R.J. (1989) 'rofiling United States artificial reef development.', *Bull. Mar. Sci.*, Vol.44(2), pp.1004-1013.

Mead, S., and Black, K. (1999) 'A multipurpose, artificial reef at Mount Maunganui Beach, New Zealand. ', *Coastal Management*, Vol.27, pp. pp.355-365.
Mingham, C. G., and Causon, D.M. (1998) 'Calculation of unsteady bore diffraction using a high resultion finite volume method', *Journal of Hydraulic Research*, Vol.38, pp. 49-56.

Miyoshi, T., and Kusano, K. (2005) 'A multi-state HLL approximate Riemann solver for ideal magnetohydrodynamics', *Journal of Computational Physics*, Vol.208, pp.315-344.

Mottet, M. G. (1981) *Enhancement of the marine environment for fisheries and aquaculture in Japan-Department of Fisheries, State of Washington.*

Msadek, R. (2005) *Hydrodynamic tidal model of Cook Strait-NIWA (National Institute of Water and Atmospheric Research).*

Nicoletti, L., Marzialetti, S., Paganelli, D., and Ardizzone, G.D. (2007) 'Long-term changes in a benthic assemblage associated with artificial reefs.', *Hydrobiologia*, Vol.580, pp.233-240.

Orszag, S. A., Yakhot, V., Flannery, W.S., Boysan, F., Choudhury, D., Maruzewski, J., and Patel, B. (1993) 'Renormalization Group Modeling and Turbulence Simulations', *International Conference on Near-Wall Turbulent Flows, Tempe, Arizona.*

Osher, S., and Solomon, F. (1982) 'Upwind difference schemes for hyperbolic conservation laws.', *Mathematics of Computation*, Vol.38, pp. 339-374.

Osman, R. W. (1977) 'Establishment and Development of a Marine Epi-FaunalCommunity', *Ecological Monographs*, Vol.47, pp. 37-63.

Page, H. M., Dugan, J.E., Schroeder, D.M., Nishimoto, M.M., Love, M.S., and Hoesterey, J.C. (2007) 'Trophic links and condition of a temperate reef fish:comparisons among offshore oil platform and natural reef habitats', *Marine Ecology Progress Series*, Vol.344, pp.245-256.

Palmer, M. A., Kjerfve, B., and Schwing, F.B. (1980) 'Tidal analysis and prediction in a south carlina estuary', *Contributions in Marine Science*, Vol.23, pp. 19-23.

Parker, B. (1991) *Tidal Hydrodynamics-New York, J. Wiley*-pp.883.

Parkinson, K. M. (1999) 'Environmental consequences of offshore wind powe generation', (Dissertation submitted as part of MSc Estuarine and Coastal Science and Management, University of Hull.).

Pawlik, J. R. (1992) 'Chemical ecology of the settlement of benthic marine invertebrates', *Oceanography and Marine Biology*, Vol.30, pp. 273-335.

Perlin, A., Moum, J.N., Klymak, J.M., Levine, M.D., Boyd, T., and Kosro, P.M. (2005) 'A modified law-of-the-wall applied to oceanic bottom boundary layers', *JOURNAL OF GEOPHYSICAL RESEARCH*, Vol.110, pp.C10S10.

Pickering, H., and Whitmarsh, D. (1997) 'Artificial reefs and fisheries exploitation: a review of the 'attraction versus production' debate, the influence of design and its significance for policy.', *Fisheries Research*, Vol.31, pp. 39-59.

Pitcher, T. J., Buchary, E.A., and Hutton, T. (2002) 'Forecasting the benefits of notake human-made reefs using spatial ecosystem simulation', *ICES Journal of Marine Science*, Vol.59, pp. S17-S26.

Polovina, J. J., and Sakai, I. (1989) 'Impacts of artificial reefs on fishery production in Shimamaki, Japan.', *Bull. Mar. Sci.*, Vol.44, pp. 997-1003.

Polovina, J. J. (1991) *Fisheries Applications and Biological Impacts of Artificial Habitats. In Artificial Habitats for Marine and Freshwater Fisheries-Ed. by W. Seaman and L. M. Sprague. Academic Press, Inc, San Diego-* pp.153-176.

Pondella, D. J., and Stephens, J.S. (1994) 'Factors affecting the abundance of juvenile fish species on a temperate artificial reef', *Bulletin of Marine Science*, Vol.55, pp.1216-1223.

Popinet, S. (2005) *Lunar tides in Cook Strait, New Zealand website-* (*http://gerris.dalembert.upmc.fr/gerris/examples/examples/tides.html#htoc20*).

Popinet, S. (2011) *Gerris examples"-* (*http://gfs.sourceforge.net/examples/examples/index.html*)

Praagman, N., Dijkzeul, J., van Dijk, R., and Plieeger, R. (1989) 'A finite difference simulation model for tidal flow in the English channel and the Southern North Sae', *Adv. Water Resources*, Vol.12, pp. 155-164.

Pugh, D. T. (1996) *Tides, Surges and Mean Sea-Level-JOHN WILEY SONS June 1996.* pp.72-82.

Relini, G. (1997) 'Biomass on artificial reefs. Proceedings of the 1st Conference of the European Artificial Reef Research Network', *Ancona, Italy*, Vol. 26-30 March 1996, pp.61-83.

Relini, G. (2000) 'The Loano Artificial Reef. In Artificial Reefs in European Seas', *Ed. by A. C. Jensen, K. J. Collins and A. P. M. Lockwood. Kluwer Academic Publishers.*, pp. 129-149.

Revenga, S., Fernandez, F., Gonzalez, J.L., and Santaella, E. (2000) 'Artificial Reefs in Spain: The Regulatory Framework. In Artificial Reefs in European Seas', *Ed. by A. C. Jensen, K. J. Collins and A. P. M. Lockwood. Kluwer Academic Publishers*, pp.185-194.

Rodda, K. R., Keesing, J.K., and Foureur, B.L (1997) 'Variability in larval settlement of abalone on artificial collectors', *Molluscan Research*, Vol.18(2), pp. 253-264.

Roe, P. L. (1981) 'Approximate riemann solvers, parameter vectors, and difference schemes.', *Journal of Computational Physics*, Vol.43, pp. 357-372.

Rogers, B. D., Borthwick, AGL., and Taylor, P.H. (2003) 'Mathematical balancing of flux gradient and source terms prior to using Roe's approximate Riemann solver', *Journal of Computational Physics* 192(2), pp. 422-451.

Rose, C. (2005) *Modelling and measuring the habitat complexity of artificial reefs-thesis - School of Marine scienece and technology- Newcastle University.*

Roulund, A., Sumer, B.M., Fredsoe, J., and Michelsen, J. (2005) 'Numerical and experimental investigation of flow and scour around a circular pile', *Journal of Fluid Mechanics*, Vol.534, pp. 351-401.

Sale, P. F. (1969) 'A suggested mechanism for habitat selection by the juvenile manini, Acanthurus triostegus sandvicensis Streets', *Behaviour*, Vol.35, pp. 27-44.

Sale, P. F. (1980) 'The ecology of fishes on coral reefs.', *Oceanography and Marine Biology Annual Review*, Vol.18, pp.367-421.

Salmon, R. (1999) 'The Lattice Boltzmann method as a basis for ocean circulation modeling', *J. Mar. Res.*, vol.57, pp.503-535.

Sanchez-Jerez, P., Gillanders, B.M., Rodriquez-Ruiz, S., and Ramos-Espla, A.A. (2002) 'Effect of an artificial reef in Posidonia meadows on fish assemblage and diet of Diplodus annularis', *ICES Journal of Marine Science*, Vol.59, pp. S59-S68.

Sanford, T. B., and Lien, R.C. (1999) 'Turbulent properties in a homogeneous tidal bottom boundary layer', *J. Geophys. Res.,*, Vol.104, pp. 245-1257.

Santos, M. N., Monteiro, C.C., and Lasserre, G. (1997) 'Finfish attraction and fisheries enhancement with artificial reefs: A review. In European Artificial Reef Research', *Proceedings of the 1st EARRN conference, Ancona, Italy March 1996*, Ed. by A. C. Jensen. Southampton Oceanography Centre, pp. 97-114.

Sauvaget, P., David, E., and Guedes Soares, C. (2000) 'Modelling tidal currents on the coast of Portugal', *Coastal Engineering*, Vol.40, pp. 393-409.

Sayer, M. D. J., and Wilding, T.A. (2002) 'Planning, licensing, and stakeholder consultation in an artificial reef development: the Loch Linnhe reef, a case study', *ICES Journal of Marine Science*, Vol.59, pp. S178-S185.

Schurman, P. (1941) *Manual of harmonic analysis and prediction of tides-U. S. Coast and Geodetic Survey -special publication No.98*-pp.311.

Seaman, W., and Sprague, L.M. (1991) 'Artificial Habitat Practices in Aquatic Systems. In Artificial Habitats for Marine and Freshwater fisheries', *Ed. by W. Seaman and L. M. Sprague. Academic Press, Inc, San Diego*, pp. 1-29.

Seaman, W., and Jensen, A.C. (2000) *Purposes and Practices of Artificial reef Evaluation. In Artificial reef evaluation: with application to natural marine habitats-CRC Press, LLC, Boca Raton, Florida, USA.* pp. 1-19.

Sheehy, D. J. (1982) 'The use of designed and prefabricated artificial reefs in the United-States.', *Marine Fisheries Review*, Vol.44, pp. 4-15.

Sheng, P. Y. (2000) 'Physical characteristics and engineering at reef sites. In: W.J.E. Seaman (Editor), Artificial reef evaluation: with application to natural marine habitats', *CRC Marine Science Series, CRC Press LLC, Boca Raton, Florida, USA.*, pp. 51-94.

Shepherd, S. A., Godoy, C. and Clarke, S.M. (1992) 'Studies on southern Australian abalone (genus Haliotis) XV. Fecundity of H. laevigata', *Journal of Malacological Society of Australia*, Vol.13, pp.115-121.

Shepherd, S. A., and Brown, L.D. (1993) 'What is an abalone stock: Implications for the role of refugia in conservation', *Canadian Journal of Fisheries and Aquatic Sciences,*, Vol.50, pp. 2001-2009.

Shyue, S. W., and Yang, K.T. (2002) 'Investigating terrain changes around artificial reefs by using a multi-beam echosounder.', *ICES Journal of Marine Science*, Vol.59, pp.S338-S342.

Simard, F. (1996) 'Socio-economic aspects of artificial reefs in Japan', *Proceedings of the First European Artificial Reef Research Network Conference, Ancona, Italy*, pp.233-240.

Simpson, R. L. (1996) 'Aspects of turbulent boundary-layer separation', *Prog. Aerospace Sci.*, Vol.32, pp. 457-521.

Sosa-Cordero, E., Arce, A.M., Aguilar-Davila, W., and Ramirez-Gonzalez, A. (1998) 'Artificial shelters for spiny lobster Panulirus argus (Latreille): an evaluation of occupancy in different benthic habitats', *Journal of Experimental Marine Biology and Ecology*, Vol.229, pp. 1-18.

Stanton, B. R., Goring, D.G., and Bell, R.G. (2001) 'Observed and modelled tidal currents in the New Zealand region', *New Zealand Journal of Marine and Freshwater Research*, Vol.35(2), pp.397-415.

Steimle, F., Foster, K., Kropp, R., and Conlin, B. (2002) 'Benthic macrofauna productivity enhancement by an artificial reef in Delaware Bay, USA', *ICES Journal of Marine Science*, Vol.59, pp. S100-S105.

Steinberg, P. D., Schneider, R., and Kjelleberg, S (1997) 'Chemical defenses of seaweeds against microbial colonization.', *Biodegradation* Vol.8, pp. 211-220.

Stephens, J. J., and Pondella, D.I. (2002) 'Larval production of a mature artificial reef: the ichthyoplankton of King Harbor, California, 1974-1997', *ICES Journal of Marine Science*, Vol.59, pp. S51-S58.

Stevens, C., and Sutton, P. (2007) 'Measuring Tidal Currents near Cook Strait, NZ (ADCP Flow Surveys)', *Hydro International* Vol.11,number 8.

Stewart, R. H. (2008) 'introduction to physical oceanography ', pp. 48-50.

Stone, R. B. (1985) 'History of artificial reef use in the United States. In: D'Itri FM (ed) Artificial reefs: marine and freshwater applications.', *Lewis Publishers Inc., Michigan*, pp.3-11.

Su, D. T., Liu, T.L., and Ou, C.H. (2007) 'A Comparison of the PIV Measurements and Numerical Predictions of the Flow Field Patterns within an Artificial Reef', *17th international offshore and polar engineering conference (ISOPE), Lisbon*, Vol.1-4, pp.2239-2245.

Sumer, B. M. a. F., J. (2001) 'Scour around Pile in Combined Waves and Current', *Journal of Hydraulic Engineering*, Vol.127(5), pp. 403-411.

Svane, I., and Peterson, J.K. (2001) 'On the problems of epibioses, fouling and artificial reefs, a review', *Marine Ecology-Pubblicazioni Della Stazione Zoologica Di Napoli I*, Vol.22, pp.169-188.

Tegner, M. J., and R. A. Butler (1985) 'Drift-tube study of the dispersal potential of green abalone (*Haliotis fulgens*) in the Southern Californ ia Bight: Implications for recovery of depleted populations', *Marine Ecology Progress Series*, Vol.26, pp. 73-84.

The Danish Forest and Nature Agency, D. E., Vattenfall, Danish Energy Authority (2006) 'Danish offshore wind - key environmental issues. ISBN: 87-7844-625-0, (Copenhagen, Denmark) (http://193.88.185.141/Graphics/Publikationer/Havvindmoeller/havvindmoellebog_nov_2006_skrm.pdf)'.

Thierry, J. M. (1988) 'Artificial reefs in Japan - a general outline', *Aquacultural Engineering*, Vol.7, pp.321-348.

Toro, E., Spruce, M., and Speares, W. (1994) 'Restoration of the contact surface in the HLL-Riemann solver', *Shock Waves*, Vol.4(1), pp.25-34.

Toro, E. F. (1997) *Riemann Solvers and Numerical Methods for Fluid Dynamics: A Practical Introduction- Berlin/New York: Spinger.*

Toro, E. F. (2001) *shock-capturing methods for free-surface shallow flows-Chichester:John Wiley & Sons.*

Trujillo, A. P., and Thurman, H.V. (2010) *Essentials of Oceanography-Publisher: Prentice Hall.*

Tsimplis, M. N. (2012) 'Vertical structure of tidal currents over the Camarinal Sill at the Strait of Gibraltar', *Journal of Geophysical Research: Oceans*, Vol.105(C8), pp.19709-19728.

Turpin, R. K., and Bortone, S.A. (2002) 'Pre- and post-hurricane assessment of artificial reefs: evidence for potential use as refugia in a fishery management strategy', *ICES Journal of Marine Science*, Vol.59, pp.S74-S82.

Valiani, A., Caleffi, V., and Zanni, A. (1999) 'Finite volume scheme for 2D shallow-water equations application To a flood event in the Toce river', *CADAM*.

VanLeer, B. (1977) 'Towards the ultimate conservative difference scheme iv. a new approach to numerical convection.', *Journal of Computational Physics*, Vol.23, pp.276-299.

Venayagamoorthy, S. K., Ku.H., Fringer, O.B., Chiu, A., Naylor, R.L. and Koseff, J.R. (2011) 'Numerical modeling of aquaculture dissolved waste transport in a coastal embayment', *Environmental Fluid Mechanics* Vol.11(4), pp.329-352.

Wall, R. G., Nystrom, E.A. and Litten, S. (2006) *Use of an ADCP to Compute Suspended–Sediment Discharge in the Tidal Hudson River, New York-Scientific Investigations Report 2006- U.S. Department of the Interior -U.S. Geological Survey.* pp.1-3.

Walters Roy, A. (1989) 'A comparison of two finite element models of tidal hydrodynamics using a North Sea data set', *Advances in Water Resources*, Vol.12(4), pp.184-193.

Wang, C.-H., and Sato, Osamu. (1986) 'Hydrodynamic Characteristics in Simplified Components of Artificial Reef Structures', *Bull. Fac. Fish. Hokkaido Univ.*, Vol.37, pp.190-206.

Weisburd, S. (1986) 'Artificial reefs', *Science News*, Vol.30, pp.59.

Werner, F. E., and Lynch, D.R. (1987) 'Field verification of wave equation tidal dynamics in the English Channel and southern North Sea', *Advances in Water Resources*, Vol.10, pp.115-130.

Whitmarsh, D., Pickering, H., and Sarch, M.T. (1995) *Economic appraisal of artificial reef structures for lobster production - final report. Centre for Coastal Zone Managen1ent-University of Portsmouth*. pp.130.

Whitmarsh, D., Santos, M.N., Ramos, J., and Monteiro, C.C. (2008) 'Marine habitat modification through artificial reefs off the Algarve (southern Portugal): An economic analysis of the fisheries and the prospects for management', *Ocean & Coastal Management*, Vol.51, pp. 463-468.

WHOI (2012) *Ocean Instruments (http://www.whoi.edu/instruments/viewInstrument.do?id=819)*.

Wickins, J. (1994) 'Understanding young lobsters', *Fishing News*,

Wilding, T. A., and Sayer, M.D.J. (2002a) 'Evaluating artificial reef performance: approaches to pre- and post-deployment research', *ICES Journal of Marine Science*, Vol.59, pp. S222-S230.

Wilding, T. A., and Sayer, M.D.J. (2002b) 'The physical and chemical performance of artificial reef blocks made using quarry by-products', *ICES Journal of Marine Science*, Vol.59, pp.S250-S257.

Wilding, T. A. (2003) 'The prediction and assessment of the environmental impacts of the Loch Linnhe Artificial Reef-Thesis-Sep.2003',

Wilding, T. A. (2006) 'The benthic impacts of the Loch Linnhe artificial reef.', *Hydrobiologia* Vol.555, pp. 345-353.

Wilding, T. A. (2010) *The Loch Linnhe Artificial Reef overview, status and science programme-Scottish Association for Marine Science-Presentation.*

Wilhelmsson, D., Malm, T., and Ohman, M.C. (2006) 'The influence of offshore windpower on demersal fish', *ICES Journal of Marine Science*, Vol.63, pp. 775-784.

Wilson, J., Osenberg, C.W., Mary, C. ST., Watson, C.A., and Lindberg, W.J. (2001) 'Artificial reefs, the attraction-production issue, and density dependence in marine ornamental fishes', *Aquarium Sciences and Conservation*, Vol.3, pp. 95-105.

Wolf, J., Hubbert, K.P., and Flather, R.A. (1988) 'A feasibility study for the development of a joint surge and wave model', *Proudman Oceanographic Laboratory Report*, Vol.1, pp.109.

Wolf, J., and Prandle, D. (1999) 'Some observations of wave–current interaction', *Coastal Engineering*, Vol.37, pp. 471-485.

Wolfson, A., Van Blaricom, G., Davis, N., and Lewbel, G.S. (1979) 'Marine life of an offshore oil platform', *Marine Ecology-Progress Series*, Vol.1, pp.81-89.

Wu, J. (1982) 'Wind-Stress Coefficients Over Sea Surface From Breeze to Hurricane', *Journal of geophysical research* Vol.87, pp. 9704-9706.

Yamane, T. (1989) 'Status and future-plans of artificial reef projects in Japan.', *Bulletin of Marine Science*, Vol.44, pp. 1038-1040.

Yang, J., Kitazawa, D., and Yamanaka, R. (2008) 'Numerical Study on the Hydrological Change due to Water Level Rising in the Caspian Sea ', *OCEANS 2008 - MTS/IEEE Kobe Techno-Ocean*, (8-11 Aprill 2008), pp. 1 - 5.

Yu, Z., and Kyozuka, Y. (2004) 'A Discontinuous Galerkin Finite Element Shallow Water Model in Simulating Tidal Flows', *OCEANS '04. MTTS/IEEE TECHNO-OCEAN '04*, Vol.3(9-12 Nov. 2004), pp. 1526 – 1531.

Zhang, H. H., and Sun, L. (2001) 'On reproduction increase of the sea aquatic resources by artificial fish-reef engineering', *Resources Science*, Vol.23(5), pp. 6-10.

Zhao, D. H., Shen, H.W., Tabios III, G.Q., Lai, J.S., and Tan, W.Y. (1994) 'A finite volume two-dimensional unsteady flow model for river basins', *J Hydraul Eng ASCE*, Vol.120, pp. 863–883.

Zhao, D. H., Shen, H.W., Lai, J.S., and Tabios III, G.Q. (1996) 'Approximate Riemann solvers in FVM for 2D hydraulic shock modelling', *J Hydraul Eng ASCE*, Vol.122, pp.692–702.

Zhixing, Y., and Kyozuka, Y. (2004) 'A discontinuous Galerkin finite element shallow water model in simulating tidal flows', *OCEANS '04. MTTS/IEEE TECHNO-OCEAN '04*, Vol.3, pp. 1526-1531.

Zhong, L., Feng, S., and Gao, S. (2005) 'Wind-driven ocean circulation in shallow water Lattice Boltzmann Model', *Adv. in Atmospheric Sci.*, Vol. 22, pp. 349-358.

Zhou, J. G., Causon, D.M., Mingham, C.G., and Ingram, D.M. (2001) 'The Surface Gradient Method for the Treatment of Source Terms in the Shallow-Water Equations', *Journal of Computational Physics*, Vol.168, pp. 1-25.

Zhou, J. G. (2002) 'A lattice Boltzmann model for the shallow water equations', *Comput. Methods Appl. Mech. Engrg.*, Vol.191, pp.3527–3539.

Zintzen, V., Norro, A., Massin, C., and Mallefet, J. (2008) 'Spatial variability of epifaunal communities from artificial habitat: Shipwrecks in the Southern Bight of the North Sea', *Estuarine Coastal and Shelf Science*, Vol.76, pp.327-344.

Zoppou, C., and Roberts, S. (1999) 'Catastrophic Collapse of Water Supply Reservoirs in Urban Areas.', *Journal of Hydraulic Engineering, ASCE*, Vol.125(7), pp.686-695.